

University of Modena and Reggio Emilia
Doctorate School in Industrial Innovation Engineering
XXXII Cycle

**Critical Issues in Design of
High-Performance Synchronous
Machines**

Doctoral Dissertation of
Ambra Torreggiani

Tutor:

Prof. Emilio Lorenzani

Doctorate School Dean:

Prof. Franco Zambonelli

Index

Glossary	IX
Symbols	XI
Abstract	1
Abstract	3
Introduction.....	5
1. Maxwell's Equations and their Application in Finite Element Analysis [2].....	9
1.1. Differential Maxwell's Equations in the Vacuum	9
1.2. Forces Associated to the Electric and Magnetic Fields	10
1.3. Media Polarization	11
1.3.1. Ohm's Law	11
1.3.2. Dielectric Media	12
1.3.3. Magnetic Media	13
1.3.4. Charge Conservation Law with Media Polarization.....	13
1.4. Maxwell's Equations with Media Polarization	14
1.5. Potential Equations.....	16
1.5.1. Magnetostatics	17
1.5.2. Magneto-Dynamics.....	19
1.6. Application of Maxwell's Equations to Finite Element Analysis.....	21
1.6.1. Magnetostatics Problems [3]	21
1.6.2. Time-Harmonic Magnetic Problems [3].....	22
1.7. Two-Dimensional Finite Element Analysis (2D-FEA) [4].....	24
1.7.1. Boundary Conditions	26
1.7.2. Calculations of the Final Solution	27
2. Control Equations of Brushless Sinusoidal Synchronous Machine.....	31
2.1. Isotropic Electrical Machine	32
2.1.1. Total Linkage Flux Component $\Lambda_{s,cp}$	32
2.1.2. Permanent-Magnet linkage Flux $\lambda_{s,pm}$	35
2.1.3. Motor Equation in the Two-Axis Stationary Frame	35
2.1.4. Motor Equations in Two-Axis Rotational Frame	37
2.1.5. Mechanical Torque Expression	40

2.1.6.	Model of the Isotropic Machine	42
2.2.	Anisotropic Electrical Machine	42
2.2.1.	Total Linkage Flux Component $\Lambda_{s,cp}$	42
2.2.2.	Motor Equations in Two-Axis Stationary Frame	46
2.2.3.	Motor Equations in Two-Axis Rotational Frame	47
2.2.4.	Mechanical Torque Expression for Anisotropic Machines	47
2.2.5.	Model of the Anisotropic Machine	48
2.3.	Control Strategies	49
2.3.1.	Stationary State Model	50
2.3.2.	Working Domain	50
2.3.3.	Maximum Torque Per Ampère Control Strategy (MTPA)	53
2.3.4.	Flux-Weakening Control Strategy (FW)	54
2.3.5.	Maximum Torque per Volt Strategy	55
3.	Analytical Design of Surface Permanent-Magnets Machine	57
3.1.	The Output Equation [5]	58
3.1.1.	Electric Loading \mathbf{A}	58
3.1.2.	Magnetic Loading \mathbf{B}	59
3.1.3.	TRV – Torque per Rotor Volume Equation	59
3.1.4.	Air Gap Shear Stress σ_g	60
3.1.5.	TRV Equation for an AC Sinusoidal Machine	62
3.2.	Analytical Design of Surface Permanent-Magnet Synchronous Machines	64
3.2.1.	Calculation of Carter’s Coefficient	67
3.2.2.	Design of Permanent-Magnets	68
3.2.3.	Geometrical Parameters	69
3.2.4.	Design Method with Constant Current Density	72
3.2.5.	Design Method with Constant Joule Losses	76
3.2.6.	Analytic Results Comparison of two Design Approaches	80
3.3.	Analytical and Finite Element Analysis Comparison	82
3.3.1.	Validation of Constant Current Density Approach	83
3.3.2.	Validation of Constant Joule Losses Approach	90
3.4.	Future Developments	95
4.	Robustness Analysis of Fractional-Slot Surface Permanent-Magnet Machines	97

4.1.	Fractional-Slot Surface Permanent-Magnet Machines	97
4.2.	Slot-Pole Combination	100
4.2.1.	Cogging Torque [17]	100
4.2.2.	Stator Magneto-Motive Force (MMF).....	100
4.3.	Analyzed Slot-Pole Combinations: Characteristics and Optimization	102
4.3.1.	Machine Optimization at Healthy Condition.....	103
4.3.2.	Performance of Optimized Slot-Pole Combinations at Healthy Condition 106	
4.4.	Robustness Analysis with Respect to Manufacturing Imperfections.....	107
4.4.1.	Eccentricity	107
4.4.2.	Permanent-Magnets Defects	112
4.5.	Machines Performance as Function of Manufacturing Defects Severity.....	114
4.6.	Robustness Analysis toward Manufacturing Defects as a Function of Slot-Pole Combinations	118
4.7.	Activity results	121
5.	Demagnetization Issues in Low Cost Synchronous Machines	123
5.1.	Low-Cost Synchronous Machines	123
5.2.	Design Techniques to Reduced Permanent-Magnet Eddy Currents	124
5.3.	Analyzed PM-SMs Motors	126
5.4.	Finite Element Analysis	131
5.5.	Experimental Tests.....	135
5.6.	Activity Results on Permanent-Magnet Demagnetization Issues	141
6.	Ironless Dual-Rotor Surface Permanent-Magnet Machine for Flywheel Batteries 142	
6.1.	Distributed Energy Generation	143
6.2.	Electrical Machine Requirements	145
6.3.	Finite Element Analysis of Iron Core and Ironless Surface Permanent-Magnet Machines.....	147
6.4.	MechSTOR Prototype.....	156
6.5.	Experimental Tests of MechSTOR Prototype.....	157
6.6.	Activity Results.....	160
7.	Design Optimization Issues for Pure Synchronous Reluctance Machines	161
7.1.	Principles of Pure Reluctance Machines.....	162
7.1.1.	Torque and Power Factor.....	163

7.1.2.	Rotor Basic Design.....	166
7.1.3.	D-axis Magnetizing Inductance $L_{s,mD}$	167
7.1.4.	Q-axis Magnetizing Inductance $L_{s,mQ}$	168
7.1.5.	Harmonic Losses	175
7.2.	Analytical Design Method for Reducing for Pulsating Torque in Pure and Assisted SyncRel Machines	176
7.2.1.	Torque Ripple Origin and Limitation Methods.....	178
7.2.2.	Analytical Design Method with Flux-Barrier Shifting	180
7.2.3.	Method Validation via Finite Element Analysis	182
7.3.	Design Optimization for Fault-Tolerant Applications.....	193
7.3.1.	Dual Three-Phase Winding Arrangement	194
7.3.2.	Machine FEA Optimization	196
7.3.3.	Dual Three-Phase Windings Magnetic Mutual Coupling	199
7.3.4.	Magnetic Model Variations.....	202
7.3.5.	Torque Behavior Variations	204
7.4.	Research Activities Results	208
8.	Conclusions	209
	References	213
	Acknowledgments	221
	Ringraziamenti	222
	Appendix	223
A.	Brief Review of Vectors	223
	Recall of Products with Vectors	224
B.	Scalar and Vectors Fields	227
	Scalar Field.....	227
	Vector Field.....	227
	Nabla Operator	229
C.	Charge Conservation Law	233
D.	Clarke's and Park's Transformations	234
	Clarke's Transformation: from a three-phase system to a two-axis stationary frame	234
	Park's Transformation: from two-axis stationary frame to two-axis rotational frame	238

Glossary

- FEA: Finite Element Analysis;
- PM: Permanent-Magnet;
- SPM: Surface Permanent-Magnet;
- FS: Fractional-Slots;
- THD: Total Harmonic Distortion;
- SPP: slot per pole per phase;
- SL: Single-Layer;
- DL: Double-Layer
- SyncRel: Synchronous Reluctance;
- MTPA: Maximum Torque per Ampère;
- FW: Flux-Weakening;
- MTPV: Maximum Torque per Volt.

Symbols

- j : imaginary unit (in engineering connotation);
- ∇ : Nabla operator;
- Q : electric charge [C]
- \vec{E} : electric field vector $\left[\frac{V}{m}\right] = \left[\frac{N}{C}\right]$;
- \vec{B} : magnetic flux density vector or induction vector [T];
- \vec{D} :
- \vec{H} : magnetic field vector $\left[\frac{A}{m}\right]$;
- \vec{A} : magnetic vector potential $\left[\frac{Vs}{m}\right]$;
- \vec{j} : current density vector $\left[\frac{A}{m^2}\right]$;
- \vec{j}_e : polarization current density $\left[\frac{A}{m^2}\right]$;
- \vec{j}_m : magnetization current density $\left[\frac{A}{m^2}\right]$;
- ϵ_0 : vacuum permittivity $8.854 \cdot 10^{-12} \left[\frac{F}{m}\right]$;
- μ_0 : magnetic vacuum permeability $4\pi \cdot 10^{-7} \left[\frac{H}{m}\right]$;
- c_0 : speed of light in vacuum $\approx 3 \cdot 10^9 \left[\frac{m}{s}\right]$;
- ϵ_r : relative permittivity;
- μ_r : magnetic relative permeability;
- ϵ : permittivity $\left[\frac{F}{m}\right]$;
- μ : magnetic permeability $\left[\frac{H}{m}\right]$;
- ρ : resistivity [$\Omega \cdot m$] or electric charge density per unit volume $\left[\frac{C}{m^3}\right]$;
- σ : conductivity $\left[\frac{C}{m}\right]$;
- \vec{M}_e : electric dipole moment [$C \cdot m$];
- \vec{M}_m : magnetic dipole moment [$A \cdot m^2$];
- ρ^* : polarization charge density per unit volume $\left[\frac{C}{m^3}\right]$;
- \vec{P} : electric polarization field vector $\left[\frac{C}{m^2}\right]$;
- \vec{M} : magnetic polarization [T];
- χ_e : electric susceptibility;
- χ_m : magnetic susceptibility;
- Φ : magnetic flux linked by a single turn [Wb];
- λ : linkage flux [Wb];
- L : self-inductance [H];
- M : mutual-inductance [H];
- C : capacitance [F];
- ξ : saliency ratio;
- L_S : synchronous inductance [H];

- L_{sd} : d-axis synchronous inductance [H];
- L_{sq} : q-axis synchronous inductance [H];
- $T_{u,v,w}^{\alpha,\beta}$: Clarke's matrix;
- $T_{u,v,w}^{\alpha,\beta t}$: Clarke's transpose matrix;
- $T_{\alpha,\beta}^{d,q}$: Park's matrix;
- $T_{\alpha,\beta}^{d,q t}$: Park's transpose matrix;
- D_o : stator outer diameter [mm];
- D_b : stator bore diameter [mm];
- x : stator diameter ratio;
- L_{stk} : lamination stack length [mm];
- g : air gap thickness [mm];
- k_C : Carter's coefficient;
- g_e : equivalent air gap thickness [mm];
- k_{fill} : slot filling factor;
- p : pole pairs;
- Q : stator slots;
- m : phase number;
- q : slot per pole per phase;
- w_{so} : slot opening [mm];
- w_t : tooth width [mm];
- τ_s : slot pitch [mm];
- N_{ph} : number of turns in series per phase;
- N : number of conductors in series per phase;
- n_{cs} : number of conductors in series per slots;

Abstract

The interest in permanent-magnets or pure reluctance synchronous machines has increased rapidly in the last years. This trend is a combination of factors: the technological progress and a closer attention to environmental issues to reduce greenhouse gas emissions and to support a green economy.

The diffusion of electrical machines in the industrial industry, transports and household appliances could be split in two types:

- Electrification, that means changing the technologies relying on non-renewable sources with hybrid or full electric systems;
- The transition from electrical machines based on traditional technologies, but less efficient, to more efficient electrical machines.

The automotive is major industry of the electrification process followed to the other transportation industries e.g. railways, aircraft, etc.

The 50% of global electric energy is converted in electric motor of which the 80% relies on traditional technologies. These motors are reliable, but less efficient. As a consequence, many companies are adopting more efficient motors or more convenient ones from a control point of view under the pressure of International Standards and European Directives.

The contribution of this thesis is developing design methods of synchronous electrical machines with the aim to improve their performance, reliability and fault-tolerant capability.

For that purpose, the research activity has focused on some fundamental issues. The first topic is the study of optimization machine design methods inclusive of typical manufacturing defects even in healthy machine conditions. The aim is analyzing the defect influence on performance and improving machine reliability and robustness. After this study, it is followed a research on the demagnetization issue of surface permanent-magnet machines with a special consideration of magnets eddy currents. The activity result is a new design of interior permanent-magnet rotor which has prototyped and tested.

The machine geometry has optimized according to both optimal and fault conditions; the design with the best performance in fault conditions has been chosen and it has been analyzed with respect to different parameters in healthy condition and with one faulty winding.

Abstract

L'interesse per le macchine elettriche sincrone a magneti permanenti o a riluttanza pura è cresciuto esponenzialmente negli ultimi anni. Questo trend è effetto di un insieme di fattori: l'evoluzione tecnologica e una maggiore attenzione alle tematiche ambientali per la riduzione dei gas a effetto serra e un'economia eco-sostenibile.

La diffusione delle macchine elettriche nell'industria, nei trasporti e nell'uso domestico potrebbe essere suddivisa in due tipologie:

- Elettrificazione, cioè il passaggio da tecnologie tradizionali basate su fonti non rinnovabili, a sistemi ibridi o completamente elettrici (full electric);
- Passaggio da macchine elettriche basate su vecchie tecnologie poco efficienti a macchine elettriche più efficienti.

Il processo di elettrificazione trova il suo massimo esponente nell'industria dell'automotive assieme agli altri settori dei trasporti e.g. ferroviario, aeronautico, etc.

Circa il 50% dell'energia elettrica mondiale è convertita da motori elettrici, di cui circa l'80% sono basati su vecchie tecnologie affidabili, ma meno efficienti. Sotto la spinta delle normative internazionali e delle direttive europee molte aziende stanno sostituendo di questi motori con altri più efficienti o che presentano vantaggi dal punto di vista del controllo.

Il contributo sviluppato in questa tesi di ricerca è focalizzato nel definire metodi di design delle macchine elettriche sincrone con l'obiettivo di migliorarne prestazioni, affidabilità e robustezza al guasto.

A tal scopo il lavoro di tesi si è concentrato su alcuni aspetti fondamentali. Il primo è stato lo studio di metodi di ottimizzazione del design della macchina, comprensivi dei tipici difetti di produzione anche in condizioni di macchina sana. Lo scopo è stato studiare gli effetti sulle performance, per migliorare affidabilità e robustezza alle imperfezioni. A questo, è seguita una ricerca sulla demagnetizzazione delle macchine a magneti permanenti superficiali con particolare attenzione alle correnti parassite nei magneti. Il risultato dell'attività è un nuovo design del rotore a magneti permanenti interni di cui sono stati realizzati e testati alcuni prototipi.

L'ultimo tema ha riguardato la capacità di resistenza al guasto di una macchina sincrona a riluttanza pura avente due avvolgimenti trifase indipendenti alimentanti da due inverter. La geometria della macchina è stata ottimizzata rispetto a condizioni ottimali e di guasto; la geometria con prestazioni al guasto migliori è stata scelta per analizzarne le prestazioni rispetto diversi parametri sia in condizioni ottimali che di guasto di uno dei due avvolgimenti.

Introduction

The employment of synchronous electrical machines has been exponentially increased in the last few years. This phenomenon could be attributed to a combination of factors: the technology improvement of the components for power electronics, e.g. SiC and GaN, more efficient storage energy systems, e.g. lithium-ion batteries, and new material and manufacturing technologies for electrical machines e.g. lower cost of rare-earth permanent-magnet or high frequency electric steels.

Simultaneously, the awareness towards environmental and climatic issues has been increasing with the aim to reduce global greenhouse emissions (e.g. CO₂) and moving towards a greener economy. As a consequence, many legislative authorities and International Organizations included in their Directives and Standards more and more attention toward an efficient use of energy, pushing different countries to incentivize the transition from fossil-based energy systems to renewable-based energy systems.

Focusing on the electric energy, the electric industry is accountable of nearly the 35% of greenhouse emission, moreover this energy is produced exploiting fossil fuels such as coal (43%) and natural gas (19%) as shown in Figure 0-1 [1].

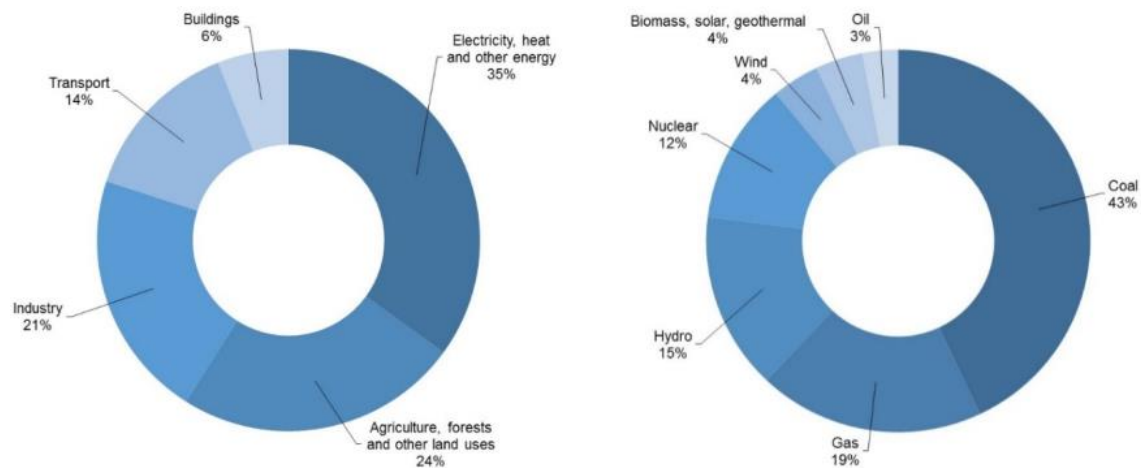


Figure 0-1: on the left the share quote of gas emissions shared by economic sectors, with a total amount of 49 Gt CO₂ equivalent per year 2010. On the right, the global electricity productions shares by energy source, with a total generation of 20000 TWh in 2015.

Since the nearly the 50% of the global electric energy consumption is transformed in mechanical energy by means electric motors [1], the electrical machines are one of the key points to save electric energy. According to this, electrical machine manufacturers and users have been moving from traditional line supplied induction motors (IM) to variable speed electric machines fed by inverter such permanent-magnets or pure synchronous reluctance machines or improving machine efficiency with design expedients and employing new materials.

The aforementioned spread of electrical machines in industrial applications, household appliances and transport could be split into two main categories:

- Electrification process, that is the transition from traditional technologies based on fossil energies to hybrid systems (i.e. internal combustion motor supported by a bi-directional electrical machine) or full-electric vehicles.
- Transition from traditional and less efficient electrical machines to more efficient ones (e.g. washing machine industry, little-medium size household appliance, etc.).

The main representative of the electrification process is the automotive industry, in fact in the last few years many automotive companies made huge investments in research and development in order to place on the market new hybrid or full electric vehicles. The electrification process is involving the entire transportation industry in more general terms such as railway, aircraft, naval or earth-moving machines.

Thanks to the technology improvement of power converters and the reduction of rare-earth magnet cost, the permanent-magnet synchronous machine (PM-SM) has been being one of the most adopted machine topologies. It is appreciated for its high efficiency, high power and torque density and power factor. On the other hand, pure synchronous reluctance (SyncRel) machine is getting more and more interest nowadays for its performance and in particular for the absence of permanent-magnet which allows to reduce the manufacturing cost. Nevertheless, SyncRel machine requires a very careful rotor design because of its high cogging torque and torque ripple.

The state-of-the-art offers many design optimization methods for the aforementioned synchronous machines, however, the spread of electrical machines is opening new design issues that needs to be addressed.

According to this, the novel contribution of this extensive research activity is to address the new requirements of electrical machines proposing design optimization method in order to improve performance, reliability and fault-tolerant capability. Reliability and fault-tolerance are becoming key features in those industries where human's safety and equipment downtime costs have a strong impact.

This thesis exposes the results activities achieved during these three years of PhD course on the design of synchronous electrical machines. The first part recalls some basic theories on the physical principals of electro-magnetic vector fields, Finite Element Analysis (FEA) tools and machine control models and strategies, then the contributions of this research work is in-depth exposed. The carried-out research activities have been oriented to improve their performance, reliability and fault-tolerant capability of synchronous electrical machines adopted in different applications.

The thesis is organized as follows: chapter §1 recalls Maxwell's equations and their application in FEA simulation software, while chapter §2 recalls the control basic of isotropic and anisotropic synchronous machines.

The chapter §3 proposed a simple analytical design approach for surface permanent-magnet synchronous machines (SPM-SMs) for low speed applications. The aim of this work is to propose a machine design strategy which allows a complete machine optimization. The proposed analytical approach has been analyzed according two different design assumptions which leads to different machine performance. The chapter §4 shows an extensive FEA simulation activity aimed to analyze the influence of the slot-pole combination on machine robustness with respect to typical manufacturing

imperfections. Since the slot-pole combination is a key design parameter, this research activity analyzed its influence not only on machines performance, but also machines reliability with respect to unavoidable manufacturing defects.

The chapter §5 shows a rotor re-design activity oriented to increase the fault-tolerant capability of a low-cost SPM-SM susceptible to permanent-magnets (PMs) demagnetization mounted on the rotor surface. Demagnetization could be the effect of the increase of PMs working temperature due to eddy currents induced by PWM switching frequency, space harmonics and MMF sub and higher order harmonics in case of concentrated winding. A new rotor geometry with inner permanent-magnets (IPM) is presented taking into account also leakage flux and mechanical stress issue of IPM rotor. Chapter §6 deals with the design of particular SPM-SM typology connected to a flywheel battery storage system of few kW for household application. The proposed machine is an ironless dual-rotor SPM-SM which allows eliminating the iron losses and obtaining an air gap MMF equivalent to that of traditional iron core machines.

Chapter §7 shows two different research activities on the design of synchronous reluctance (SyncRel) machines oriented to improve their performance in terms of pulsating torque and fault reliability by means a proper design of the machine rotor.

Finally, the conclusions sum up the contributions achieved through this research work on the design of synchronous electrical machines.

1. Maxwell's Equations and their Application in Finite Element Analysis [2]

This chapter deals Maxwell's Equation theory and its application in the electro-magnetic design of electrical machines by means Finite Element Analysis (FEA).

The Maxwell's equations are a set of differential equations that form the foundation of electromagnetism and electric circuits alongside the generalized Lorentz's Force Law. The appendix §A provides a brief recall of the vector theory used in Maxwell's equations.

Nowadays the electrical machine design is realized by means sophisticated FEA simulations tools (MagNet, FEMM, Motor-CAD etc.). Most of FEA softwares solve electro-magnetic problems by means Maxwell's equations; thus, a good knowledge should be required on the part of the machines designers in order to understand electro-magnetic phenomena occurring during the simulation and to correctly manipulate FEA results during post-processing.

The research activity results of this thesis have been carried out using finite element open software FEMM by David Meeker.

1.1. Differential Maxwell's Equations in the Vacuum

The electric vector field \vec{E} and the magnetic flux density vector field \vec{B} (or magnetic induction) are completely defined by their divergence and curl (see appendix B).

$$\begin{aligned}\nabla \cdot \vec{E} &= \frac{\rho}{\varepsilon_0} & \nabla \cdot \vec{B} &= 0 \\ \nabla \times \vec{E} &= -\frac{\partial \vec{B}}{\partial t} & c_0^2 \nabla \times \vec{B} &= \vec{j} + \frac{\partial \vec{E}}{\partial t}\end{aligned}\tag{Eq. 1-1}$$

where c_0^2 is the speed of light in vacuum expressed as:

$$c_0^2 = \frac{1}{\mu_0 \varepsilon_0}\tag{Eq. 1-2}$$

Dividing by c_0^2 the first and the second member the fourth equations of Eq. 1-1, the Maxwell's equations becomes are follows:

$$\begin{aligned}\nabla \cdot \vec{E} &= \frac{\rho}{\varepsilon_0} & \nabla \cdot \vec{B} &= 0 \\ \nabla \times \vec{E} &= -\frac{\partial \vec{B}}{\partial t} & \nabla \times \vec{B} &= \mu_0 \vec{j} + \mu_0 \varepsilon_0 \frac{\partial \vec{E}}{\partial t}\end{aligned}\tag{Eq. 1-3}$$

The divergence equations can be obtained from the curl equations by means the Divergence Theorem and the Stokes' Theorem (see appendix §B), the Charge Conservation Law (see appendix §C) and postulating to zero the constants terms of Maxwell's equations.

1.2. Forces Associated to the Electric and Magnetic Fields

The generalized Lorentz's Force describes the force \vec{F} acting on a moving point charge q in presence of electromagnetic fields.

$$\vec{F} = q(\vec{E} + \vec{v} \times \vec{B}) \quad \text{Eq. 1-4}$$

The electric field is described by means the Coulomb's Force \vec{F}_e acting on a point charge q plunged in the electric field \vec{E} :

$$\vec{F}_e = q\vec{E} \quad \text{Eq. 1-5}$$

$$\vec{E} = \frac{\vec{F}_e}{q} \left[\frac{N}{C} \right] = \left[\frac{V}{m} \right] \quad \text{Eq. 1-6}$$

The work of the electric field is always non-zero valued according to the physical definition of work which is given by the dot product of the force and the unit vector position \vec{dl} along the path from the initial point A to the final point B.

$$W_e = \int_A^B \vec{F}_e \cdot \vec{dl} = \int_A^B q\vec{E} \cdot \vec{dl} \neq 0 \quad \text{Eq. 1-7}$$

The induction magnetic field is described by the Lorentz's Force acting on a moving point charge q in a induction magnetic field \vec{B} .

$$\vec{F}_m = q(\vec{v} \times \vec{B}) \quad \text{Eq. 1-8}$$

$$\vec{B} = \frac{\vec{F}_m}{qv \sin\theta} [T] \quad \text{Eq. 1-9}$$

The work of the magnetic field is zero because of the cross product.

$$W_m = \int_A^B \vec{F}_m \cdot \vec{dl} = \int_A^B q(\vec{v} \times \vec{B}) \cdot \vec{dl} = 0 \quad \text{Eq. 1-10}$$

1.3. Media Polarization

The electric and magnetic fields have an influence on the simple media. The strengths of electric and magnetic fields rely on material properties denoted as conductivity for conductors, permittivity for dielectrics and permeability for magnetic materials.

1.3.1. Ohm's Law

The traditional model of electric conductivity is explained by Ohm's Law, which generalized formula is expressed as follows:

$$\vec{j} = \sigma \vec{E} \quad \text{Eq. 1-11}$$

The term σ is the electric conductivity and its unit of measurement is Siemens to meter $\left[\frac{S}{m}\right]$. The inverse of the electric conductivity σ is the electric resistivity with symbol ρ and unit measure $[\Omega m]$. In terms of electric resistivity, the Ohm's law becomes as:

$$\vec{E} = \rho \vec{j} \quad \text{Eq. 1-12}$$

The symbol \vec{j} is the electric current density and it is worth noting how the electric current density is always non-negative and in the same direction of the applied electric field \vec{E} as shown in Figure 1-1.

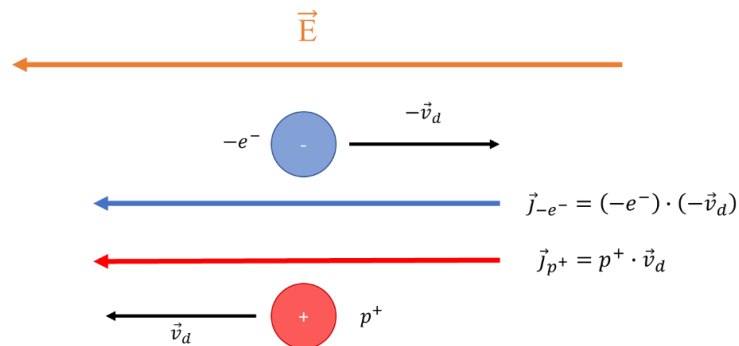


Figure 1-1: direction of density current vector \vec{j} .

1.3.2. Dielectric Media

When the non-conductive media called dielectric is subjected to an electric field \vec{E} the phenomenon of the electric polarization occurs. Given two-point charges q^+ and q^- placed at distance d , as in Figure 1-2, the amplitude of the electric dipole moment \vec{M}_e is defined as:

$$|\vec{M}_e| = q \cdot d \quad \text{Eq. 1-13}$$

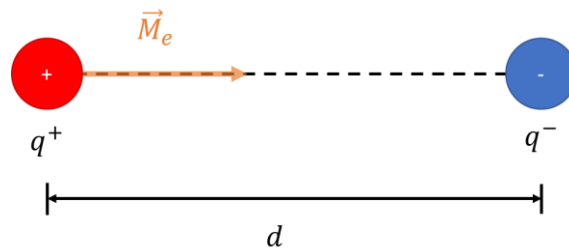


Figure 1-2: dipole moment between two-point charges at distance d .

The applied electric field \vec{E} acts on the dielectric media inducing electric dipoles, pulling positive charges (nucleus) and repelling electrons clouds. The final result is shown in Figure 1-3:

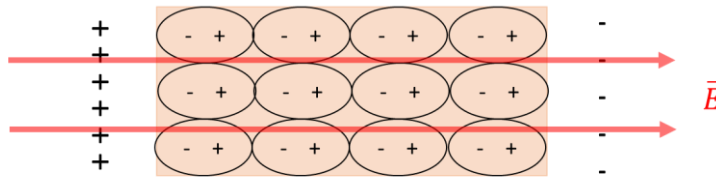


Figure 1-3: electric dipoles of a polarized dielectric media.

The state of the polarization is can by characterized by means a vector quantity called polarization density \vec{P} expressed as Eq. 1-14 and then the charge density distribution ρ^* inside the dielectric can be expressed as Eq. 1-15.

$$\vec{P} = \frac{\partial \vec{M}_e}{\partial \tau} \quad \text{Eq. 1-14}$$

$$\rho^* = -\nabla \cdot \vec{P} \quad \text{Eq. 1-15}$$

If steady conditions are not verified $\vec{E} = f(t)$, a current density vector \vec{j}_e is associated to electric charges.

$$\vec{j}_e = \frac{\partial \vec{P}}{\partial t} \quad \text{Eq. 1-16}$$

1.3.3. Magnetic Media

When a magnetic field \vec{H} is applied on a magnetic media, the magnetic domains point in the direction of the applied field, this phenomenon is called magnetic induction \vec{B} . In addition to \vec{B} there is also the contribution of the magnetic dipoles which has associated a magnetic field. This magnetic field arises either from electrons orbiting around atoms nucleus or from spinning charged particles, these moving charges form a current that rises to a magnetic dipole moment \vec{M}_m as shown in Figure 1-4.

$$|\vec{M}_m| = i \cdot d\Sigma \quad \text{Eq. 1-17}$$

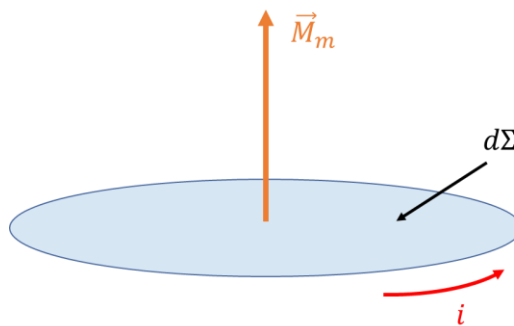


Figure 1-4: magnetic dipole moment \vec{M}_m on an infinitesimal surface.

Each infinitesimal part of the media becomes the location of an infinitesimal magnetic dipole moment $d\vec{M}_m$ which is proportional to the infinitesimal volume $d\tau$.

$$\vec{M} = \frac{d\vec{M}_m}{d\tau} \quad \text{Eq. 1-18}$$

where \vec{M} is the magnetization which is the cumulative contribution to induced magnetic dipoles to \vec{B} . This fact involves a current density \vec{j}_m :

$$\vec{j}_m = \nabla \cdot \vec{M} \quad \text{Eq. 1-19}$$

1.3.4. Charge Conservation Law with Media Polarization

Considering the new charge density ρ^* and current densities \vec{j}_e and \vec{j}_m ; the Charge Conservation Law with media polarization can be expressed as:

$$\nabla \cdot (\vec{j} + \vec{j}_e + \vec{j}_m) = -\frac{\partial}{\partial t}(\rho + \rho^*) \quad \text{Eq. 1-20}$$

Substituting the new physical quantities according to Eq. 1-15, Eq. 1-16 and Eq. 1-19, respectively, it will demonstrate that the charge conservation (appendix §C) is still valid also in presence of media polarization.

1.4. Maxwell's Equations with Media Polarization

The media polarization introduces new physical quantities that can be included in Maxwell's equations. Actually, only two Maxwell's equations are involved as shown in Eq. 1-21:

$$\nabla \cdot \vec{E} = \frac{\rho}{\varepsilon_0} \quad \nabla \times \vec{B} = \mu_0 \vec{j} + \mu_0 \varepsilon_0 \frac{\partial \vec{E}}{\partial t} \quad \text{Eq. 1-21}$$

The polarization charge density ρ^* can be added in the second member of the divergence of the electric field as follows:

$$\nabla \cdot \varepsilon_0 \vec{E} = (\rho + \rho^*) \quad \text{Eq. 1-22}$$

$$\nabla \cdot \varepsilon_0 \vec{E} = \rho - \nabla \cdot \vec{P} \quad \text{Eq. 1-23}$$

$$\nabla \cdot (\varepsilon_0 \vec{E} + \vec{P}) = \rho \quad \text{Eq. 1-24}$$

The electric polarization current density \vec{j}_e and the magnetic polarization current density \vec{j}_m are added to the current density \vec{j} in the second member of the curl of the magnetic flux density as:

$$\nabla \times \vec{B} = \mu_0 (\vec{j} + \vec{j}_e + \vec{j}_m) + \mu_0 \varepsilon_0 \frac{\partial \vec{E}}{\partial t} \quad \text{Eq. 1-25}$$

$$\nabla \times \frac{\vec{B}}{\mu_0} = \vec{j} + \frac{\partial \vec{P}}{\partial t} + \nabla \times \vec{M} + \varepsilon_0 \frac{\partial \vec{E}}{\partial t} \quad \text{Eq. 1-26}$$

$$\nabla \times \left(\frac{\vec{B}}{\mu_0} - \vec{M} \right) = \vec{j} + \frac{\partial}{\partial t} (\varepsilon_0 \vec{E} + \vec{P}) \quad \text{Eq. 1-27}$$

According to Eq. 1-24 and Eq. 1-27, Maxwell's equations with media polarization are expressed as in Eq. 1-28.

$$\begin{aligned} \nabla \cdot (\varepsilon_0 \vec{E} + \vec{P}) &= \rho & \nabla \cdot \vec{B} &= 0 \\ \nabla \times \vec{E} &= -\frac{\partial \vec{B}}{\partial t} & \nabla \times \left(\frac{\vec{B}}{\mu_0} - \vec{M} \right) &= \vec{j} + \varepsilon_0 \frac{\partial}{\partial t} (\varepsilon_0 \vec{E} + \vec{P}) \end{aligned} \quad \text{Eq. 1-28}$$

From the first and the fourth equations of Eq. 1-28 can be defined two new vector quantities: the electric displacement field \vec{D} and the magnetic field \vec{H} expressed with the following formulas.

$$\vec{D} = \epsilon_0 \vec{E} + \vec{P}$$

$$\vec{H} = \frac{\vec{B}}{\mu_0} - \vec{M} \quad \text{Eq. 1-29}$$

If media is considered with a linear and isotropic behavior, the vectors \vec{P} and \vec{M} can be expressed in terms of the electric and the magnetic fields by means two linear equations and two constants: electric susceptibility χ_e and the magnetic susceptibility χ_m .

$$\vec{P} = \epsilon_0 \chi_e \vec{E} \quad \text{Eq. 1-30}$$

$$\vec{M} = \chi_m \vec{H} \quad \text{Eq. 1-31}$$

Substituting Eq. 1-30 and Eq. 1-31 in equation Eq. 1-29, the electric permittivity ϵ and magnetic permeability μ are defined as follows:

$$\epsilon = \epsilon_0(1 + \chi_e) \quad \text{Eq. 1-32}$$

$$\mu = \mu_0(1 + \chi_m) \quad \text{Eq. 1-33}$$

Thus, the constitutive equations are expressed as follows:

$$\vec{D} = \epsilon \vec{E} \quad \text{Eq. 1-34}$$

$$\vec{B} = \mu \vec{H} \quad \text{Eq. 1-35}$$

Eq. 1-36 shows the Maxwell's equations including the electric displacement \vec{D} and the magnetic field \vec{H} .

$$\begin{aligned} \nabla \cdot \vec{D} &= \rho & \nabla \cdot \vec{B} &= 0 \\ \nabla \times \vec{E} &= -\frac{\partial \vec{B}}{\partial t} & \nabla \times \vec{H} &= \vec{j} + \frac{\partial \vec{D}}{\partial t} \end{aligned} \quad \text{Eq. 1-36}$$

1.5. Potential Equations

The divergence of vector field \vec{B} is assumed equal to zero, thus the induction field is defined as a solenoidal field. According to this assumption, the vector \vec{B} can be expressed as the curl of a vector potential with symbol \vec{A} and called magnetic vector potential.

$$\vec{B} = \nabla \times \vec{A} \quad \text{Eq. 1-37}$$

Since, the divergence of the curl is always equal to zero, the Eq. 1-37 is verified.

The vector potential admitted by a solenoidal field is not unique, indeed there are a lot of different magnetic vector potentials \vec{A} that can give rise to the same induced magnetic field \vec{B} . This change of vector potential \vec{A} is called *gauge transformation* and it states that any vector potential can be defined up to an additive gradient of a scalar field φ .

$$\vec{A}' = \vec{A} + \nabla\varphi \quad \text{Eq. 1-38}$$

This fact is true because the curl of a gradient is always zero, thus the curl of Eq. 1-38 becomes as:

$$\nabla \times \vec{A}' = \nabla \times \vec{A} \quad \text{Eq. 1-39}$$

Since a vector field is completely defined by its divergence and curl, the divergence of vector potential has to be expressed.

$$\nabla \cdot \vec{A}' = \nabla \cdot \vec{A} + \nabla \cdot \nabla\varphi \quad \text{Eq. 1-40}$$

The divergence of vector potential can be expressed in two different conditions: magnetostatics and magneto-dynamics.

1.5.1. Magnetostatics

The magnetostatics studies the time-invariant magnetic fields, where the electric currents induce the magnetic field and are approximately at the steady state. The magnetostatics equations can be used to predict very fast magnetic switching events that occur on scale time of nanoseconds or less.

$$\frac{\partial \vec{H}}{\partial t} \approx 0 \quad \frac{\partial \vec{D}}{\partial t} \ll \vec{j} \quad \text{Eq. 1-41}$$

In magnetostatics, the divergence of the magnetic vector potential \vec{A} is set to zero because of the assumption of the Coulomb's gauge:

$$\nabla \cdot \vec{A} = 0 \quad \text{Eq. 1-42}$$

The Maxwell's equations connected to the magnetic field become:

$$\begin{aligned} \nabla \cdot \vec{B} &= 0 \\ c_0^2 \nabla \times \vec{B} &= \frac{\vec{j}}{\varepsilon_0} \end{aligned} \quad \text{Eq. 1-43}$$

where $\vec{B} = \mu_0 \vec{H}$. The induction vector \vec{B} is substituted with the vector potential:

$$c_0^2 \nabla \times (\nabla \times \vec{A}) = \frac{\vec{j}}{\varepsilon_0} \quad \text{Eq. 1-44}$$

$$\nabla(\nabla \cdot \vec{A}) - \nabla^2 \vec{A} = \mu_0 \vec{j} \quad \text{Eq. 1-45}$$

Since the divergence is zero, Eq. 1-45 becomes as:

$$\nabla^2 \vec{A} = -\mu_0 \vec{j} \quad \text{Eq. 1-46}$$

Since in the time domain derivatives are approximately zero, the electric field is a conservative field and can be expressed as the gradient of a scalar field φ .

$$\vec{E} = -\nabla \varphi \quad \text{Eq. 1-47}$$

By so doing, the divergence of the electric field becomes as:

$$\nabla^2 \varphi = -\frac{\rho}{\varepsilon_0} \quad \text{Eq. 1-48}$$

Finally, the potential equations on magnetostatics condition are:

$$\nabla^2 \vec{A} = -\mu_0 \vec{J}$$

$$\nabla^2 \varphi = -\frac{\rho}{\varepsilon_0}$$

Eq. 1-49

The first equation of Eq. 1-49 is called Poisson's Equation.

1.5.2. Magneto-Dynamics

In the magneto-dynamics condition, the time domain derivatives are different from zero. In addition, it is here possible to understand the origin of the electric displacement \vec{D} .

Given the Ampère's law and dividing by c_0^2 , the following equation is obtained:

$$\nabla \times \vec{B} = \mu_0 \vec{J} \quad \text{Eq. 1-50}$$

If the divergence is applied on Eq. 1-50, the divergence of current density would be zero. However, this statement is in conflict with the charge conservation law, thus in order to overcome this condition, it is necessary to add another term to Ampère's law.

$$\nabla \times \vec{B} = \mu_0 \vec{J} + \mu_0 \epsilon_0 \frac{\partial \vec{E}}{\partial t} \quad \text{Eq. 1-51}$$

Applying the divergence on each member of Eq. 1-51, the charge conservation law is always verified.

Given the Faraday-Lenz's law and magnetic induction field \vec{B} expressed according to Eq. 1-37, the Faraday-Lenz's law becomes as:

$$\nabla \times \left(\vec{E} + \frac{\partial \vec{A}}{\partial t} \right) = 0 \quad \text{Eq. 1-52}$$

According to Eq. 1-52, the $\left(\vec{E} + \frac{\partial \vec{A}}{\partial t} \right)$ term is a conservative vector field; thus, a potential can be associated to it.

$$\left(\vec{E} + \frac{\partial \vec{A}}{\partial t} \right) = -\nabla \varphi \quad \text{Eq. 1-53}$$

The electric field \vec{E} has a new description as follows:

$$\vec{E} = -\nabla \varphi - \frac{\partial \vec{A}}{\partial t} \quad \text{Eq. 1-54}$$

Substituting the new definition of the electric field \vec{E} , in the Gauss' Law of Maxwell's equations, it becomes as:

$$\nabla^2 \varphi + \frac{\partial}{\partial t} (\nabla \cdot \vec{A}) = -\frac{\rho}{\epsilon_0} \quad \text{Eq. 1-55}$$

At the same time, the divergence of the magnetic vector potential can be expressed as:

$$\nabla \cdot \vec{A} = -\frac{1}{c_0^2} \frac{\partial \varphi}{\partial t} \quad \text{Eq. 1-56}$$

Thus, the first potential equation can be expressed as substituting Eq. 1-56 in Eq. 1-55:

$$\nabla^2 \varphi + -\frac{1}{c_0^2} \frac{\partial^2 \varphi}{\partial t^2} = -\frac{\rho}{\varepsilon_0} \quad \text{Eq. 1-57}$$

The second potential equation is found by means Ampère's Law:

$$c^2 \nabla \times \vec{B} = \vec{J} + \frac{\partial \vec{E}}{\partial t} \quad \text{Eq. 1-58}$$

Moving the time domain derivative of \vec{E} to the first member, substituting it as Eq. 1-54 and expressing the induction magnetic field \vec{B} as Eq. 1-37, the following equation is obtained:

$$c_0^2 \nabla(\nabla \cdot \vec{A}) - c_0^2 \nabla^2 \vec{A} + \frac{\partial}{\partial t} \nabla \varphi + \frac{\partial^2 \vec{A}}{\partial t^2} = \frac{\vec{J}}{\varepsilon_0} \quad \text{Eq. 1-59}$$

Substituting the divergence of the magnetic vector potential with Eq. 1-56, the second potential equation is obtained.

$$\nabla^2 \vec{A} - \frac{1}{c_0^2} \frac{\partial^2 \vec{A}}{\partial t^2} = -\frac{\vec{J}}{\varepsilon_0 c_0^2} \quad \text{Eq. 1-60}$$

Finally, the two potential equations are:

$$\nabla^2 \vec{A} - \frac{1}{c_0^2} \frac{\partial^2 \vec{A}}{\partial t^2} = -\frac{\vec{J}}{\varepsilon_0 c_0^2} \quad \text{Eq. 1-61}$$

$$\nabla^2 \varphi + -\frac{1}{c_0^2} \frac{\partial^2 \varphi}{\partial t^2} = -\frac{\rho}{\varepsilon_0} \quad \text{Eq. 1-62}$$

Most of FEA simulation tools use the potential equations to solve electro-magnetic problems because they are simpler to evaluate than electric and induction magnetic vector fields equations.

1.6. Application of Maxwell's Equations to Finite Element Analysis

Finite Element Analysis (FEA) software use Maxwell's equations to solve magnetic problems. Given a specific magnetic problem, the FEA addresses some limiting cases of Maxwell's equations.

The magnetic problems addressed by FEA are so called "low frequency problems" in which the displacement current \vec{D} can be ignored. In fact, at low frequencies the conduction current \vec{j} is higher and higher than the displacement current \vec{D} .

The FEA can address both magnetostatics and time-harmonic magnetic problems by solving Maxwell's equations.

1.6.1. Magnetostatics Problems [3]

The magnetostatics problems is characterized by time-invariant the fields. Thus, the Maxwell's Equations related to the magnetic field are as follows.

$$\nabla \times \vec{H} = \vec{j} \quad \text{Eq. 1-63}$$

$$\nabla \cdot \vec{B} = 0 \quad \text{Eq. 1-64}$$

In addition, it is also considered the constitutive relationship between the flux density vector field \vec{B} and the magnetic vector field \vec{H} . If the media is non-linear, the permeability μ is expressed as a function of \vec{B} as:

$$\mu = \frac{\vec{B}}{\vec{H}(\vec{B})} \quad \text{Eq. 1-65}$$

The FEA goes about finding a field that satisfies Eq. 1-63÷Eq. 1-65 via the magnetic vector potential approach seen in chapter §0. The FEA retains also Eq. 1-65, so magnetostatics problems can be solved also with a non-linear $\vec{B} - \vec{H}$ relationship.

According to this definition, the divergence of \vec{B} is always zero, thus the Ampère's law can be written as:

$$-\frac{1}{\mu} \nabla^2 \vec{A} = \vec{j} \quad \text{Eq. 1-66}$$

If FEA is a two-dimensional problem solver, the vector \vec{A} has only one component in the "out of the page" direction. The great advantage of using the vector potential formulation is that all the conditions to satisfy are combined in a single equation. If the vector potential \vec{A} is found, then vectors \vec{B} and \vec{H} can be deduced by differentiating vector potential \vec{A} .

1.6.2. Time-Harmonic Magnetic Problems [3]

If the magnetic field is time-varying, eddy current can be induced in materials with non-zero conductivity. Thus, Maxwell's equations related to the electric field distribution must also be taken into account.

Considering the curl of electric field \vec{E} , the induction field \vec{B} can be substituted with Eq. 1-37, thus the equation becomes as:

$$\nabla \times \left(\vec{E} + \frac{\partial \vec{A}}{\partial t} \right) = 0 \quad \text{Eq. 1-67}$$

In two-dimensional problems, the Eq. 1-67 can be integrated to yield:

$$\vec{E} = -\frac{\partial \vec{A}}{\partial t} - \nabla V \quad \text{Eq. 1-68}$$

The electric field \vec{E} of Eq. 1-68 can be expressed by mean Eq. 1-11 and a new expression for the current density is obtained.

$$\vec{j} = -\sigma \frac{\partial \vec{A}}{\partial t} - \sigma \nabla V \quad \text{Eq. 1-69}$$

This current density can be substituted in the Ampère law for non-linear media:

$$\nabla \times \left(\frac{1}{\mu(\vec{B})} \nabla \times \vec{A} \right) = -\sigma \frac{\partial \vec{A}}{\partial t} + \vec{j}_{src} - \sigma \nabla V \quad \text{Eq. 1-70}$$

The current density \vec{j}_{src} represents the applied current source and ∇V term is an additional voltage gradient that, in two dimensional problems, is constant over a conductive body. FEA uses this voltage gradient in some harmonic problems to enforce constraints on the current carried by conductive regions.

If the field oscillates at one fixed frequency, FEA considers Eq. 1-70. Thus, a phasor transformation yields a steady-state equation that is solved for the amplitude and phase of vector potential \vec{A} . The phasor transformation is:

$$\vec{A} = \Re[a(\cos(\omega t) + j \sin(\omega t))] = \Re[ae^{j\omega t}] \quad \text{Eq. 1-71}$$

Substituting Eq. 1-71 in Eq. 1-70 and dividing out the complex exponential term yield to the equation solved by FEA for harmonic magnetic problems:

$$\nabla \times \left(\frac{1}{\mu_{eff}(\vec{B})} \nabla \times a \right) = -j\omega\sigma a + \bar{J}_{src} - \sigma \nabla V \quad \text{Eq. 1-72}$$

where \bar{J}_{src} represents the phasor transform of the applied current source.

The permeability μ should be constant for harmonic problems. However, FEA retains a non-linear relationship in the harmonic formulation, allowing to approximating the effect of saturation on the phase and the amplitude of the fundamental frequency of the field distribution. The form of the $\vec{B} - \vec{H}$ curve is not exactly the same as in the DC case. Instead, “effective permeability” μ_{eff} is selected to give the corret amplitude of the fundamental component of the waveform under sinusoidal excitation.

FEA also allows for the inclusion a complex and frequency-dependent permeability in time harmonic problems. These features allow the program to model materials with thin laminations and approximately model hysteresis effects.

1.7. Two-Dimensional Finite Element Analysis (2D-FEA) [4]

The design of electrical machines is generally led by solving magnetostatics problem via a Finite Element Analysis simulation tools. More accurate design and analysis should also require solving electrostatics, thermal, etc. problems.

FEA could be both two-dimensional (2D) and three-dimensional (3D), but the latter is more time consuming and requires performing computers. According to this the 2D-FEA is often chosen to carry out the design of electrical machines.

The electrical machine is conveniently divided according to its symmetries that could be of two types:

- Plane symmetry or x-y symmetry: the magnetic phenomena are assumed identical on each x-y plane which is orthogonal to an axis, denoted as z (see Figure 1-5). Generally, according to this symmetry type, the edge phenomena are disregarded;
- Axial symmetry or r-z symmetry: the magnetic phenomena are assumed identical on each semi-plane r-z obtained by the rotation around the symmetry axis z.

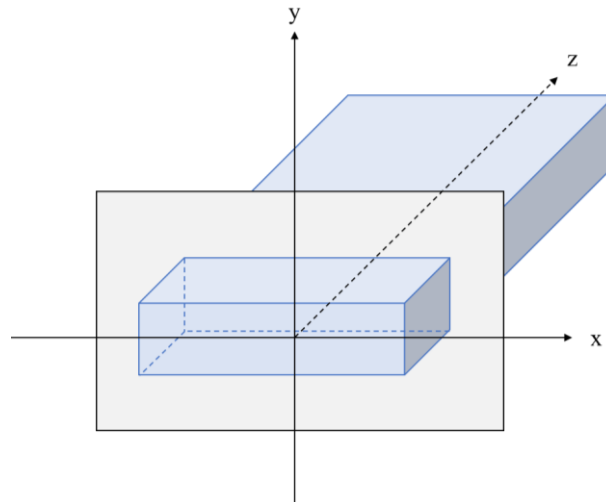


Figure 1-5: plane or x-y symmetry.

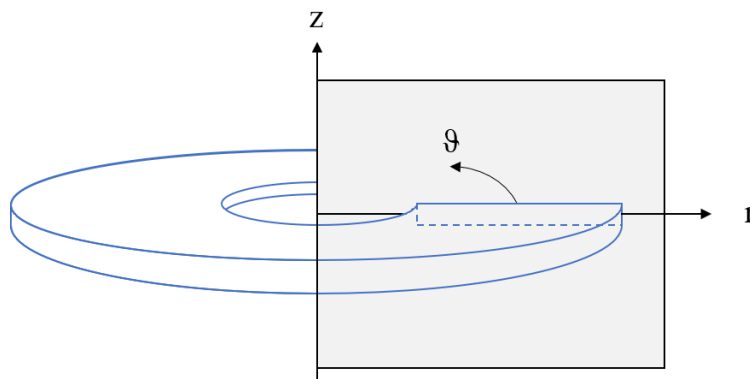


Figure 1-6: axial or r-z symmetry.

The 2D-FEA electrical machine design is carried out assuming plane symmetry where the z-axis is perpendicular to x-y planes. During the 2D-FEA design other assumptions are considered:

- The current density vector \vec{j} has only the z-axis component:

$$\vec{j} = [0, 0, \vec{j}_z] \quad \text{Eq. 1-73}$$

- The magnetic vector potential \vec{A} has only the z-axis component:

$$\vec{A} = [0, 0, \vec{A}_z] \quad \text{Eq. 1-74}$$

Therefore, magnetic vector potential \vec{A} is parallel to vector \vec{j} , in addition the Coulomb's gauge assumption is considered, thus $\nabla \cdot \vec{A} = 0$.

- The flux density field vector \vec{B} has component only on the plane (x, y):

$$\vec{B} = \left(\frac{\partial^2 A_z}{\partial y^2}, -\frac{\partial^2 A_z}{\partial x^2}, 0 \right) \quad \text{Eq. 1-75}$$

- The magnetic problem could be described according to Poisson's equation (see Eq. 1-46), considering a constant magnetic permeability μ :

$$\frac{\partial^2 A_z}{\partial x^2} + \frac{\partial^2 A_z}{\partial y^2} = -\mu j_z \quad \text{Eq. 1-76}$$

1.7.1. Boundary Conditions

According to Eq. 1-76, once the current density vector \vec{j}_z has been fixed, it could be found the magnetic vector potential \vec{A}_z for each point of the domain D, unless the behavior of the vector potential is known on the domain boundary Γ .

The assignment of boundary conditions is a key task, because on it depends the magnetostatics problem solutions. Given a 2D-FEA magnetostatics problem, three types of boundary conditions could be assigned:

- Dirichlet's condition;
- Neumann's condition;
- Periodic and antiperiodic conditions.

1.7.1.1. Dirichlet's Condition

The Dirichlet's condition states the value of magnetic vector potential \vec{A} on a specific boundary. Once the value of vector potential is fixed, the boundary becomes an equipotential line; therefore the flux density vector field \vec{B} are tangent to the equipotential boundary. This means that no field line crosses the equipotential boundary.

Generally, the homogeneous Dirichlet's condition is imposed fixing the vector potential equal to zero on the entire boundary or a part of it.

$$A_z = 0 \qquad \text{Eq. 1-77}$$

1.7.1.2. Neumann's Condition

This boundary condition imposes a fixed angle of incidence of vector field lines on a boundary. If the homogeneous Neumann's condition is considered, the vector field lines are orthogonal respect Dirichlet's conditions. According to homogeneous Neumann's condition, the magnetic flux density \vec{B} has only the perpendicular component respect the boundary.

Neumann's condition can be useful when the analyzed structure has one or more symmetry axes. The structure could be cut along the symmetry axis on which the Neumann's condition is applied. By so doing the FEA is done only over a portion of the analyzed structure and the final solution is the symmetrical one for the neglected part.

1.7.1.3. Periodic and Antiperiodic Conditions

These conditions impose a correspondence between the vector potential values on two or more boundaries of the analyzed structure. Given two or more boundaries, their vector potentials are expressed as a function of the vector potential of the main boundary.

These boundary conditions are useful when the analyzed structures present a periodicity of the electromagnetic phenomena even if they don't present either equipotential lines or symmetry axes.

If electrical machines present a periodicity t greater than 1 it is possible to analyse only a section of the machine, according to the ratio $\frac{1}{t}$, by imposing the following boundary conditions.

$$A_z(r, \vartheta) = +A_z\left(r, \vartheta + (2k)\frac{\pi}{t}\right); \quad k = 1, 2, 3, \dots \quad \text{Eq. 1-78}$$

The Eq. 1-78 is denoted as odd periodic boundary, in addition is possible to analyze a smaller sector of the electrical machine imposing the even or antiperiodic boundary expressed as Eq. 1-79.

$$A_z(r, \vartheta) = -A_z\left(r, \vartheta + (2k - 1)\frac{\pi}{t}\right); \quad k = 1, 2, 3, \dots \quad \text{Eq. 1-79}$$

Once the electrical machine geometry has been defined and the boundary conditions assigned, the next step is to define the electromagnetic characteristics of materials and magnetic field source (current density or permanent-magnets). Then the magnetostatics problem is solved via 2D-FEA.

1.7.2. Calculations of the Final Solution

The solution of the 2D-FEA is the value of magnetic vector potential A_z in each point of the domain D which can be used to compute the magnetic flux density vector field \vec{B} and the magnetic vector field \vec{H} .

1.7.2.1. Vector Field Line of Magnetic Flux Density \vec{B}

The magnetic flux density vector field \vec{B} is parallel to the equipotential lines of magnetic vector potential A_z as shown in Figure 1-7.

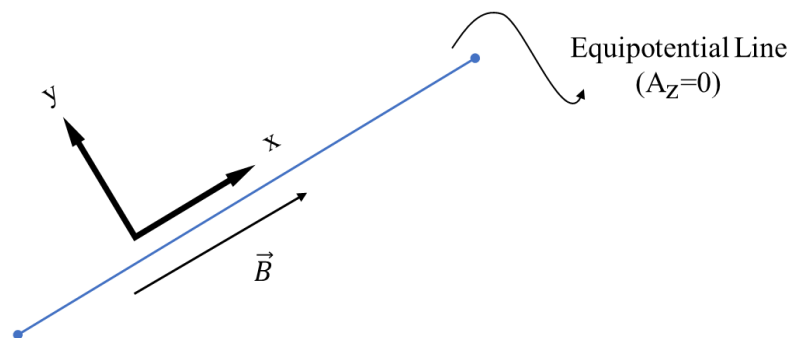


Figure 1-7: magnetic flux density behavior.

1.7.2.2. Magnetic Flux and Linkage Flux

The magnetic flux of the induction magnetic vector field \vec{B} through an oriented surface Σ is expressed as follows:

$$\Phi = \int_{\Sigma} \vec{B} \cdot \vec{n} \, d\Sigma = L_{stk} \int_{\Gamma} \vec{B} \cdot \vec{n} \, dl \tag{Eq. 1-80}$$

The Eq. 1-80 states that the surface integral corresponds to a line integral on the oriented path Γ since the magnetostatics problem is 2D as shown in Figure 1-9.

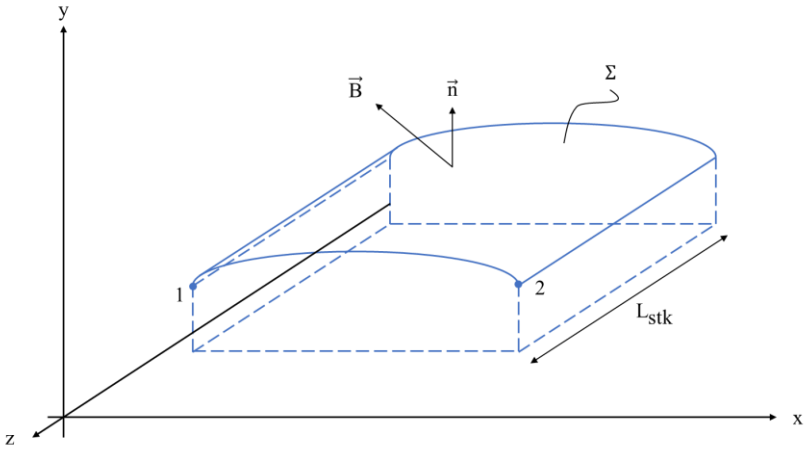


Figure 1-8: surface integration in three-dimensional problem.

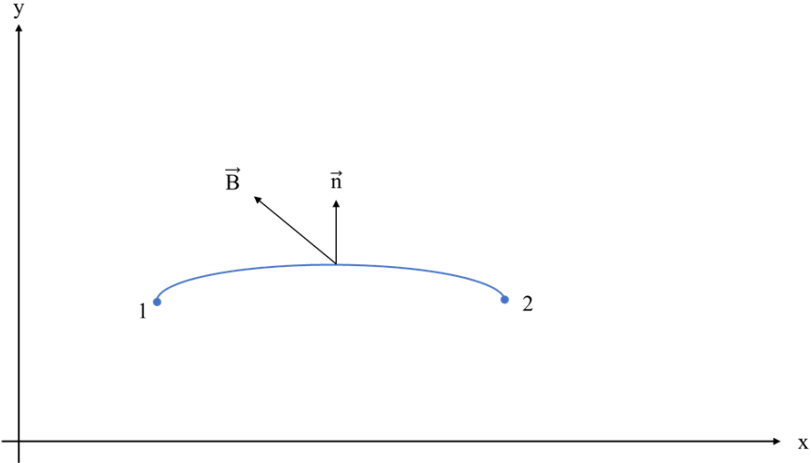


Figure 1-9: surface integration in two-dimensional problem.

Thus, given an oriented path, the magnetic flux Φ is the product of the line integral of the magnetic flux density perpendicular to the oriented path and the lamination stack length.

Since the FEA solution provides the value of magnetic vector potential A_z , the magnetic flux Φ can be also expressed as:

$$\Phi = \int_{\Sigma} (\nabla \times \vec{A}) \cdot \vec{n} d\Sigma \quad \text{Eq. 1-81}$$

where the magnetic flux density is expressed according Eq. 1-37. Then according to the Stokes' theorem, the magnetic flux can be expressed as the circulation of the magnetic vector potential along the closed path Γ which is the edge of the open surface Σ :

$$\Phi = \int_{\Gamma} \vec{A} \cdot d\vec{l} \quad \text{Eq. 1-82}$$

Considering Figure 1-10 and a 2D magnetostatics problem, the circulation of vector potential results zero on the oriented path $1' \rightarrow 2'$ and $2 \rightarrow 1$, since the magnetic vector potential \vec{A} has only z-axis component. The remaining oriented paths have length L_{stk} and are parallel to magnetic vector potential \vec{A} which has a constant value equal to A_z . According to these considerations, the magnetic flux is the product between difference of the vector potential values of the two extreme points 1 and 2 and lamination stack length as:

$$\Phi = (A_{z1} - A_{z2})L_{stk} \quad \text{Eq. 1-83}$$

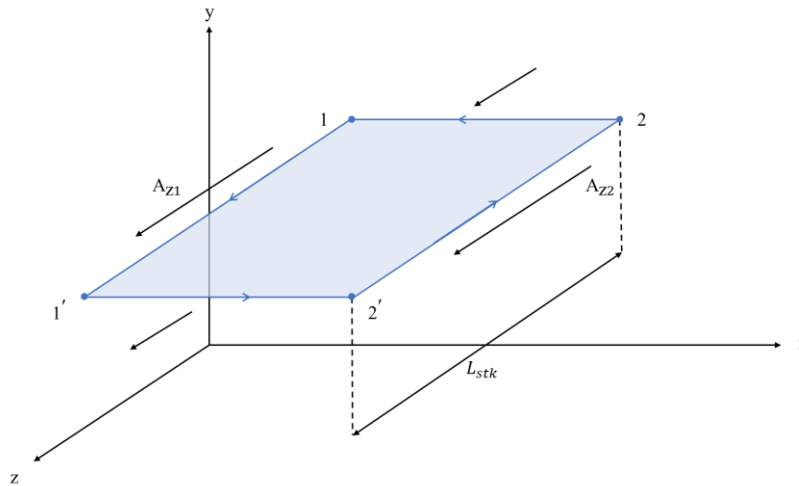


Figure 1-10: magnetic flux calculation by means vector potential \vec{A} .

2. Control Equations of Brushless Sinusoidal Synchronous Machine

This chapter describes the method to express the equations of brushless sinusoidal electrical machine in the rotating $d - q$ axis reference frame.

The equations will be described both for the isotropic machine and for the anisotropic machine. The *isotropic* term states that the stator synchronous inductances of $d - q$ axis have the same values, that is, the rotor magnetic permeance μ is equal in any radial direction. Whereas the *anisotropic* term suggests that the q -axis inductance is greater than the d -axis inductance if it is assumed the typical representation of $d - q$ rotational frame where the d -axis is oriented in the North direction of permanent-magnet magnetic axis.

The saliency ratio, denoted with the Greek letter ξ , gives information about the difference between the synchronous inductances of the two axes. The saliency ratio is expressed as follows:

$$\xi = \frac{L_{sq}}{L_{sd}} \quad \text{Eq. 2-1}$$

According to Eq. 2-1, isotropic machine has $\xi = 1$, while anisotropic machine has $\xi > 1$.

Generally, surface permanent-magnet machines (SPM) exhibit a saliency ratio equal to 1, thus $L_{sd} = L_{sq}$. On the other hand, inner permanent-magnet (IPM), assisted synchronous reluctance (PMSyncRel) and pure synchronous reluctance (SyncRel) machines exhibit a saliency ratio greater than 1 and $L_{sd} < L_{sq}$.

It should be highlighted that for SyncRel machines is usually assumed another convention of the $d - q$ rotational frame as it will be shown in chapter §7.

2.1. Isotropic Electrical Machine

According to the passive sign convention, the voltage equations of a three-phase sinusoidal machine are:

$$\begin{cases} v_{su}(t) = R_s i_{su}(t) + \frac{d\Lambda_{su}(t)}{dt} \\ v_{sv}(t) = R_s i_{sv}(t) + \frac{d\Lambda_{sv}(t)}{dt} \\ v_{sw}(t) = R_s i_{sw}(t) + \frac{d\Lambda_{sw}(t)}{dt} \end{cases} \quad \text{Eq. 2-2}$$

where i_{su} , i_{sv} and i_{sw} are the phase currents that flows in the three-phase winding and Λ_{su} , Λ_{sv} and Λ_{sw} are total magnetic fluxes linkage to each stator phase. The R_s term is the stator phase resistance and it is assumed equal for each stator winding.

The Eq. 2-2 states that each winding terminal voltage is the sum of the resistance voltage drop and the inductive voltage drop occurring along the winding.

In the following, it is assumed that magnetic circuits work in linear magnetization conditions, thus far from the saturation point, that is, the magnetic permeance μ is a constant and equal to μ_{Fe} . The total magnetic flux is supposed to be the sum of two contributions:

- $\Lambda_{s,cp}$ is the magnetic flux induced by stator currents and it relies on winding distribution and type;
- $\Lambda_{s,pm}$ is the magnetic flux produced by permanent-magnets and its value is a function of the relative position of the rotor to stator windings.

By so doing, the total magnetic flux for a three-phase winding can be expressed as follows:

$$\begin{cases} \Lambda_{su}(t) = \Lambda_{su,cp}(t) + \Lambda_{su,pm}(t) \\ \Lambda_{sv}(t) = \Lambda_{sv,cp}(t) + \Lambda_{sv,pm}(t) \\ \Lambda_{sw}(t) = \Lambda_{sw,cp}(t) + \Lambda_{sw,pm}(t) \end{cases} \quad \text{Eq. 2-3}$$

2.1.1. Total Linkage Flux Component $\Lambda_{s,cp}$

The current flowing in each phase produces a Magneto-Motive Force (MMF), according to the Ampère's Law, which induces a magnetic flux. The induced magnetic flux links both with same phase winding and the other two phases.

Given the above, the magnetic flux can be split in two components: the *self-inductance* coefficient L considers the magnetic flux linked with the winding in which flows the same current that establish the magnetic flux and the *mutual-inductance* coefficient M which considers the magnetic flux linked to the other windings of the two phases. According to this, the total linkage fluxes per each phase can be expressed as follows:

$$\begin{cases} \Lambda_{su,cp}(t) = L_u i_{su}(t) + M_{uv} i_{sv}(t) + M_{uw} i_{sw}(t) \\ \Lambda_{sv,cp}(t) = M_{vu} i_{su}(t) + L_v i_{sv}(t) + M_{vw} i_{sw}(t) \\ \Lambda_{sw,cp}(t) = M_{wu} i_{su}(t) + M_{wv} i_{sv}(t) + L_w i_{sw}(t) \end{cases} \quad \text{Eq. 2-4}$$

Given the assumption of a symmetric three-phase system, the self- and mutual-coefficients are equal to each other:

$$\begin{aligned} L_u = L_v = L_w = L \\ M_{uv} = M_{uw} = M_{vu} = M_{vw} = M_{wu} = M_{wv} = M \end{aligned} \quad \text{Eq. 2-5}$$

Thus, Eq. 2-4 becomes as follows:

$$\begin{cases} \Lambda_{su,cp}(t) = L i_{su}(t) + M i_{sv}(t) + M i_{sw}(t) \\ \Lambda_{sv,cp}(t) = M i_{su}(t) + L i_{sv}(t) + M i_{sw}(t) \\ \Lambda_{sw,cp}(t) = M i_{su}(t) + M i_{sv}(t) + L i_{sw}(t) \end{cases} \quad \text{Eq. 2-6}$$

Since three-phase winding are generally connected with wye-connection without the neutral wire, the first Kirchhoff principle is verified at any time t . Thus, the following system of equations is true:

$$\begin{cases} i_{sv}(t) + i_{sw}(t) = -i_{su}(t) \\ i_{su}(t) + i_{sw}(t) = -i_{sv}(t) \\ i_{su}(t) + i_{sv}(t) = -i_{sw}(t) \end{cases} \quad \text{Eq. 2-7}$$

The Eq. 2-6 can also written as:

$$\begin{cases} \Lambda_{su,cp}(t) = L i_{su}(t) + M [i_{sv}(t) + i_{sw}(t)] \\ \Lambda_{sv,cp}(t) = L i_{sv}(t) + M [i_{su}(t) + i_{sw}(t)] \\ \Lambda_{sw,cp}(t) = L i_{sw}(t) + M [i_{su}(t) + i_{sv}(t)] \end{cases} \quad \text{Eq. 2-8}$$

and the current sums in the brackets substituted with Eq. 2-7.

$$\begin{cases} \Lambda_{su,cp}(t) = L i_{su}(t) - M i_{su}(t) \\ \Lambda_{sv,cp}(t) = L i_{sv}(t) - M i_{sv}(t) \\ \Lambda_{sw,cp}(t) = L i_{sw}(t) - M i_{sw}(t) \end{cases} \quad \text{Eq. 2-9}$$

$$\begin{cases} \Lambda_{su,cp}(t) = (L - M) i_{su}(t) \\ \Lambda_{sv,cp}(t) = (L - M) i_{sv}(t) \\ \Lambda_{sw,cp}(t) = (L - M) i_{sw}(t) \end{cases} \quad \text{Eq. 2-10}$$

The term in round brackets is the so-called *synchronous inductance* L_s and it is a fictional inductance that takes into account all the voltage drops in each phase of a sinusoidal synchronous machine with a balanced three-phase winding.

$$L_s = L - M \quad \text{Eq. 2-11}$$

The synchronous inductance is the sum of different self- and mutual- inductance contributions:

- L_{g0} is the air gap self-inductive component associated with the air gap flux;
- L_σ is the leakage self-inductive component associated with the slot leakage flux and end-winding leakage flux;
- M_{g0} is air gap mutual-inductive component which considers the mutual coupling of the air gap flux of one phase linked with the other phase windings. It is worth noticing that for a non-salient pole synchronous machine with sinusoidal distributed winding M_{g0} is equal to $-\frac{L_{g0}}{2}$;
- M_σ is the leakage mutual-inductive component.

The Eq. 2-15 is the expression of the synchronous inductance, as the sum of self- and mutual- contributions.

$$L_s = L - M = L_{g0} + L_\sigma - (M_{g0} + M_\sigma) \quad \text{Eq. 2-12}$$

$$L_s = L - M = L_{g0} + L_\sigma - \left(-\frac{L_{g0}}{2}\right) - M_\sigma \quad \text{Eq. 2-13}$$

$$L_s = L - M = \frac{2L_{g0} + L_{g0}}{2} + L_\sigma - M_\sigma \quad \text{Eq. 2-14}$$

$$L_s = L - M = \frac{3}{2}L_{g0} + (L_\sigma - M_\sigma) \quad \text{Eq. 2-15}$$

Thus, the linkage fluxes per each phase produced by the phase currents becomes as:

$$\begin{cases} \Lambda_{su,cp}(t) = L_s i_{su}(t) \\ \Lambda_{sv,cp}(t) = L_s i_{sv}(t) \\ \Lambda_{sw,cp}(t) = L_s i_{sw}(t) \end{cases} \quad \text{Eq. 2-16}$$

2.1.2. Permanent-Magnet linkage Flux $\lambda_{s,pm}$

The magnetic flux of the permanent-magnet links each stator winding, assuming a sinusoidal distribution of flux density vector field \vec{B} . The linkage permanent-magnet flux for each phase is expressed with the following system of equations:

$$\begin{cases} \Lambda_{su,pm}(t) = \hat{\Lambda}_{PM} \cos(\theta) \\ \Lambda_{sv,pm}(t) = \hat{\Lambda}_{PM} \cos\left(\theta - \frac{2}{3}\pi\right) \\ \Lambda_{sw,pm}(t) = \hat{\Lambda}_{PM} \cos\left(\theta - \frac{4}{3}\pi\right) \end{cases} \quad \text{Eq. 2-17}$$

where $\hat{\Lambda}_{PM}$ is peak value of the permanent-magnet linkage flux.

According to systems of equations Eq. 2-16 and Eq. 2-17, the initial system of equation Eq. 2-3 of total magnetic linkage flux can be expressed as follows:

$$\begin{cases} \Lambda_{su}(t) = L_s i_{su}(t) + \Lambda_{su,pm}(t) \\ \Lambda_{sv}(t) = L_s i_{sv}(t) + \Lambda_{sv,pm}(t) \\ \Lambda_{sw}(t) = L_s i_{sw}(t) + \Lambda_{sw,pm}(t) \end{cases} \quad \text{Eq. 2-18}$$

where the permanent-magnet linkage flux is considered in the implicit form.

2.1.3. Motor Equation in the Two-Axis Stationary Frame

The machine equations in the three-phase system are transformed to the two-axis stationary frame by means Clarke's transformation (see appendix §0). In order to get to the new notation, it is useful to express the machine equations in the compact matrix form as:

$$[i_s]_{uvw} = \begin{bmatrix} i_{su} \\ i_{sv} \\ i_{sw} \end{bmatrix} \quad \text{Eq. 2-19}$$

By so doing, the Eq. 2-2 becomes as Eq. 2-20.

$$[v_s]_{uvw} = [R_s]_{uvw} [i_s]_{uvw} + \frac{d[\Lambda_s]_{uvw}}{dt} \quad \text{Eq. 2-20}$$

$$[v_s]_{uvw} = [R_s]_{uvw} [i_s]_{uvw} + L_s \frac{d[i_s]_{uvw}}{dt} + \frac{d[\Lambda_{s,pm}]_{uvw}}{dt} \quad \text{Eq. 2-21}$$

The phase resistances are the same for the three-phases, since a symmetric wye three-phase system has been assumed. In addition, $[R_s]_{uvw}$ is a diagonal matrix as shown in Eq. 2-22.

$$[R_s]_{uvw} = \begin{bmatrix} R_s & 0 & 0 \\ 0 & R_s & 0 \\ 0 & 0 & R_s \end{bmatrix} \quad \text{Eq. 2-22}$$

In order to obtain machine equation in the two-axis stationary frame, both members of Eq. 2-21 are multiplied by Clarke's transformation matrix.

$$T_{uvw}^{\alpha\beta} [v_s]_{uvw} = [R_s]_{uvw} T_{uvw}^{\alpha\beta} [i_s]_{uvw} + L_s \frac{dT_{uvw}^{\alpha\beta} [i_s]_{uvw}}{dt} + \frac{dT_{uvw}^{\alpha\beta} [\Lambda_{s,pm}]_{uvw}}{dt} \quad \text{Eq. 2-23}$$

The diagonal matrix of phase resistance is still valid also for the stationary frame and it can be obtained expressing the three-phase current as Eq. 2-24 and substituting it in the first addend of the second member of Eq. 2-23. The results of the substitution are shown in Eq. 2-25.

$$[i_s]_{uvw} = T_{uvw}^{\alpha\beta t} [i_s]_{\alpha\beta} \quad \text{Eq. 2-24}$$

$$[R_s]_{uvw} T_{uvw}^{\alpha\beta} T_{uvw}^{\alpha\beta t} [i_s]_{\alpha\beta} \quad \text{Eq. 2-25}$$

Since the R_s is a diagonal matrix the product $[R_s]_{uvw} T_{uvw}^{\alpha\beta} T_{uvw}^{\alpha\beta t}$ can be wrote also as $T_{uvw}^{\alpha\beta} [R_s]_{uvw} T_{uvw}^{\alpha\beta t}$; in addition assuming the constant power Clarke's transformation, the resistance matrix in two-axis stationary frame is be expressed as:

$$[R_s]_{\alpha\beta} = \sqrt{\frac{2}{3}} \cdot \begin{bmatrix} 1 & -\frac{1}{2} & -\frac{1}{2} \\ 0 & \frac{\sqrt{3}}{2} & -\frac{\sqrt{3}}{2} \end{bmatrix} \cdot \begin{bmatrix} R_s & 0 & 0 \\ 0 & R_s & 0 \\ 0 & 0 & R_s \end{bmatrix} \cdot \sqrt{\frac{2}{3}} \cdot \begin{bmatrix} 1 & 0 \\ -\frac{1}{2} & \frac{\sqrt{3}}{2} \\ -\frac{1}{2} & -\frac{\sqrt{3}}{2} \end{bmatrix} \quad \text{Eq. 2-26}$$

$$[R_s]_{\alpha\beta} = \frac{2}{3} \cdot \begin{bmatrix} 1 & -\frac{1}{2} & -\frac{1}{2} \\ 0 & \frac{\sqrt{3}}{2} & -\frac{\sqrt{3}}{2} \end{bmatrix} \cdot \begin{bmatrix} R_s & 0 \\ -\frac{R_s}{2} & \frac{\sqrt{3}}{2} R_s \\ -\frac{R_s}{2} & -\frac{\sqrt{3}}{2} R_s \end{bmatrix} \quad \text{Eq. 2-27}$$

$$[R_s]_{\alpha\beta} = \frac{2}{3} \begin{bmatrix} \frac{6}{4} R_s & 0 \\ 0 & \frac{6}{4} R_s \end{bmatrix} \quad \text{Eq. 2-28}$$

$$[R_s]_{\alpha\beta} = \begin{bmatrix} R_s & 0 \\ 0 & R_s \end{bmatrix} \quad \text{Eq. 2-29}$$

The same result can be obtained considering the Clarke's transformation for a constant amplitude transformation.

The machine equations in two-axis stationary frame become as:

$$[v_s]_{\alpha\beta} = [R_s]_{\alpha\beta}[i_s]_{\alpha\beta} + L_s \frac{d[i_s]_{\alpha\beta}}{dt} + \frac{d[\Lambda_{s,pm}]_{\alpha\beta}}{dt} \quad \text{Eq. 2-30}$$

$$[v_s]_{\alpha\beta} = [R_s]_{\alpha\beta}[i_s]_{\alpha\beta} + \frac{d[\Lambda_s]_{\alpha\beta}}{dt} \quad \text{Eq. 2-31}$$

$$\begin{cases} v_{s\alpha} = R_s i_{s\alpha} + \frac{d\Lambda_{s\alpha}}{dt} \\ v_{s\beta} = R_s i_{s\beta} + \frac{d\Lambda_{s\beta}}{dt} \end{cases} \quad \text{Eq. 2-32}$$

2.1.4. Motor Equations in Two-Axis Rotational Frame

The Park's transformation (see appendix §D) is used to pass from stationary two-axis frame to rotational two-axis frame, synchronous with the rotor. Multiplying Eq. 2-31 by Park's transformation matrix, see Eq. 2-33, and expressing the current as Eq. 2-34.

$$T_{\alpha\beta}^{dq}[v_s]_{\alpha\beta} = T_{\alpha\beta}^{dq}[R_s]_{\alpha\beta}[i_s]_{\alpha\beta} + T_{\alpha\beta}^{dq} \frac{d[\Lambda_s]_{\alpha\beta}}{dt} \quad \text{Eq. 2-33}$$

$$[i_s]_{\alpha\beta} = T_{\alpha\beta}^{dq^{-1}}[i_s]_{dq} \quad \text{Eq. 2-34}$$

The Eq. 2-33 becomes as:

$$[v_s]_{dq} = T_{\alpha\beta}^{dq}[R_s]_{\alpha\beta}T_{\alpha\beta}^{dq^{-1}}[i_s]_{dq} + T_{\alpha\beta}^{dq} \frac{d[\Lambda_s]_{\alpha\beta}}{dt} \quad \text{Eq. 2-35}$$

$$[v_s]_{dq} = [R_s]_{dq}[i_s]_{dq} + T_{\alpha\beta}^{dq} \frac{d[\Lambda_s]_{\alpha\beta}}{dt} \quad \text{Eq. 2-36}$$

where $[R_s]_{\alpha\beta} = [R_s]_{dq}$.

The second addend of second member in Eq. 2-36 would be expressed in terms of the magnetic linkage flux in the rotational two-axis system as Eq. 2-37.

$$\frac{d}{dt} [T_{\alpha\beta}^{dq}[\Lambda_s]_{\alpha\beta}] = \frac{d}{dt} [\Lambda_s]_{dq} \quad \text{Eq. 2-37}$$

In order to do this, a mathematical trick can be used as shown in the following equations.

$$\frac{d}{dt} [T_{\alpha\beta}^{dq} [\Lambda_s]_{\alpha\beta}] = \frac{d}{dt} [T_{\alpha\beta}^{dq}] [\Lambda_s]_{\alpha\beta} + T_{\alpha\beta}^{dq} \frac{d[\Lambda_s]_{\alpha\beta}}{dt} \quad \text{Eq. 2-38}$$

$$T_{\alpha\beta}^{dq} \frac{d[\Lambda_s]_{\alpha\beta}}{dt} = \frac{d}{dt} [T_{\alpha\beta}^{dq} [\Lambda_s]_{\alpha\beta}] - \frac{d}{dt} [T_{\alpha\beta}^{dq}] [\Lambda_s]_{\alpha\beta} \quad \text{Eq. 2-39}$$

At this point the magnetic linkage flux in the vector compact form can be expressed as:

$$[\Lambda_s]_{\alpha\beta} = T_{\alpha\beta}^{dq^{-1}} [\Lambda_s]_{dq} \quad \text{Eq. 2-40}$$

Thus Eq. 2-40 is substituted in Eq. 2-39 as:

$$T_{\alpha\beta}^{dq} \frac{d[\Lambda_s]_{\alpha\beta}}{dt} = \frac{d}{dt} [T_{\alpha\beta}^{dq} T_{\alpha\beta}^{dq^{-1}} [\Lambda_s]_{dq}] - \frac{d}{dt} [T_{\alpha\beta}^{dq}] T_{\alpha\beta}^{dq^{-1}} [\Lambda_s]_{dq} \quad \text{Eq. 2-41}$$

$$T_{\alpha\beta}^{dq} \frac{d[\Lambda_s]_{\alpha\beta}}{dt} = \frac{d}{dt} [\Lambda_s]_{dq} - \frac{d}{dt} \begin{bmatrix} \cos \theta_e & \sin \theta_e \\ -\sin \theta_e & \cos \theta_e \end{bmatrix} T_{\alpha\beta}^{dq^{-1}} [\Lambda_s]_{dq} \quad \text{Eq. 2-42}$$

$$T_{\alpha\beta}^{dq} \frac{d[\Lambda_s]_{\alpha\beta}}{dt} = \frac{d}{dt} [\Lambda_s]_{dq} - \begin{bmatrix} -\omega_{el} \sin \theta_e & \omega_{el} \cos \theta_e \\ -\omega_{el} \cos \theta_e & -\omega_{el} \sin \theta_e \end{bmatrix} T_{\alpha\beta}^{dq^{-1}} [\Lambda_s]_{dq} \quad \text{Eq. 2-43}$$

$$T_{\alpha\beta}^{dq} \frac{d[\Lambda_s]_{\alpha\beta}}{dt} = \frac{d}{dt} [\Lambda_s]_{dq} - \omega_{el} \begin{bmatrix} -\sin \theta & \cos \theta \\ -\cos \theta & -\sin \theta \end{bmatrix} \begin{bmatrix} \cos \theta & -\sin \theta \\ \sin \theta & \cos \theta \end{bmatrix} [\Lambda_s]_{dq} \quad \text{Eq. 2-44}$$

$$T_{\alpha\beta}^{dq} \frac{d[\Lambda_s]_{\alpha\beta}}{dt} = \frac{d}{dt} [\Lambda_s]_{dq} - \omega_{el} \begin{bmatrix} 0 & 1 \\ -1 & 0 \end{bmatrix} [\Lambda_s]_{dq} \quad \text{Eq. 2-45}$$

$$T_{\alpha\beta}^{dq} \frac{d[\Lambda_s]_{\alpha\beta}}{dt} = \frac{d}{dt} [\Lambda_s]_{dq} + j\omega_{el} [\Lambda_s]_{dq} \quad \text{Eq. 2-46}$$

where j is imaginary unit and it is expressed as Eq. 2-47.

$$-j = \begin{bmatrix} 0 & 1 \\ -1 & 0 \end{bmatrix} \quad \text{Eq. 2-47}$$

Integrating Eq. 2-46 in Eq. 2-36, the voltage equations in the $d - q$ rotating frame become as:

$$[v_s]_{dq} = [R_s]_{dq} [i_s]_{dq} + \frac{d}{dt} [\Lambda_s]_{dq} + j\omega [\Lambda_s]_{dq} \quad \text{Eq. 2-48}$$

¹ $\omega = \frac{d}{dt} \theta$

$$\begin{cases} v_{sd} = R_s i_{sd} + \frac{d\Lambda_{sd}}{dt} + j\omega\Lambda_{sd} \\ v_{sq} = R_s i_{sq} + \frac{d\Lambda_{sq}}{dt} + j\omega\Lambda_{sq} \end{cases} \quad \text{Eq. 2-49}$$

The addend $j\omega[\Lambda_s]_{dq}$ represents the counter electromotive force and it is due to the rotational motion of the $d - q$ frame. The two terms $[\Lambda_s]_{dq}$ and $j[\Lambda_s]_{dq}$ are perpendicular to each other and have the same amplitude, in particular a multiplication by j means a counter clock rotation of 90° , as shown in Figure 2-1.

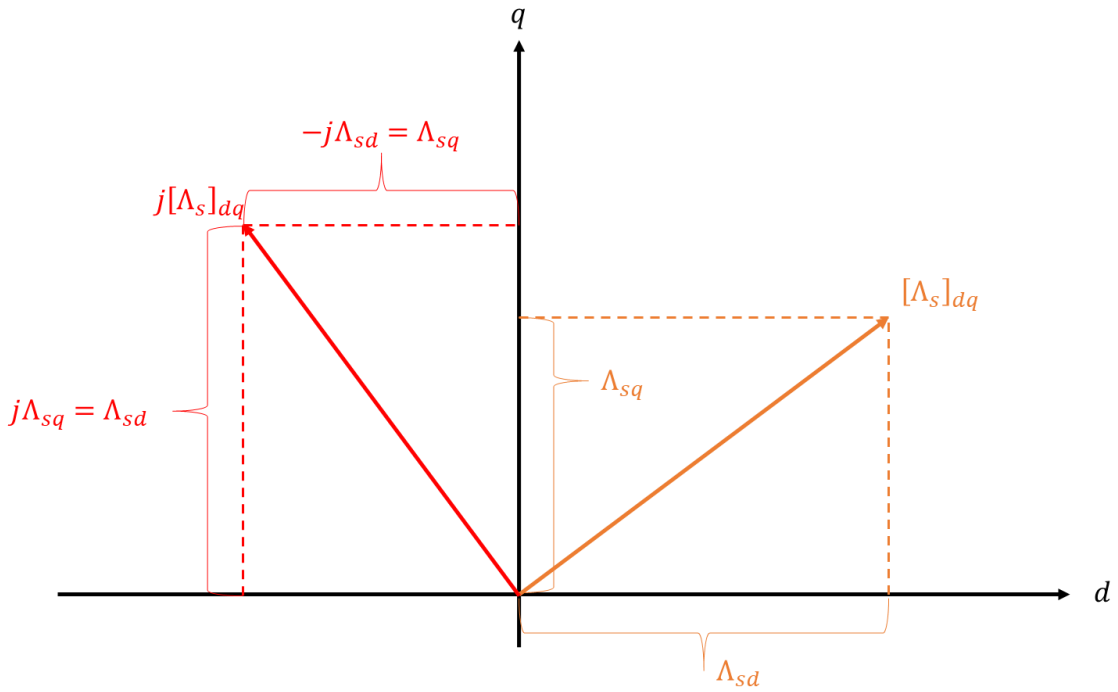


Figure 2-1: correlation between vectors $[\Lambda_s]_{dq}$ and $j[\Lambda_s]_{dq}$.

By so doing the following equivalences are true:

$$\begin{aligned} j\Lambda_{sd} &= -\Lambda_{sq} \\ j\Lambda_{sq} &= \Lambda_{sd} \end{aligned} \quad \text{Eq. 2-50}$$

By substituting Eq. 2-50 in the Eq. 2-49, the terminal voltage equations are:

$$\begin{cases} v_{sd} = R_s i_{sd} + \frac{d\Lambda_{sd}}{dt} - \omega_{el}\Lambda_{sq} \\ v_{sq} = R_s i_{sq} + \frac{d\Lambda_{sq}}{dt} + \omega_{el}\Lambda_{sd} \end{cases} \quad \text{Eq. 2-51}$$

The magnetic linkage flux can be expressed as:

$$\begin{cases} \Lambda_{sd} = L_s i_{sd} + \Lambda_{sd,pm} \\ \Lambda_{sq} = L_s i_{sq} + \Lambda_{sq,pm} \end{cases} \quad \text{Eq. 2-52}$$

Since the direct axis d coincides with the rotor polar axis, the permanent-magnets produce a constant flux $\Lambda_{sd,pm}$ in the d -axis direction and is null in q -axis. According to this, Eq. 2-52 becomes as:

$$\begin{cases} \Lambda_{sd} = L_s i_{sd} + \Lambda_{sd,pm} \\ \Lambda_{sq} = L_s i_{sq} \end{cases} \quad \text{Eq. 2-53}$$

Substituting Eq. 2-53 in Eq. 2-51 the well-known voltage equations in the $d - q$ rotating frame are obtained in Eq. 2-54.

$$\begin{cases} v_{sd} = R_s i_{sd} + \frac{d}{dt}(L_s i_{sd} + \Lambda_{sd,pm}) - \omega_{el}(L_s i_{sq}) \\ v_{sq} = R_s i_{sq} + \frac{d}{dt}(L_s i_{sq}) + \omega_{el}(L_s i_{sd} + \Lambda_{sd,pm}) \end{cases} \quad \text{Eq. 2-54}$$

$$\begin{cases} v_{sd} = R_s i_{sd} + L_s \frac{di_{sd}}{dt} - \omega_{el} L_s i_{sq} \\ v_{sq} = R_s i_{sq} + L_s \frac{di_{sq}}{dt} + \omega_{el} L_s i_{sd} + \omega_{el} \Lambda_{sd,pm} \end{cases} \quad \text{Eq. 2-55}$$

2.1.5. Mechanical Torque Expression

The mechanical torque equation could be obtained from Eq. 2-55 multiplying both equations members by current i_{sd} and i_{sq} .

$$\begin{cases} v_{sd} i_{sd} = R_s i_{sd}^2 + L_s \frac{di_{sd}}{dt} i_{sd} - \omega_{el} L_s i_{sq} i_{sd} \\ v_{sq} i_{sq} = R_s i_{sq}^2 + L_s \frac{di_{sq}}{dt} i_{sq} + \omega_{el} L_s i_{sd} i_{sq} + \omega_{el} \Lambda_{sd,pm} i_{sq} \end{cases} \quad \text{Eq. 2-56}$$

The next step is to sum the members of the system of equations in Eq. 2-56 in order to obtain the equation of power balance.

$$\begin{aligned} v_{sd} i_{sd} + v_{sq} i_{sq} &= R_s i_{sd}^2 + R_s i_{sq}^2 + L_s \frac{di_{sd}}{dt} i_{sd} + L_s \frac{di_{sq}}{dt} i_{sq} \\ &+ \omega_{el} \Lambda_{sd,pm} i_{sq} \end{aligned} \quad \text{Eq. 2-57}$$

where:

- $v_{sd} i_{sd} + v_{sq} i_{sq} = P_{Ab}$ is the input power absorbed by the electrical machine;
- $R_s (i_{sd}^2 + i_{sq}^2) = P_{Joule}$ represents the Joule losses inside the windings;
- $L_s \left(\frac{di_{sd}}{dt} i_{sd} + \frac{di_{sq}}{dt} i_{sq} \right) = P_{Mag}$ represents the magnetic energy stored inside the stator magnetic circuits;
- $\omega_{el} \Lambda_{sd,pm} i_{sq} = P_{Mec}$ represents the mechanical power produced by the electrical machine.

$$P_{abs} = P_{Joule} + P_{mag} + P_{mec} \quad \text{Eq. 2-58}$$

The classical definition of mechanical power produced by an electrical rotating machine is expressed:

$$P_{mec} = T_{mec}\omega_{mec} \quad \text{Eq. 2-59}$$

where T is the mechanical torque expressed in Newton-meter and ω_{mec} is the rotor mechanical speed expressed in radian per second. According to this the two expression of the mechanical power can be compared in order to express the torque.

$$T_{mec}\omega_{mec} = \omega_{el}\Lambda_{sd,pm}i_{sq} \quad \text{Eq. 2-60}$$

$$T_{mec} = \frac{\omega_{el}\Lambda_{sd,pm}i_{sq}}{\omega_{mec}} \quad \text{Eq. 2-61}$$

Considering the relationship between the mechanical frequency and the electric frequency $f_{el} = pf_{mec}$ where p are the pole pairs, the mechanical speed can be express as:

$$\omega_{mec} = \frac{\omega_{el}}{p} \quad \text{Eq. 2-62}$$

Thus, the mechanical torque expression is:

$$T_{mec} = p\Lambda_{sd,pm}i_{sq} \quad \text{Eq. 2-63}$$

Generally, the Clarke's transformation from a three-phase system to a two-axis stationary frame is conducted using the coefficient for a constant amplitude transformation $K = \frac{2}{3}$. According to this transformation, the mechanical power in the two-axis stationary frame would be less than that in the three-phase system:

$$P_{\alpha\beta} = \frac{2}{3}P_{uvw} \quad \text{Eq. 2-64}$$

Accordingly, the mechanical torque is also reduced of a coefficient of $\frac{2}{3}$.

$$T_{\alpha\beta} = \frac{2}{3}T_{uvw} \quad \text{Eq. 2-65}$$

In order to guarantee the energy balances the torque equation in Eq. 2-63 has to be multiplied by a coefficient equal to $\frac{3}{2}$.

$$T_{mec} = \frac{3}{2}p\Lambda_{sd,pm}i_{sq} \quad \text{Eq. 2-66}$$

2.1.6. Model of the Isotropic Machine

Finally, the model of the isotropic machine is expressed by following the system of equations:

$$\begin{cases} v_{sd} = R_s i_{sd} + L_s \frac{di_{sd}}{dt} - \omega_{el} L_s i_{sq} \\ v_{sq} = R_s i_{sq} + L_s \frac{di_{sq}}{dt} + \omega_{el} L_s i_{sd} + \omega_{el} \Lambda_{sd,pm} \\ T_{mec} = \frac{3}{2} p \Lambda_{sd,pm} i_{sq} \end{cases} \quad \text{Eq. 2-67}$$

2.2. Anisotropic Electrical Machine

The rotor design of anisotropic machine involves the presence of magnetic paths with different magnetic permeance values; therefore, the magnetic linkage flux exhibits some preferential paths. As mentioned at the beginning of this chapter, this characteristic gives a saliency ratio ξ greater than one, thus $L_{sd} < L_{sq}$.

Among permanent-magnet synchronous machines, the inner permanent-magnet ones could exhibit high or low saliency ratio values according to their magnets arrangement.

According to the passive convention, the equations of three-phase electrical machine are the same for the isotropic machine as in Eq. 2-2.

The following paragraph is going to examine only the total linkage flux component $\Lambda_{s,cp}$ produced by the sinusoidal three-phase currents of machine windings. In fact, because of anisotropy the machine inductances present an additional sinusoidal component, while the magnetic flux related to permanent-magnet $\Lambda_{s,pm}$ expressed by means the same equations seen for the isotropic machine.

2.2.1. Total Linkage Flux Component $\Lambda_{s,cp}$

Due to anisotropy, the self- and mutual-inductance parameters are a function also of the rotor position θ_{mec} , thus they are expressed as follows:

$$\begin{aligned} L_{su} &= L_{g0} + L_{\sigma} + \hat{L}_{g2} \cos(2\theta_{mec}) \\ L_{sv} &= L_{g0} + L_{\sigma} + \hat{L}_{g2} \cos\left(2\theta_{mec} - \frac{2}{3}\pi\right) \\ L_{sw} &= L_{g0} + L_{\sigma} + \hat{L}_{g2} \cos\left(2\theta_{mec} + \frac{2}{3}\pi\right) \end{aligned} \quad \text{Eq. 2-68}$$

$$\begin{aligned} M_{suv} &= M_{g0} + M_{\sigma} + \hat{L}_{g2} \cos\left(2\theta_{mec} - \frac{2}{3}\pi\right) \\ M_{svw} &= M_{g0} + M_{\sigma} + \hat{L}_{g2} \cos(2\theta_{mec}) \\ M_{swu} &= M_{g0} + M_{\sigma} + \hat{L}_{g2} \cos\left(2\theta_{mec} + \frac{2}{3}\pi\right) \end{aligned} \quad \text{Eq. 2-69}$$

where:

- L_{g0} and L_{g2} are air gap self-inductance components associated with the air gap flux;
- L_{σ} is the self-inductance component associated with the linkage flux which is the sum of two contributions: slot leakage inductance L_{slot} and end-winding leakage inductance L_{end} ;
- M_{g0} is air gap mutual-inductance component associated with the air gap flux;
- M_{σ} is the leakage mutual-inductive component. This component will be neglected in the following calculations.

The self-inductance has a positive mean term plus a double-frequency variation with the rotor position θ_{mec} which contains second and higher-order even harmonics. The mutual-inductance has a negative mean value that is approximately half the mean term of the self-inductance and it has a double-frequency variation containing second and higher-order harmonics. If the electrical machine windings are sine-distributed, it is accepted that there is only a second order variation of the inductances and higher-order harmonics are ignored as shown in Figure 2-2.

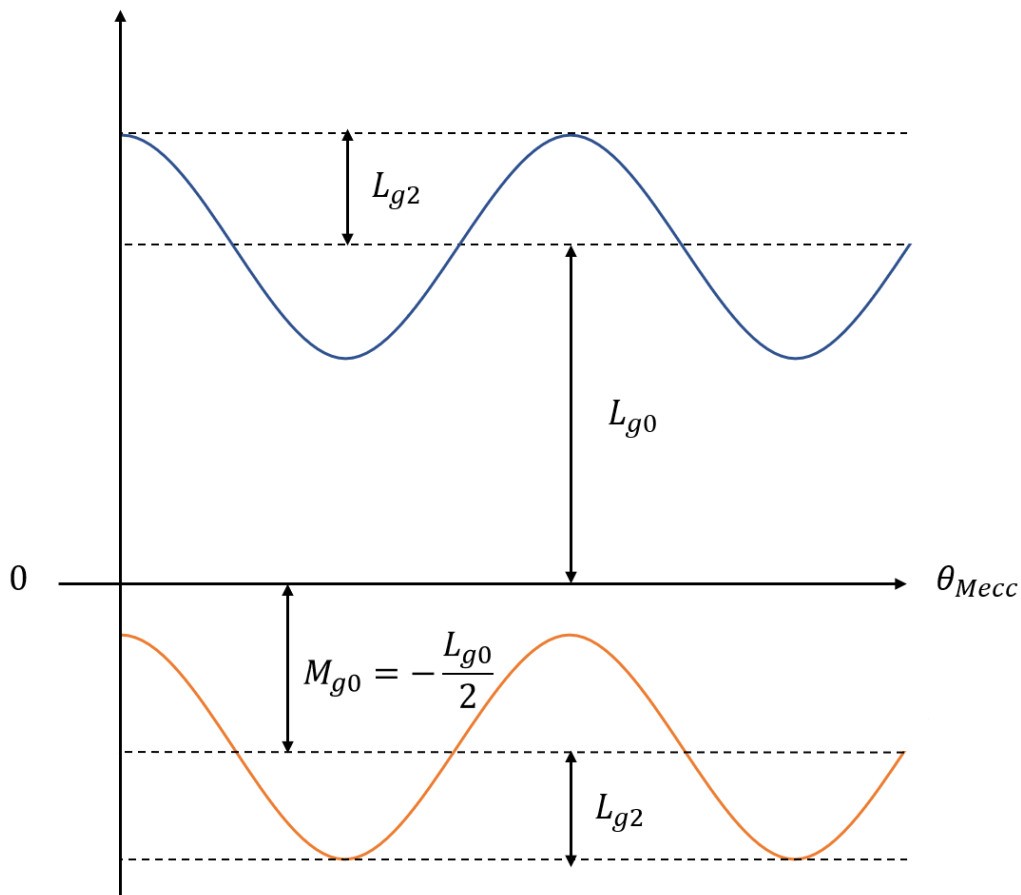


Figure 2-2: self and mutual-inductances of the anisotropic PM-SM [5].

The Figure 2-3 shows the behavior of the phase self-inductance of the anisotropic machine and if the electrical machine is non-salient pole machine with a three-phase balanced winding with a sinusoidal distribution, the mean value of the mutual-inductance M_{g0} is equal to $-\frac{L_{g0}}{2}$.

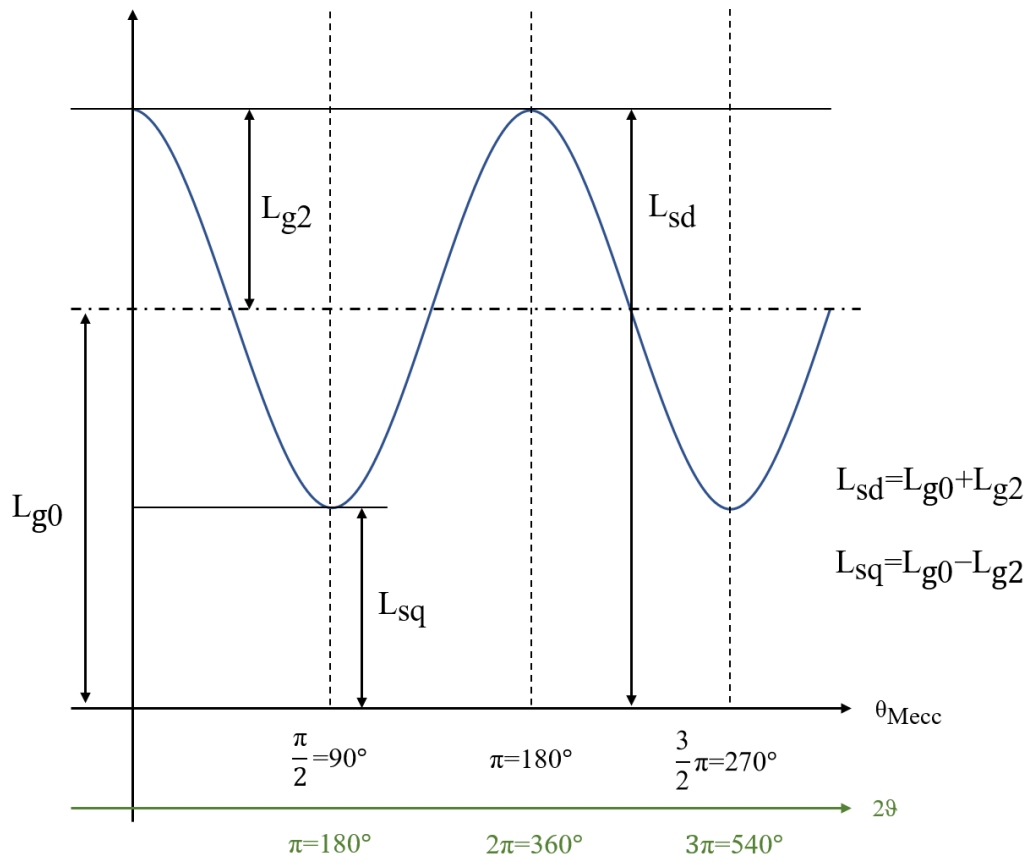


Figure 2-3: self-inductance behavior of the anisotropic machine. [7]

The inductance matrix $[L_s]_{uvw}$ of the anisotropic machine is shown in Eq. 2-70.

$$[L_s]_{uvw} = \begin{bmatrix} L_{g0} + L_\sigma + \hat{L}_{g2} \cos(2\theta_{el}) & -\frac{L_{g0}}{2} + \hat{L}_{g2} \cos\left(2\theta_{el} - \frac{2}{3}\pi\right) & -\frac{L_{g0}}{2} + \hat{L}_{g2} \cos\left(2\theta_{el} + \frac{2}{3}\pi\right) \\ -\frac{L_{g0}}{2} + \hat{L}_{g2} \cos\left(2\theta_{el} - \frac{2}{3}\pi\right) & L_{g0} + L_\sigma + \hat{L}_{g2} \cos\left(2\theta_{el} - \frac{2}{3}\pi\right) & -\frac{L_{g0}}{2} + \hat{L}_{g2} \cos(2\theta_{el}) \\ -\frac{L_{g0}}{2} + \hat{L}_{g2} \cos\left(2\theta_{el} + \frac{2}{3}\pi\right) & -\frac{L_{g0}}{2} + \hat{L}_{g2} \cos(2\theta_{el}) & L_{g0} + L_\sigma + \hat{L}_{g2} \cos\left(2\theta_{el} + \frac{2}{3}\pi\right) \end{bmatrix} \quad \begin{array}{l} \text{Eq.} \\ 2-70 \end{array}$$

The inductance matrix can be decomposed in two matrices: the first is related to the constant components and the second to sinusoidal one:

$$[L_s]_{uvw} = \begin{bmatrix} L_{g0} + L_\sigma & -\frac{L_{g0}}{2} & -\frac{L_{g0}}{2} \\ -\frac{L_{g0}}{2} & L_{g0} + L_\sigma & -\frac{L_{g0}}{2} \\ -\frac{L_{g0}}{2} & -\frac{L_{g0}}{2} & L_{g0} + L_\sigma \end{bmatrix} + \begin{bmatrix} \hat{L}_{g2} \cos(2\theta_{el}) & \hat{L}_{g2} \cos\left(2\theta_{el} - \frac{2}{3}\pi\right) & \hat{L}_{g2} \cos\left(2\theta_{el} + \frac{2}{3}\pi\right) \\ \hat{L}_{g2} \cos\left(2\theta_{el} - \frac{2}{3}\pi\right) & \hat{L}_{g2} \cos\left(2\theta_{el} - \frac{2}{3}\pi\right) & \hat{L}_{g2} \cos(2\theta_{el}) \\ \hat{L}_{g2} \cos\left(2\theta_{el} + \frac{2}{3}\pi\right) & \hat{L}_{g2} \cos(2\theta_{el}) & \hat{L}_{g2} \cos\left(2\theta_{el} + \frac{2}{3}\pi\right) \end{bmatrix} \quad \begin{array}{l} \text{Eq.} \\ 2-71 \end{array}$$

According to this, the matrix form of total linkage fluxes $[\lambda_s]_{uvw}$ is:

$$\begin{bmatrix} \Lambda_{su} \\ \Lambda_{sv} \\ \Lambda_{sw} \end{bmatrix} = \begin{bmatrix} L_{g0} + L_\sigma & -\frac{L_{g0}}{2} & -\frac{L_{g0}}{2} \\ -\frac{L_{g0}}{2} & L_{g0} + L_\sigma & -\frac{L_{g0}}{2} \\ -\frac{L_{g0}}{2} & -\frac{L_{g0}}{2} & L_{g0} + L_\sigma \end{bmatrix} \cdot \begin{bmatrix} i_{su} \\ i_{sv} \\ i_{sw} \end{bmatrix} + \begin{bmatrix} \hat{L}_{g2} \cos(2\theta_{el}) & \hat{L}_{g2} \cos\left(2\theta_{el} - \frac{2}{3}\pi\right) & \hat{L}_{g2} \cos\left(2\theta_{el} + \frac{2}{3}\pi\right) \\ \hat{L}_{g2} \cos\left(2\theta_{el} - \frac{2}{3}\pi\right) & \hat{L}_{g2} \cos\left(2\theta_{el} - \frac{2}{3}\pi\right) & \hat{L}_{g2} \cos(2\theta_{el}) \\ \hat{L}_{g2} \cos\left(2\theta_{el} + \frac{2}{3}\pi\right) & \hat{L}_{g2} \cos(2\theta_{el}) & \hat{L}_{g2} \cos\left(2\theta_{el} + \frac{2}{3}\pi\right) \end{bmatrix} \cdot \begin{bmatrix} i_{su} \\ i_{sv} \\ i_{sw} \end{bmatrix} \quad \begin{array}{l} \text{Eq.} \\ 2-72 \end{array}$$

As previously seen for the isotropic machine, the following chapters will show the transformation from a three-phase system into a two-phase rotational frame synchronous with rotor speed, so that the electrical quantities and parameters have constant values.

2.2.2. Motor Equations in Two-Axis Stationary Frame

Both member of Eq. 2-73 are multiplied by the Clarke's transformation:

$$[v_s]_{uvw} = [R_s]_{uvw}[i_s]_{uvw} + [L_s]_{uvw} \frac{d[i_s]_{uvw}}{dt} + \frac{d[\Lambda_{s,pm}]_{uvw}}{dt} \quad \text{Eq. 2-73}$$

$$\begin{aligned} T_{uvw}^{\alpha\beta}[v_s]_{uvw} &= T_{uvw}^{\alpha\beta}[R_s]_{uvw}[i_s]_{uvw} + T_{uvw}^{\alpha\beta}[L_s]_{uvw} \frac{d[i_s]_{uvw}}{dt} \\ &\quad + \frac{dT_{uvw}^{\alpha\beta}[\Lambda_{s,pm}]_{uvw}}{dt} \end{aligned} \quad \text{Eq. 2-74}$$

The current and permanent-magnet flux vectors can be expressed as:

$$[i_s]_{uvw} = T_{\alpha\beta}^{dq^{-1}}[i_s]_{\alpha\beta} \quad \text{Eq. 2-75}$$

$$[\Lambda_{s,pm}]_{uvw} = T_{\alpha\beta}^{dq^{-1}}[\Lambda_{s,pm}]_{\alpha\beta} \quad \text{Eq. 2-76}$$

Thus Eq. 2-74 becomes as:

$$\begin{aligned} [v_s]_{\alpha\beta} &= T_{uvw}^{\alpha\beta}[R_s]_{uvw}T_{uvw}^{\alpha\beta^{-1}}[i_s]_{\alpha\beta} + T_{uvw}^{\alpha\beta}[L_s]_{uvw}T_{uvw}^{\alpha\beta^{-1}} \frac{d[i_s]_{\alpha\beta}}{dt} \\ &\quad + \frac{dT_{uvw}^{\alpha\beta}T_{uvw}^{\alpha\beta^{-1}}[\Lambda_{s,pm}]_{\alpha\beta}}{dt} \end{aligned} \quad \text{Eq. 2-77}$$

The same considerations made for the three-phase resistance matrix $[R_s]_{uvw}$ of the isotropic machine are still valid for the anisotropic one. The same principle is also applied to the three-phase inductance matrix $[L_s]_{uvw}$. The inductance matrix in the two-axis stationary frame of anisotropic machine is expressed as:

$$[L_s]_{\alpha\beta} = \begin{bmatrix} L_{g0} + \hat{L}_{g2} \cos(2\theta_{el}) & \hat{L}_{g2} \sin(2\theta_{el}) \\ \hat{L}_{g2} \sin(2\theta_{el}) & L_{g0} - \hat{L}_{g2} \cos(2\theta_{el}) \end{bmatrix} \quad \text{Eq. 2-78}$$

Thus, the matrix form in the two-axis stationary frame is expressed as:

$$[v_s]_{\alpha\beta} = [R_s]_{\alpha\beta}[i_s]_{\alpha\beta} + \frac{d[\Lambda_s]_{\alpha\beta}}{dt} \quad \text{Eq. 2-79}$$

2.2.3. Motor Equations in Two-Axis Rotational Frame

In order to use constant physical quantities, the Park's transformation is used to pass from two-axis stationary system to a two-axis rotational frame. The Eq. 2-79 is multiplied by the Clark's transformation as:

$$T_{\alpha\beta}^{dq}[v_s]_{\alpha\beta} = T_{\alpha\beta}^{dq}[R_s]_{\alpha\beta}[i_s]_{\alpha\beta} + T_{\alpha\beta}^{dq} \frac{d[\Lambda_s]_{\alpha\beta}}{dt} \quad \text{Eq. 2-80}$$

The anisotropic machine presents two synchronous inductances due to the saliency of the rotor. The d-axis and q-axis synchronous inductances are expressed as follows:

$$L_{sd} = \frac{L_{g0} + L_{g2}}{2} \quad \text{Eq. 2-81}$$

$$L_{sq} = \frac{L_{g0} - L_{g2}}{2} \quad \text{Eq. 2-82}$$

The voltage equations in the two-axis rotational frame are:

$$\begin{cases} v_{sd} = R_s i_{sd} + L_{sd} \frac{di_{sd}}{dt} - \omega_{el} L_{sq} i_{sq} \\ v_{sq} = R_s i_{sq} + L_{sq} \frac{di_{sq}}{dt} + \omega_{el} L_{sd} i_{sd} + \omega_{el} \Lambda_{sd,pm} \end{cases} \quad \text{Eq. 2-83}$$

2.2.4. Mechanical Torque Expression for Anisotropic Machines

Applying the power balance method of paragraph §2.1.5 to Eq. 2-83, the torque equation of the anisotropic machine is expressed as:

$$T_{mec} = \frac{3}{2} p \Lambda_{sd,pm} i_{sq} + \frac{3}{2} p (L_{sd} - L_{sq}) i_{sd} i_{sq} \quad \text{Eq. 2-84}$$

The mechanical torque is the sum of two torque contributions:

- the mechanical torque produced by the permanent-magnet magnetic flux and orthogonal to the q-axis stator current;
- the reluctance torque due to the saliency of rotor. The d-axis current has a negative value as well as the difference between the d-axis and q-axis inductances, since $L_{sd} < L_{sq}$.

The torque equation is terms of the saliency ratio ξ is expressed as:

$$T_{mec} = \frac{3}{2} p i_{sq} [\Lambda_{sd,pm} + L_{sd} (1 - \xi) i_{sd}] \quad \text{Eq. 2-85}$$

It is worth noticing that the isotropic machine equations of paragraph §2.1 are a simplification of the equations of the anisotropic machine. In mechanical torque production, the contribution of the reluctance torque is zero since d-axis and q-axis inductances are similar $L_{sd} \cong L_{sq}$.

2.2.5. Model of the Anisotropic Machine

The model the anisotropic machine is expressed by the following system of equations:

$$\begin{cases} v_{sd} = R_s i_{sd} + L_{sd} \frac{di_{sd}}{dt} - \omega_{el} L_{sq} i_{sq} \\ v_{sq} = R_s i_{sq} + L_{sq} \frac{di_{sq}}{dt} + \omega_{el} L_{sd} i_{sd} + \omega_{el} \Lambda_{sd,pm} \\ T = \frac{3}{2} p \Lambda_{sd,pm} i_{sq} + \frac{3}{2} p (L_{sd} - L_{sq}) i_{sd} i_{sq} \end{cases} \quad \text{Eq. 2-86}$$

2.3. Control Strategies

The electrical machine models of paragraphs §2.1 and §2.2 are used to implement the control strategies of the sinusoidal brushless machine. The control aims to set the right input values for the electrical machine in order to produce the required mechanical torque T_{mec} at a given reference mechanical speed ω_{mec}^* .

The machine control issue cannot be uniquely defined, since the mathematical models of Eq. 2-67 and Eq. 2-86 have four unknown variables, while the systems have three equations. According to this a control strategy is needed to fix the control issue of electrical machine.

Different control strategies are implemented according to machine working point on the operating region and machine parameters. The machine operating region sets the values of torque and power of the electrical machine as a function of the mechanical speed. Figure 2-4 shows a general operating region with the physical quantities expressed in per unit.

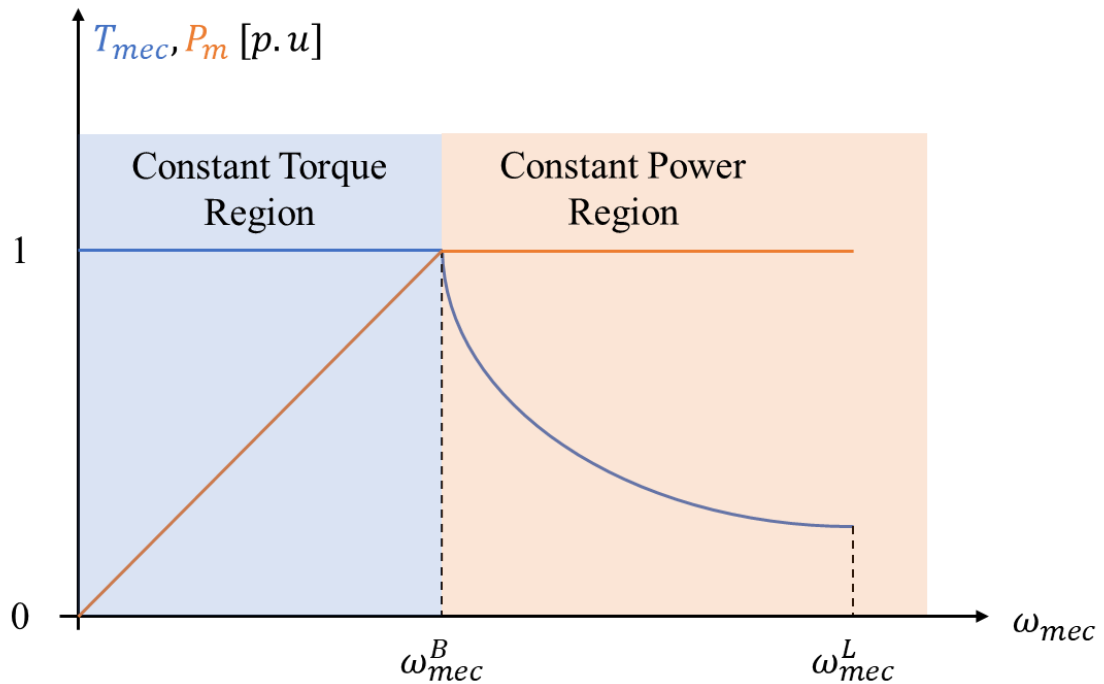


Figure 2-4: synchronous machine operating regions.

2.3.1. Stationary State Model

Generally, the machine control strategies are studied assuming the stationary state because machines models of Eq. 2-67 and Eq. 2-86 are simpler. According to this assumption, voltages and currents are sinusoidal and have fixed amplitude and frequency, thus the following expressions are verified:

$$\begin{aligned}\frac{di_{sd}}{dt} &\cong 0 \\ \frac{di_{sq}}{dt} &\cong 0\end{aligned}\quad \text{Eq. 2-87}$$

In addition, a second assumption is to disregard the resistive drops of the windings such as:

$$\begin{aligned}R_s i_{sd} &= 0 \\ R_s i_{sq} &= 0\end{aligned}\quad \text{Eq. 2-88}$$

According to these assumptions, the simplified models for isotropic and anisotropic machines becomes as follows:

$$\begin{cases} v_{sd} = -\omega_{el} L_s i_{sq} \\ v_{sq} = \omega_{el} L_s i_{sd} + \omega_{el} \Lambda_{sd,pm} \\ T = \frac{3}{2} p \lambda_{sd,pm} i_{sq} \end{cases} \quad \text{Eq. 2-89}$$

$$\begin{cases} v_{sd} = -\omega_{el} L_{sq} i_{sq} \\ v_{sq} = \omega_{el} L_{sd} i_{sd} + \omega_{el} \Lambda_{sd,pm} \\ T = \frac{3}{2} p \Lambda_{sd,pm} i_{sq} + \frac{3}{2} p (L_{sd} - L_{sq}) i_{sd} i_{sq} \end{cases} \quad \text{Eq. 2-90}$$

2.3.2. Working Domain

The brushless machine has to be controlled in accordance with the limits of the power supply and of the electrical machine. The current and the voltage are constrained below specific limits which are expressed with the following of relations:

$$I_s = \sqrt{i_{sd}^2 + i_{sq}^2} \leq I_{sL} \quad \text{Eq. 2-91}$$

$$V_s = \sqrt{v_{sd}^2 + v_{sq}^2} \leq V_{sL} \quad \text{Eq. 2-92}$$

The Eq. 2-91 is the current limit condition and the Eq. 2-92 is the voltage limit one. The two vectors I_s and V_s are the current and voltage vectors of the power supply and I_{sL} and V_{sL} are the current and voltage limit values.

Considering the $i_{sd} - i_{sq}$ plane, if Eq. 2-91 is exactly an equation, it represents a circumference of radius I_{sL} and centred in the axes origin, as shown in Figure 2-5. This circumference is denoted as current limit circumference and it is fixed on the plane, since the radius I_{sL} is set by the system (power supply and the electrical machine) limits.

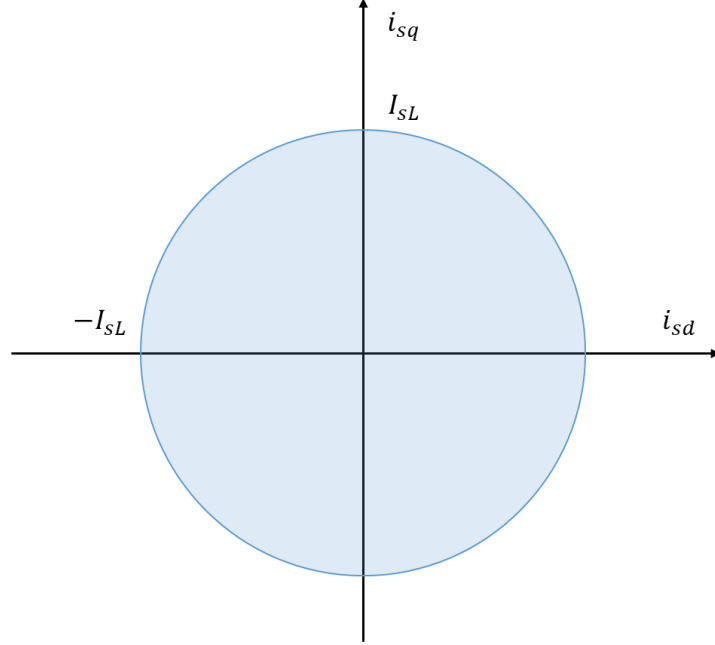


Figure 2-5: current limit circumference on $i_{sd} - i_{sq}$ plane.

The voltage constraint is generally expressed in the $i_{sd} - i_{sq}$ reference plane and if it is considered as an equation, it becomes:

- the voltage limit circumference for the isotropic machine (see Eq. 2-93 and Figure 2-6a);
- the voltage limit ellipse for the anisotropic machine (see Eq. 2-94 and Figure 2-6b).

$$\left(i_{sd} + \frac{\Lambda_{s,pm}}{L_s}\right)^2 + i_{sq}^2 \leq \left(\frac{V_{sL}}{p\omega_{mec}L_s}\right)^2 \quad \text{Eq. 2-93}$$

$$\frac{\left(i_{sd} + \frac{\Lambda_{s,pm}}{L_{sd}}\right)^2}{\left(\frac{V_{sL}}{p\omega_{mec}L_{sd}}\right)^2} + \frac{i_{sq}^2}{\left(\frac{V_{sL}}{p\omega_{mec}L_{sq}}\right)^2} \leq 1 \quad \text{Eq. 2-94}$$

The voltage limit circumference and ellipse have respectively a circumference radius equal to $\frac{V_{sL}}{p\omega_{mec}L_s}$ and semi-major and semi-minor axes equal to $\frac{V_{sL}}{p\omega_{mec}L_{sd}}$ and $\frac{V_{sL}}{p\omega_{mec}L_{sq}}$. These parameters are function of the mechanical speed ω_{mec} and their values shirk respectively to the center of the circumference $\left(-\frac{\Lambda_{s,pm}}{L_s}, 0\right)$ and the center of the ellipse $\left(-\frac{\Lambda_{s,pm}}{L_{sd}}, 0\right)$ as the mechanical speed increases.

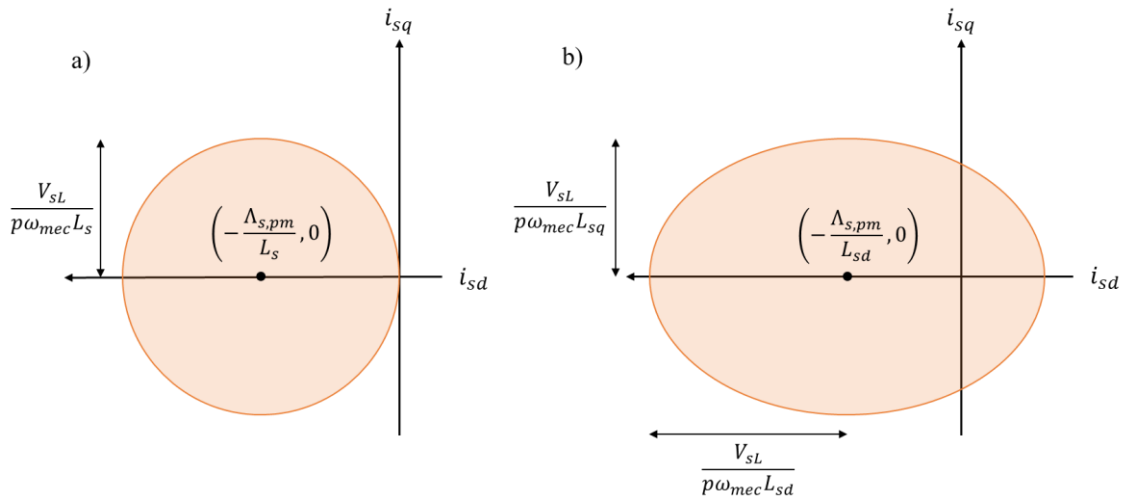


Figure 2-6: a) voltage limit circumference of isotropic machine, b) voltage limit ellipse of anisotropic machine.

The machine operating domain is given by the intersection of the current limit circumference and the voltage limit circumference/ellipse on the $i_{sd} - i_{sq}$ plane. Since the voltage limit is a function of the mechanical speed ω_{mec} , this limit becomes more and more restrictive as the mechanical speed increases.

According to the position of the center of the voltage limit circumference/ellipse, two different situations can be found. If the stator magnetic field on the d-axis ($L_{sd}i_{sd}$) is less than the permanent-magnet field (CASE I), the center of the voltage limit is outside the current limit circumference, thus there are not admissible machine working point beyond a certain mechanical speed. On the other hand, if the stator magnetic field on the d-axis is greater than the permanent-magnet magnetic field (CASE II), the current and voltage limits are always intersected and the machine working points belong to this intersection.

The Figure 2-7 shows the two possible situations for the isotropic machine (Figure 2-7a and Figure 2-7c) and anisotropic machine (Figure 2-7b and Figure 2-7d).

The x-coordinate of the center of the voltage limit circumference/ellipse is denoted as characteristic current I_{ch} and it is characteristic parameter of the electrical machine.

The following characteristic mechanical speeds represent transitions working points from one to another machine control strategy:

- ω_{mec}^B : mechanical base speed;
- ω_{mec}^0 : maximum reachable speed without flux-weakening;
- ω_{mec}^L : mechanical speed limit, maximum reachable speed with flux-weakening;
- ω_{mec}^{tr} : transition mechanical speed, at this speed the magnetic rotor is cancelled.

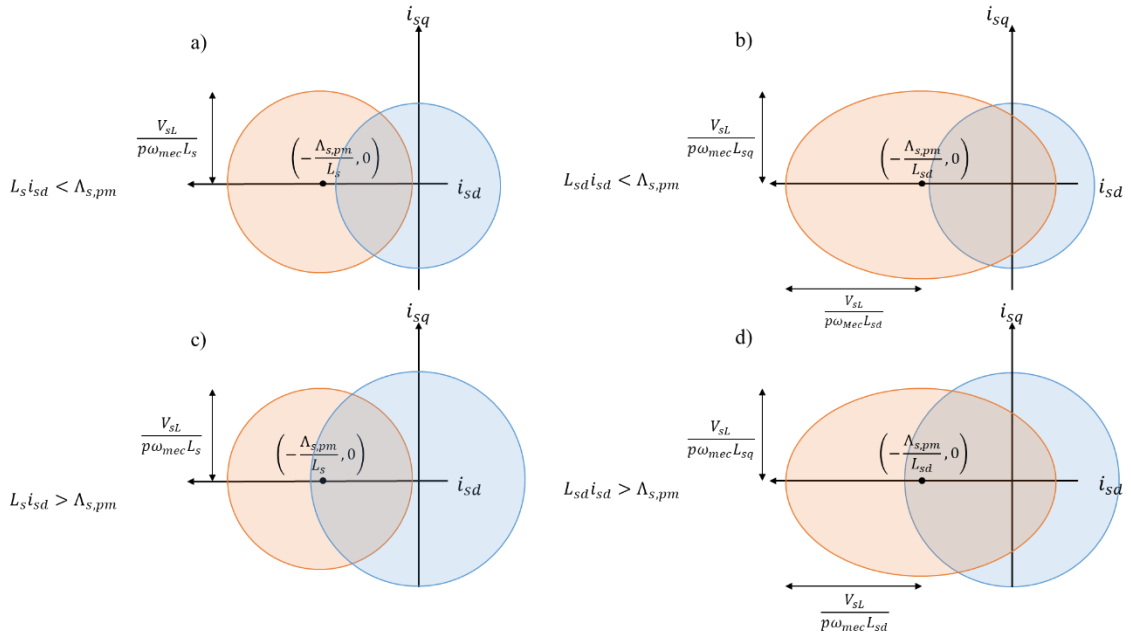


Figure 2-7: possible machine working points according the d-axis stator magnetic field vs the permanent-magnet field. Isotropic machine a) and c); anisotropic machine b) and d).

2.3.3. Maximum Torque Per Ampère Control Strategy (MTPA)

The Maximum Torque Per Ampère (MTPA) strategy aims to improve machine performance minimizing the copper losses P_j for a given torque value. Thus, the machine power supply has to be set to maximize the torque to current I_s ratio that means producing the maximum torque at a given current value.

The Eq. 2-95 has to be verified during the MTPA control strategy where I_s is the amplitude of the current vector.

$$\frac{T_m}{I_s} = \max \quad \text{Eq. 2-95}$$

The MTPA strategy is adopted in the constant torque region (see Figure 2-4), up to the base speed ω_{mec}^B . When the mechanical speed is equal to the base speed the maximum torque is produced with $I_s = I_{sL}$; beyond this speed both the current and voltage limits have to be respected.

The MTPA strategy can be adopted also between the base speed ω_{mec}^B and ω_{mec}^0 , but the produced torque is lower than one that can be produced by adopting the flux-weakening the control strategy at given speed.

2.3.4. Flux-Weakening Control Strategy (FW)

The flux-weakening strategy allows extending the machine working region beyond the constant torque one, as shown in Figure 2-4. This strategy does not guarantee the maximum torque to current ratio, but it allows operating over an extended mechanical speed range.

2.3.4.1. CASE I: $L_{sd} i_{sd} < \Lambda_{s,pm}$

The following paragraphs are on the machine control strategies for mechanical speeds beyond the base speed and for electrical machines with the center of the voltage limit circumference/ellipse laying outside the current limit circumference.

2.3.4.1.1. Mechanical Speed between ω_{mec}^B and ω_{mec}^0

It is necessary to apply the flux-weakening strategy in order to extend the machine operating region beyond the base speed. This means to reduce the amplitude of voltage vector V_s by reducing the stator magnetic field at a given mechanical speed.

The d-axis stator current is gradually increased in the negative direction; thus, it opposes the permanent-magnet magnetic flux which is in the positive direction of the d-axis.

The flux-weakening allows increasing the produced torque in the speed range between ω_{mec}^B and ω_{mec}^0 compared to the control strategy without flux-weakening.

2.3.4.1.2. Mechanical Speed between ω_{mec}^0 and ω_{mec}^L

The flux-weakening should be important in this speed range in order to reach permissible working points by respecting current and voltage limits at the same time.

When the mechanical speed is equal to ω_{mec}^L , the q-axis current is zero and the d-axis current gets its maximum values equal to $-I_{sL}$. At this operating condition the current limit and the voltage limit are intersected in only one point as shown in Figure 2-8a).

Over the speed limit ω_{mec}^L there are not permissible working points because the current and the voltage limits are no longer intersected, as shown in Figure 2-8b).

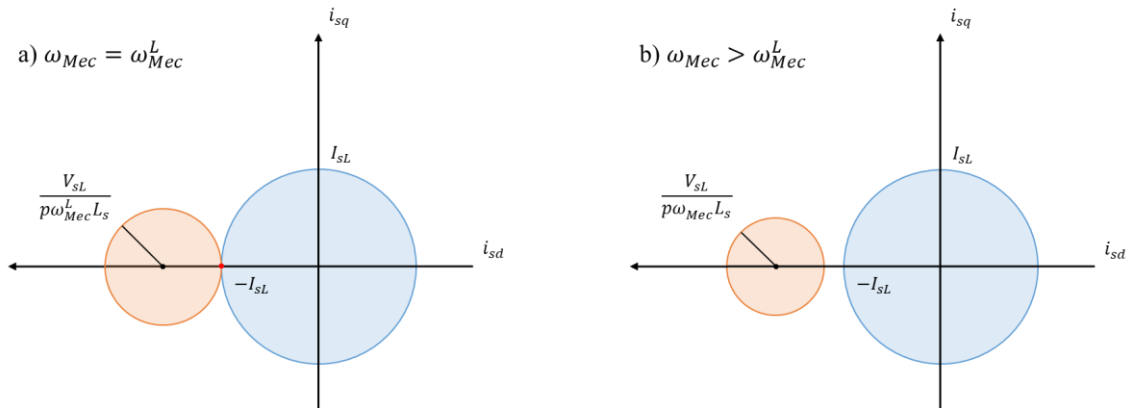


Figure 2-8: a) current and voltage limit of isotropic machine at mechanical speed limit; b) current and voltage limits for mechanical speed higher than mechanical speed limit.

2.3.4.2. CASE II: $L_{sd} i_{sd} > \Lambda_{s,pm}$

The considerations of paragraphs §2.3.4.1.1 and §2.3.4.1.2 are valid also when the center of the voltage limit circumference/ellipse is inside the current limit circumference up to the transition speed.

2.3.4.2.1. Mechanical Speed between ω_{mec}^0 and ω_{mec}^{tr}

The flux-weakening can be applied until the transient speed ω_{mec}^{tr} , at this mechanical speed the voltage limit circumference/ellipse intersects the current limit circumference with a d-axis current equal to the characteristic current I_{ch} . The stator magnetic field cancels the permanent-magnet magnetic field at this point.

In order to not demagnetize the permanent-magnet, the d-axis current amplitude has not to exceed the value of the characteristic current.

Over the transition speed, it is necessary to change the machine control strategy to limit d-axis current below the current limit value $|I_{SL}|$. Thus, ω_{mec}^{tr} is the maximum mechanical speed that can be reached with the flux-weakening, when the center of the voltage limit circumference/ellipse is inside the current limit circumference.

2.3.5. Maximum Torque per Volt Strategy

The machine can still operate beyond the transition speed ω_{mec}^{tr} , theoretically up to an infinite speed by adopting the Maximum Torque per Volt (MTPV) strategy. This strategy aims to maximize the ratio of torque to terminal voltage, in other words the MTPV minimizes the machine iron losses which depends on the machine electric frequency f_e and the peak value of the induced magnetic flux density \hat{B} .

The iron losses minimization is due to the fact that during MTPV strategy, the electrical machine is heavily flux-weakened and, thus, the peak value of the induced magnetic flux density is heavily reduced.

Finally, Figure 2-9 shows the complete machine operating regions for the electrical machine with the center of the voltage limit circumference/ellipse outside the current limit circumference. While Figure 2-10 shows the complete machine operating regions for the electrical machine with the center of the voltage limit circumference/ellipse inside the current limit circumference.

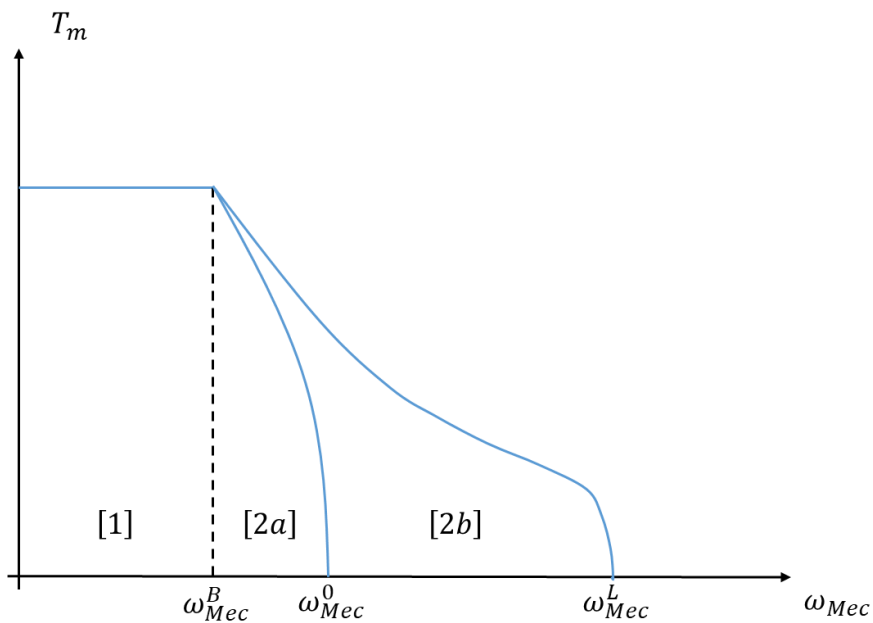


Figure 2-9: machine operating region when the center of the voltage limit circumference/ellipse is outside the current limit circumference.

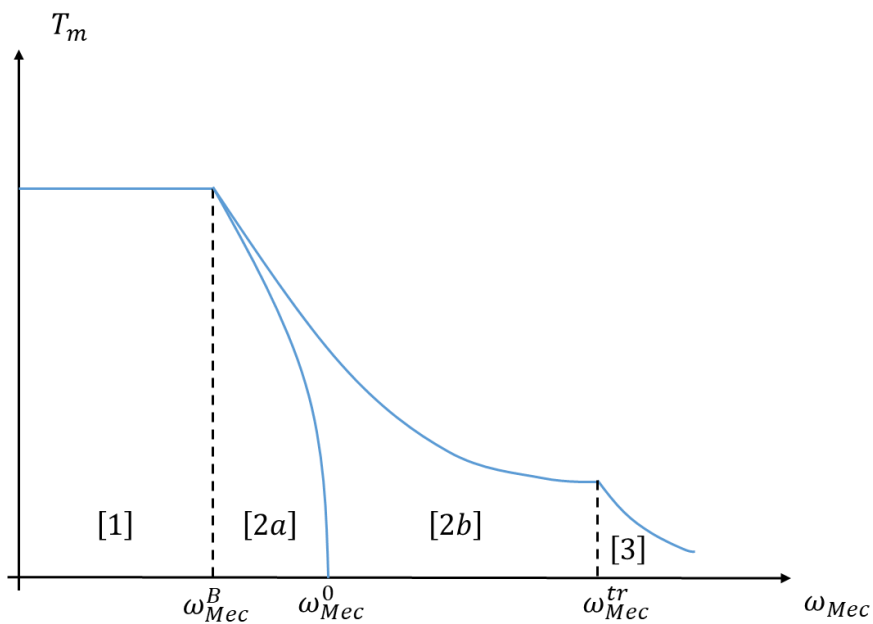


Figure 2-10: machine operating region when the center of the voltage limit circumference/ellipse is inside the current limit circumference.

Where:

[1] is the operating region with the MTPA strategy;

[2a] is the operating region over the base speed without flux-weakening, thus the MTPA strategy is still adopted, but it does not allow to maximize the torque to current ratio;

[2b] is the operating region with flux-weakening strategy;

[3] is the operating region with the MTPV strategy.

3. Analytical Design of Surface Permanent-Magnets Machine

This chapter shows a research activity dealing with an analytic design method for surface permanent-magnet machines (SPM-SMs). The proposed design method aims to provide a simple process to select the most suitable electrical machines given the design requirements and constraints.

Different slot-pole combinations can be compared in terms of performance so that the designer could evaluate the most appropriate one.

The proposed design approach has been developed for low range mechanical speeds where the main critical design issue is due to Joule losses. In addition, two different assumptions were carried out: the first design process assume constant current density, while the second assumes constant Joule losses. The first approach could be adopted when the machine design is more oriented to optimize the maximum performance of the electrical machine, while the second when the efficiency is the main design issue.

In order to compare the results of different machines, the calculation of the proposed design method has been referred to a parameter which is the stator diameters ratio given by the ratio of stator outer diameter to stator bore diameter. The bore diameter has been chosen as the unique variable choice of the design process, while the other geometrical and electromagnetic parameters are chosen by the designer at the beginning of the design process.

The performance of the machines is computed using the output equation which computes the electromechanical torque considering the electric load and the magnetic load of the machine.

The chapter is organized as follows: the first part recalls the theoretical basic of the output equation [5], while the following chapters are dedicated to the proposed method with constant current density and then assuming constant Joule losses.

3.1. The Output Equation [5]

The output equation is a univocal analytical method to compute the torque produced by an electrical machine. The output equation can be used from tiniest machines up to largest AC motors for process plants or traction applications.

Generally, the output equation of rotating electrical machines can be expressed as:

$$T_{mec} = \Phi * I^2 \quad \text{Eq. 3-1}$$

where Φ is the linkage magnetic flux and I is the current. From a design point of view, it's convenient to work with magnet flux-density \vec{B} and current density \vec{j} , since these parameters are independent from the machine dimensions. In addition, flux and current densities are closely related to the power losses density which determines the cooling requirements and the temperature distribution throughout the machine.

The output equation relates the following quantities:

- The torque per rotor volume, called TRV;
- The electric loading A ;
- The magnetic loading B .

3.1.1. Electric Loading A

The electric loading is defined as the linear current density around the air gap circumference, which is the number of Ampère-conductors per meter around the stator surface facing the air gap. The electric loading is expressed as:

$$A_{rms} = \frac{2mN_{ph}I_{rms}}{\pi D_b} \left[\frac{A}{m} \right] \quad \text{Eq. 3-2}$$

where m is the number of phases, N_{ph} is the number of turns in series per phase and D_b is the air gap diameter. The product $2N_{ph}$ is the number of conductors in series per phase N , thus Eq. 3-2 can be also written as:

$$A_{rms} = \frac{mNI_{rms}}{\pi D_b} \left[\frac{A}{m} \right] \quad \text{Eq. 3-3}$$

The limit of the electric loading is due to Joule losses expressed as Eq. 3-4 for a three-phase system where R_{ph} is the phase resistance.

$$P_{Joule} = 3R_{ph}I_{rms}^2 \quad \text{Eq. 3-4}$$

² $[Wb] * [A] = [T * m^2] \times \left[\frac{C}{m} \right] = \left[\frac{Vs}{mC} * m^2 \right] \times \left[\frac{C}{m} \right] = [Nm]$

3.1.2. Magnetic Loading B

The magnetic loading is the average flux density over the rotor surface. The distribution of the flux density in an AC motor is sinusoidal, thus the fundamental flux per pole is expressed as:

$$\Phi_1 = B_g \times \frac{\pi D_b L_{stk}}{2p} [Wb] \quad \text{Eq. 3-5}$$

where p is the number of pole pairs and L_{stk} is the lamination stack length multiplied by the stacking factor k_{stk} .

It is important to highlight that the flux density peak value \hat{B}_t in the teeth of a slotted motor must be limited around 1.6 T, otherwise the magnetizing current and/or iron losses may exceed due to the drop of steel inductance above the $\vec{B} - \vec{H}$ knee and /or the high value of \hat{B}_t .

The air gap peak flux density \hat{B}_g is related to the teeth peak flux density according to:

$$\hat{B}_g \approx \tau \hat{B}_t \quad \text{Eq. 3-6}$$

where τ is ratio of tooth width to slot-pitch expressed as:

$$\tau = \frac{w_t}{\tau_Q} \quad \text{Eq. 3-7}$$

The typical value of τ is around 0.5. By so doing, the mean value of the induced flux at the air gap is limited around 0.5 T.

3.1.3. TRV – Torque per Rotor Volume Equation

The induced EMF per phase is expressed as:

$$E = \frac{2\pi}{\sqrt{2}} k_{w1} N_{ph} \Phi_1 f_1 [V] \quad \text{Eq. 3-8}$$

where f_1 is the fundamental electric frequency, k_{w1} is the fundamental harmonic winding factor. The product $k_{w1} N_{ph}$ is the effective number of turns in series per phase. Substituting Eq. 3-5 in Eq. 3-8, the EMF per phase becomes as:

$$E = \frac{\pi^2}{\sqrt{2}} \frac{k_{w1} N_{ph} B D_b L_{stk} f_1}{p} [V] \quad \text{Eq. 3-9}$$

The maximum available electromagnetic power at the air gap is expressed as:

$$P_e = mEI \quad \text{Eq. 3-10}$$

Supposing to convert completely the electric power in mechanical power, the output torque could be obtained as follow:

$$mEI = T_{mec} \frac{2\pi f_1}{p} \text{ [W]} \quad \text{Eq. 3-11}$$

$$T_{mec} = m \frac{\pi}{\sqrt{2}} \frac{k_{w1} N_{ph} B D_b L_{stk} I}{2} \text{ [Nm]} \quad \text{Eq. 3-12}$$

The TRV equation is obtained by ratio of the torque equation (Eq. 3-12) to the rotor volume.

$$TRV = \frac{\pi}{\sqrt{2}} \frac{2mk_{w1}N_{ph}IB}{\pi D_b} \left[\frac{\text{Nm}}{\text{m}^3} \right] \quad \text{Eq. 3-13}$$

where term $\frac{2mN_{ph}I}{\pi D_b}$ is the electric load A , thus the TRV is given by:

$$TRV = \frac{\pi}{\sqrt{2}} k_{w1} AB \left[\frac{\text{Nm}}{\text{m}^3} \right] \quad \text{Eq. 3-14}$$

It is worth noticing that the higher the winding factor, the higher the utilization of the magnetic flux and the current in producing output torque. The winding factor is also called the *utilization factor* and its typical values are around 0.85 ÷ 0.95, thus Eq. 3-14 becomes as:

$$TRV = 2AB \left[\frac{\text{N}}{\text{m}^2} \right] \quad \text{Eq. 3-15}$$

3.1.4. Air Gap Shear Stress σ_g

The TRV is also related to the air gap shear stress σ , which represents the tangential force per unit of swept rotor surface area as shown in Figure 3-1 and Figure 3-2.

For every unit rotor surface area $d\Sigma$, the electromagnetic force is expressed as:

$$r\sigma = \frac{D_b\sigma}{2} \quad \text{Eq. 3-16}$$

Thus, according to the physics definition of torque, the electromagnetic torque can be written as:

$$T = \pi D_b L_{stk} \frac{D_b \sigma}{2} = 2\sigma \frac{\pi D_b^2 L_{stk}}{4} = 2\sigma V_R \quad \text{Eq. 3-17}$$

According to Eq. 3-17, the TRV can be expressed as follows:

$$TRV = \frac{T}{V_R} = 2\sigma \quad \text{Eq. 3-18}$$

where $\sigma \approx AB$ according to Eq. 3-15. The air gap shear stress is expressed in $\left[\frac{kN}{m^2}\right]$.

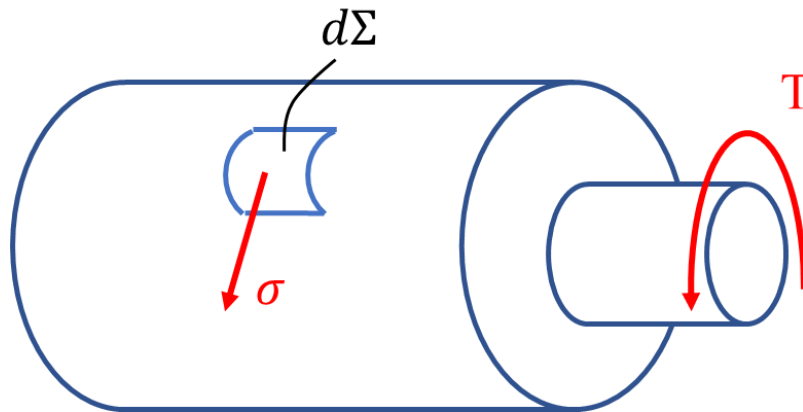


Figure 3-1: application of the shear stress on a unit of rotor surface [5].

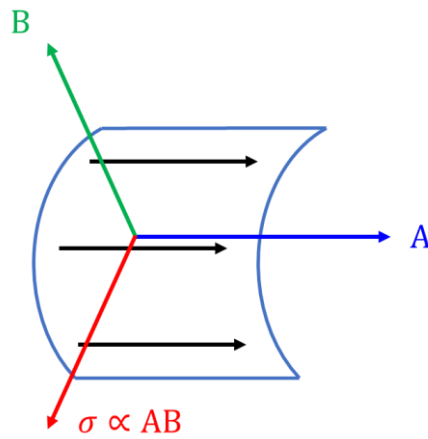


Figure 3-2: shear stress as the result of the electric load and magnetic load [5].

3.1.5. TRV Equation for an AC Sinusoidal Machine

The coefficient $\frac{\pi}{2}k_{w1}$ of Eq. 3-14 is characteristic to AC machines where the electric load A and the flux-density B are sinusoidally distributed in the space around the air gap.

$$A(\theta) = \hat{A} \sin \theta \quad \text{Eq. 3-19}$$

$$B(\theta) = \hat{B} \sin \theta \quad \text{Eq. 3-20}$$

The product $A(\theta)B(\theta)$ is the force per unit of rotor surface expressed in $\frac{N}{m^2}$, therefore the torque can be obtained by integration of Eq. 3-21:

$$r A(\theta)B(\theta)d\theta = r\hat{A}\hat{B} \sin^2 \theta \quad \text{Eq. 3-21}$$

where r is rotor radius and $d\theta$ the infinitesimal angular displacement. Since the stator currents are in phase with the rotor magnetic flux density, the term $\sin^2 \theta$ appears in Eq. 3-21. The torque T_{mec} can be obtained as follow:

$$T_{mec} = \int_0^{L_{stk}} \int_0^{2\pi} r^2 \hat{A} \hat{B} \sin^2 \theta d\theta dl \quad \text{Eq. 3-22}$$

Since the integral of $\sin^2 x$ is equal to:

$$\int \sin^2 x = -\frac{1}{2} \sin x \cos x + \frac{1}{2} x + c \quad \text{Eq. 3-23}$$

Solving the inner integral from 0 to 2π in $d\theta$, the Eq. 3-22 becomes as:

$$T_{mec} = \int_0^{L_{stk}} r^2 \pi \hat{A} \hat{B} dl \quad \text{Eq. 3-24}$$

The product $r^2 \pi \hat{A} \hat{B}$ is constant with respect to the integration variable dl , thus it can be carried out of the integral sign and the torque becomes as:

$$T_{mec} = \frac{D^2}{4} \pi \hat{A} \hat{B} L_{stk} \quad \text{Eq. 3-25}$$

Dividing the torque of Eq. 3-25 to the rotor volume, the TRV equation is obtained:

$$TRV = \hat{A} \hat{B} \quad \text{Eq. 3-26}$$

The Eq. 3-26 expresses the TRV in terms of peak values of the electric and magnetic loads, but from a design point of view is better to adopt the RMS value for the electric load (Eq. 3-27), because its related to the Joule losses, and the mean value of the magnetic flux (Eq. 3-28), because it provides information of the iron exploitation. The magnetic flux value is restricted by the supply power voltage and core iron losses.

$$A_{rms} = \frac{\hat{A}}{\sqrt{2}} \quad \text{Eq. 3-27}$$

$$B = \frac{2\hat{B}}{\pi} \quad \text{Eq. 3-28}$$

By substituting the two last equations in Eq. 3-26, the TRV can be expressed as:

$$TRV = \frac{\pi}{\sqrt{2}} A_{rms} B \quad \text{Eq. 3-29}$$

The fundamental winding factor is the single space-harmonic of current distribution that produces the torque interacting with the fundamental harmonic of the magnetic flux. Therefore, the fundamental winding factor conveys the winding effectiveness in producing the fundamental component.

3.2. Analytical Design of Surface Permanent-Magnet Synchronous Machines

This paragraph shows the proposed analytical design method for surface permanent-magnet synchronous machine based on the output equation to estimate the machine electromagnetic torque.

As aforementioned written, two design approaches are shown: the first approach does not consider the Joule losses as a design constraint, thus a constant current density value is imposed, while the latter computes the current density for a given value of Joule losses, by so doing the current density is a function of electrical machine geometry.

The design approaches are expressed as a function of the stator diameters ratio that is the ratio of the outer stator diameter D_o to the bore diameter D_b :

$$x = \frac{D_o}{D_b} \tag{Eq. 3-30}$$

The ratio x allows comparing different machine geometries with different slot-pole combinations. The values of x range over the range $[1, +\infty[$ as shown in Figure 3-3. Actually, only a restricted range of x represents feasible machines, in general this range could be assumed from 1.25 to 2.5 according to the slot-pole combination and outer stator diameter. The Figure 3-4 shows the x profile in a possible feasible range of stator bore diameter considering a 12-10 slot-pole combination.

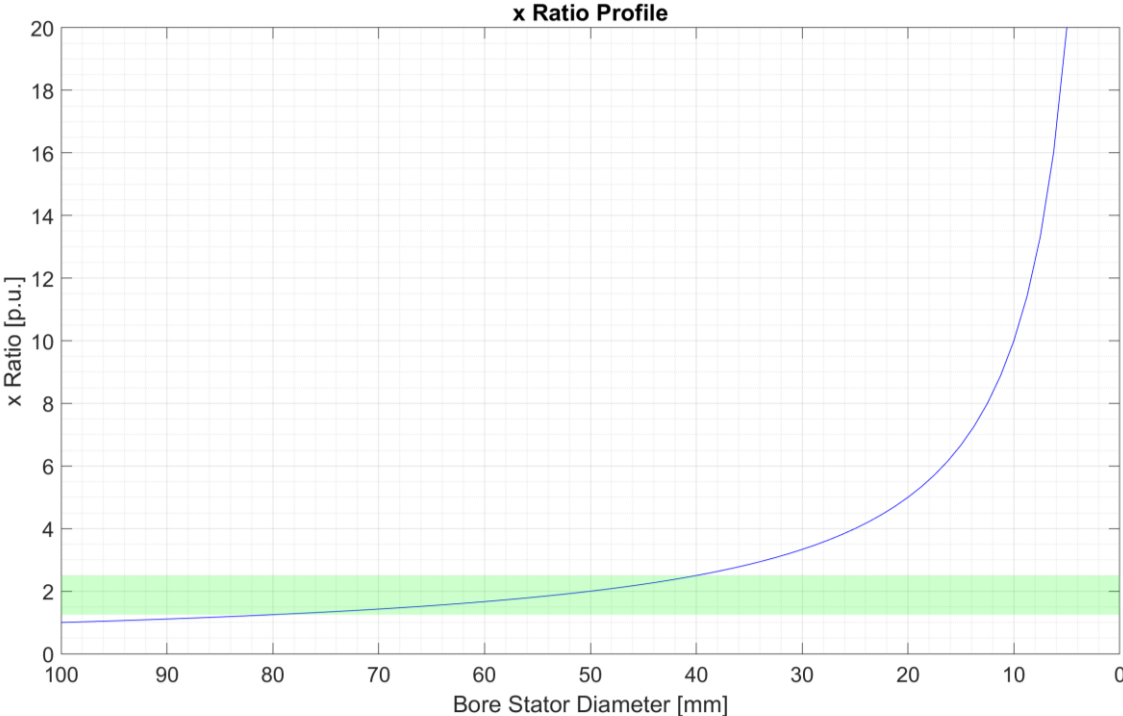


Figure 3-3: stator diameters ratio profile as a function on decreasing stator bore diameter.

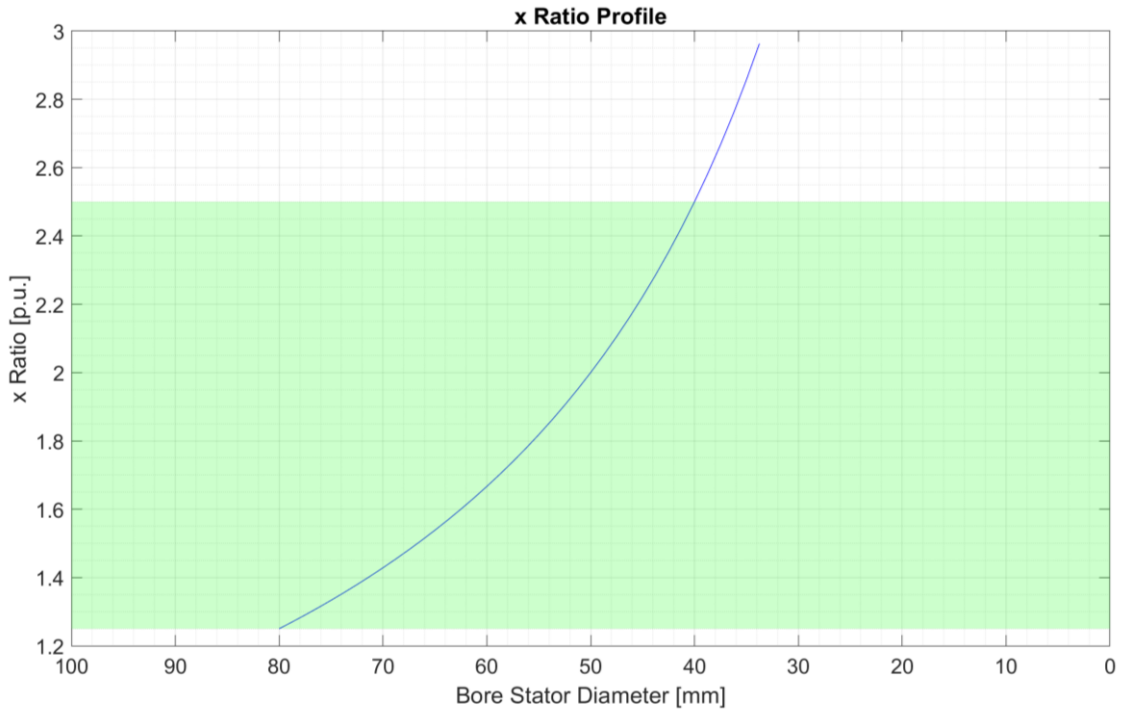


Figure 3-4: stator diameter profile over feasible values of stator bore diameter.

The Table 3-1 shows the design parameters assumed constant in the proposed design approach, their values are set by the designers. The outer stator diameter and the lamination stack length are equal to 100 mm. The single variable of the design approach is the stator bore diameter D_b .

Parameter	Symbol	Value	Unit of Measurement
Outer Stator Diameter	D_o	100	[mm]
Lamination Stack Length	L_{stk}	100	[mm]
Air Gap Thickness	g	0.8	[mm]
Peak Value of Tooth Magnetic flux Density	\hat{B}_t	1.65	[T]
Peak Value of Yoke Magnetic flux Density	\hat{B}_y	1.65	[T]
Peak Value of Air Gap Magnetic Flux Density	\hat{B}_g	0.95	[T]
Slot Filling Factor	k_{fill}	0.38	--
Iron Core Saturation Coefficient	α_i	0.84	--
Increasing Iron Factor due to Tooth Polar Shoe	k_{pp}	0.93	--
Lamination Stacking Factor	k_{stk}	0.96	--
Slot Opening Width	w_{so}	3	[mm]
Permanent Magnets Thickness	l_m	4	[mm]

Table 3-1: constant design parameter.

Assuming Q as the number of stator slots, p as the pole pair number and m as the number of phases, the number of slots per phase per pole (SPP) is expressed as:

$$q = \frac{Q}{2 p m} \quad \text{Eq. 3-31}$$

Further geometrical data can be obtained from data of Table 3-1:

- Air gap perimeter l_g :

$$l_g = \pi D_g \quad \text{Eq. 3-32}$$

- Slot pitch τ_s :

$$\tau_s = \frac{l_g}{Q} \quad \text{Eq. 3-33}$$

- Tooth polar shoe width $w_{t_{pp}}$:

$$w_{t_{pp}} = \tau_s - w_{so} \quad \text{Eq. 3-34}$$

Hereafter, the calculations are assumed for a three-phase fractional-slot SPM-SM with 12 slots and 10 poles.

3.2.1. Calculation of Carter's Coefficient

The Carter's coefficient is used to compute the effective air gap g_e seen by the stator. The stator faces a thicker air gap because of permanent-magnet mounted on the rotor surface which has a magnetic permeability around μ_0 .

The Carter's coefficient is calculated according the following procedure.

$$\rho_{w_{so}} = \frac{w_{so}}{g} \quad \text{Eq. 3-35}$$

where $\rho_{w_{so}}$ is the ratio of slot opening to the air gap thickness. Given Eq. 3-35, the Carter's coefficient σ_C can be obtained by linear interpolation between ratios of slot opening to air gap thickness and slot opening parameter. The slot opening parameters rely on the slot opening type that could be an open slot opening or a semi-open slot opening. The proposed design approach assumes a semi-open slot opening and the Carter's coefficient is expressed as:

$$k_{C_{semi-open}} = \frac{w_{t_{pp}} + w_{so}}{w_{t_{pp}} + (1 - \sigma_{C_{semi-open}}) w_{so}} \quad \text{Eq. 3-36}$$

where $\sigma_{C_{semi-open}}$ is the semi-open slot opening parameter.

Given the Carter's coefficient, the equivalent air gap thickness g_e is given by:

$$g_e = g * k_{C_{semi-open}} \quad \text{Eq. 3-37}$$

3.2.2. Design of Permanent-Magnets

The peak air gap flux density \hat{B}_g depends on the PMs working point $(-H_m; \hat{B}_m)$ along the demagnetization curve as shown in Figure 3-5

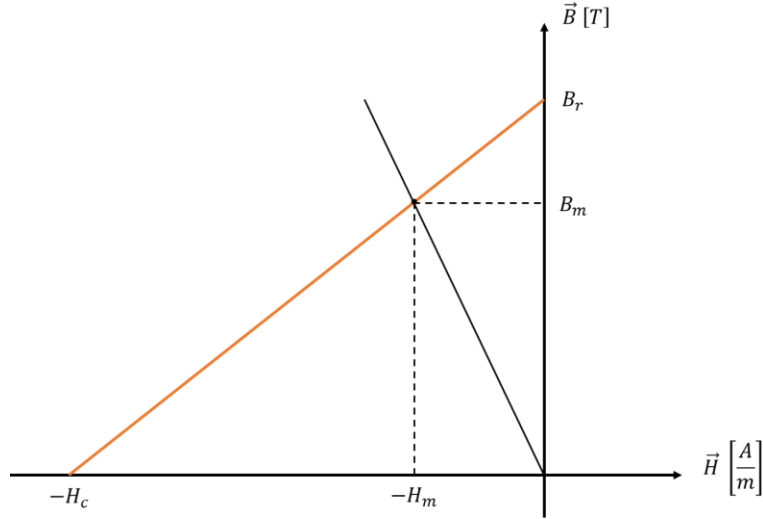


Figure 3-5: permanent-magnet working points on the demagnetization curve.

The magnet working point is a result of its magnetic characteristics such as coercive magnetic field $-H_c$ and the residual flux density \hat{B}_r , magnet type and magnetic circuit geometry.

The system of equations in Eq. 3-38 allows to compute the magnet working point, when it is part of electromagnetic circuit with an air gap of thickness g_e .

$$\begin{cases} -\hat{H}_m l_m = \hat{H}_g g_e \\ \hat{B}_g = \hat{B}_m \\ \hat{B}_g = \mu_0 \hat{H}_g \end{cases} \quad \text{Eq. 3-38}$$

The first equation of Eq. 3-38 states that the PM magneto-motive force (MMF) drops entirely along the air gap and the third equation is constitutive equation in the vacuum.

Substituting the third equation of Eq. 3-38 in the first one and assuming the equivalence of the second equation, the magnet flux density is expressed as:

$$\hat{B}_m = -\hat{H}_m \frac{l_m}{g_e} \mu_0 \quad \text{Eq. 3-39}$$

The magnet flux density can be also expressed with the following system of equations:

$$\begin{cases} \hat{B}_m = \hat{B}_r + \mu_0 \mu_r \hat{H}_m \\ \hat{B}_m = -\hat{H}_m \frac{l_m}{g_e} \mu_0 \end{cases} \quad \text{Eq. 3-40}$$

The magnetic field of the magnet working point can be found solving the system of Eq. 3-40 and the result is shown in Eq. 3-41.

$$\hat{H}_m = -\frac{\hat{H}_c}{\left(\frac{l_m}{g_e \mu_r} - 1\right)} \quad \text{Eq. 3-41}$$

According to the second equation of Eq. 3-38, the air gap flux density is equal to the magnet working point flux density \hat{B}_m . This is true from a theoretical point of view, actually because of iron saturation phenomenon the air gap flux is less than the magnet flux density. The saturation phenomenon can be taken into account with the coefficient α_i [6] as follows, thus the air gap flux density becomes as:

$$\hat{B}_g = \hat{B}_m \alpha_i \quad \text{Eq. 3-42}$$

Considering a sinusoidal flux density, the mean value of \hat{B}_g corresponds to the magnetic load.

$$B_g = \frac{2 \hat{B}_g}{\pi} \quad \text{Eq. 3-43}$$

3.2.3. Geometrical Parameters

The total air gap magnetic flux is expressed as:

$$\hat{\Phi}_g = \hat{B}_m \alpha_i \pi D_g L_{stk} \quad \text{Eq. 3-44}$$

and it could be used to compute the stator tooth width w_t and the stator yoke radial thickness h_y as follows:

$$w_t = \frac{\hat{\Phi}_g}{\hat{B}_t L_{stk} k_{stk} Q} \quad \text{Eq. 3-45}$$

$$h_y = \frac{\hat{\Phi}_g}{2 \cdot 2p L_{stk} \hat{B}_{pk}} \quad \text{Eq. 3-46}$$

The iron teeth surface of the stator is computed as follows:

$$S_{sFe_t} = Q w_t \left(\frac{D_{sl} - D_b}{2} \right) \quad \text{Eq. 3-47}$$

where D_{sl} is the stator diameter at the bottom of the stator slots.

The iron yoke surface is expressed as:

$$S_{sFe_y} = \frac{\pi}{4} (D_o^2 - D_{sl}^2) \quad \text{Eq. 3-48}$$

The sum of Eq. 3-47 and Eq. 3-48 is the total iron stator surface $S_{sFe_{tot}}$. The total stator surface S_{stot} , expressed in terms of stator diameters ratio x , is:

$$S_{stot} = \frac{\pi}{4} D_o^2 \left(1 - \frac{1}{x^2} \right) \quad \text{Eq. 3-49}$$

Given the total stator iron surface and Eq. 3-49, it is possible to express the percentage of the iron over the stator surface as shown in Eq. 3-50.

$$\zeta_{sFe} = \frac{S_{sFe_{tot}}}{S_{stot}} \quad \text{Eq. 3-50}$$

Eq. 3-50 can be used to find out the stator surface taken up by stator slots with the following formula:

$$S_{sSlot_{tot}} = S_{stot} (1 - \zeta_{sFe}) k_{pp} \quad \text{Eq. 3-51}$$

It is useful now to express the electric load A in terms of current density, instead of the phase RMS current. Denoting n_{cs} as the number of conductors in series per slots, the number of conductors in series per phase N is expressed as follows:

$$N = n_{cs} q 2 p \quad \text{Eq. 3-52}$$

Considering the following Eq. 3-53 and substituting it with Eq. 3-52 in Eq. 3-3, the electric load equation can be expressed as follows:

$$n_{cs} I_{rms} = S_{sSlot} k_{fill} j_{rms} \quad \text{Eq. 3-53}$$

$$A_{rms} = \frac{m q 2 p S_{sSlot} k_{fill} j_{rms}}{\pi D_g} \quad \text{Eq. 3-54}$$

where S_{sSlot} is the area of a single stator slot. Given Eq. 3-31, the electric load equation can be reduced as:

$$A_{rms} = \frac{S_{sSlot_{tot}} k_{fill} j_{rms}}{\pi D_g} \quad \text{Eq. 3-55}$$

The electric load as a function of the stator diameters ratio x becomes is expressed as:

$$A_{rms} = \frac{\frac{\pi}{4} D_o^2 \left(1 - \frac{1}{x^2}\right) (1 - \zeta_{sFe}) k_{pp} k_{fill} j_{rms} x}{\pi D_o} \quad \text{Eq. 3-56}$$

The torque equation is expressed as the product between the TRV and rotor volume. According to Eq. 3-29 the torque is expressed as follows:

$$T_{mec} = \frac{D_g^2}{4} \pi L_{stk} k_{stk} \frac{\pi}{\sqrt{2}} A_{rms} B_g k_{w1} \quad \text{Eq. 3-57}$$

The torque equation expressed in terms of the stator diameters ratio x is as follows:

$$\begin{aligned} T_{mec} \\ = \frac{D_o^2}{4 x^2} \pi L_{stk} k_{stk} \frac{\pi}{\sqrt{2}} \frac{\frac{\pi}{4} D_o^2 \left(1 - \frac{1}{x^2}\right) (1 - \zeta_{sFe}) k_{pp} k_{fill} j_{rms} x}{\pi D_o} B_g k_{w1} \end{aligned} \quad \text{Eq. 3-58}$$

3.2.4. Design Method with Constant Current Density

The first design method computes machine performance assuming a constant current density \vec{j} . This assumption could be useful when the machine has to be designed in order to operate at its maximum performance and the Joule losses are not a strict constraint.

The Figure 3-6 shows the torque profile as a function of stator diameter ratio x of 12-10 slot-pole combination assuming a current density equal to $4 A_{RMS}/mm^2$.

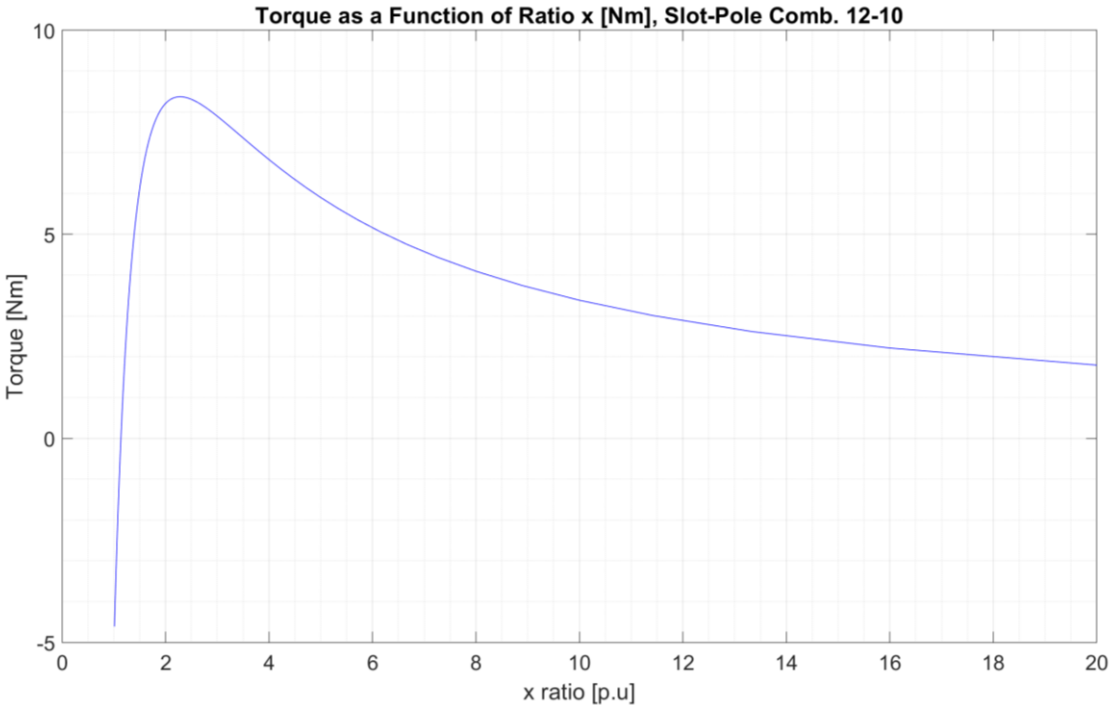


Figure 3-6: torque profile as a function of the stator diameters ratio ξ .

The design process can be extended to any slot-pole combination; in fact Figure 3-7 and Figure 3-8 show the torque profiles of different slot-pole combinations. The torque profiles of Figure 3-8 were normalized with respect to the maximum torque value of the considered slot-pole combinations.

The Figure 3-9 is similar to Figure 3-7, but the torque profiles are plotted as a function of stator bore diameter.

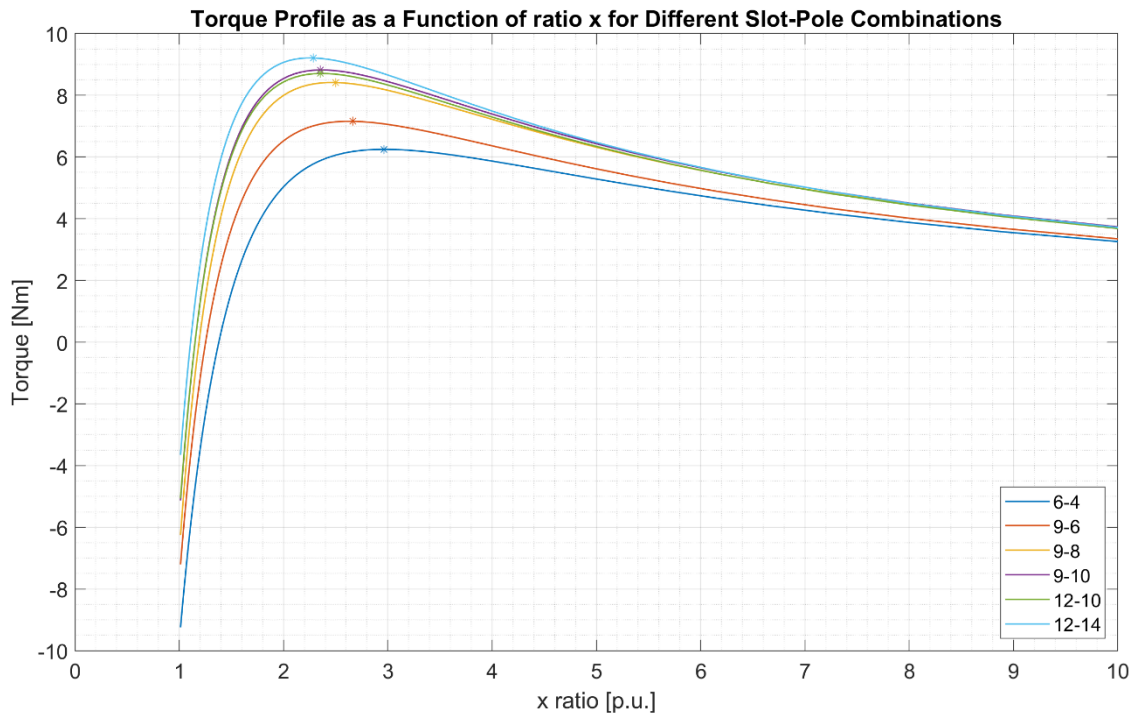


Figure 3-7: torque profile as a function of the stator diameters ratio x of different slot-pole combinations at constant RMS current density.

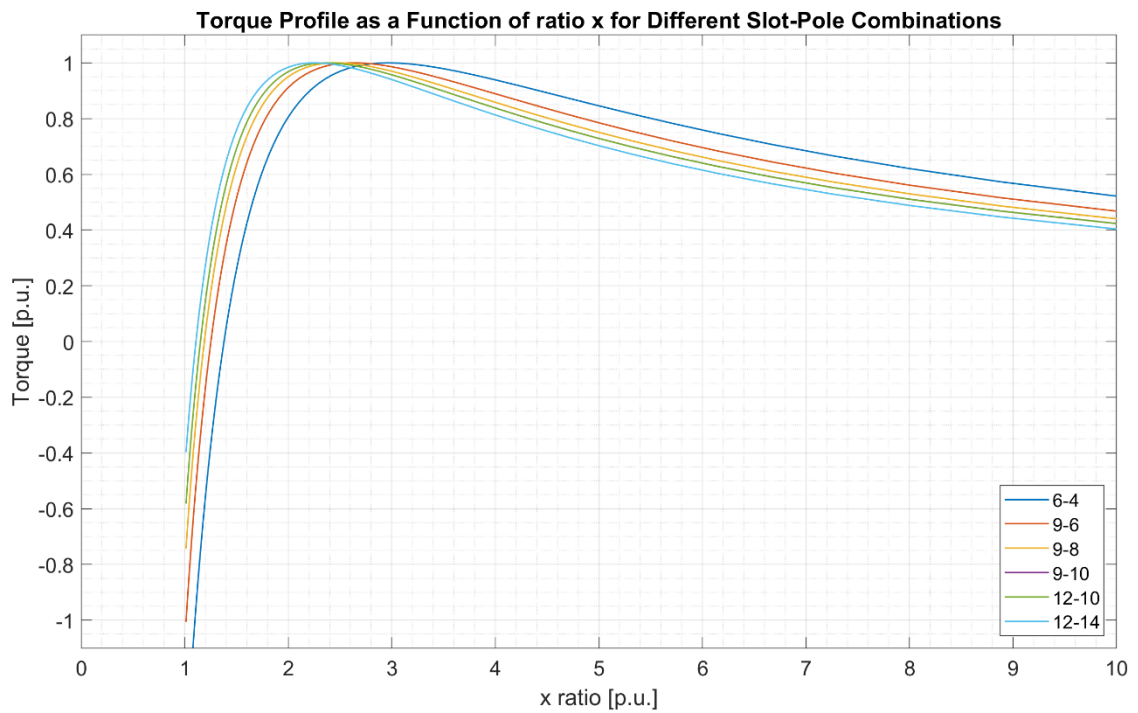


Figure 3-8: torque profile in p.u. as a function of the stator diameters ratio x of different slot-pole combinations at constant RMS current density.

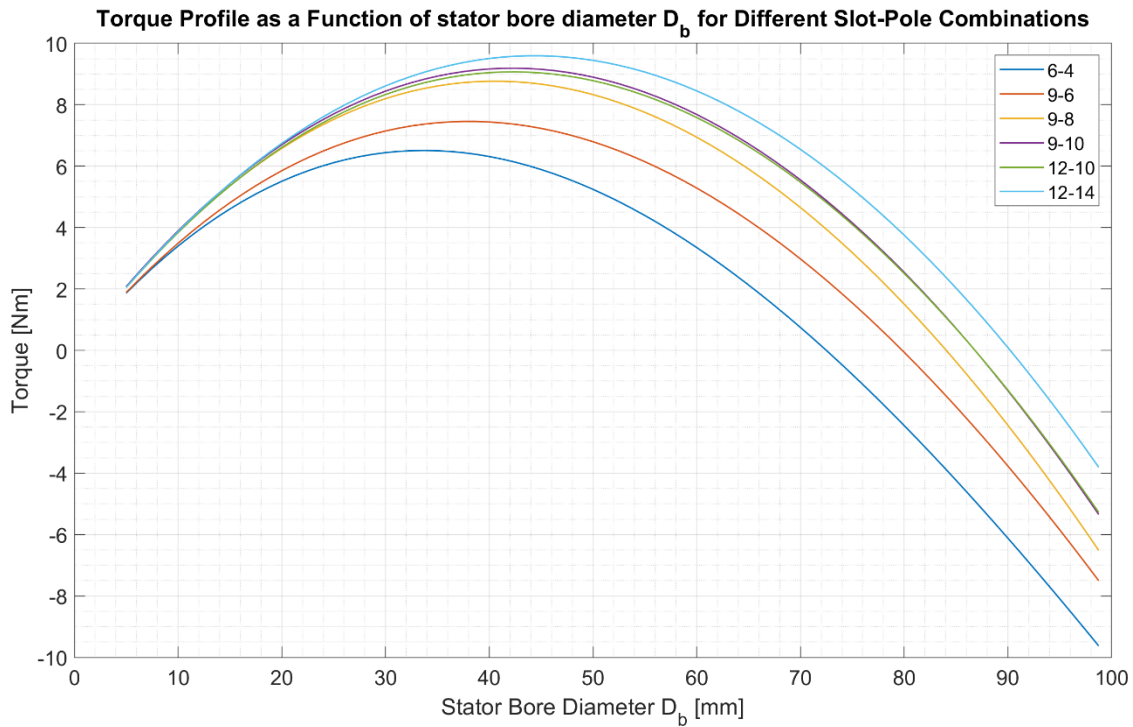


Figure 3-9: torque profile as a function of the stator bore diameter ratio D_b of different slot-pole combinations at constant RMS current density.

The previous figures showed the general trend of the torque profile over an extended range of stator diameters ratio x , actually it is reasonable to study the torque profile over a restricted range of x . The Figure 3-10 and Figure 3-11 show the torque profiles as a function of stator diameter ratio x and the bore diameter over a shorter range.

It can be noticed that the 6-4 slot-pole combination is feasible over a shorter range of stator bore diameter because at lower values of x the stator slots area is nearly zero and it is an unfeasible geometry. This fact is also confirmed by the position of the maximum torque value of 6-4 respect of the other slot-pole combinations, shown in Figure 3-8.

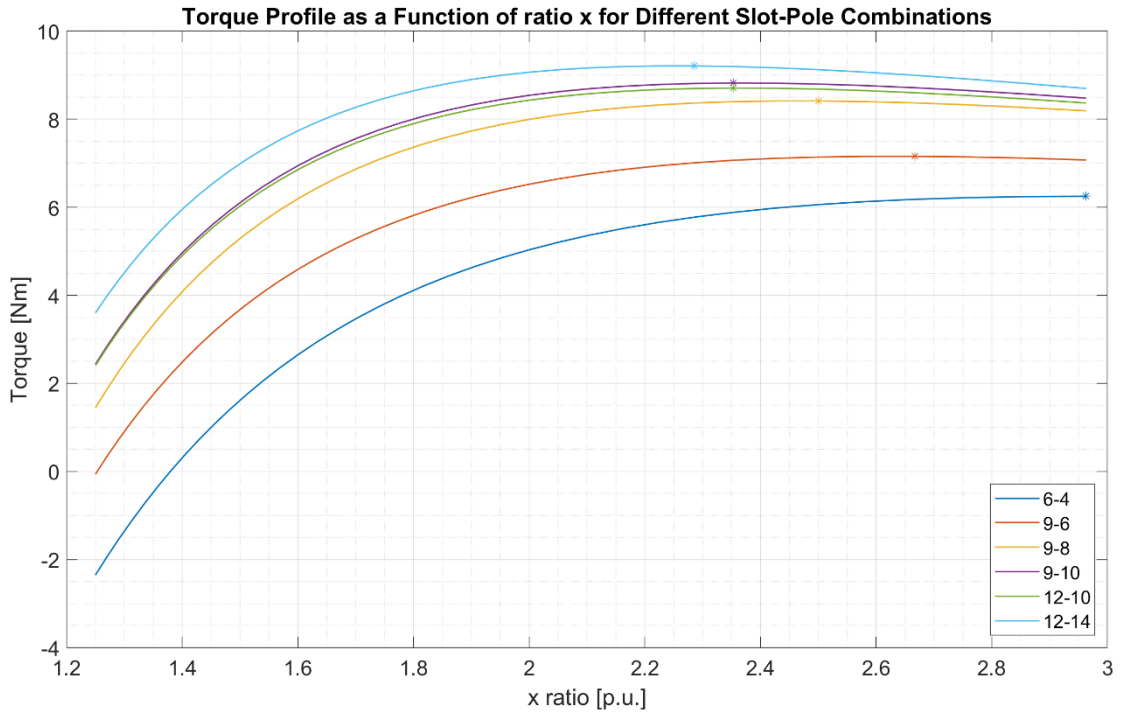


Figure 3-10: torque profile as a function of the stator diameters ratio x of different slot-pole combinations at constant RMS current density.

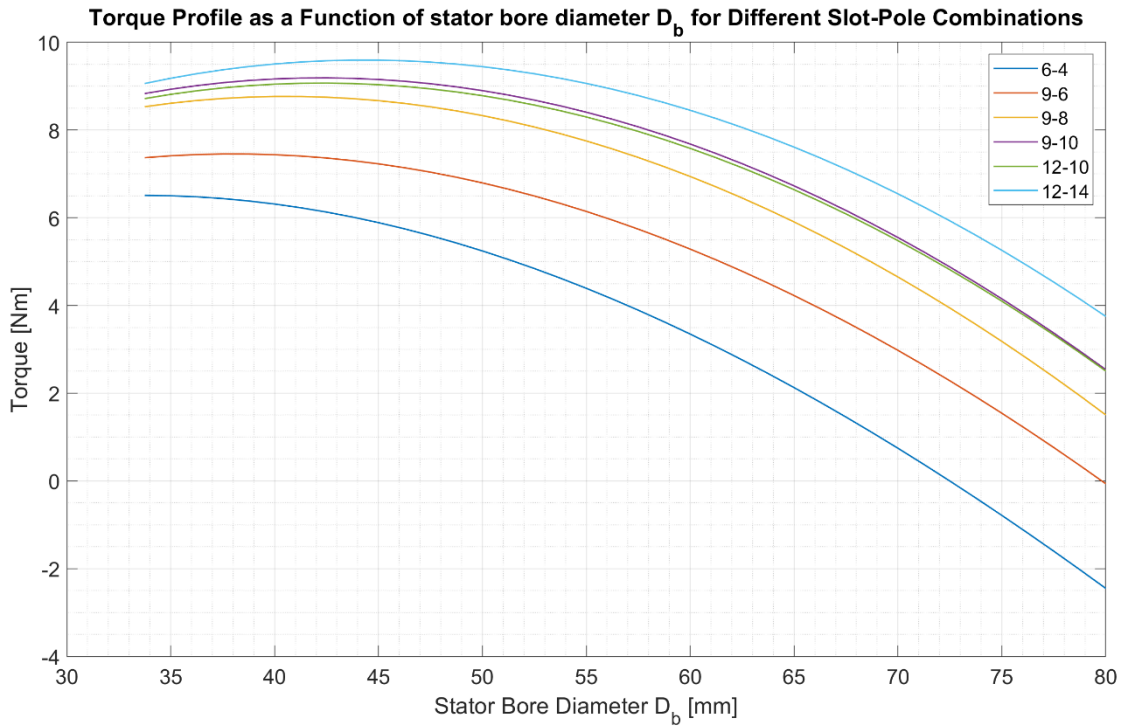


Figure 3-11: torque profile as a function of the stator bore diameter ratio D_b of different slot-pole combinations at constant RMS current density.

3.2.5. Design Method with Constant Joule Losses

The Joule losses are an important concern that has to be taken into account during electrical machines design, in particular for low speeds applications. In fact, at low mechanical speeds the Joule losses prevail on the iron ones, since the iron losses depend on the electric frequency f_e which is related to the mechanical frequency f_m by the pole pairs p . Given a required value of Joule losses, the current density has to be limited in order to respect the thermal constraint. In addition, as the stator bore diameter changes, the current density value changes too because the stator slots area varies.

Given a slot-pole combination, Joule losses value is set to the mean value of the Joule losses values obtained from the design at constant current density over a stator bore diameter range.

The Joule losses of a three-phase electrical machine can be expressed according to Eq. 3-4. Substituting the RMS phase current according to Eq. 3-53, the Joule losses are expressed in terms of RMS current density.

$$P_J = 3R_{ph} \left(\frac{S_{slot} k_{fill} j_{rms}}{n_{cs}} \right)^2 \quad \text{Eq. 3-59}$$

The phase resistance can be expressed in terms of the resistivity and geometrical parameter of the winding conductors: the phase conductor length l_{Cu} and the phase conductor cross-sectional area S_{Cu} . The phase conductor is assumed to be copper.

$$R_{ph} = \rho_{Cu_{100^\circ C}} \frac{l_{Cu}}{S_{Cu}} \quad \text{Eq. 3-60}$$

The copper conductor cross-sectional area can be expressed in terms of stator slot area, number of conductors in series and filling factor as:

$$S_{Cu} = \frac{S_{slot} k_{fill}}{n_{cs}} \quad \text{Eq. 3-61}$$

According to Eq. 3-60 and Eq. 3-61, from Eq. 3-59 the RMS current density can be computed in terms of the Joule losses.

$$j_{rms} = \sqrt{\frac{P_J n_{cs}}{3 \rho_{Cu_{100^\circ C}} l_{Cu} S_{slot} k_{fill}}} \quad \text{Eq. 3-62}$$

Assuming the same machine data of Table 3-1 and an electrical machine with 12-10 slot-pole combination, the Figure 3-12 shows the current density profile as a function of stator diameters ratio x . The Joule losses are fixed at 40.68 W.

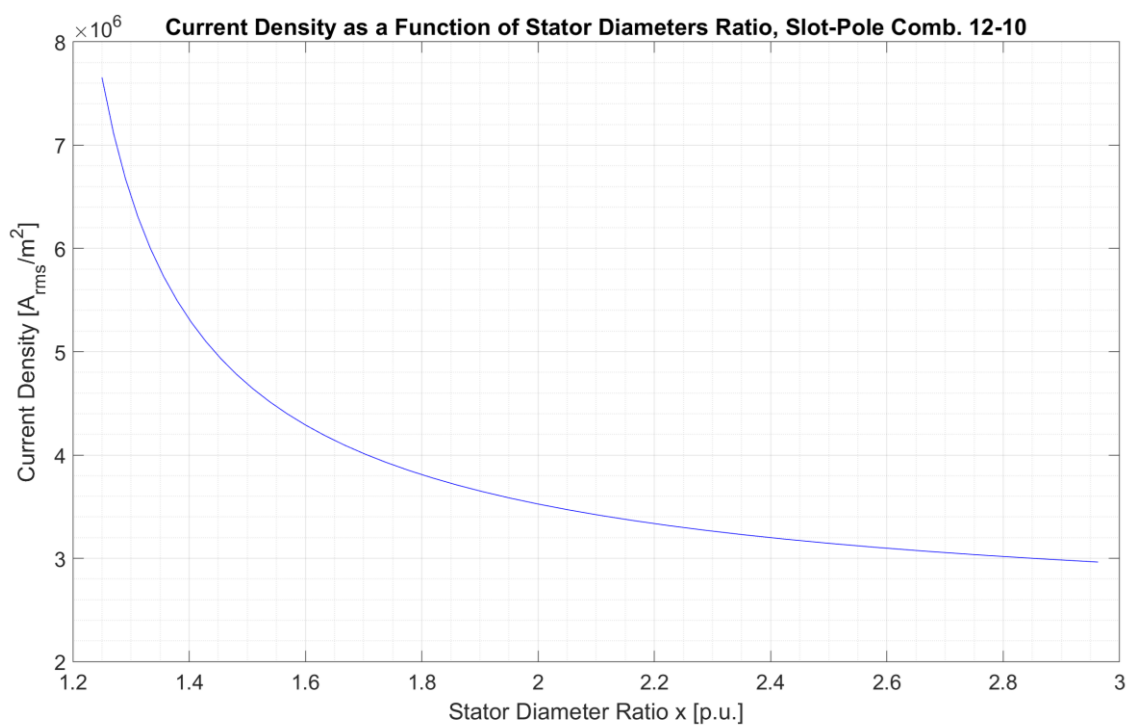


Figure 3-12: current density as a function of stator diameters ratio.

Once the RMS current density is computed for each stator diameter ratio the torque can be computed according to output equation. The Figure 3-13 and Figure 3-14 show torque profile of 12-10 combination as a function of stator diameter ratio x and stator bore diameter respectively.

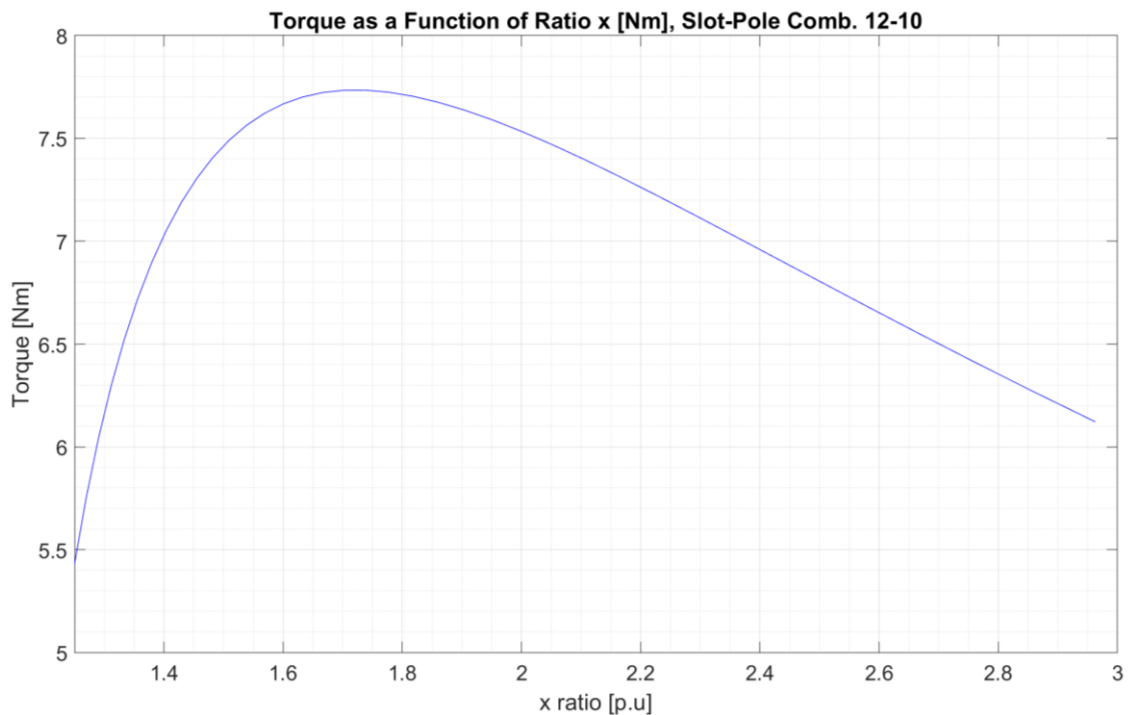


Figure 3-13: torque as a function of stator diameters ratio x .

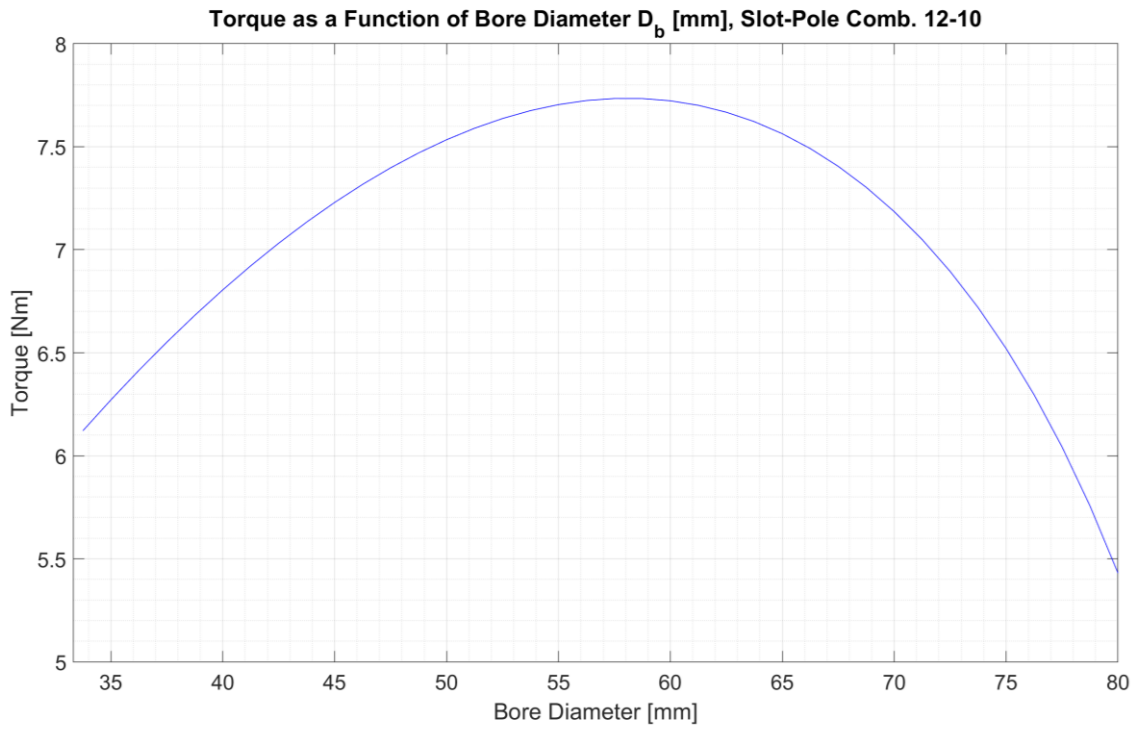


Figure 3-14: torque as a function of stator bore diameter.

The design process can be extended to any slot pole combinations and the following figures show the torques profile of different slot-pole combination as a function of stator diameters ratio x and stator bore diameter.

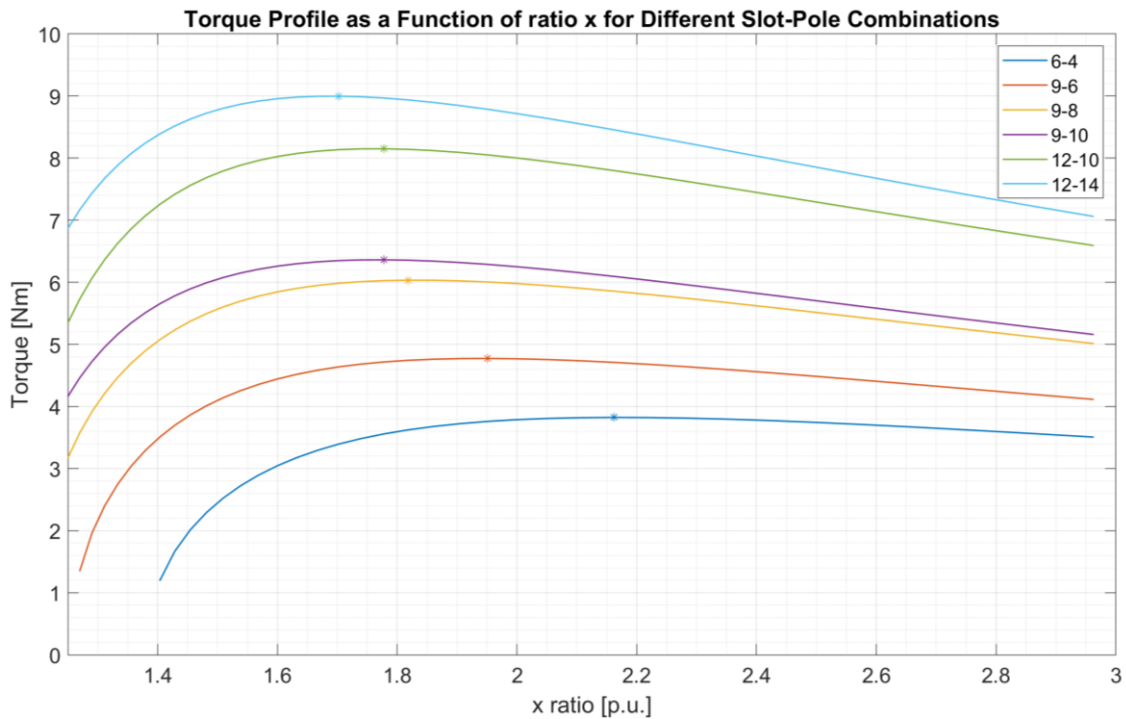


Figure 3-15: torque profile as a function of the stator diameters ratio x of different slot-pole combinations at constant Joule losses.

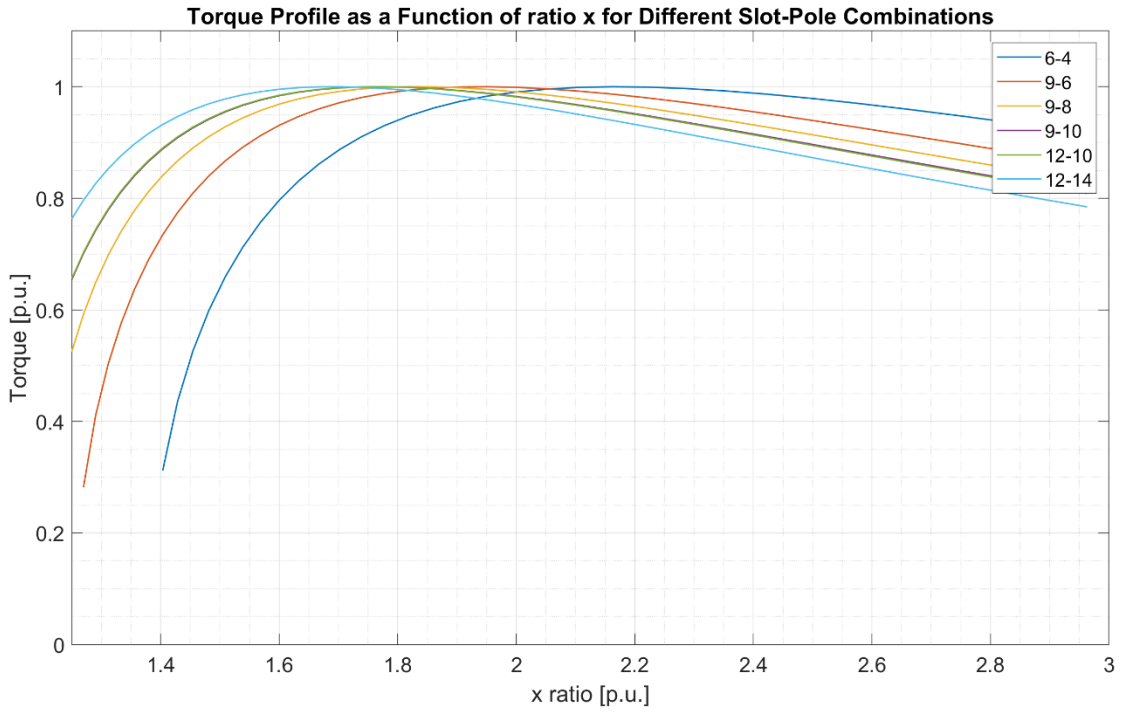


Figure 3-16: torque profile in p.u. as a function of the stator diameters ratio x of different slot-pole combinations at constant Joule losses.

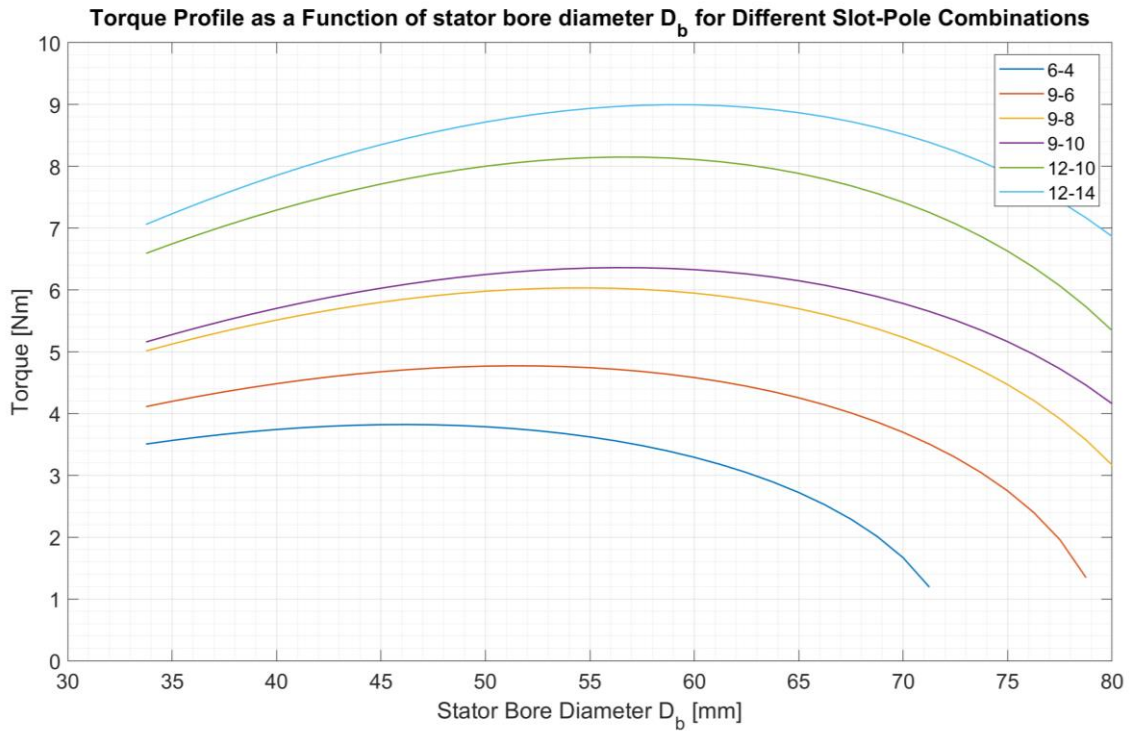


Figure 3-17: torque profile as a function of the stator bore diameter ratio D_b of different slot-pole combinations at constant Joule losses.

3.2.6. Analytic Results Comparison of two Design Approaches

The two design approaches lead to different machine performance in terms of torque production. The Figure 3-18 shows the torque profile of 12-10 slot-pole combination at constant current density (red solid line) and at constant Joule losses (blue solid line) and as it can be observed that:

- The maximum torque value with constant current density approach is around 1 Nm higher than the one with constant Joule losses;
- The maximum torque value shifts towards higher stator bore diameter moving from the design approach with constant current density to the design approach with constant Joule losses.

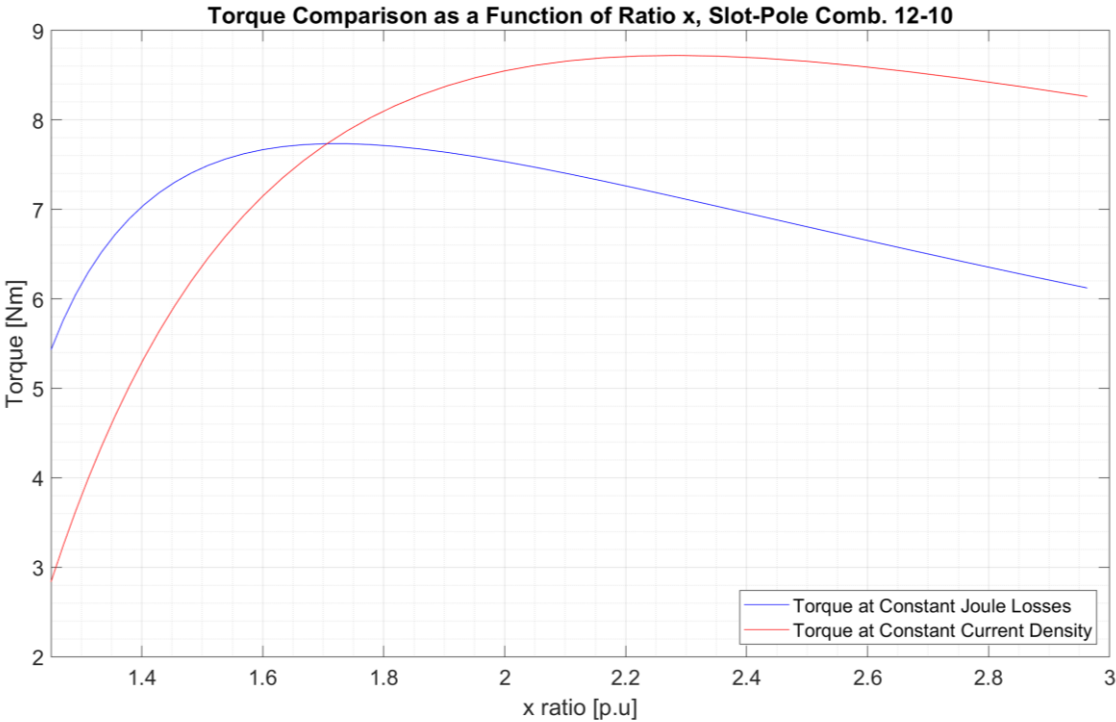


Figure 3-18: torque at constant current density Vs. torque at constant Joule losses as a function of stator diameter ratio.

The Figure 3-19 shows the same results in terms of torque production as a function of stator bore diameter.

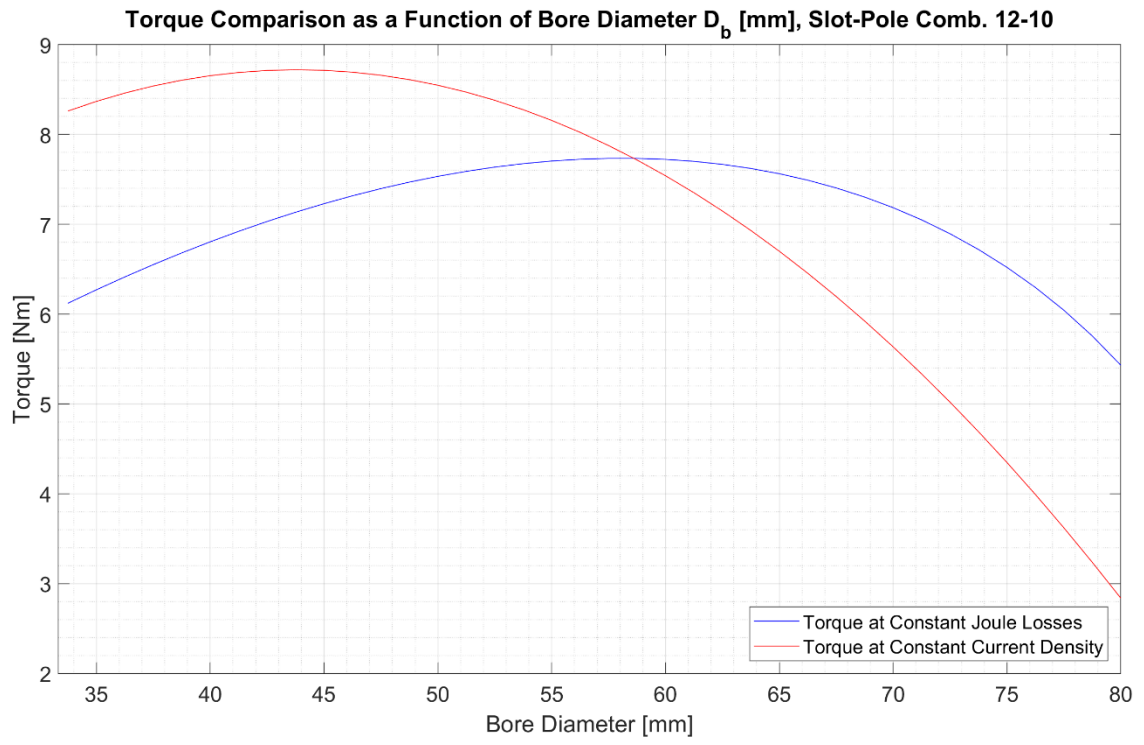


Figure 3-19: torque at constant current density Vs. torque at constant Joule losses as a function of stator bore diameter.

3.3. Analytical and Finite Element Analysis Comparison

Four different slot-pole combinations have been design based on the geometrical calculation of paragraphs §3.2.1, §0 and §3.2.3; the chosen combinations are 9-6, 9-8, 12-10 and 12-14 since they represent the typical slot-pole combinations adopted in the industrial automation.

The slot-pole combinations have been studied over a stator bore diameter range from 40 mm to 75 mm, with a step 5 mm. The Table 3-2 summarizes the geometrical data of the studied slot-pole combinations, while Table 3-3 shows Joule losses mean values computed with constant current density approach and used to compute current densities with the second design approach and shown in Table 3-4.

D_b	40	45	50	55	60	65	70	75
<i>x</i>	2.50	2.22	2.00	1.82	1.67	1.54	1.43	1.33
9-6								
w_t	6.6	7.4	8.3	9.1	10.0	10.8	11.7	12.5
h_y	4.8	5.4	6.0	6.6	7.2	7.8	8.4	9.0
9-8								
w_t	6.6	7.4	8.3	9.1	10.0	10.8	11.7	12.5
h_y	3.6	4.0	4.5	4.9	5.4	5.8	6.3	6.8
12-10								
w_t	8.6	8.0	7.5	6.9	6.3	5.7	5.2	4.6
h_y	5.2	4.8	4.5	4.1	3.8	3.4	3.1	2.8
12-14								
w_t	8.6	8	7.5	6.9	6.3	5.7	5.2	4.6
h_y	2.8	3.2	3.6	3.9	4.3	4.7	5	5.4

Table 3-2: main stator geometrical data of different slot-pole combinations.

	9-6	9-8	12-10	12-14
Joule Losses	33.10	38.91	40.69	44.9

Table 3-3: Joule losses values of studied slot-pole combinations at constant current density.

D_b	40	45	50	55	60	65	70	75
<i>x</i>	2.50	2.22	2.00	1.82	1.67	1.54	1.43	1.33
9-6	2.973	3.181	3.440	3.771	4.204	4.836	5.880	8.089
9-8	3.121	3.301	3.534	3.818	4.175	4.674	5.405	6.656
12-10	3.184	3.367	3.581	3.844	4.173	4.616	5.235	6.191
12-14	3.268	3.436	3.635	3.877	4.168	4.546	5.065	5.753

Table 3-4: current density values of different slot-pole combinations.

The FEA has been used to validate analytical process and then FEA results have been compared with the analytical ones.

3.3.1. Validation of Constant Current Density Approach

This chapter compares the analytical and FEA results of different slot-pole combinations assuming a constant current density equal to $4 \text{ A}_{\text{RMS}}/\text{mm}^2$ and a mechanical speed of 1000 r/min.

The Figure 3-20 shows the FEA performance where the torque is plotted as a function of stator diameter ratio x and stator bore diameter.

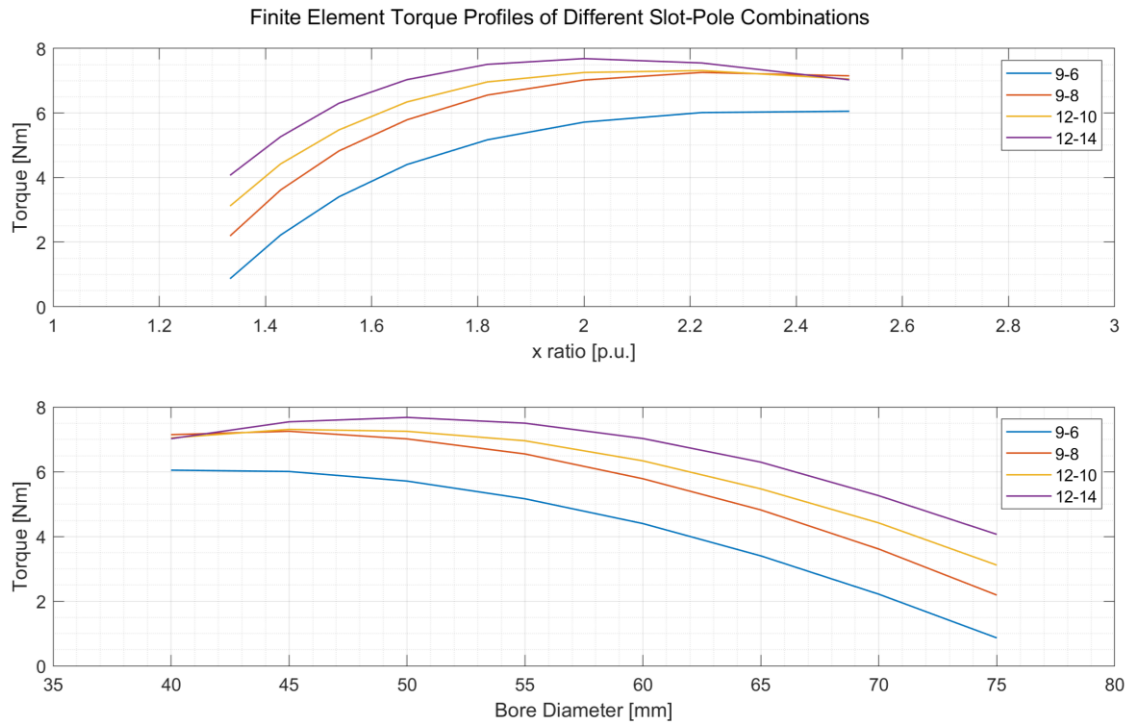


Figure 3-20: FEA torque profiles for different slot-pole combinations at constant current density.

The Figure 3-21 compares analytical and FEA performance of the four slot-pole combinations as a function of stator diameters ratio x .

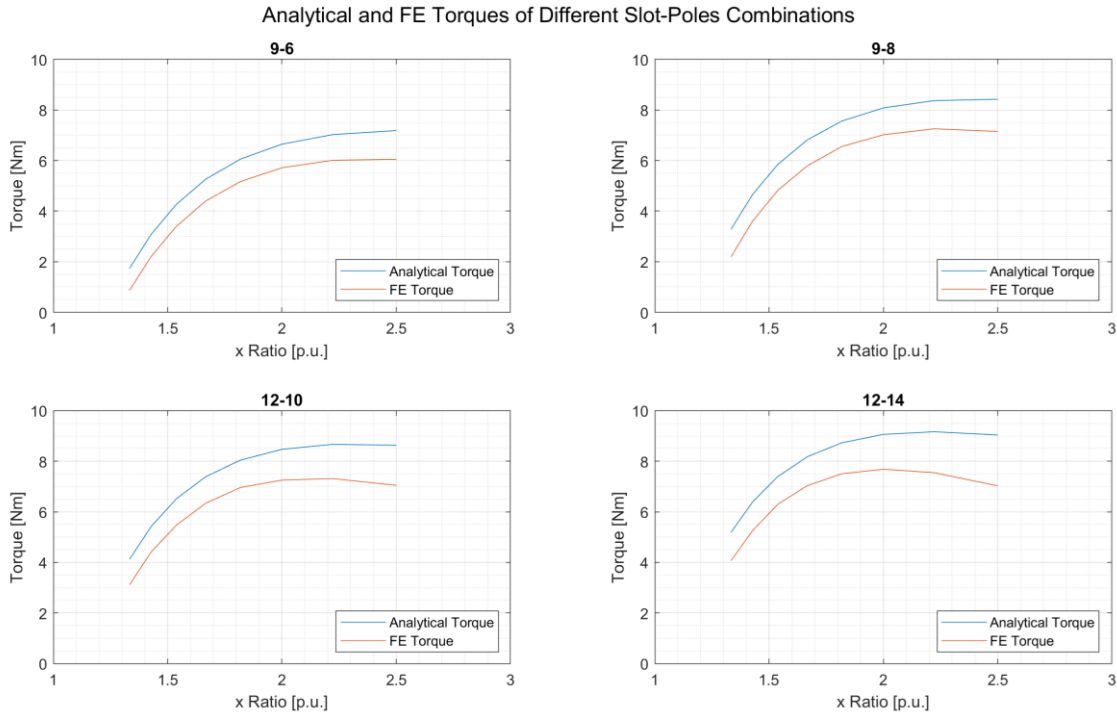


Figure 3-21: comparison of analytical and FEA torque profiles at constant current density.

As it can be seen in Figure 3-21, FEA results are lower around the 20% than analytical ones. This difference suggests that the analytical method tends to overestimate the produced torque because it does not take into account leakage fluxes that reduces the available magnetic load. According to this, the analytical method has been improved to take into account the leakage phenomena.

A portion of PM flux does not take part in torque production because it flows from one magnet to the adjacent one and from the magnet to the rotor core. In order to consider this phenomenon, an air gap leakage flux coefficient k_{Lg} has been considered as shown in [8].

Eq. 3-63 expresses the air gap magnetic reluctance where w_m represents the length of a magnet in [mm].

$$\mathcal{R}_g = \frac{g}{\mu_0(w_m + 2g)L_{stk}} \quad \text{Eq. 3-63}$$

Then given the area of a permanent-magnet A_m , the magnetic reluctance of the PM is computed as:

$$\mathcal{R}_{pm} = \frac{h_m}{\mu_0\mu_{r_{pm}}A_m} \quad \text{Eq. 3-64}$$

The reluctance of magnetic paths from two adjacent magnets \mathcal{R}_{m-m} and from the magnet to the iron core \mathcal{R}_{m-r} are computed by means the magnetic permeance \mathcal{P}_{ith} . Then, the magnetic reluctance is the inverse of the magnetic permeance.

$$\mathcal{P}_{m-r} = \frac{\mu_0 L_{stk}}{\pi} \ln \left(1 + \frac{\pi \min \left(g, \frac{w_f}{2} \right)}{2} \right) \quad \text{Eq. 3-65}$$

$$\mathcal{P}_{m-m} = \frac{\mu_0 L_{stk}}{\pi} \ln \left(1 + \frac{\pi g}{w_f} \right) \quad \text{Eq. 3-66}$$

The available magnetic flux in the air gap and magnetic flux from PMs are expressed as follows:

$$\Phi_g = \frac{\Phi_r}{1 + \left(\frac{\mathcal{R}_g}{\mathcal{R}_{pm}} \right) (1 + 2\eta_{lipo} + 4\lambda_{lipo})} \quad \text{Eq. 3-67}$$

$$\Phi_m = \frac{1 + \left(\frac{\mathcal{R}_g}{\mathcal{R}_{pm}} \right) (2\eta_{lipo} + 4\lambda_{lipo})}{1 + \left(\frac{\mathcal{R}_g}{\mathcal{R}_{pm}} \right) (1 + 2\eta_{lipo} + 4\lambda_{lipo})} \Phi_r \quad \text{Eq. 3-68}$$

Where Φ_r is the residual flux in the air gap, η_{lipo} and λ_{lipo} are two ratio which formula is provided in [8]. Finally, the air gap leakage flux coefficient is expressed as the ratio of the available magnetic flux in the air gap and the permanent-magnet magnetic flux.

$$k_{Lg} = \frac{\Phi_g}{\Phi_m} \quad \text{Eq. 3-69}$$

This new coefficient reduces the effective PM flux density that contributes to producing the electromagnetic torque.

$$\hat{B}'_g = \hat{B}_m \alpha_i k_{Lg} \quad \text{Eq. 3-70}$$

The authors of [8] proposes also a zig zag leakage flux coefficient, but the results obtained for the analyzed slot-pole combinations with the given formulas do not agree with those shown in the paper. This portion of leakage flux will be further analyzed in order to include in the analytic method also the zig zag leakage magnetic flux.

The Figure 3-22 shows the improvement of analytical model with the inclusion of the air gap leakage flux coefficient. The agreement between analytical model and FEA results is more remarkable when the torque reaches its maximum value.

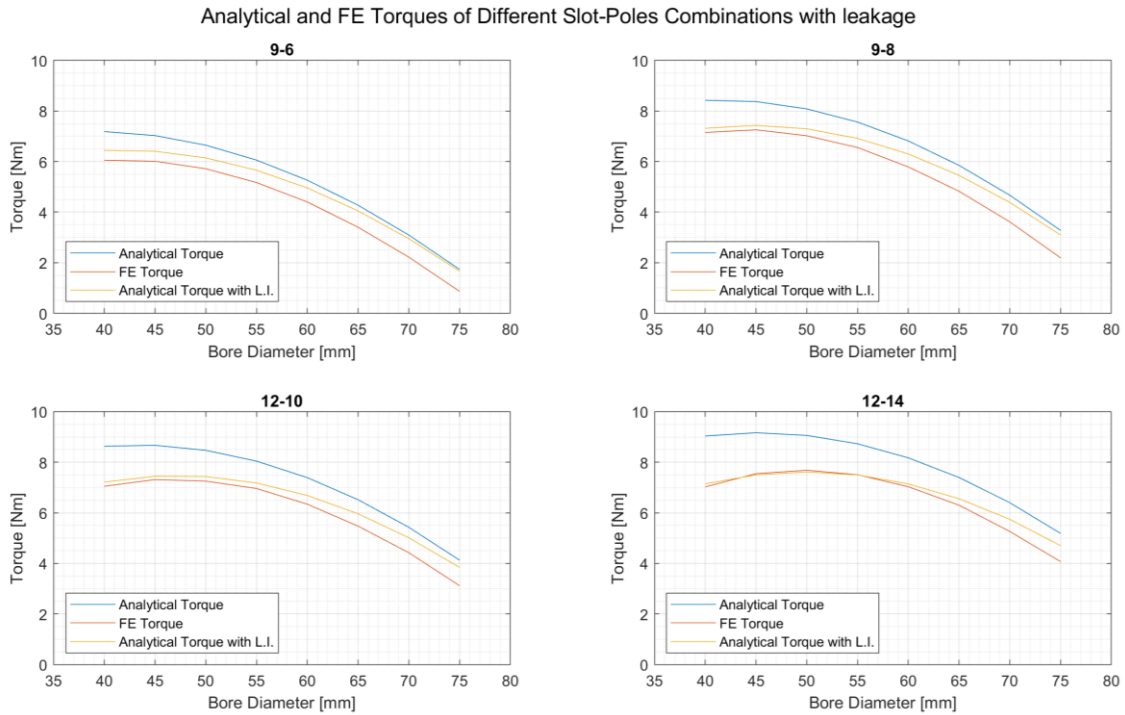


Figure 3-22: comparison of analytical torques without and with air gap leakage inductance coefficient and FEA torque at constant current density.

The agreement between analytical and FEA results could be used to understand the feasibility of a given electrical machine geometry function of stator diameters ratio x . The results agreement decreases as the stator bore diameter increases because the slots area for the windings decreases. This is particularly true for those slot-pole combinations with a low slot-poles number since they need more back iron and have larger stator teeth. The Figure 3-32 compares two geometries of 9-8 slot-pole combination with a stator bore diameter of 60 mm and 75 mm; it is evident how the 9-8 combination with 75 mm is not feasible from a design point of view since the slot cross-sectional area is too poor.

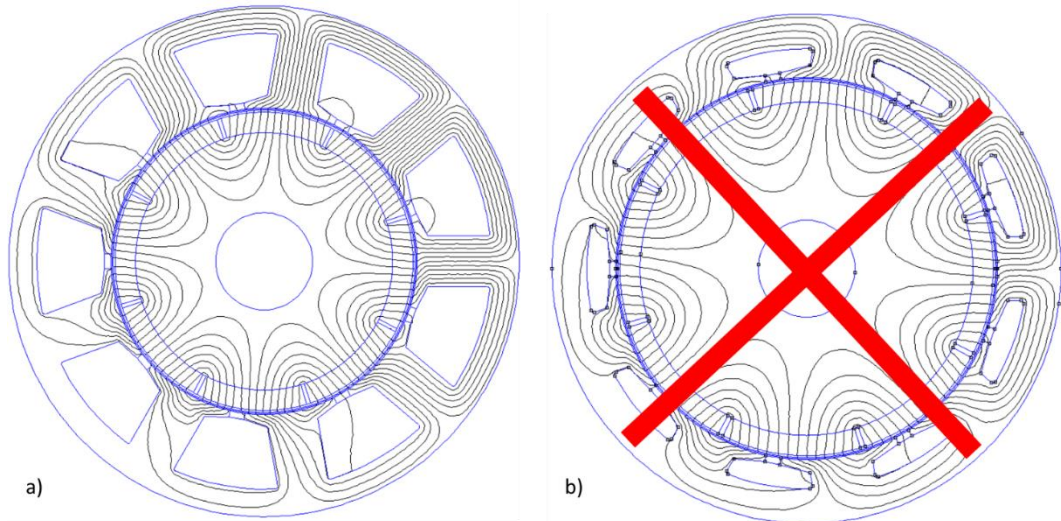


Figure 3-23: a) 9-8 having a bore diameter of 60 mm ($x=1.67$) and b) 9-8 having a bore diameter of 75 mm ($x=1.33$).

The design feasibility index k_{fea} is defined as the ratio of the corrected analytical torque to FEA torque. The more the ratio is close to the unity, the more the machine geometry is feasible. The Figure 3-24 shows the profiles of feasibility index of the studied slot-combinations; as it can be seen the feasibility index increases as the bore diameter increases.

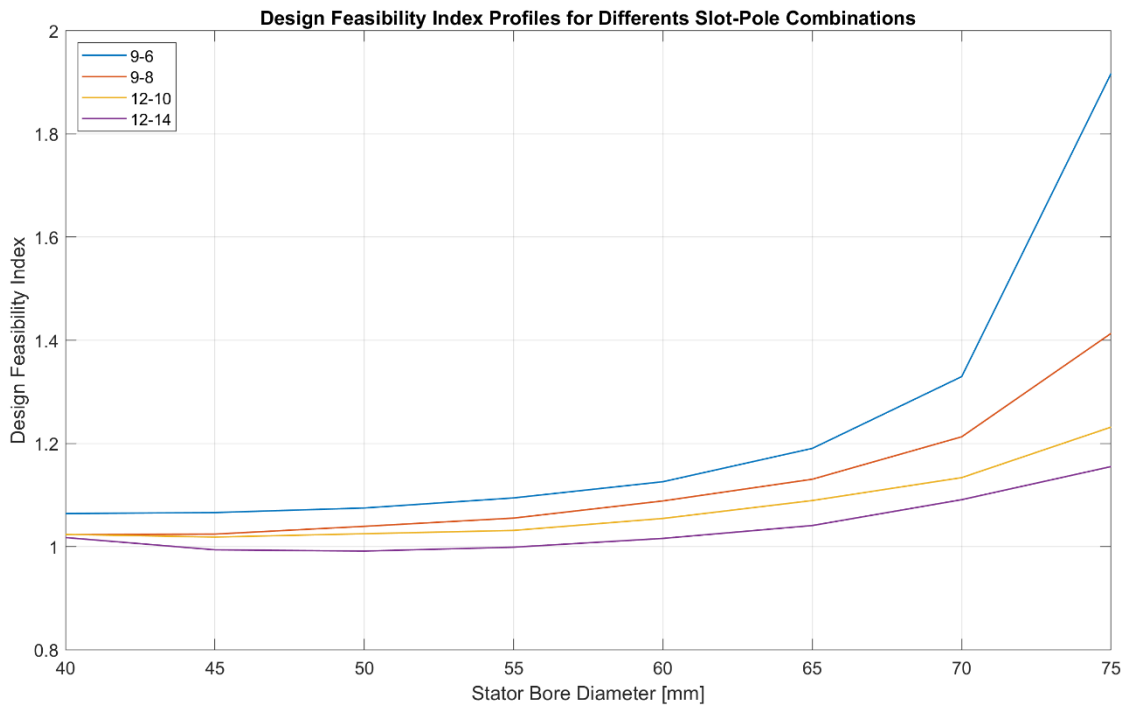


Figure 3-24: feasibility index profiles as a function of the stator bore diameter at constant current density.

The Figure 3-25 shows the power factor profiles as function of stator diameters ratio x for the analyzed slot-pole combinations; as it can be seen the power factor decreases as the stator bore diameter decreases too. This behavior is due to the increase of winding inductive component given by the higher stator slot area available for the copper windings. In addition, the power factor of 12-14 combination is strictly affected by the stator bore diameter. The maximum torque is for a stator bore diameter equal to 50 mm, ($x = 2$) and the corresponding power factor is equal to 0.92549, thus nearly the 4.5% less than the 12-10 combination.

The Figure 3-26 shows the Joule losses profiles as a function of stator diameter ratio x . The Joule losses increase as the stator slot area increases, since there is more copper in which flows the same current density \vec{j} .

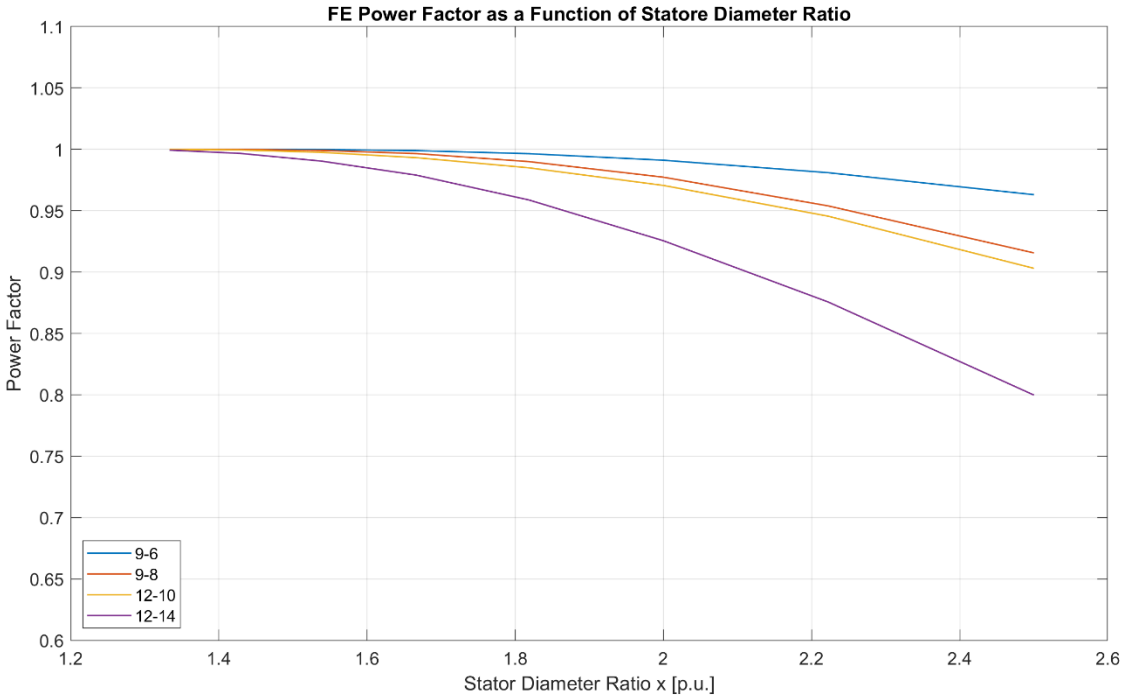


Figure 3-25: FEA power factor as a function of stator diameter ratio for different slot-pole combinations at constant current density.

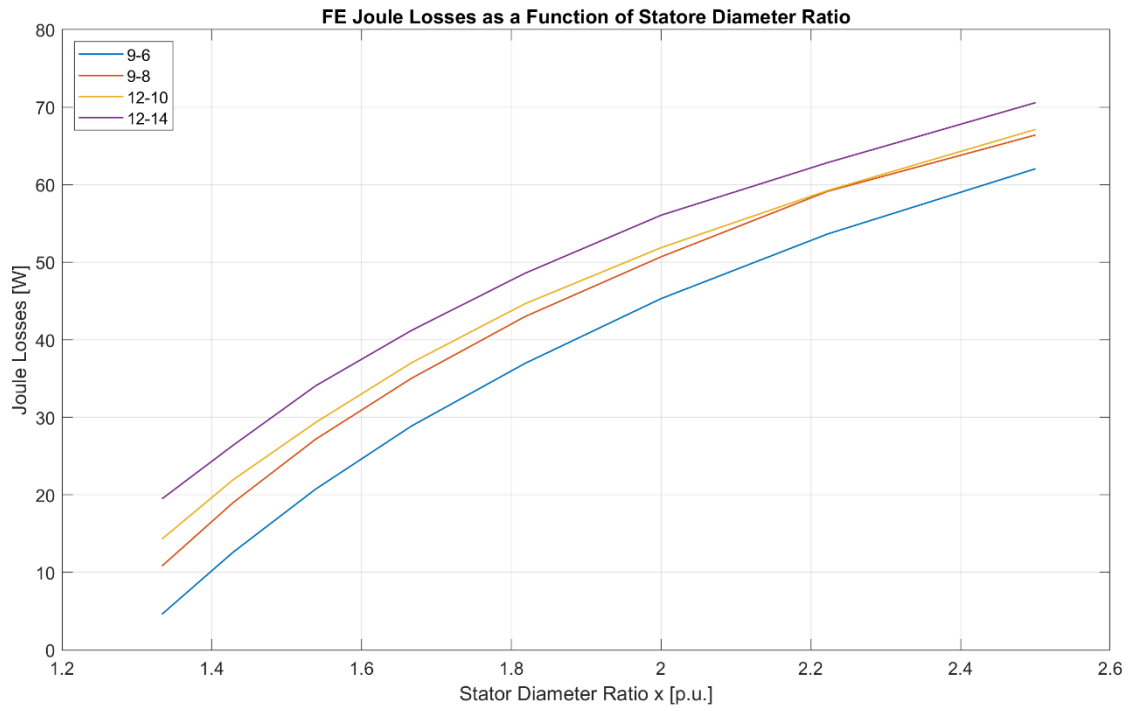


Figure 3-26: FEA Joule Losses as a function of stator diameter ratio for different slot-pole combinations at constant current density.

3.3.2. Validation of Constant Joule Losses Approach

The studied slot-pole combinations geometries have been simulated via FEA imposing variable current density values computed with the constant Joule losses design approach. The current density values are listed in Table 3-4.

Figure 3-27 shows the FEA torque as a function of stator diameter ratio x and stator bore diameter, while Figure 3-28 compares the analytic torque and FEA torque of the four studied slot-pole combinations. As it already seen for the previous case, FEA results are lower than analytic ones, since the design process does not take into account leakage inductance phenomena.

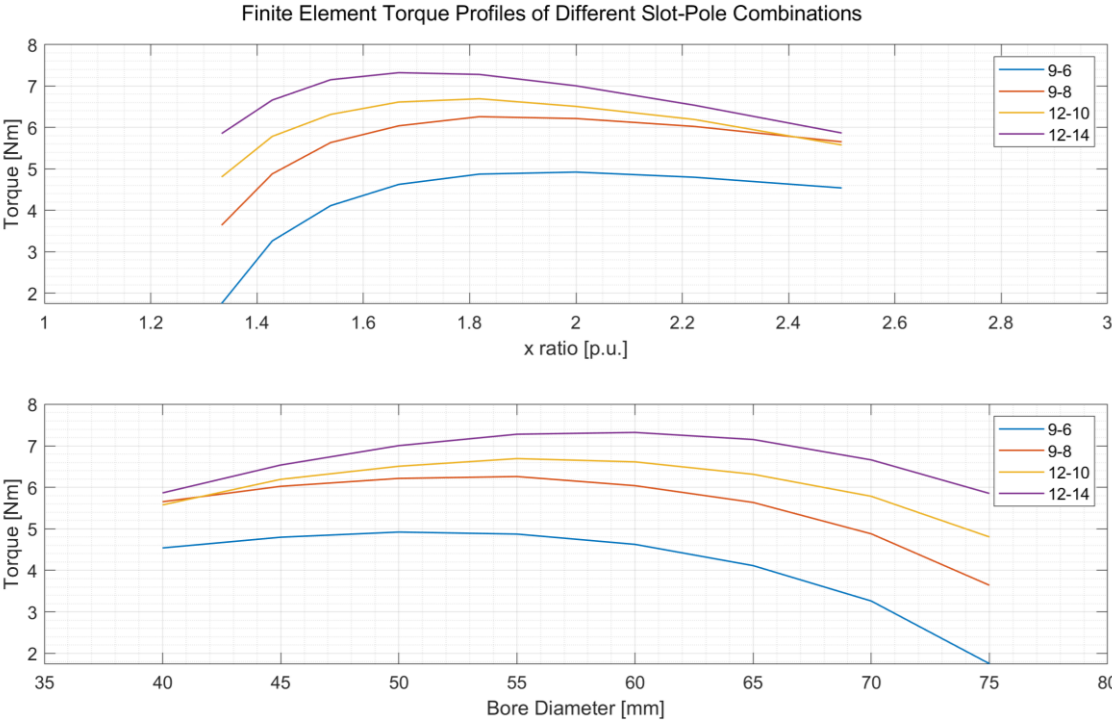


Figure 3-27: FEA torque profiles for different slot-pole combinations at constant Joule losses.

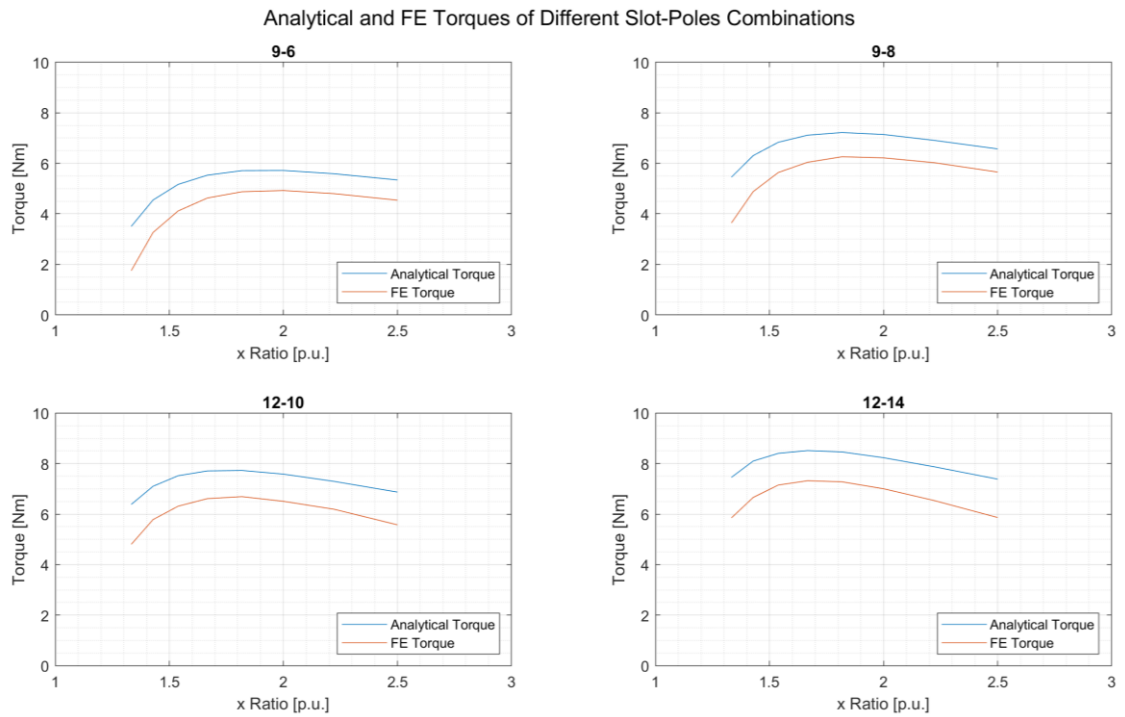


Figure 3-28: comparison of analytical and FEA torque profiles at constant Joule losses.

The Figure 3-29 shows the improved analytical results including also the air gap leakage flux coefficient k_{Lg} that takes into account the portion of PMs flux that does not take part in the output torque production.

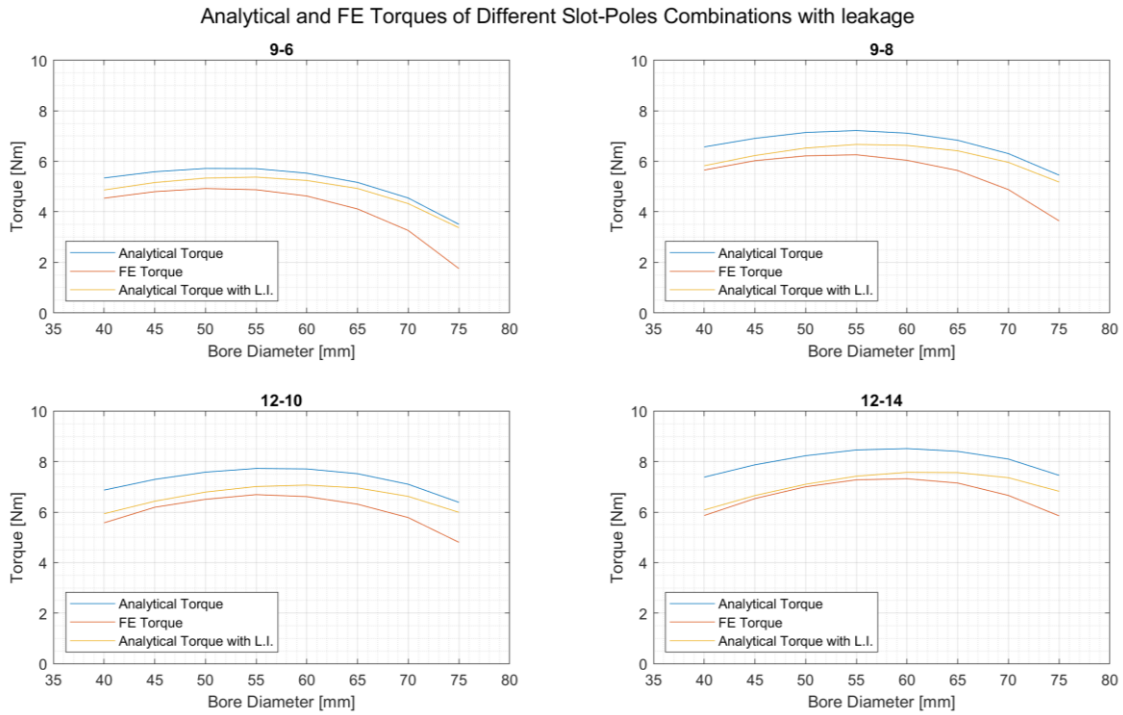


Figure 3-29: comparison of analytical torques without and with air gap leakage inductance coefficient and FEA torque at constant Joule losses.

The feasibility index shows also in this case that machine geometries are feasible if stator bore diameter is not so close the stator outer diameter.

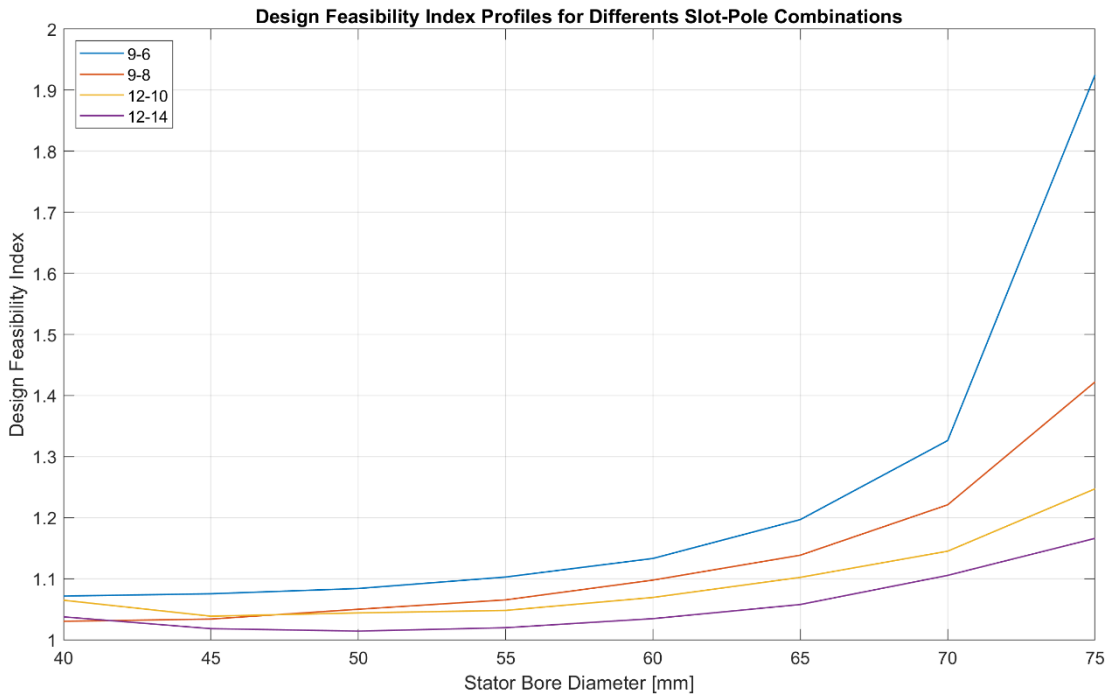


Figure 3-30: feasibility index profiles as a function of the stator bore diameter at constant Joule losses.

The Figure 3-31 shows the power factor profiles as function of stator diameters ratio for different slot-pole combinations. The profiles of power factors are confirmed also in this case, but the 12-14 combination exhibits the maximum torque at 60 mm ($x = 1.6$), thus most performant machine has a higher power factor than the one design with a constant current density.

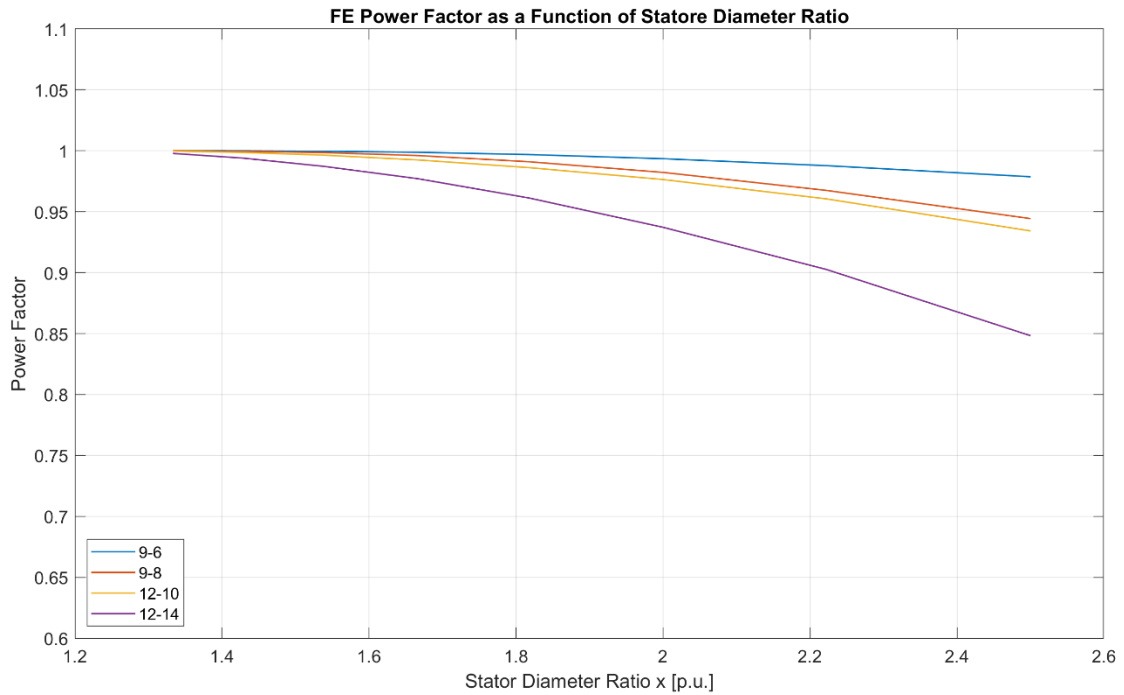


Figure 3-31: FEA power factor as a function of stator diameter ratio for different slot-pole combinations at constant Joule losses.

The Figure 3-32 shows the Joule power losses as a function of stator diameter ratio; as it can be seen the Joule losses are maintained pretty constant over the range of studied stator bore diameter. When the stator bore diameter is closer to stator outer diameter Joule losses rapidly decrease due the quadratic proportion to stator slot area which is very low.

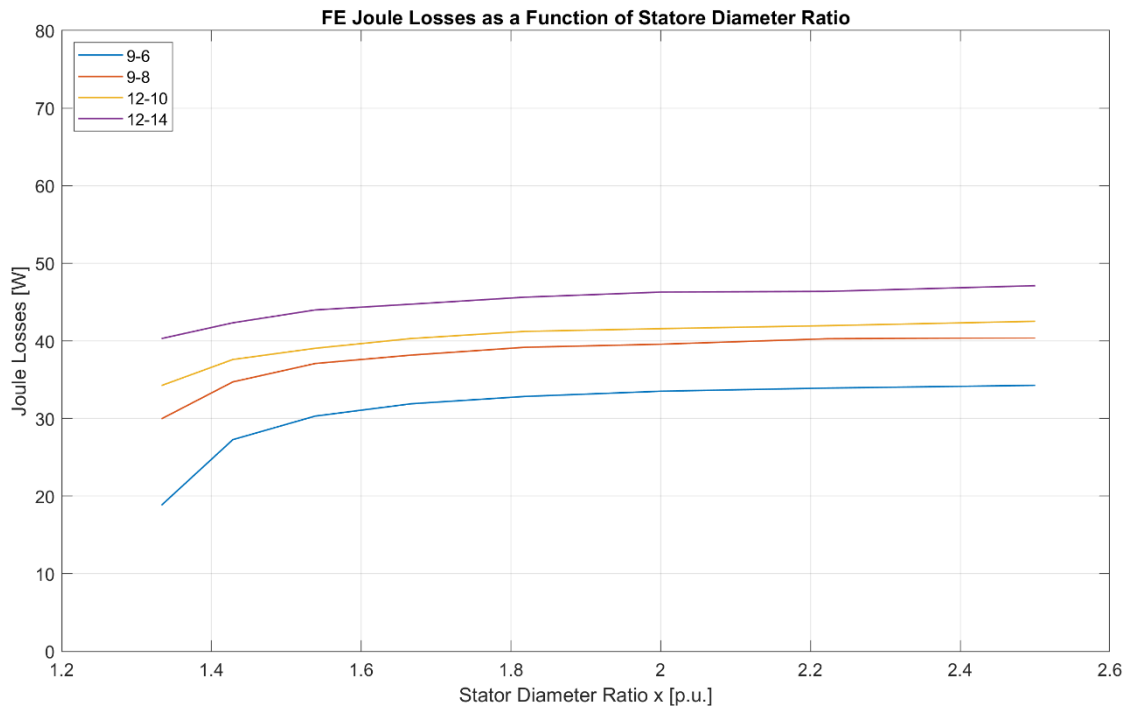


Figure 3-32: FEA Joule losses as a function of stator diameter ratio for different slot-pole combinations at constant Joule losses.

3.4. Future Developments

This chapter shows an analytical design approach for SPM-SMs intended for low speed applications. The unique design variable of the proposed analytical design is stator bore diameter, while the other design variables are defined a priori by the machine designer.

The performance of the machine geometries over a restricted range of stator bore diameter has been analyzed according to two different assumptions: imposing a constant current density and imposing constant Joule losses. The first assumption could be considered a design approach aimed to study the maximum performance of the electrical machine, disregarding the constraint of thermal stress. The second assumption is oriented to analyze machine performance at rated conditions considering a thermal constraint which imposes a variation of current density as a function of stator bore diameter, since the stator slot area tends to decrease as the stator bore diameter gets closer to the outer one.

The results of the analytical model have been analyzed and then validated via FEA simulation. The design according to a constant current density leads to a slightly higher maximum torque than the one at constant Joule losses, but the power factor of the electrical machine is lower. This is particularly true for the 12-14 slot-pole combination which shows a very strong sensibility to stator bore diameter. The difference of power factors is due to the fact that the maximum torque is obtained at two different stator bore diameters according to the adopted assumption. In general, it has been observed that at constant current density the maximum torque occurs at lower stator bore diameters.

The validation via FEA highlighted a results overestimation of the analytical model because it does not take into account the magnetic leakage flux components such as the air gap leakage flux and zig zag leakage flux. According to [8], it has been introduced a air gap leakage flux coefficient which reduces the useful magnetic flux producing the output torque. After this correction, the agreement between analytical and FEA results increased in particular at lower and medium stator bore diameter values.

From the agreement between corrected analytical results and FEA ones, it has been defined a feasibility index which provides to the machine designer an idea on the geometrical feasibility of the machine. It has been observed that for lower slot-pole combinations such as 6-4 and 9-6 as the stator bore diameter tends toward the outer diameter the machine feasibility rapidly decreases since there is less and less area for stator slots.

In view of the obtained results, possible future developments could be:

- The integration of zigzag leakage coefficient in order to include also the magnetic flux lost due to stator slots;
- The extension of the analytical approach to iron losses for high speed applications.

4. Robustness Analysis of Fractional-Slot Surface Permanent-Magnet Machines

This chapter deals with a robustness analysis with respect to manufacturing imperfections of Fractional-Slot (FS) SPM-SMs as a function of slot-pole combinations. Nowadays, machine robustness is one of the most important requirements in order to guarantee the performance of the electrical machine and also of the system of which it is part.

From a design point of view, the slot-pole combination is one the most important design parameter and it influences both the performance and the robustness of FS-SPM machines.

The contribution of this research activity is to define a design for sensibility method which models and includes manufacturing defects since from the initial optimization design process of the electrical machines by means the FEA.

The performance of main slot-pole combinations has been studied and compared both at healthy and defective conditions. Generally, the state-of-the-art offers many studies on design optimization at healthy condition, but then during experimental tests some deviation between experimental and FEA results could occur due to unavoidable manufacturing defects. In fact, the manufacturing process introduces some unavoidable defects related to mechanical tolerances or to PMs.

Some authors have compared the performance of healthy and defective machines by means FEA simulation, but the comparison relies on a limited set of benchmarks e.g. cogging torque [9], [10] or radial force [11],[12]. Other authors compared healthy and defective machines to define a set a diagnostic index, e.g. demagnetization, in order to effectively identify specific faults [13].

The proposed method provides optimal design to compute maximum performance and the robustness respect with unavoidable imperfections introduced during the manufacturing process of the electrical machines.

4.1. Fractional-Slot Surface Permanent-Magnet Machines

Surface Permanent-Magnet synchronous machines are used in many different applications such as industrial automation, home appliance and in the last years electric traction.

One of the most attractive typologies is Fractional-Slot (FS) SPM-SM which has been gained more and more interest thanks to its high torque density, low cogging torque, high power factor and high efficiency. The term *fractional slot* refers to a not integer SPP number, thus it is not a multiple of the number of poles p .

As drawbacks, the SPM-SMs are prone to defect and suffer of poor magnets quality which could affect machine performance in terms of torque production capability. Moreover, SPM-SMs are generally considered poor candidates for high-speed

applications because the characteristic current is higher than rated one, while optimal flux-weakening condition occurs when two current values are equal.

Authors of [14] propose a stator winding design approach to increase SPM-SM flux-weakening operation. The proposed solution is a concentrated fractional-slot stator winding which significantly increases d-axis inductance L_{sd} reducing characteristic current until reaching equality with rated current.

Concentrated windings are feasible only on FS machines and have an SPP number less than 0.5. Generally, non-overlapping winding is the most adopted configuration due to its short length of end-windings. In addition, concentrated winding allows optimizing manufacturing solutions such as modular stator tooth and thus high filling factor, short end turns and copper volume reduction that decreases production costs and reduces parasitic resistances. The FS machines could also have distributed windings where the SPP is higher than 1, but they are less common than concentrated windings machines.

The concentrated winding exhibits a higher harmonic content of air gap MMF than distributed winding. The typical MMF Fourier harmonic decomposition of a concentrated winding presents: the fundamental harmonic f_1 , a set of sub- and high-order harmonics of the fundamental one. The fundamental harmonic is synchronous with the fundamental frequency of PMs magnetic field and their interaction contributes to torque production. The sub-harmonics components have amplitude which is higher than fundamental one, while the amplitude of the higher harmonics decreases as the frequency increases. The Figure 4-1 shows the typical MMF Fourier harmonic decomposition of FS-SPM with concentrated winding with a pole pair number p equal to 4.

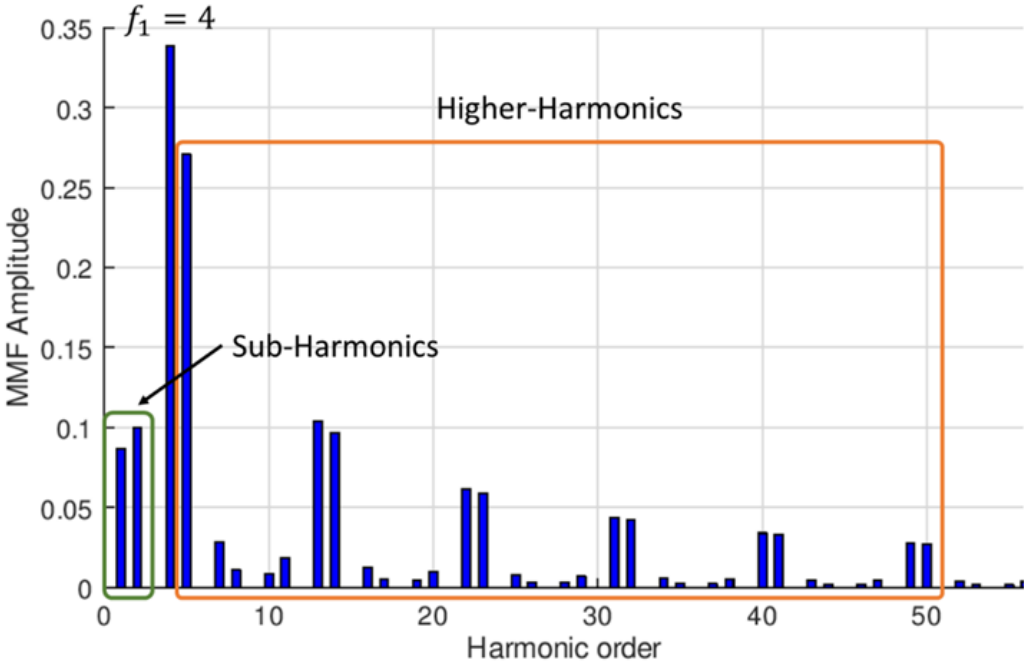


Figure 4-1: Magneto-Motive Force of 9 slots and 8 poles machine.

The distributed windings have lower harmonics content; in particular they have higher orders than the fundamental frequency which has the highest amplitude. The Figure 4-2 shows the MMF Fourier harmonic decomposition of SPM-SM with distributed winding with a pole pair number p equal to 4.

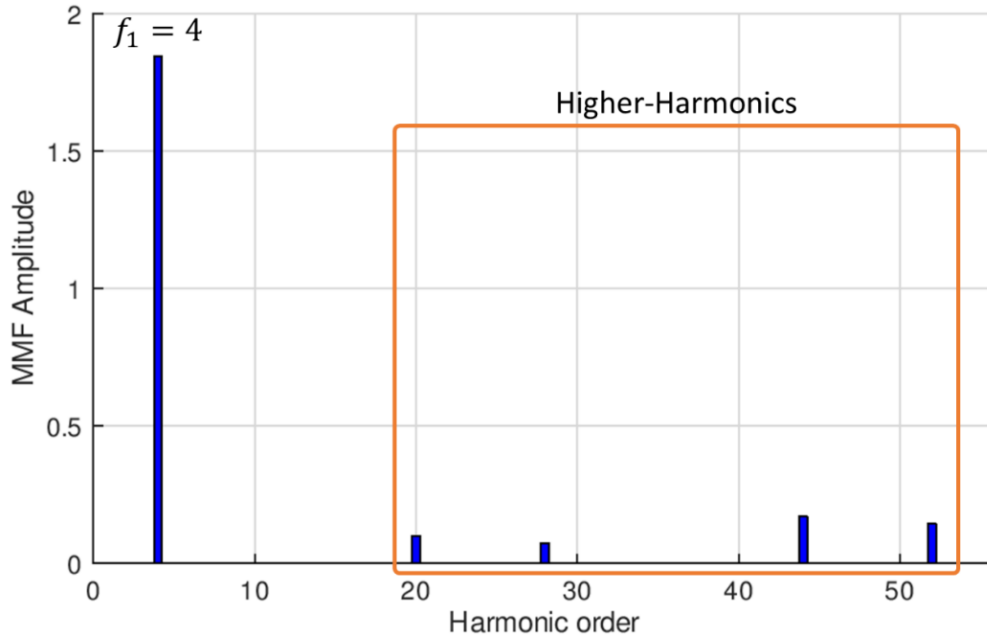


Figure 4-2: Magneto-Motive Force of 48 slots and 8 poles machine.

The higher MMF harmonic content of the concentrated winding electrical machine is key point of the increased flux-weakening capability, since the leakage inductance is higher and increases the value of d-axis synchronous inductance $L_{s,d}$ [14].

The MMF harmonic content is influenced also by the number of winding layers; the most common topologies are single- and double-layer windings because they maximize the winding factor for the main harmonics. Nevertheless single-layer winding exhibits a higher MMF harmonic content than double-layer one, thus machines performance are different [15]. The single-layer winding is not feasible for any slot-pole combination; in fact two constraints have to be followed: an even number of stator slots Q and an odd coil throw value [16]. The Figure 4-3 compares the MMF harmonic content of 12-10 combination with single- and double-layer winding.

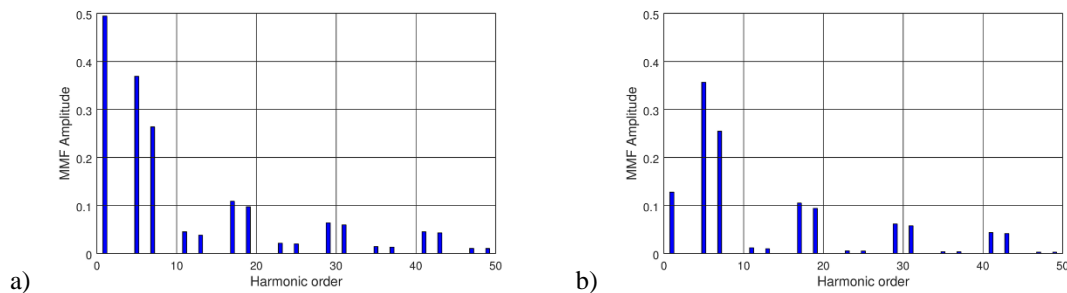


Figure 4-3: comparison of stator MMF harmonic content of 12-10 combination a) with single-layer and b) double-layer windings.

In this research activity FS-SPM machines are assumed with a concentrated winding arrangement.

4.2. Slot-Pole Combination

The slot-pole combination is one of the key design parameters and its choice relies on specific design objectives and machine dimensions. The slot-pole combination affects stator air gap MMF waveform and amplitude, cogging torque [17], torque ripple, torque density, power factor [18], etc.

The feasibility of a slot-pole combination for an electrical machine with a given number of phases m can be verified by the following expression:

$$\frac{Q}{mt} = \text{integer number} \quad \text{Eq. 4-1}$$

where t is the periodicity of the electrical machine, computed as the great common divisor between the number of slots Q and the pole pairs p .

4.2.1. Cogging Torque [17]

The cogging torque is a drawback due to the interaction between the rotor PMs and stator anisotropy due to the slotting. The cogging torque is directly affected by the slot-pole combination, since it affects the cogging torque waveform τ_g during a rotation of a slot pitch (Eq. 4-2) and the number of cogging periods N_p (Eq. 4-3).

$$\tau_{cog}(\theta_{mec}) = \sum_{k=1}^{\infty} T_k \sin(kQ\theta_{mec} + \varphi_k) \quad \text{Eq. 4-2}$$

$$N_p = \frac{2p}{HCF\{Q, 2p\}} \quad \text{Eq. 4-3}$$

The angle θ_{mec} is the rotor mechanical angular position and HCF is the Highest Common Factor. The cogging torque amplitude is inversely proportional to the number of cogging torque periods N_p , thus the higher the cogging torque periods, the lower the cogging torque amplitude.

4.2.2. Stator Magneto-Motive Force (MMF)

The slot-pole combination affects the stator MMF induced in the air gap, in particular it is remarkable that fundamental harmonic f_1 and harmonics order have difference patterns as the slot-pole combination changes.

Figure 4-4 shows the stator MMF of different slot-pole combinations with double-layer winding, given the same fixed value of three-phase supplying currents. It can be observed that different slot-pole combinations have different induced air gap stator MMF and this matter affects machine performance such as machine efficiency (iron losses and PM eddy current).

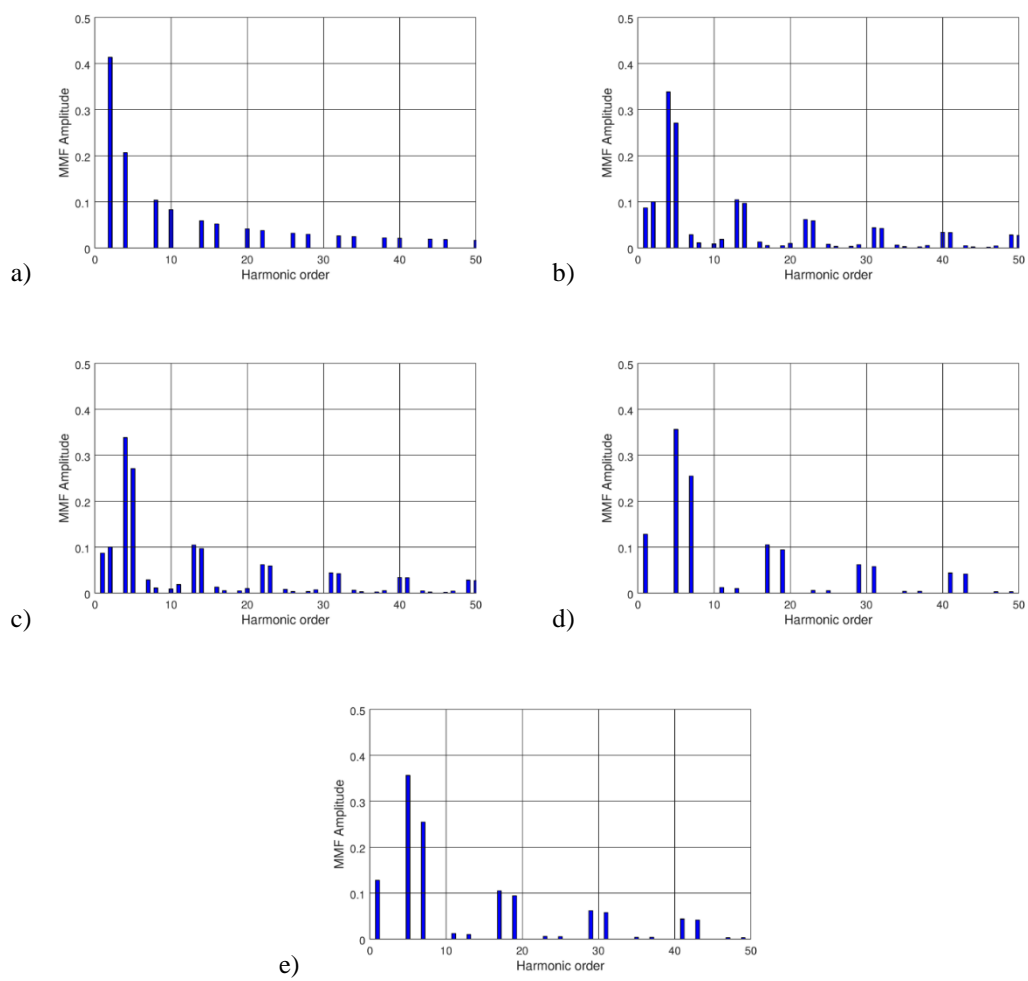


Figure 4-4: MMF of different FS-SPM slot-pole combinations with double-layer winding: a) 6s-4p; b) 9s-8p; c) 9s-10p; d) 12s-10p and e) 12s-14p.

4.3. Analyzed Slot-Pole Combinations: Characteristics and Optimization

This study aims to extend the analysis of slot-poles combinations, it is of particular interest how the slot-pole choice affects electrical machine robustness when manufacturing imperfections are included in FEA, since from the optimization design process. As it will be shown, the choice of slot-pole combination is a tool for a robust design, the aim is to reduce the impact of manufacturing defects by means the machines design.

The considered manufacturing imperfections are: static and dynamic eccentricity (mechanical defects), demagnetization, intended as a reduction of PM coercive field \hat{H}_c , deviation of the magnetic axis and dislocation of PMs (PMs defects). In addition, manufacturing imperfections were considered within standard tolerance ranges, usually provided by manufacturers.

The most employed slot-pole combinations are compared on a common reference frame of which are fixed machine volume, outer stator diameter, lamination stack, flux and current density. The Table 4-1 shows the values of these fixed parameters.

Parameter	Symbol	Valued	Unit of Measurement
Outer Diameter	D_o	92*	[mm]
Lamination Stack	L_{stk}	100	[mm]
Flux Density	B	1.6 ÷ 1.8	[T]
Current Density	\vec{J}_{RMS}	5.5	$[A_{RMS}]$
Notes:			
*) typical size of a 100 [mm] machine for automation.			

Table 4-1: fixed parameters of any slot-pole combination.

The studied slot-pole combinations are the following: 6-4 single-layer (SL) and double-layer (DL), 9-8 -DL, 9-10 DL, 12-10 SL and DL and 12-14 SL and DL. As previously mentioned, the number of winding layers influences the stator MMF harmonic content and machine performance, therefore both DL and SL winding topologies were investigated, whenever possible. These slot-pole combinations are the most widespread in the industrial automation, e.g. axis control units and electric hand operating tools. In addition, other slot-pole combinations can be derived from these basic ones, e.g. the 24-20 is a multiple of 12-10 combination.

The Table 4-2 compares slot-pole combinations in terms the following machine parameters: cogging torque periods, SPP, winding factor, and two Total Harmonic Distortions (THD) of stator MMF. The winding factor of concentrated winding is always less than the unity and it could be considered an index of machines performance [19]. The $THD_{MMF_{ripple}}$ includes only odd multiple harmonics of MMF fundamental frequency f_1 and it could be an index of torque ripple [20]. The $THD_{MMF_{tot}}$ considers any harmonic order of stator MFF and it could be an index of machine rotor losses.

The THD is computed by means the following formula where MMF_i is the amplitude of the i^{th} harmonic order.

$$THD_{MMF} = \frac{\sqrt{\sum_{n=2}^{+\infty} MMF_i^2}}{MMF_1} \quad \text{Eq. 4-4}$$

Parameters	Symbol	Slot-Poles Combinations							
		6-4		9-8	9-10	12-10		12-14	
		SL	DL	DL	DL	SL	DL	SL	DL
Cogging Torque Periods	N_p	2		8	10	5		7	
Slot per Pole per Phase	SPP	0.5		0.38	0.3	0.4		0.3	
Winding Factor	k_w	0.866		0.945	0.945	0.966	0.933	0.966	0.966
Torque Ripple MMF THD	$THD_{MMF_{ripple}}$	0.302		0.101	0.102	0.160	0.145	0.162	0.146
Total MMF THD	$THD_{MMF_{tot}}$	0.745	0.66	0.977	0.702	0.887	0.867	0.736	0.689

Table 4-2: characteristic of analyzed slot-pole combinations.

The parameters of Table 4-2 have been computed by means of FEA and results show how DL winding outperform SL ones in terms of MMF harmonic content. In addition, FEA results confirm results of [19], that is, when the SPP number is equal 0.5, the winding factor has the lowest value, nearly 0.866, and the $THD_{MMF_{ripple}}$ has the highest value.

4.3.1. Machine Optimization at Healthy Condition

The optimization of machine aims to balancing the magnetic circuits exploitation towards the best flux density, being the slot-pole combination the design degree of freedom.

The slot-pole combinations have been optimized by means an iterative design to reach optimal performance in terms of the benchmarks of Table 4-3. It is worth noticing that the mean torque is the only positive benchmark and it should to be the high as possible, while the other ones have negative meaning, thus they should be minimized.

Benchmark	Unit of Measurement
Mean Torque	[Nm]
Torque Ripple	[%]
Cogging Torque	[Nm]
Radial Force	[N]
THD of Back Electro-Motive Force (B-EMF)	[%]

Table 4-3: performance benchmarks.

During the design process, the following design parameters were kept constant: outer stator diameter, stack length, electric steel lamination material, type of PMs, iron and copper utilization coefficients. On the other hand, the design variables are listed in Table 4-4.

Variable	Symbol
Stator Bore Diameter	D_b
Slot Opening at Pole Pitch	w_{so}
Pole Pitch Thickness at Slot Opening	h_{so}
Angular Distance between two Magnets	w_{im}

Table 4-4: set of design variables.

The stator peak flux density was fixed between 1.6 to 1.8 T, but usually mechanical constraints are more restrictive than magnetic ones. Therefore, the stator yoke thickness h_y is defined considering the minimum value for a reasonable mechanical strength.

Table 4-5 summarizes optimized slot-pole combination geometries, while Figure 4-5 shows their FEA flux density distribution at load operating condition.

Parameter	Symbol	Unit of Measurement	Slot-Pole Combination				
			6-4	9-8	9-10	12-10	12-14
Outer Stator Diameter	D_o	[mm]	92				
Bore Stator Diameter	D_b	[mm]	40	46	48	50	47
Air Gap Thickness	g	[mm]	0.7				
Tooth Width	w_t	[mm]	10	6.5	5	5	4
Stator Yoke	h_y	[mm]	5.5	4.5	4.5	4.5	4.5
Polar Shoe Thickness	h_{wed}	[mm]	3.5	2.5	2.5	2	2
Polar Shoes Slot Opening	h_{so}	[mm]	1				
Slot Opening	w_{so}	[mm]	3	4	4	4	4
Magnet Height	h_m	[mm]	3				
Angular Distance Between Magnets	w_{im}	[deg]	17	3	3	4	3
Lamination Stack Length	L_{stk}	[mm]	100				

Table 4-5: machine geometry of optimized slot-pole combination at healthy condition.

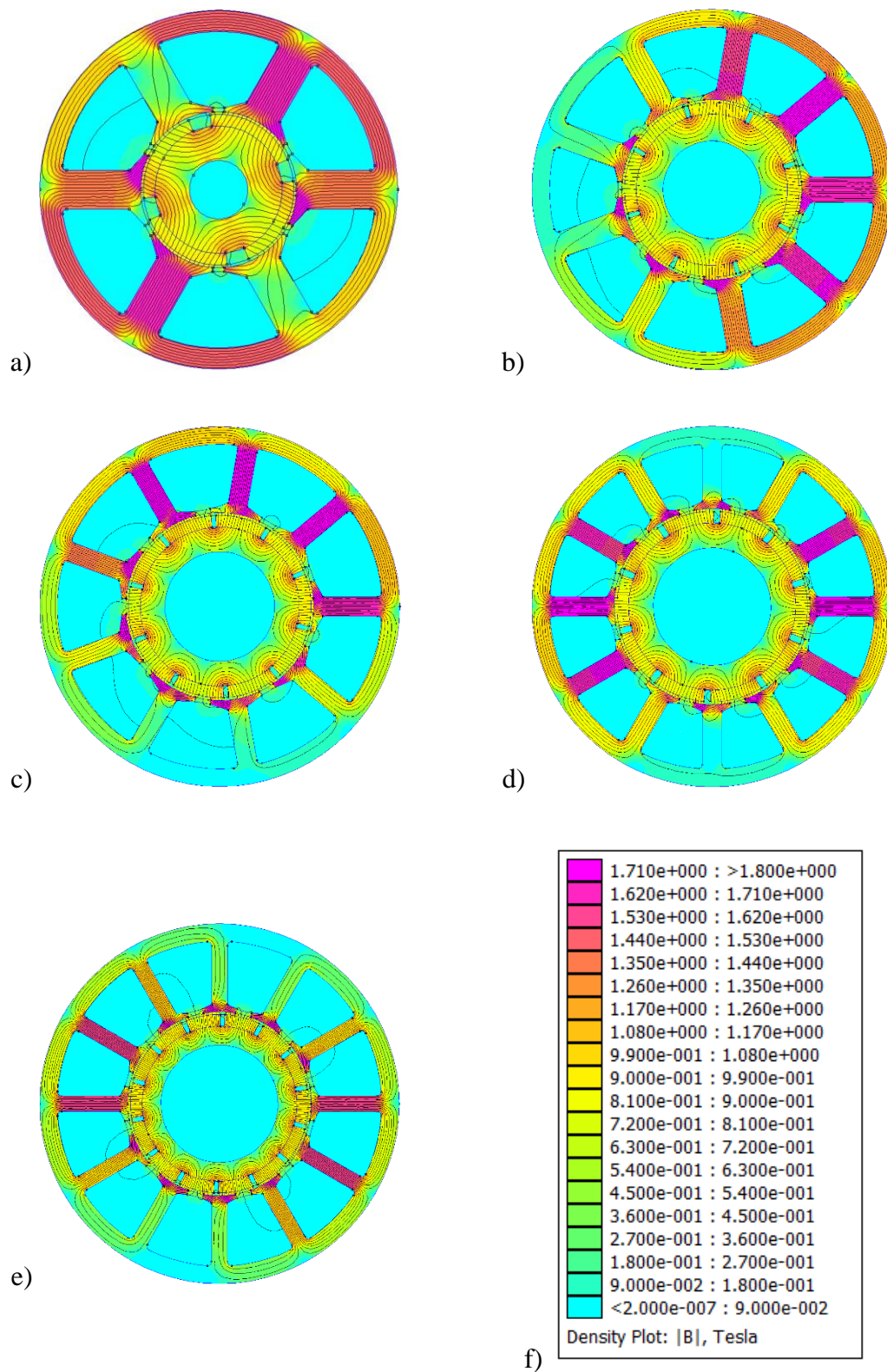


Figure 4-5: distribution of magnetic flux density of optimized machines: a) 6-4, b) 9-8, c) 9-10, d) 12-10 and e) 12-14.

4.3.2. Performance of Optimized Slot-Pole Combinations at Healthy Condition

The optimization process was done for both SL and DL winding topologies of the analyzed FS SPM machines in which PMs have radial edges. Each structure has been evaluated according to some parameters that can be classified under three categories: mechanical, mass and electrical. Table 4-6 and Table 4-7 show the performance of SL and DL of the slot-pole combinations according to the three categories.

Slot-Pole Combination	Force and Torque				Mass			Electrical
	Mean Torque [Nm]	Torque Ripple [%]	Radial Force [N]	Cogging Torque [Nm]	Iron Core [kg]	Copper [kg]	PMs [kg]	THD B-EMF [%]
6-4	6.002	22.853	187	0.884	2.175	1.347	0.207	4.462
12-10	7.599	14.568	0	0.199	1.767	1.060	0.290	6.487
12-14	8.723	4.984	0	0.097	1.674	1.217	0.270	8.015

Table 4-6: performance of single-layer slot-pole combinations.

Slot-Pole Combination	Force and Torque				Mass			Electrical
	Mean Torque [Nm]	Torque Ripple [%]	Radial Force [N]	Cogging Torque [Nm]	Iron Core [kg]	Copper [kg]	PMs [kg]	THD B-EMF [%]
6-4	6.391	15.886	0	0.884	2.175	1.195	0.207	4.448
9-8	8.392	4.179	347	0.048	1.849	1.114	0.278	5.677
9-10	8.573	5.502	35	0.072	1.647	1.157	0.286	7.755
12-10	7.918	3.956	0	0.199	1.767	0.980	0.290	2.257
12-14	8.554	3.139	0	0.091	1.674	1.113	0.270	5.699

Table 4-7: performance of double-layer slot-pole combinations.

The SL slot-pole combinations exhibit lower mechanical performance than equivalent DL combinations. Moreover, SL 6-4 features a radial force component which is absent in the DL combination.

Moving to DL slot-pole combinations, it can be observed that torque ripple decreases as the number of slots and poles increase, while B-EMF THD does not seem to be directly related to the slot-pole combination. The mean torque is around 8 Nm excepting the 6-4 combination that performs the lowest mean torque. The 9-8 and 9-10 combinations have the lowest cogging torque values during no load operation, while, as known, at load operation they are affected by a strong magnetic unbalance, characterized by a radial net force of 347 N and 35 N, respectively.

The robustness analysis with respect to manufacturing defects was done only for DL slot-pole combinations, since they outperform the equivalent SL ones.

4.4. Robustness Analysis with Respect to Manufacturing Imperfections

The validation of the optimized design is usually achieved by experimental tests on a machine prototype. Experimental results often could be different from FEA simulation results because of unavoidable manufacturing imperfections, intrinsically introduced by the production and assembly processes.

As previously mentioned, the analysis of manufacturing defects during FEA simulation could pave the way for a design for reliability, largely reducing design burden and time-to-market.

The main contribution of this work is to extend the FEA optimization process comparing different slot-pole combinations in terms of robustness with respect to manufacturing defects. The machine performance is evaluated according to benchmarks of Table 4-3.

The manufacturing imperfections are modeled by FEA: using the tolerance ranges provided by manufactures and considering their typical statistic distributions. Specifically, the mechanical defects are modeled with a deterministic function, while the magnetic defects are modeled with a Gaussian distribution.

The robustness analysis was led as follows: analysis of mechanical defects (paragraph §4.4.1) and of magnetic defects (paragraph §4.4.2). Once analyzed the effect of the single defects on machine performance, the influence of the strength of manufacturing defects on performance benchmarks is shown in paragraph §4.5. Finally, the performance comparison between healthy and defective machines is carried out for any slot-pole combination.

4.4.1. Eccentricity

The static and dynamic eccentricities were investigated as mechanical manufacturing defects. Static eccentricity occurs when the rotor is displaced from the stator geometrical axis, while the rotor is still turning upon its own axis, as shown in Figure 4-6. Dynamic eccentricity occurs when the rotor is turning upon stator geometrical axis, but not on its own center, as shown in Figure 4-7.

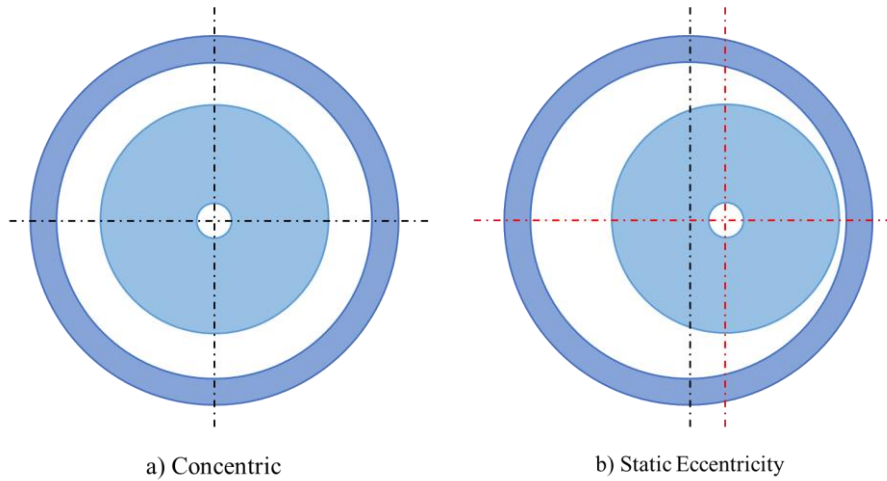


Figure 4-6: example of static eccentricity.

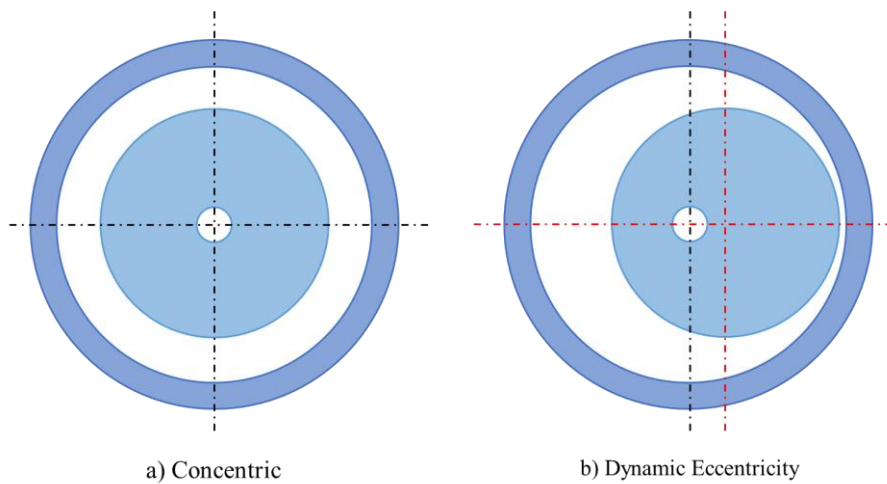


Figure 4-7: example of dynamic eccentricity.

The mechanical motor speed during FEA simulation was at 1000 r/min, corresponding to a mechanical frequency $f_m = 16.67$ Hz. The static eccentricity was modeled by FEA, moving the rotor rotational axis of 0.2 mm toward x-direction, while dynamic eccentricity was modeled moving the rotor block by 0.2 mm (corresponding to the 0.2% of the lamination stack) keeping fix its original center of rotation.

Simulations results show that both mechanical defects affect the waveforms and the THD of any studied benchmark. In particular, static and dynamic eccentricities induce additional harmonic components to typical mechanical quantities, whose amplitude is directly proportional to the fault severity.

Simulations results show that for a given mechanical frequency f_m , the static eccentricity induces an additional order harmonic, denoted as “*rotor harmonic*”, which depends on the number of magnetic poles $2p$ as follows:

$$f_{se} = f_m \cdot 2p \quad \text{Eq. 4-5}$$

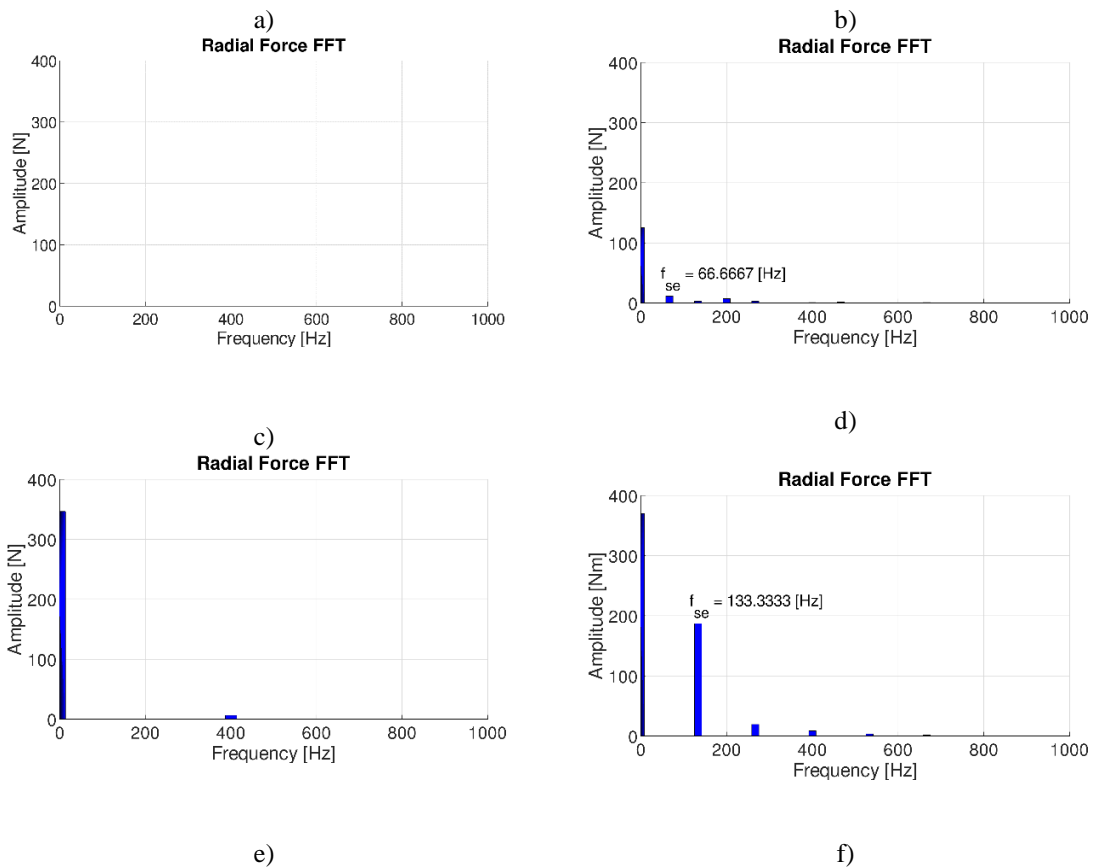
On the other hand, dynamic eccentricity induces an additional harmonic, denoted as “*stator harmonic*” which depends on the number of stator slots Q , as shown as follows:

$$f_{de} = f_m \cdot Q \quad \text{Eq. 4-6}$$

According to simulations results, some considerations could be done on the effects of mechanical imperfections in relation to the performance benchmarks and slot-poles combinations.

The radial force is the most affected benchmark by mechanical imperfections because eccentricity may magnetically unbalance the motor. FEA results show that 12-10 and 12-14 slot-pole combinations are the most affected in terms of radial force, since in healthy condition they feature zero radial force. The 9-8 is intrinsically magnetically unbalanced, in fact it has a high radial force around 347 Nm even at healthy condition, according to this the radial force of 9-8 combination is less affected by mechanical defects.

The Figure 4-8 compares the THD of the radial force of 6-4, 9-8 and 12-14 slot-poles combinations at healthy and defective conditions, when a static eccentricity of 0.2 mm is considered.



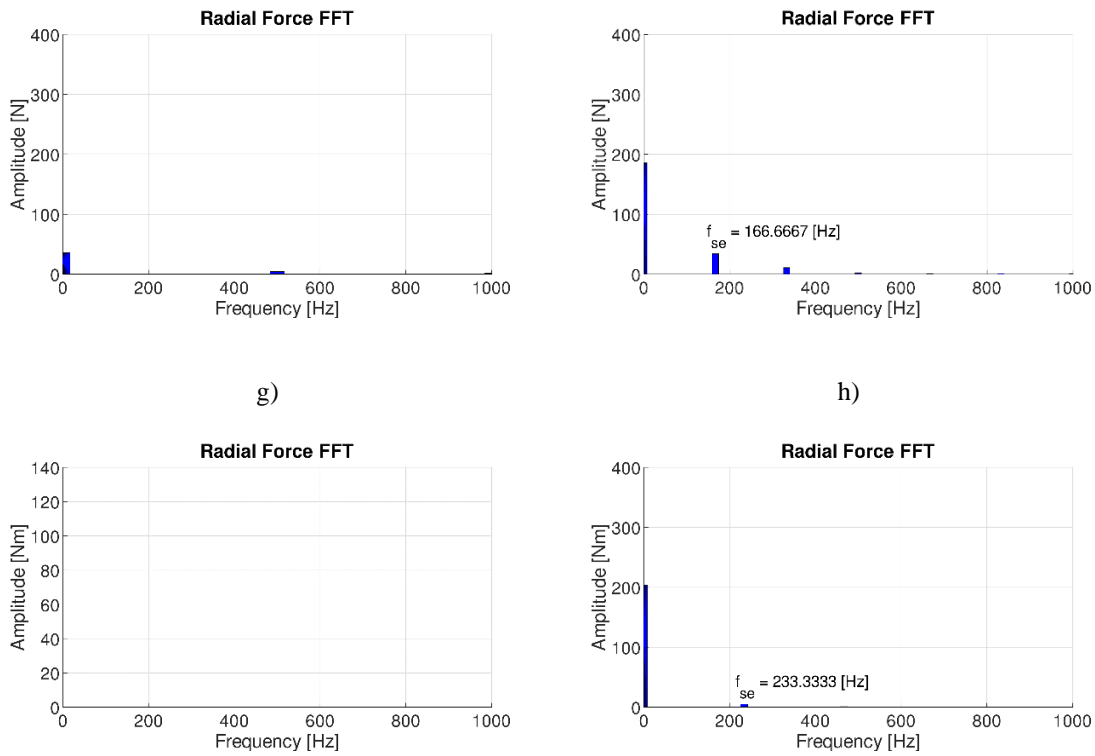


Figure 4-8: FFT of the radial forces: a) healthy 6-4, b) defective 6-4, c) healthy 9-8, d) defective 9-8, e) healthy 9-10, f) defective 9-10, g) healthy 12-14 and h) defective 12-14.

Moving to slot-pole combinations, the 9-8 and 9-10 are the most sensitive to mechanical defects, specifically the rotor harmonics induced by static eccentricity are $f_{se_{9-8}} = 133.33$ Hz and $f_{se_{9-10}} = 166.67$ Hz, while the stator harmonics due dynamic eccentricity are $f_{de_{9-8}} = 150.03$ Hz and $f_{de_{9-10}} = 150.03$ Hz.

Torque ripple and cogging torque are adversely affected by static eccentricity. Figure 4-9 compares the torque profiles of healthy and defective 9-8 and 9-10 over a B-EMF period and it can be observed how static eccentricity increases the torque ripple introducing a modulation on the original signal. Figure 4-10 compares the cogging torque profile of healthy and defective 9-8 and 9-10 over a B-EMF period at no load condition and, also in this case, it can be seen how a static eccentricity of 0.2 mm modulates the cogging torque over the B-EMF period. This modulation is due to rotor harmonic order related to the static eccentricity.

Figure 4-11 shows the comparison between mean torque spectra of 9-8 and 9-10 slot-pole combinations at healthy condition and with a dynamic eccentricity of 0.2 mm (0.2% of lamination stack). Figures on the right side clearly show the stator harmonic component of these combinations, $f_{se_{9-8}} = f_{se_{9-10}} = 150$ Hz, over imposed on the characteristic torque ripple harmonic of $f_{tr_{9-8}} = 400$ Hz and $f_{tr_{9-10}} = 500$ Hz.

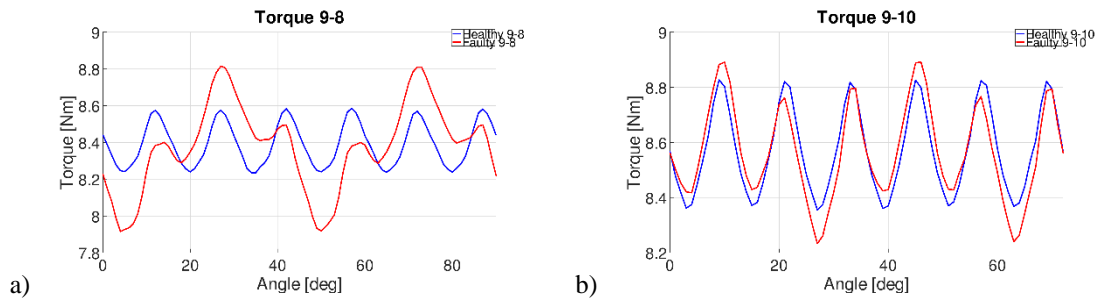


Figure 4-9: comparison between torques at healthy and defective conditions over a B-EMF period of a) 9-8 and b) 9-10 with a static eccentricity of 0.2 mm.

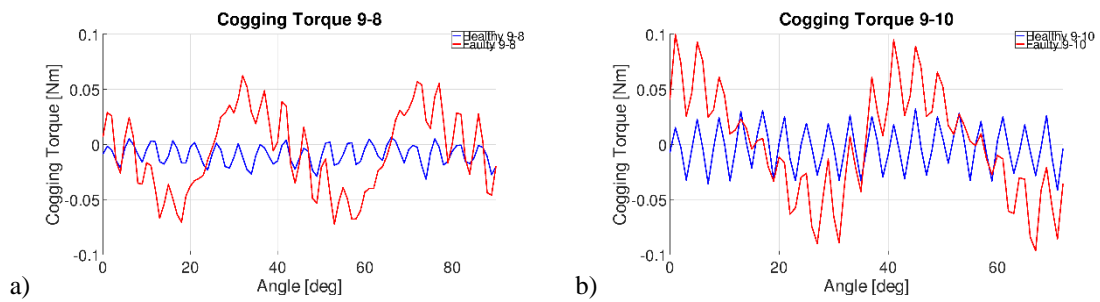


Figure 4-10: comparison between cogging torques at healthy and defective conditions over a B-EMF period of a) 9-8 and b) 9-10 with a static eccentricity of 0.2 mm.

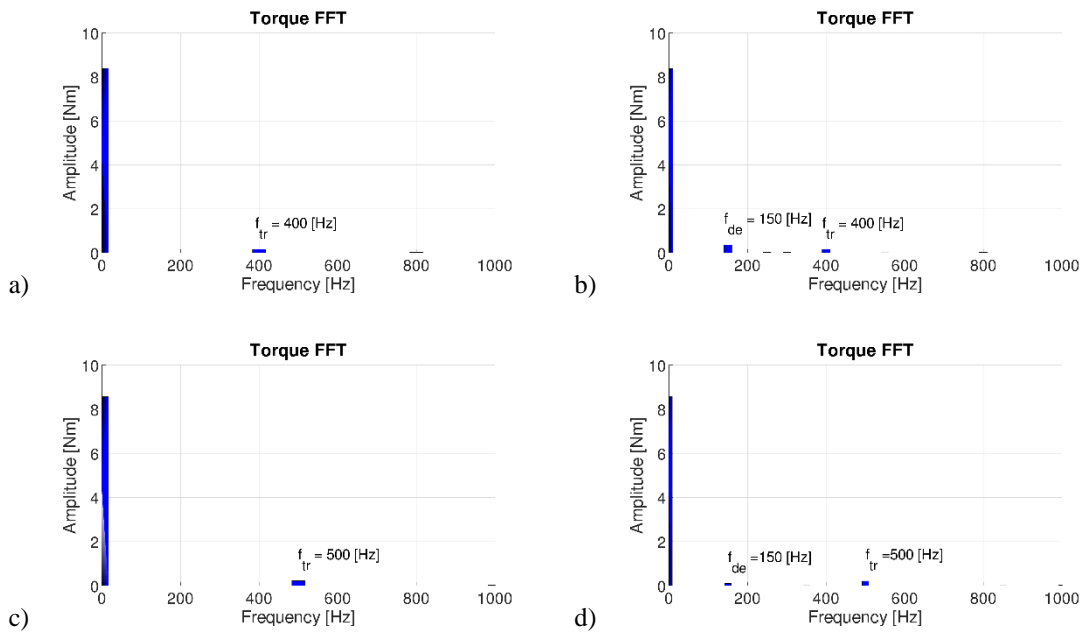


Figure 4-11: FFT of mean torque of 9-8 and 9-10 without and with dynamic eccentricity of 0.2 mm. a) 9-8 without defect; b) 9-8 with dynamic eccentricity; c) 9-10 without defect and d) 9-10 with dynamic eccentricity.

4.4.2. Permanent-Magnets Defects

The investigated magnetic defects are: demagnetization i.e. reduction of PM coercive field H_c , deviation of magnetic axis and magnets dislocation, i.e. anomalies in the distance of magnets. Figure 4-12 represents the analyzed PM imperfections.

The single magnetic defect was applied on any magnetic pole, according to a Gaussian distribution over a tolerance range.

FEA results show that the slot-pole combinations with the best performance benchmarks at healthy condition are more sensitive to magnetic defects. In particular, demagnetization increases the radial force component of 12-10 and 12-14 slot-pole combinations inducing a stator harmonic, as shown in Figure 4-13. Moreover, demagnetization induces a stator harmonic also in the cogging torque spectra, as shown in Figure 4-14 for 12-14 slot-pole combination.

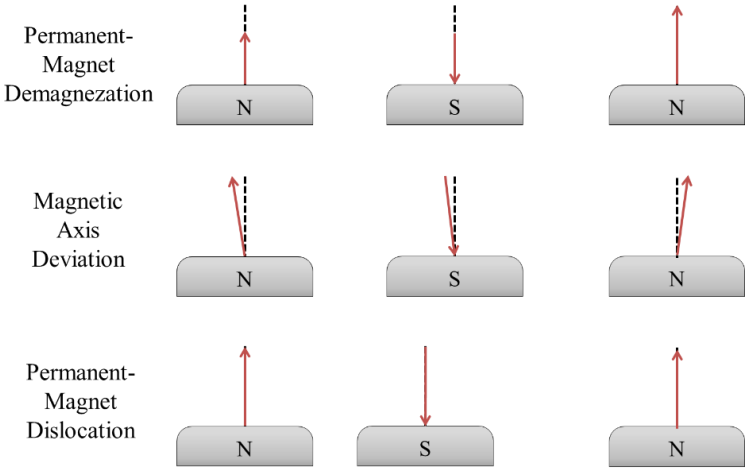


Figure 4-12: representation of permanent-magnets defects.

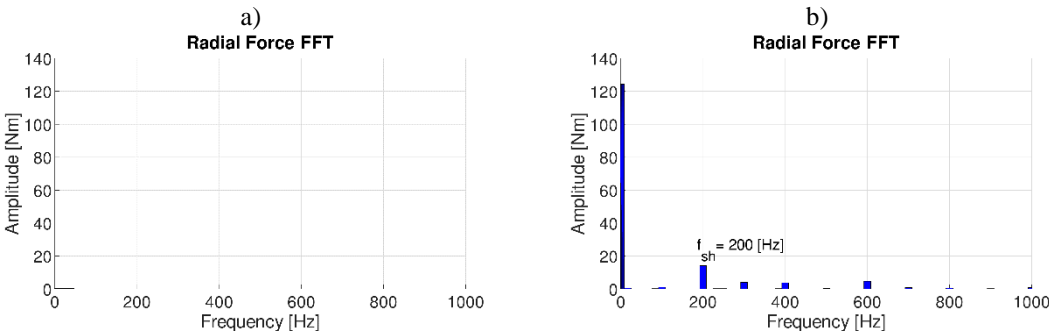


Figure 4-13: radial force comparison of 12-14 between (a) healthy condition and (b) with PMs demagnetization.

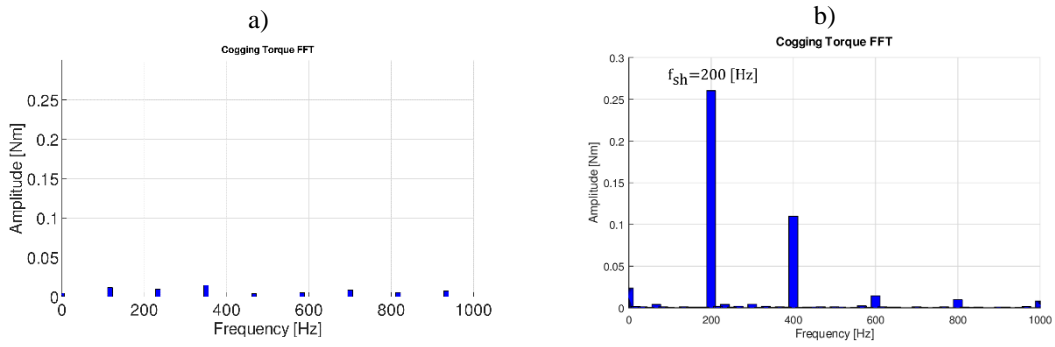


Figure 4-14: cogging torque comparison of 12-14 between a) at healthy condition and b) with PMs demagnetization.

Magnetic axis deviation and PMs dislocation affect the torque ripple of 12-10 and 12-14 slot-pole combinations. Moreover, these defects induces a stator harmonic frequency in radial force and cogging torque spectra as demagnetization, as shown in Figure 4-15 and Figure 4-16.

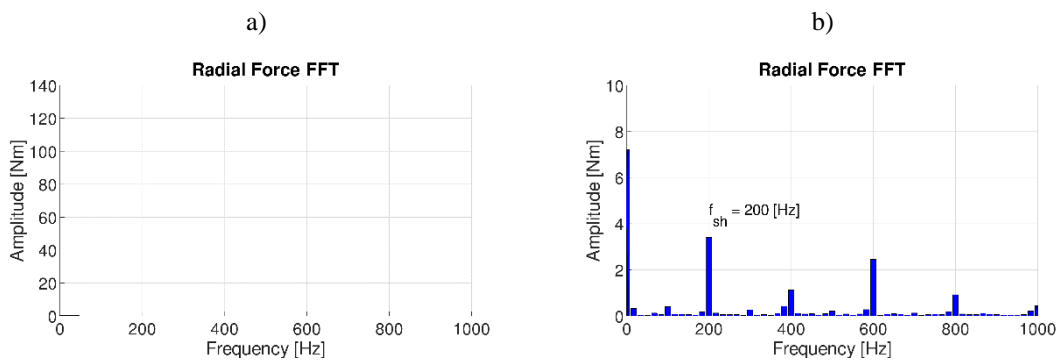


Figure 4-15: radial force comparison of 12-14 between a) healthy condition and b) with PMs dislocation.

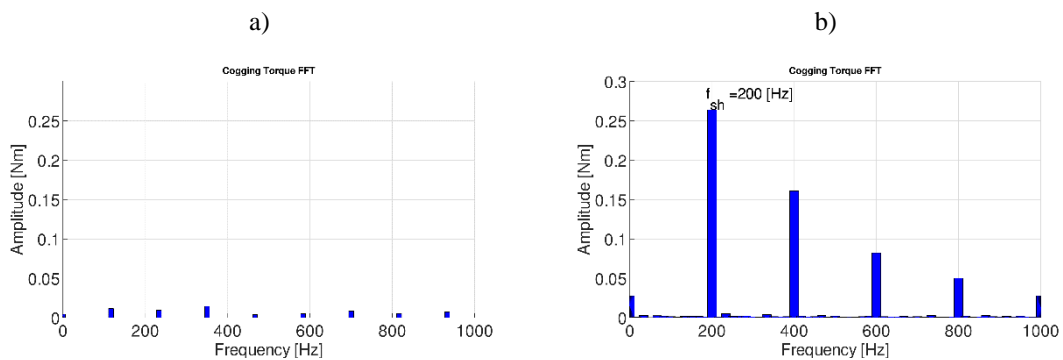


Figure 4-16: cogging torque comparison of 12-14 between a) healthy condition and b) with PMs dislocation.

4.5. Machines Performance as Function of Manufacturing Defects Severity

This paragraph shows the analysis on the performance benchmark variation because of defects severity increasing. Manufacturing defects were modeled by FEA, assuming a deterministic behavior for mechanical defects and a Gaussian distribution for magnetic defects.

Considering magnetic defects, their severity was investigated by varying the standard deviation σ of the Gaussian distribution; Table 4-8 shows the initial parameters of the Gaussian distributions of magnetic imperfections.

Type of Magnetic Imperfection	Mean Value μ	Standard Deviation σ
Demagnetization	883,310 $\left[\frac{A}{m}\right]$	0.025 $\left[\frac{A}{m}\right]$
Magnetic Axis Deviation	0 [mm]	0.6 [mm]
Dislocation	0 [mm]	0.2 [mm]

Table 4-8: bell curve parameter of permanent-magnet imperfections.

According to FEA results on magnetic defects in chapter §4.4.2, the 12-14 combination is the most sensitive to magnetic defects. Hence, this combination is used to analyze the benchmark performance variation with respect to defects severity. The mean torque decreases as demagnetization severity increases, while the mean torque is less sensitive to the deviation of magnetic axis and magnet dislocation (see Figure 4-17).

The torque ripple and the cogging torque are affected by demagnetization and PMs dislocation, as shown in Figure 4-18 and Figure 4-19, while the radial force is deeply affected by demagnetization, as shown in Figure 4-20.

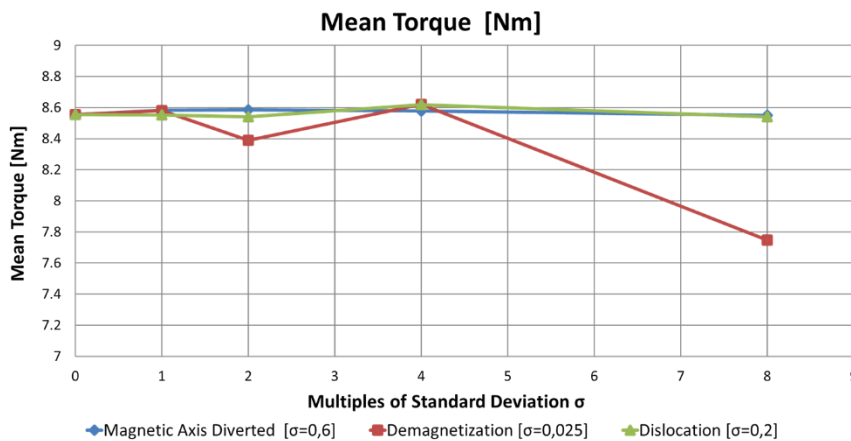


Figure 4-17: correlation between magnetic imperfections and mean torque of 12-14 combination.

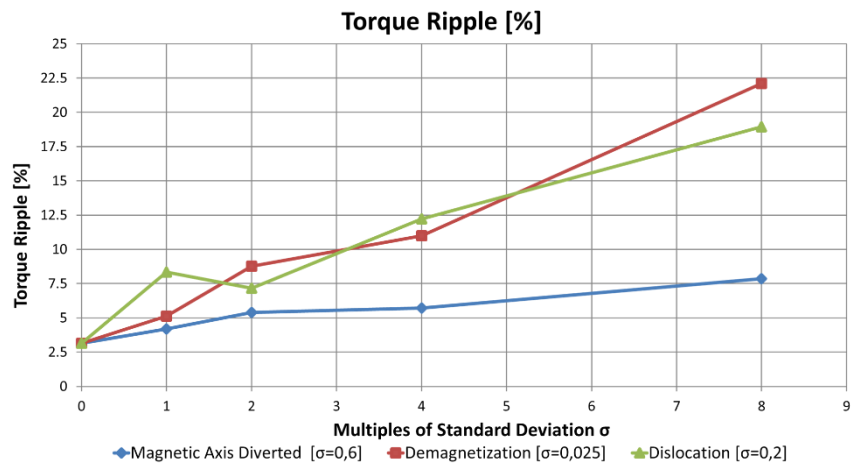


Figure 4-18: correlation between magnetic imperfections and torque ripple of 12-14 combination.

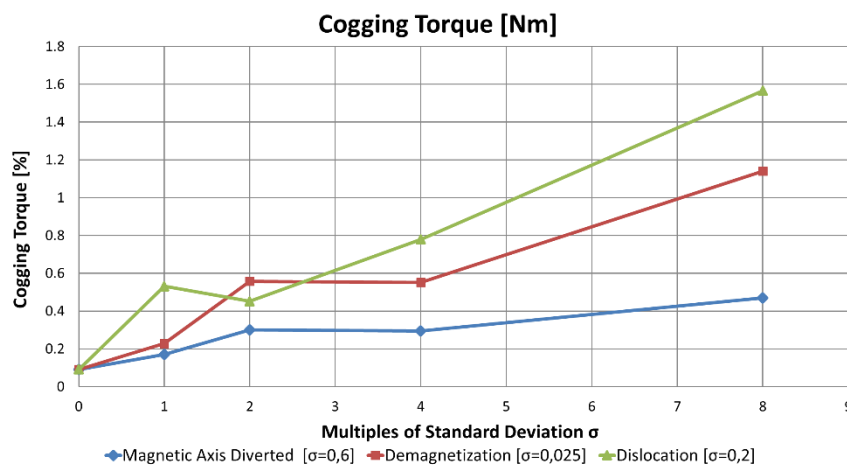


Figure 4-19: correlation between magnetic imperfections and cogging torque of 12-14 combination.

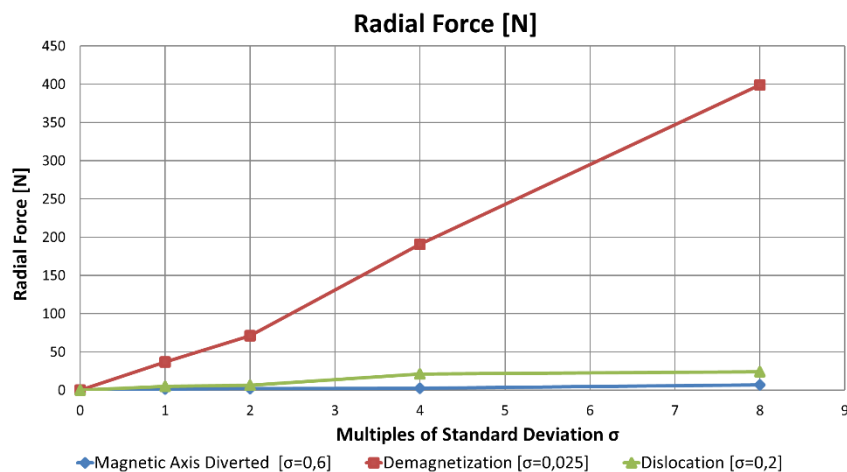


Figure 4-20: correlation between magnetic imperfections and radial force of 12-14 combination.

On the other hand, mechanical defects rely on a deterministic model; in specific the eccentricity severity was increased by steps of 0.1 mm (0.1% of the lamination stack). The analyzed slot-pole combinations are 9-8 and 12-14 according to results of chapter

§4.4.1. The mean torque of 12-14 is more sensitive to mechanical defect severity than 9-8, while in terms of torque ripple the 9-8 is more sensitive than 12-14, as shown in Figure 4-21 and Figure 4-22. The cogging torque of 9-8 is more sensitive to mechanical defectives than 12-14, as shown in Figure 4-23. The radial force of 12-14 is more sensitive to eccentricity than 9-8, as shown in Figure 4-24.

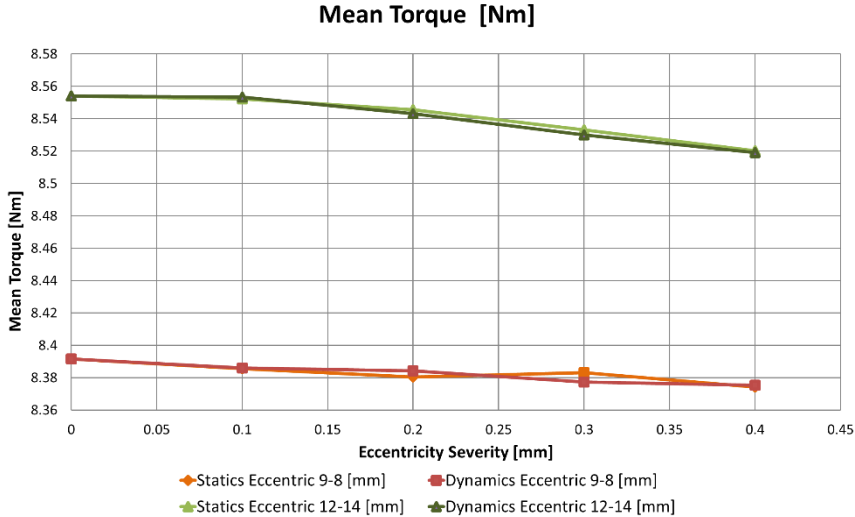


Figure 4-21: correlation between mechanical imperfections and mean torque of 9-8 and 12-14 combinations.

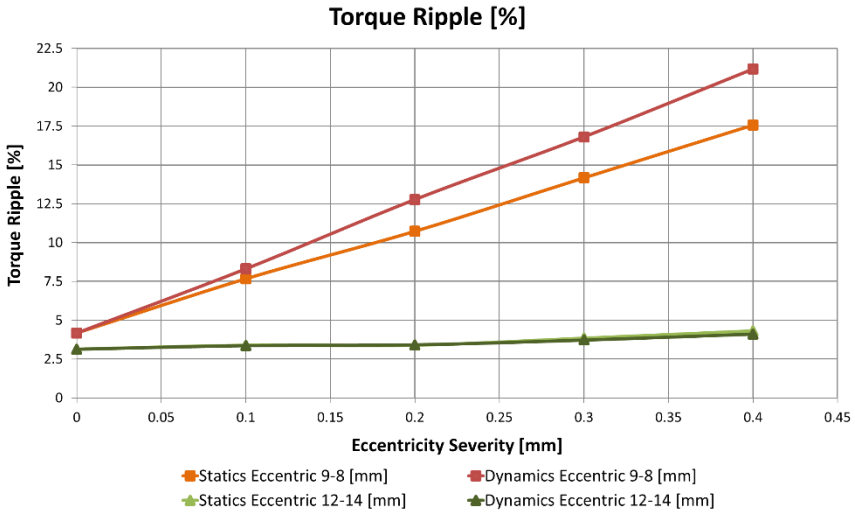


Figure 4-22: correlation between mechanical imperfections and torque ripple of 9-8 and 12-14 combinations.

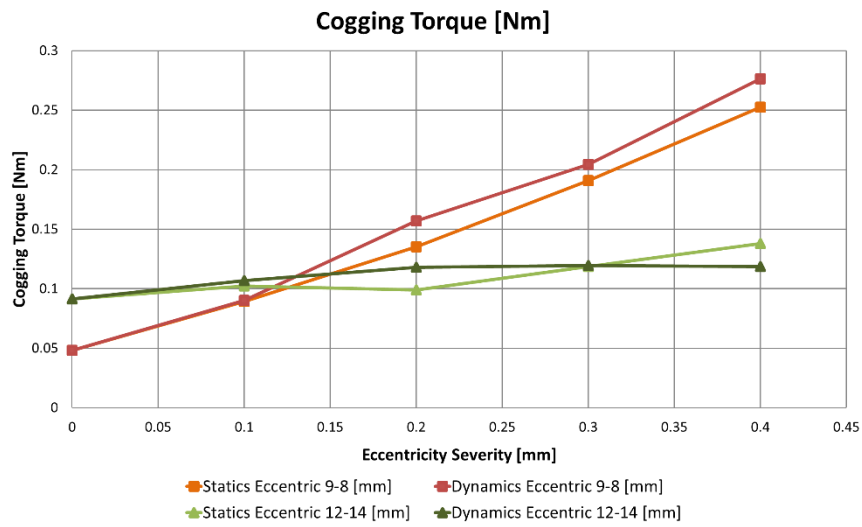


Figure 4-23: correlation between mechanical imperfections and cogging torque of 9-8 and 12-14 combinations.

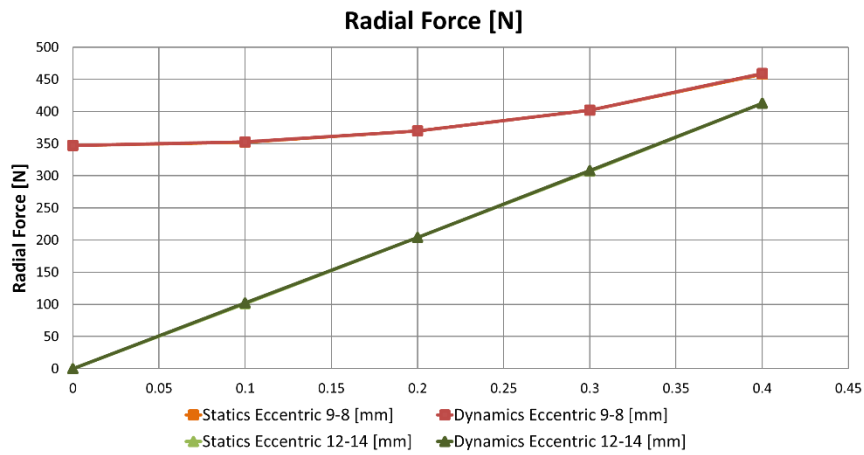


Figure 4-24: correlation between mechanical imperfections and radial force of 9-8 and 12-14 combinations.

4.6. Robustness Analysis toward Manufacturing Defects as a Function of Slot-Pole Combinations

The robustness analysis was carried out investigating the effects of all imperfections applied at the same time. The severity of the manufacturing defect was assumed based on the tolerance intervals declared by manufacturer and the applied values in FEA simulation are listed in Table 4-9.

Imperfection	Value	%
Standard Deviation of Magnetic Axis Deviation	$\pm 1^\circ$	
Standard Deviation of Coercive Field	$\pm 5\%$ the nominal value	//
Permanent-Magnets Dislocation	0.25 mm	0.25 % of Lamination Stack
Static Eccentricity	0.2 mm	0.20 % of Lamination Stack
Dynamic Eccentricity	0.2 mm	0.20 % of Lamination Stack

Table 4-9: severity of manufacturing imperfection used for robustness analysis.

Once the FEA results were obtained the performance of defective machines were compared with that of healthy combinations in terms of the performance benchmark of Table 4-3.

For a better comparison, FEA results are summarized by means a Kiviat’s diagram, which can show more than three variables on a 2D plane, being the number of vertex and edges of the polygons the number of variables. Figure 4-25 and Figure 4-26 show the different slot-pole combinations at healthy and defective conditions, respectively.

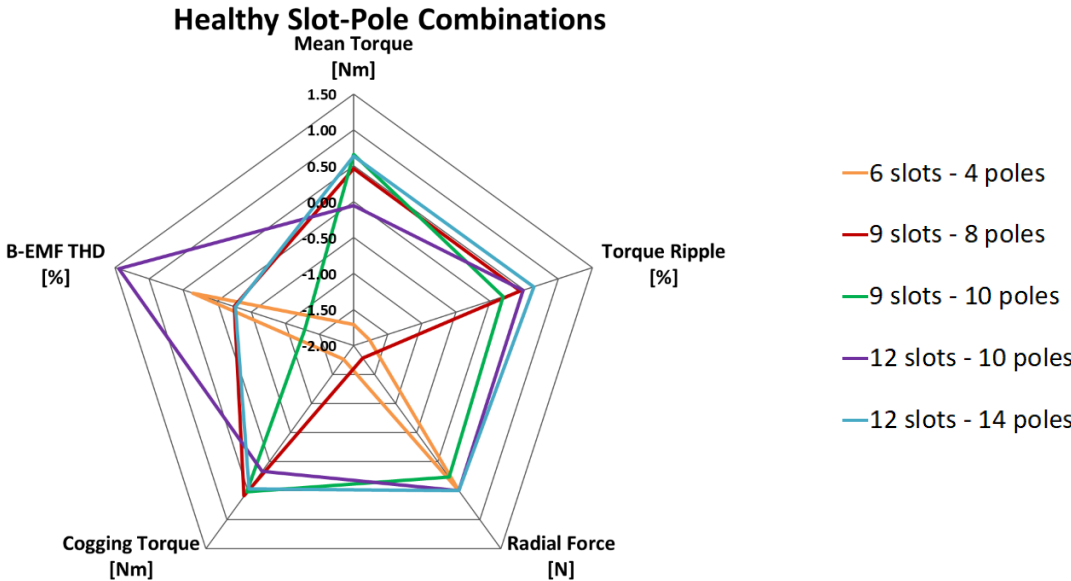


Figure 4-25: Kiviat's diagram of healthy slot-pole combinations.

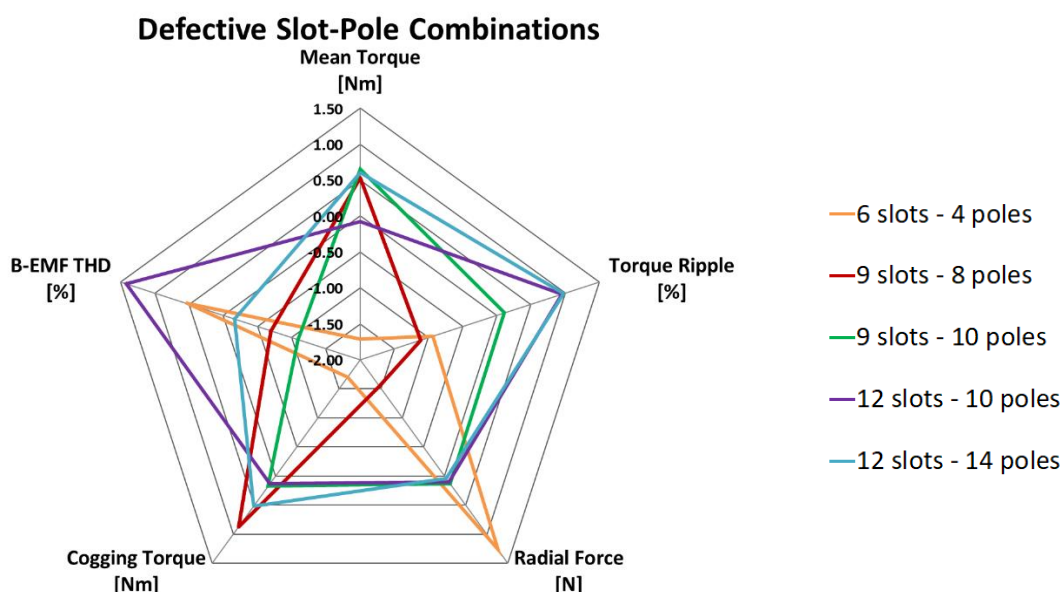


Figure 4-26: Kiviat's diagram of defective slot-pole combinations.

The ranking of slot-pole combinations is based on the areas of the polygons and the best slot-pole combinations are those featuring the largest areas and vice versa. Since performance benchmarks have different units of measurement, they are normalized according to their standard deviation as follows:

$$z^+ = \frac{x_i - M(x)}{\sigma} \quad \text{Eq. 4-7}$$

$$z^- = -\frac{x_i - m(x)}{\sigma} \quad \text{Eq. 4-8}$$

where $M(x)$ and $m(x)$ are respectively the maximum and minimum values of the statistical series x , respectively. The mean torque was normalized according to its maximum values since it has a positive meaning, while other performance benchmarks were normalized according to their minimum values because of their negative meaning. The normalized benchmarks were aggregated in a single index, denoted as Total Performance Index (TPI), both for the healthy and defective machines; the index values are listed in the first and second columns of Table 4-10.

For a given slot-pole combination, the TPI is computed as the algebraic sum of the normalized benchmarks and it is related to the area of the relative polygon of the Kiviat's diagram. By so doing the best slot-pole combination/s is/are that/those with the higher TPI. The robustness of a given slot-pole combination is evaluated considering the subtraction of the healthy TPI and defective TPI. The slot-pole combinations exhibiting the highest ΔTPI are those more sensitive to manufacturing defects, if ΔTPI

is greater than zero the slot-pole combination is sensitive in a negative meaning because it exhibits lower performance with manufacturing imperfections, while if ΔTPI is less than zero it means that the combined effects of manufacturing imperfections improve slot-pole combination performance.

According to results of Table 4-10, the best slot-pole combinations are 12-10 and 12-14 both at healthy and defective conditions, in addition they present a very little variation of ΔTPI , thus are not so much sensitive to manufacturing defects. The worst slot-pole combination is 6-4 in terms of performance, but it exhibits an improvement of performance according to a TPI lower than zero. On the other hand, the most sensitive combinations with respect to imperfections seem to be the 9-8 and 9-10. Respectively, with a ΔTPI of 1.41 and 0.38.

Slot-Pole Combination	TPI at Healthy Condition	TPI at Defective Condition	ΔTPI
6-4	-4.38	-2.56	-1.82
9-8	-0.53	-1.94	1.41
9-10	0.37	-0.01	0.38
12-10	2.55	2.53	0.02
12-14	1.99	1.98	0.01

Table 4-10: slot-pole combination comparison according to Total Performance Index (TPI).

4.7. Activity results

The result of this research activity is an optimization method leading to a robustness design analysis. The proposed optimization process selects since from the beginning of machine design, the most suitable slot-pole combinations both in terms of the performance and robustness with respect to manufacturing imperfections.

Starting from healthy slot-pole combinations, mechanical and magnetic manufacturing imperfections were modeled and analyzed. Imperfections were modeled via FEA simulation, assuming a deterministic behavior for mechanical defects and a Gaussian distribution for magnetic defects.

The slot-pole combinations were optimized via FEA and then ranked according to performance benchmarks both at healthy and defective conditions. The comparison of machines allowed identifying a set performance index useful to assess which slot-pole combinations are more or less sensitive to manufacturing defects.

The proposed optimization method has been applied on a set of typical slot-pole combinations of fractional-slot SPM-SMs with DL concentrated winding.

Some insights from the case study are here summarized:

- Static and dynamic eccentricities induce new harmonic components in the spectra of performance benchmarks. Static eccentricity induces a frequency component proportional to the number of poles $2p$, while dynamic eccentricity induces a frequency component proportional to the number of stator slots Q ;
- Radial force is the most sensitive performance benchmark to manufacturing imperfections. Specifically, FEA results show that radial force is affected both by mechanical and magnetic defects;
- The 12-10 and 12-14 slot-pole combinations are the best performing both at healthy and defective conditions. In addition, as shown by ΔTPI index, these configurations are less sensitive to manufacturing defects, when these are applied all together;
- According to ΔTPI index the 9-8 combination is the most affected machine by manufacturing imperfections. In addition, this combination is particularly sensitive to mechanical defects;
- Finally, the 6-4 combination exhibits the lowest performance both at healthy and defective condition, but the ΔTPI shows an improvement in terms of performance at defective conditions.

5. Demagnetization Issues in Low Cost Synchronous Machines

Even if SPM-SMs are appreciated for their advantages, they present some drawbacks that could hardly affect performance in terms machine fault-tolerant capability.

The previous chapter analyzed a list of defects that could affect PM-SMs performance and their robustness. Among them there is demagnetization intended as a lower value of the PM coercive magnetic field and generally it does not lead to a machine fault, but to lower performance.

The PMs demagnetization phenomenon could also happen during machine operation and if it is particularly strong it could lead to machine fault. In this case, the demagnetization is the effect of PM overheating due to eddy currents induced by high space-harmonics of stator MMF and the current ripple due to the PWM switching frequency of the inverter supply. When the PM working temperature overpasses the knee of PM demagnetization curve, the PM could be permanently demagnetized and the torque production capability compromised.

This chapter shows a real case study of rotor re-design of a low-cost SPM-SM affected by a strong demagnetization, which represents a big drawback in terms of application reliability and fault-tolerance. In order to protect PM from demagnetization, the rotor geometry of the synchronous machine has been modified, validated via FEA and then prototyped.

5.1. Low-Cost Synchronous Machines

Under the pressure of the new climate challenge the International Standards and the European Directives have been pushed industries to move towards more efficient electrical machines. Traditionally, the most spread electric motor in the industrial industry is the induction motor (IM) which is characterized by a lower energy conversion efficiency η than others technologies e.g. PM-SMs or pure SyncRel machines. Since the industrial electric motors represent the 30 % of the global energy electric consumption [1], the International Standards pushed to improve IM efficiency class [21] or to substitute them with more efficient electrical machines operating with variable speed.

The increment of IM efficiency could be achieved by means different techniques e.g. increasing total lamination stack length given the same output power, by changing the design of stator and rotor laminations, changing the lamination materials with a low losses silicon iron steel or substituting the aluminum bars of the squirrel cage with copper bars.

Nevertheless, in last year there have been some favorable conditions that make possible the adoption of the inverter technology, thus new scenarios for high efficiency application for electric energy conversion have been opened. For instance, these circumstances include the improvement of silicon components for electric power conversion e.g. SiC, the new storage systems, new material and technologies for electrical machines.

The PM-SMs have higher efficiency than IM due to the absence of rotor Joule losses, since the rotor circuit is not present, in addition the power factor of PM-SMs is higher because the magnetization current component is not needed.

Given the above, some manufacturers decided to move from IM technology to PM-SMs by substituting the IM rotor with a SPM one, as shown in [22] where the authors present different low-cost PM-SMs configurations using the traditional IM stator lamination and mechanical frame and substituting the IM rotor with PM synchronous one.

Although PM-SMs potentially present a better efficiency than IM, the lower phase inductance of PM-SMs involves a higher current ripple given the same PWM switching frequency. The current ripple tends to cause additional iron losses in the laminations and in particular significant eddy current losses in PMs [23]-[27]; even if they have lower conductivity compared to winding materials (aluminum and copper). The PMs eddy current losses due to PWM switching frequency affects particularly PM-SMs with distributed winding topologies such as low-cost PM-SMs made starting from IM mechanical frame.

These additional losses could significantly affect motor global efficiency and moreover could demagnetize PMs because of Joule losses that increase magnets working temperature. Moreover, as the machine size increases, the current ripple tends to increase for two reasons: the reduction of phase inductance and resistance with the machine size increasing and the general trend to reduce PWM switching frequencies to limit the switching losses as the rated current increases.

For these reasons, the PMs losses become more significant as the machine size increases, thus some specific design solutions have to be adopted.

5.2. Design Techniques to Reduced Permanent-Magnet Eddy Currents

The state-of-the-art offers different design solutions to limit eddy current losses e.g. PM segmentation along axial direction or circumferential.

Nevertheless, paper [25] makes clear that PMs segmentation effectiveness in eddy current losses reduction is strictly affected by eddy current reaction field which superimposes itself to the stator magnetic field induced by the stator currents. This phenomenon is related to the fact that eddy current paths have both an inductive and resistive behavior, thus it grows as eddy current frequency increases. Moreover, paper [25] remarks upon the overestimation of rotor eddy current losses if the computing method neglects the eddy current reaction field.

The skin effect could be considered a consequence of the eddy current reaction field and [26]-[28] show that if skin effect is not negligible the effectiveness of PM segmentation in eddy-current losses reduction is lowered. Authors of [28] shows that when the skin effect is operating a small number of magnet segmentation increases eddy current losses, instead of diminishing it as expected. This phenomenon is denoted as “*anomaly of segmentation*”.

The anomaly of segmentation is also documented by the authors of [23] and [26] which analyzed the effects of harmonic orders and of rotor type (e.g. surface and inner magnet

types) on magnet loss reduction effect. As shown in Figure 5-1, two profiles of eddy current losses are described: curve A is typical of low-frequency harmonic such as slots-harmonics, while curve B is typical of high-frequency harmonic orders e.g. PWM switching frequency. The curve B shows the anomaly of segmentation due to skin effect, in fact the peak of the eddy current losses per PM volume is clear. The maximum value of PMs eddy current losses occurs when magnet segmentation is nearly twice the skin depth δ [25], expressed in Eq. 5-1, where ρ is the PM resistivity, f_e is the electric frequency and μ is PM magnetic permeability.

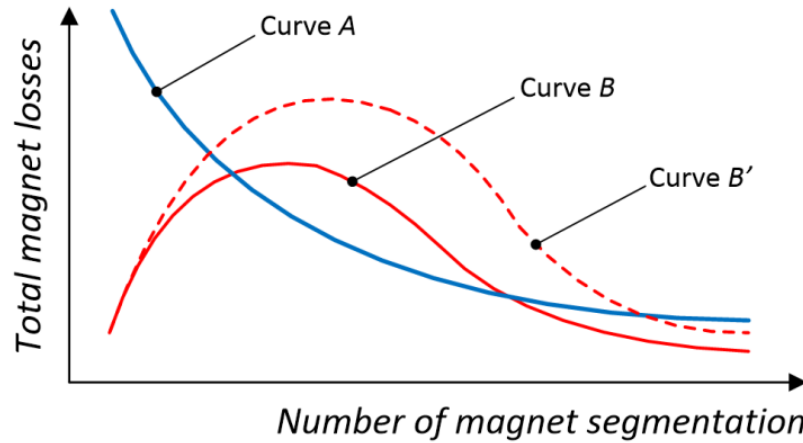


Figure 5-1: representation of permanent-magnet eddy current losses profiles as a function of magnet segmentation. Curve A at low-frequency harmonic orders and curve B and B' at high-frequency harmonic orders. [25]

The results of [26] show that segmentation effect on eddy current loss reduction is achieved when magnet segmentation is smaller than twice the skin depth δ . Moreover, it is also shown that as the frequency harmonic order increases the peak of curve B shifts to right, thus a finer PMs segmentation could exacerbate magnet eddy current losses. The curve B' of Figure 5-1 represents this behavior.

$$\delta = \sqrt{\frac{\rho}{\pi f_e \mu}} \quad \text{Eq. 5-1}$$

Another design solution to reduce PM eddy current losses is to choose IPM rotor topology. The authors of [27] and [29] show how the iron region over permanent PMs of IPM rotor acts like a harmonic filter protecting magnets from additional eddy currents. This particularly true for IPM machine with concentrated winding which exhibits a higher MMF space harmonics order as seen in chapter §4.

5.3. Analyzed PM-SMs Motors

The Figure 5-2a) shows the geometry of the SPM-SM exhibiting serious demagnetization problems due to the high temperature reached by PMs during the normal operating condition. Thus, in order to overcome this issue, this research activity proposes a different rotor configuration with inner PMs which allows reducing eddy current losses and protects PMs from demagnetization. The Figure 5-2b) shows the proposed IPM rotor.

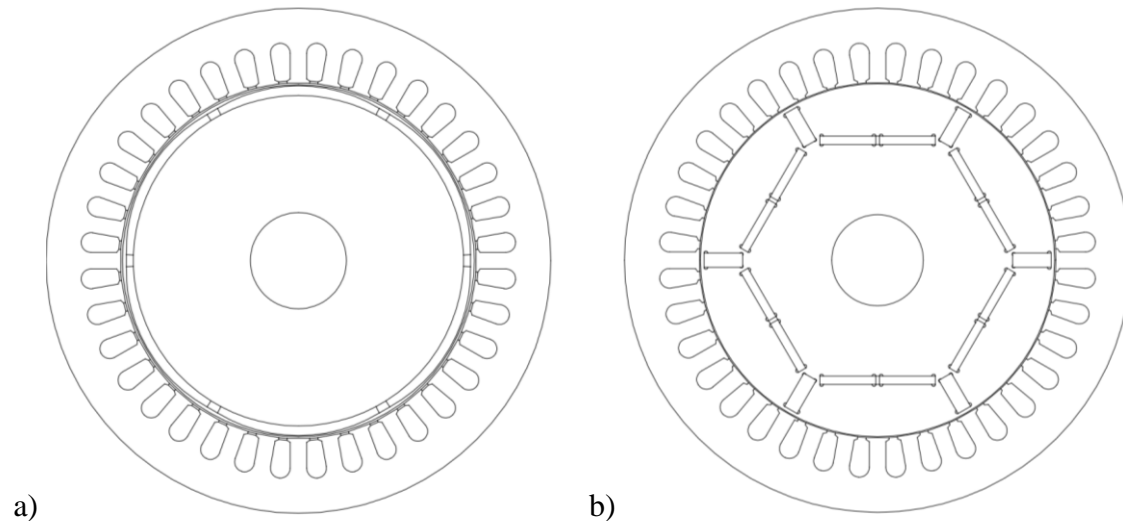


Figure 5-2: geometries of a) SPM reference rotor and b) IPM proposed rotor.

The performance of the SPM-SM, in the following denoted as the reference SPM, has been analyzed via FEA imposing a current ripple at the worst PWM switching frequencies for the studied machine. Then, the performance of reference machine has been compared with that of proposed IPM rotor, denoted as proposed IPM. The comparison has been carried out both via FEA and experimental tests, since the proposed IPM rotor was prototyped. The reference and proposed motors have the same stator lamination and distributed winding, the machines performance is compared in terms of efficiency and rotor temperature at rated conditions.

The characteristics of reference machine are listed in Table 5-1, the stator lamination is derived from an IM and the winding is manufactured with a distributed winding configuration. The mechanical frame is a standard 132 mm shaft height with wings and fan. The PMs type is NdFeB 32 SH.

The Figure 5-3 shows the no load magnetic flux density distribution of reference SPM machine which shows an adequate saturation of stator lamination for M570-50A silicon electric steel employed in FEA simulation, even if the stator geometry is derived from an IM in order to contain the total motor costs.

Parameter	Reference SPM	Proposed IPM	Unit of Measurement
Stator Slots	36	36	-
Pole Pair	3	3	-
SPP	2	2	-
Stator Outer Diameter	210	210	[mm]
Lamination Stack Length	100	100	[mm]
PM Volume	0.0002646	0.0002638	[m ³]

Table 5-1: characteristic of reference SPM and proposed IPM machines.

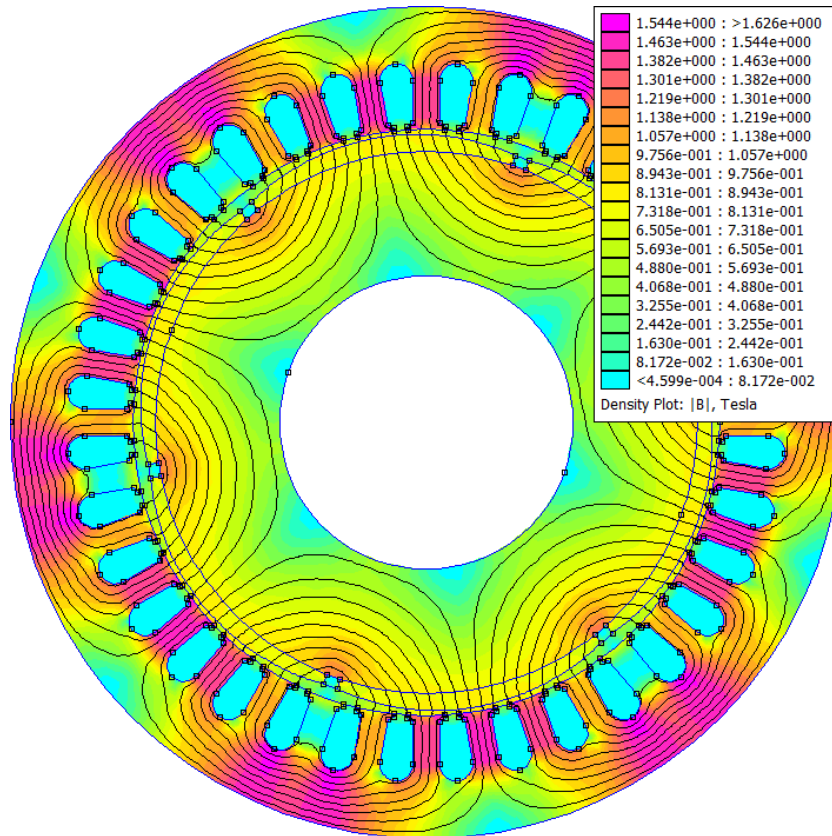


Figure 5-3: no load magnetic flux density distribution of reference SPM machine.

The reference SPM machine is fed with a 4kHz inverter which induces a stator current ripple sufficient to produce a total amount of PM losses able to drive magnet temperature over 150 °C. According to this, the magnets working point falls below the knee of the demagnetization curve and magnets are irremediably demagnetized.

It is here proposed a different rotor configuration deepening PMs below rotor surface in order to protect them from demagnetization. Three major benefits can be found from this new proposal:

- Increased synchronous inductance, which allows to reduced current ripple;
- Increased magnet protection, thanks to the iron region above them [29];
- No need of retaining sleeve which is a location of additional eddy current since generally is manufactured with staining steel or copper [25] and [30].

The basic design of IPM rotor is with PMs in radial direction, denoted as *spoke rotor*, as shown in Figure 5-4. The spoke rotor type has intrinsically a certain amount of leakage magnetic flux which does not produce electromechanical torque (red solid arrows of Figure 5-4). Moreover, the thin lamination ring near the rotor shaft is mechanically weakened when magnetic paths are thinned in order to increase their leakage flux reluctance. Figure 5-5 shows the mechanical stress on the rotor due to centrifugal force \vec{F}_c .

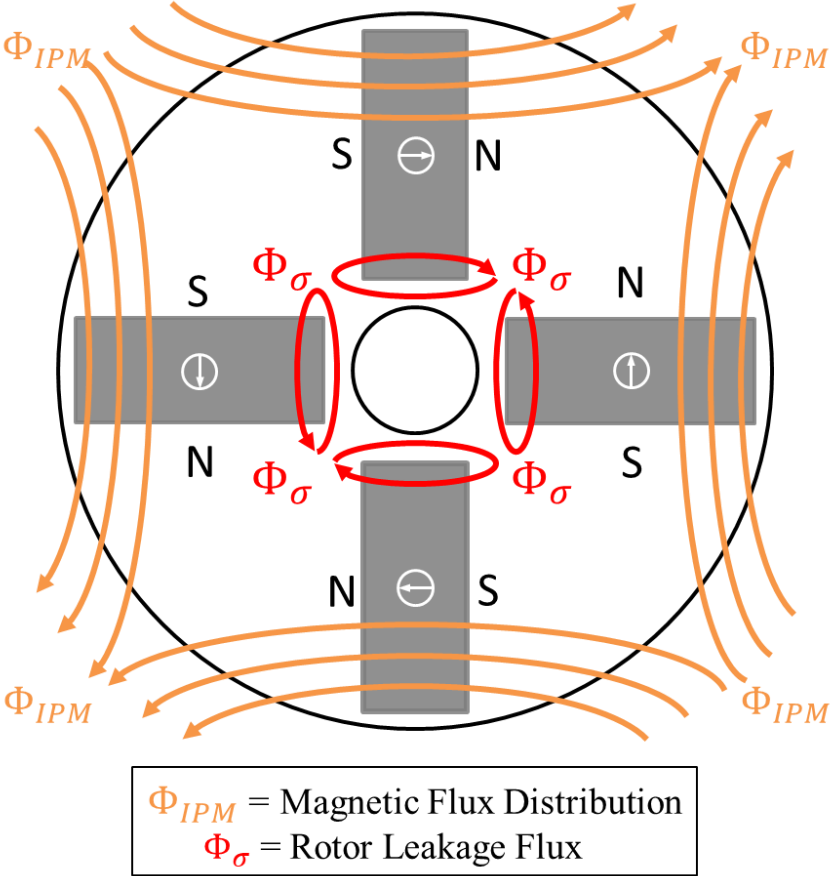


Figure 5-4: example of magnetic flux paths inside a four poles IPM spoke rotor configuration.

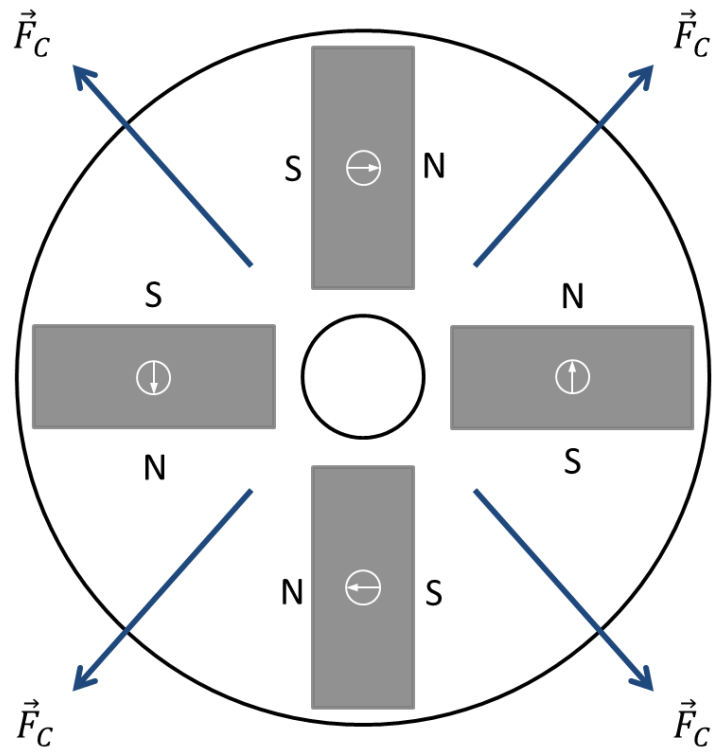


Figure 5-5: example of centrifugal force acting on a four poles IPM spoke rotor.

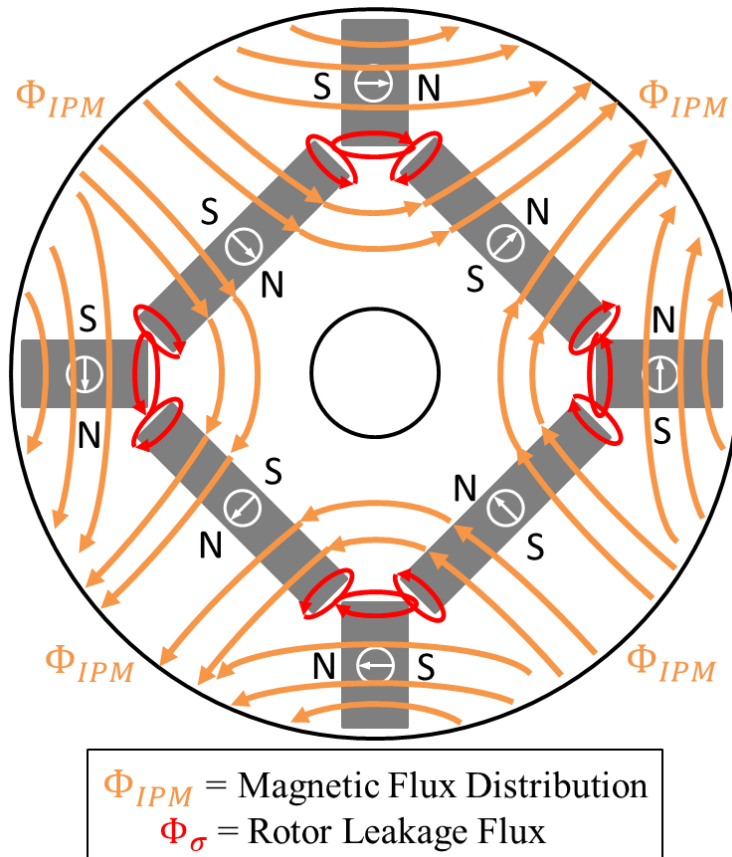


Figure 5-6: example for a four poles electric machine of magnetic flux paths of the proposed IPM rotor.

The proposed IPM rotor has been designed to reduce the leakage flux of PM and to increase the mechanical stress resistance of rotor lamination. The Figure 5-6 shows the magnetic flux paths of PMs and as it can be seen the height of radial PMs is shorter and transversal ones which are placed between them in order to reduce the leakage magnetic flux. The magnetic flux density distribution of the proposed IPM synchronous machine is shown in Figure 5-7.

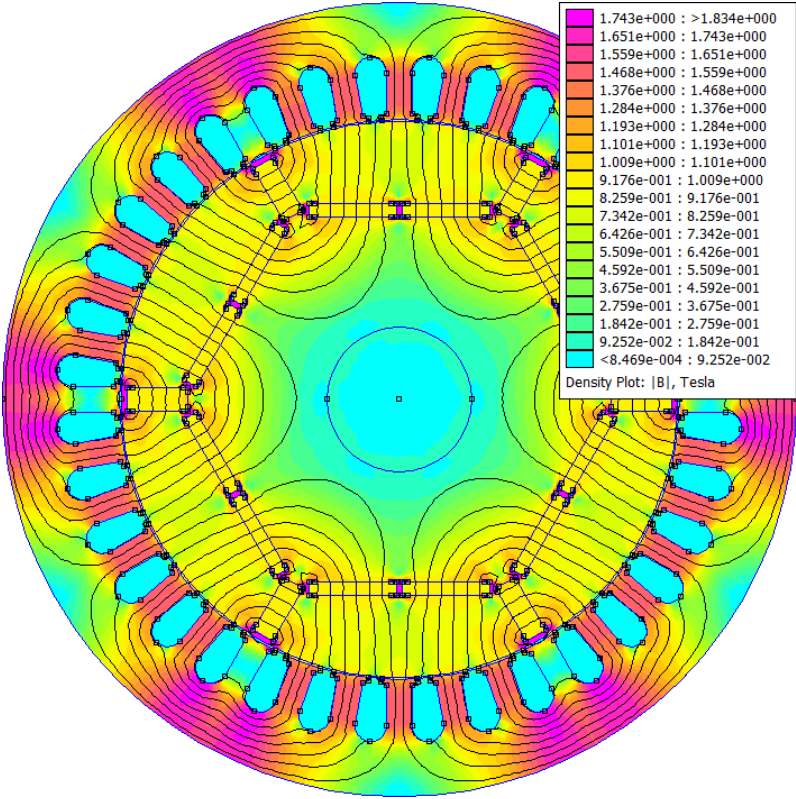


Figure 5-7: no load flux density distribution of proposed IPM machine.

5.4. Finite Element Analysis

The reference SPM machine and the proposed IPM solution were compared via FEA imposing an RMS current density of $6.7 \frac{\text{A}}{\text{mm}^2}$, considering a winding factor k_{fill} of 0.35 and a mechanical speed 3000 r/min which is a reference speed for many IM application fed with line frequency of 50 Hz.

The performance of both machines is evaluated imposing three-phase perfect sinusoidal currents (see Figure 5-8) and considering a three-phase current with the current ripple due to a PWM switching frequency of 4 kHz (see Figure 5-9). The simulation with current ripple is carried out to verify the influence of PWM switching frequency on motor losses.

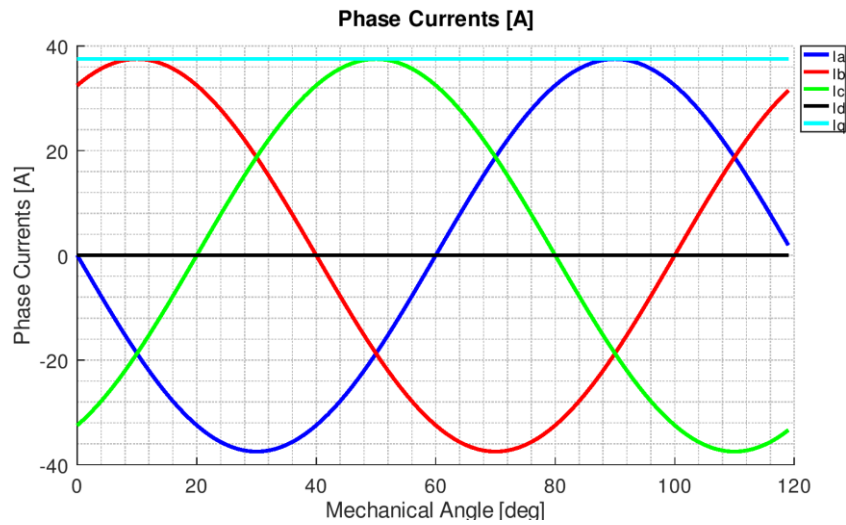


Figure 5-8: three-phase sinusoidal currents without current ripple @ $j = 6.7 A_{RMS}/\text{mm}^2$

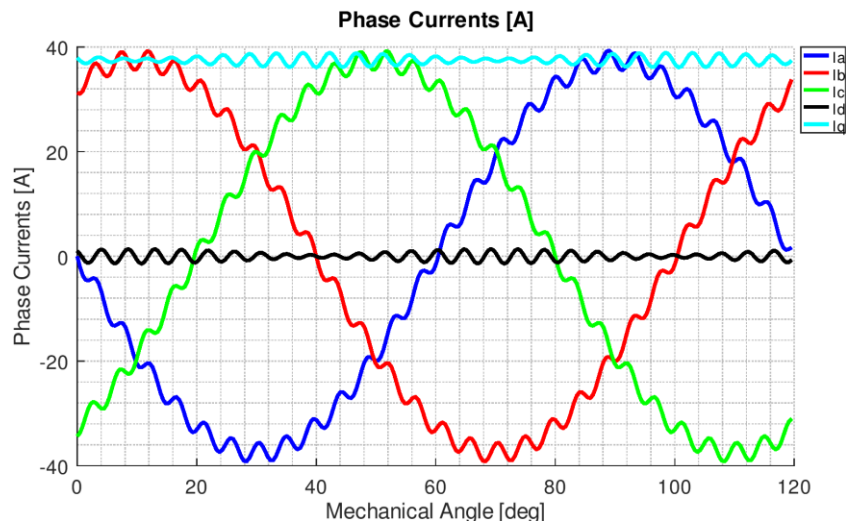


Figure 5-9: three-phase current with current ripple @ $j = 6.7 A_{RMS}/\text{mm}^2$ due to PWM switching frequency of 4 kHz.

The Figure 5-10 and Figure 5-11 show respectively the torque profiles of reference SPM machine and proposed IPM machine without current ripple, while Figure 5-12 and Figure 5-13 show the torque profiles with a current ripple due to a PWM switching frequency of 4 kHz.

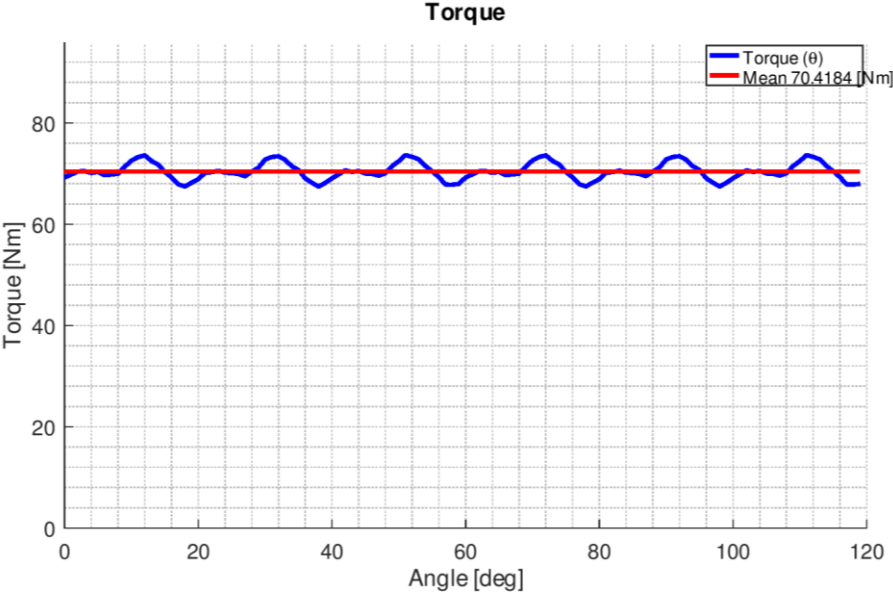


Figure 5-10: mean torque of reference SPM machine without current ripple @ $j = 6.7 A_{RMS}/mm^2$.

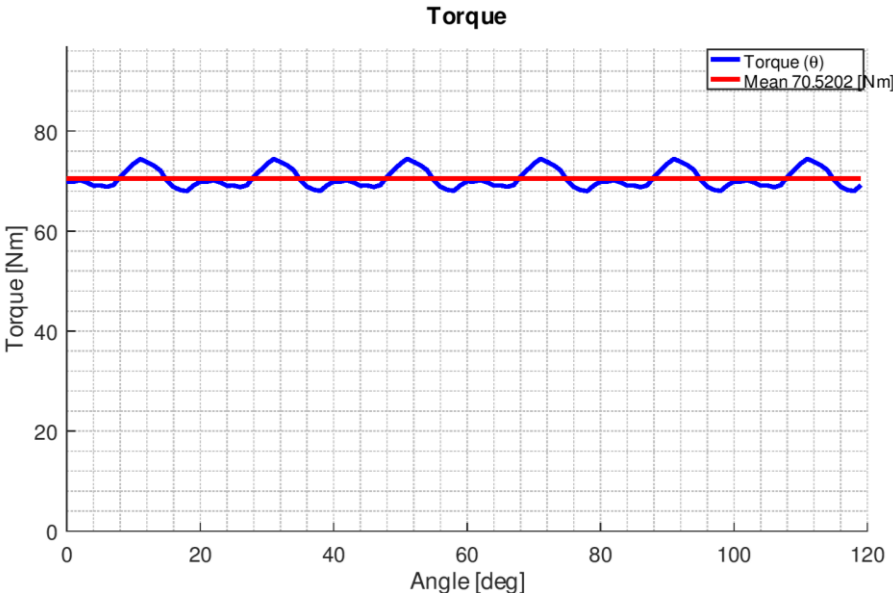


Figure 5-11: mean torque of proposed IPM machine without current ripple @ $j = 6.7 A_{RMS}/mm^2$.

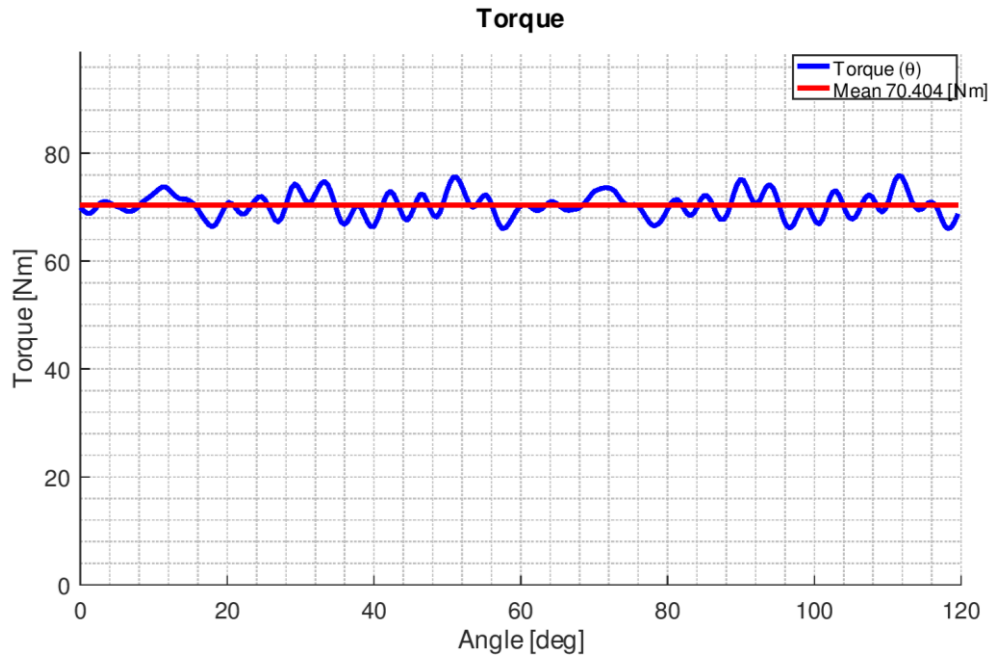


Figure 5-12: mean torque of reference SPM machine with current ripple @ $j = 6.7 A_{RMS}/mm^2$ due to PWM switching frequency of 4 kHz..

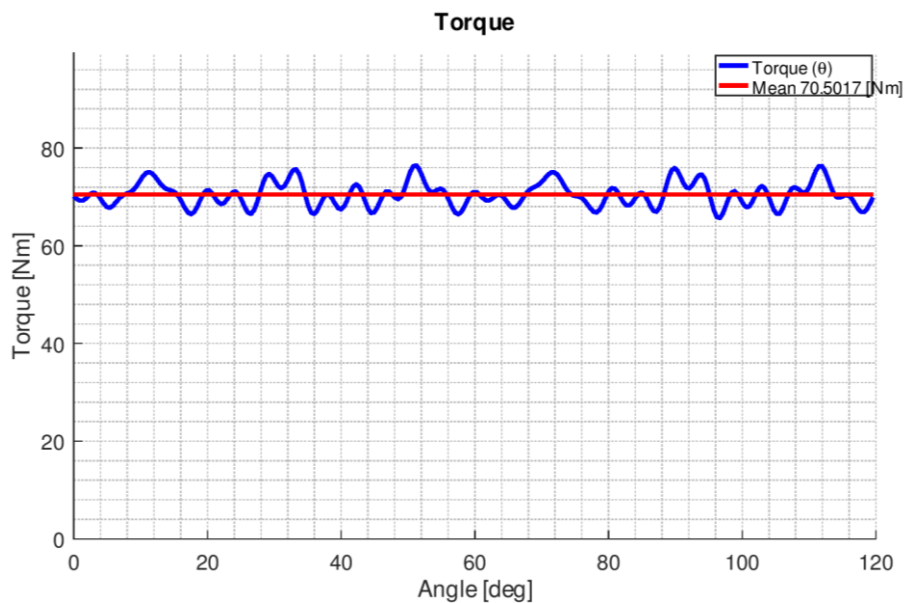


Figure 5-13: mean torque of proposed IPM machine with current ripple @ $j = 6.7 A_{RMS}/mm^2$ due to PWM switching frequency of 4 kHz..

The Figure 5-14 shows the power losses of reference SPM machine and proposed IPM machine fed with three-phase sinusoidal currents and with current ripple over a wide range of mechanical speed. As it can be seen the proposed IPM solution shows less total power losses than the reference SPM machine in both supply conditions. Considering the reference mechanical speed of 3000 r/min, the current ripple increases the machine power losses of the synchronous machines with an increase of 41% for reference SPM machine and of 30% for the proposed IPM machine. Looking at PMs losses of IPM

machine are significantly lower than SPM machine: 60% with sinusoidal currents and 40% with current ripple.

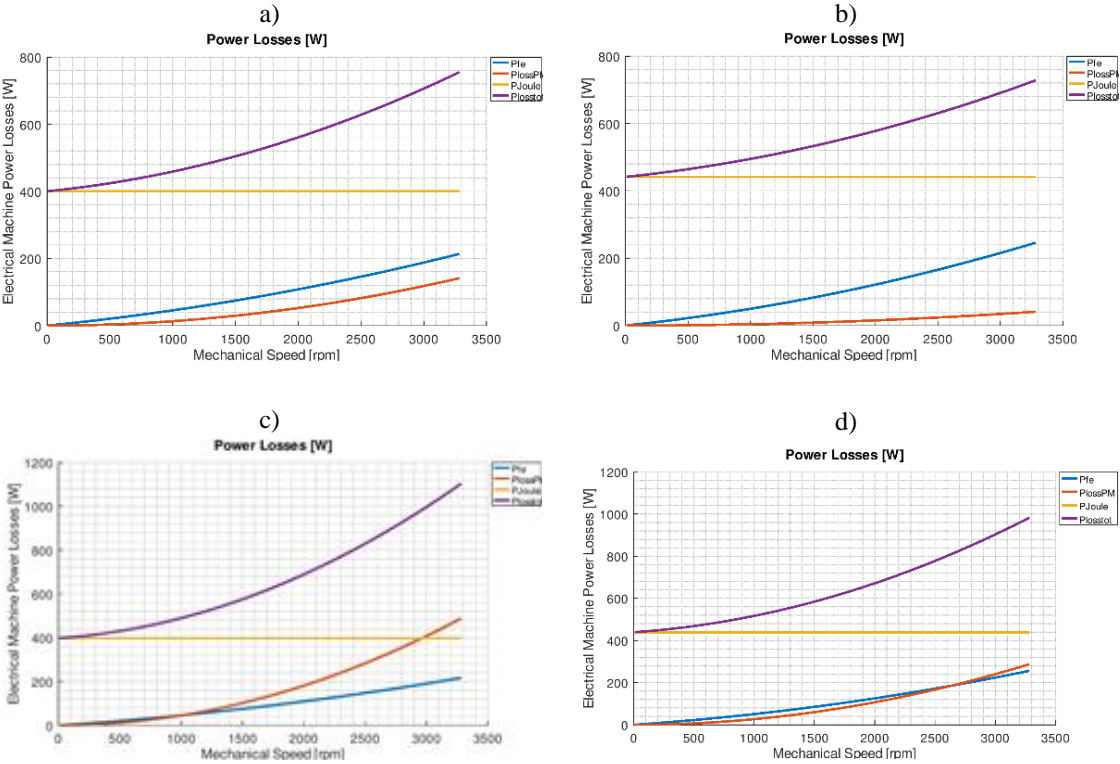


Figure 5-14: total power losses and power losses component of: a) reference SPM-SM with sinusoidal currents, b) proposed IPM-SM with sinusoidal currents, c) reference SPM-SM with current ripple and d) proposed IPM-SM with current ripple.

5.5. Experimental Tests

Experimental tests have been carried out at two PWM switching frequencies: 4 kHz and 8 kHz. The test set up can include or not input filters between the drive and the electric motor in order to reduce current ripple and to assess the influence of PWM switching frequency on PMs working temperature.

Stator and rotor temperature have been measured during experimental test by means a set of thermocouples of type K. Stator windings temperature has been measured placing four pairs of thermocouples in different locations of the stator winding as shown in Figure 5-15.

A special thermocouple set up has been built in order to measure PMs temperature. As shown in Figure 5-16, four pairs of thermocouples have been placed on the PMs on rotor surface, then they have been introduced inside a custom hole in the rotor shaft and attached to connector on the shaft side.

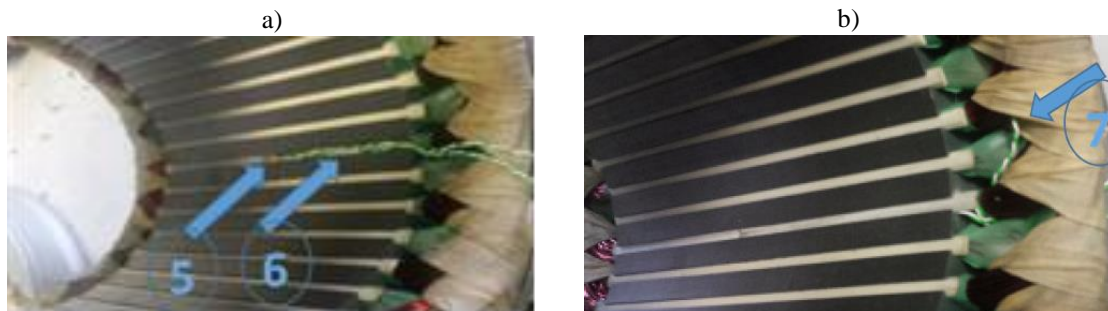


Figure 5-15: thermocouples location inside stator windings.

During the tests, once the stator windings reached the thermal equilibrium (see Figure 5-17 and Figure 5-18), the tests were stopped and PMs temperatures were sampled connecting rotor thermocouples to the measurement equipment (see Figure 5-19 and Figure 5-20). Table 5-2 shows the average values of measured temperatures at different test conditions and as it can be seen, a lower PWM switching frequency entails more thermal stress on PMs, while a more sinusoidal current waveform allows to reduce the thermal stress. The PMs temperature of reference SPM machine was around 120 °C when no filters were used and with one inductive input filter at 4 kHz; this temperature implicates a prone condition to PMs demagnetization.

In addition to PMs temperature measurements by means thermocouples, during experimental tests were also taken some pictures by mean a thermal camera THT 70. The front of the motor flange was machined in order to create a hole (see Figure 5-21) from which pictures shown in Figure 5-22 were easily taken. As it can be seen, it is confirmed that rotor temperature is around 120 °C.

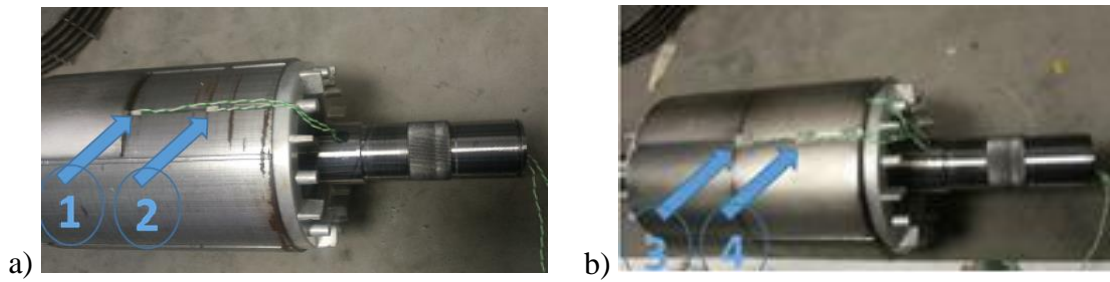


Figure 5-16: thermocouples location on rotor permanent-magnets.

	4 kHz		8 kHz	
	Stator Temperature [°C]	Rotor Temperature [°C]	Stator Temperature [°C]	Rotor Temperature [°C]
Without Filters	\	\	88.80	119.58
1 Filter	82.51	118.01	76.32	101.38
2 Filter	74.72	94.09	\	\
3 Filters	68.58	81.28	65.11	73.90

Table 5-2: stator windings and permanent-magnet temperatures at different PWM switching frequencies and input filtering conditions.

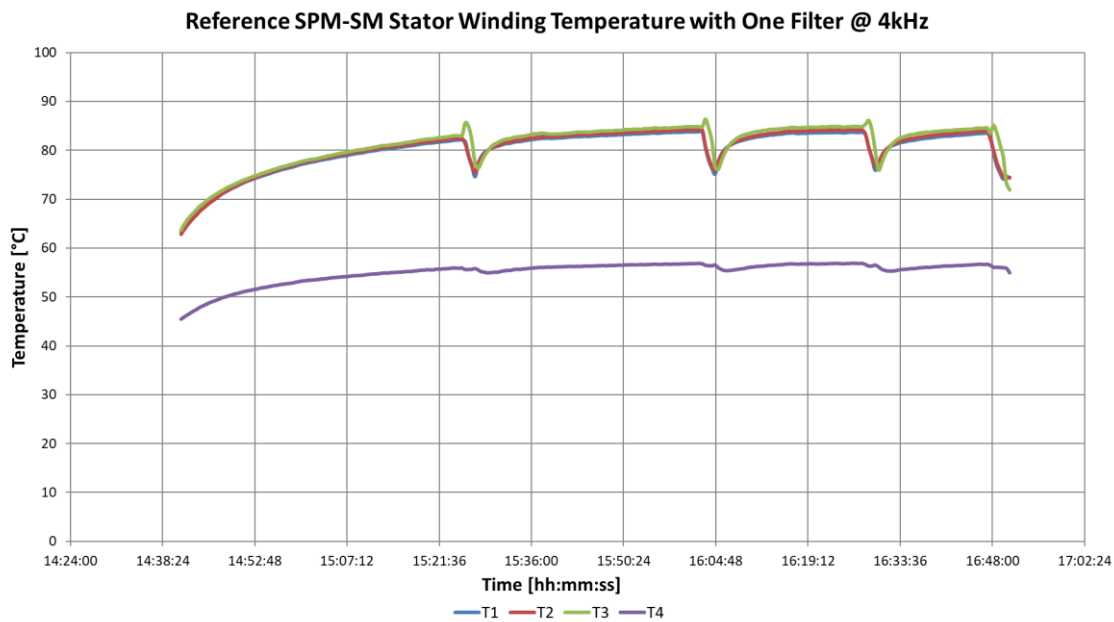


Figure 5-17: stator winding temperatures during thermal equilibrium with one inductive input filter @ 4 kHz.

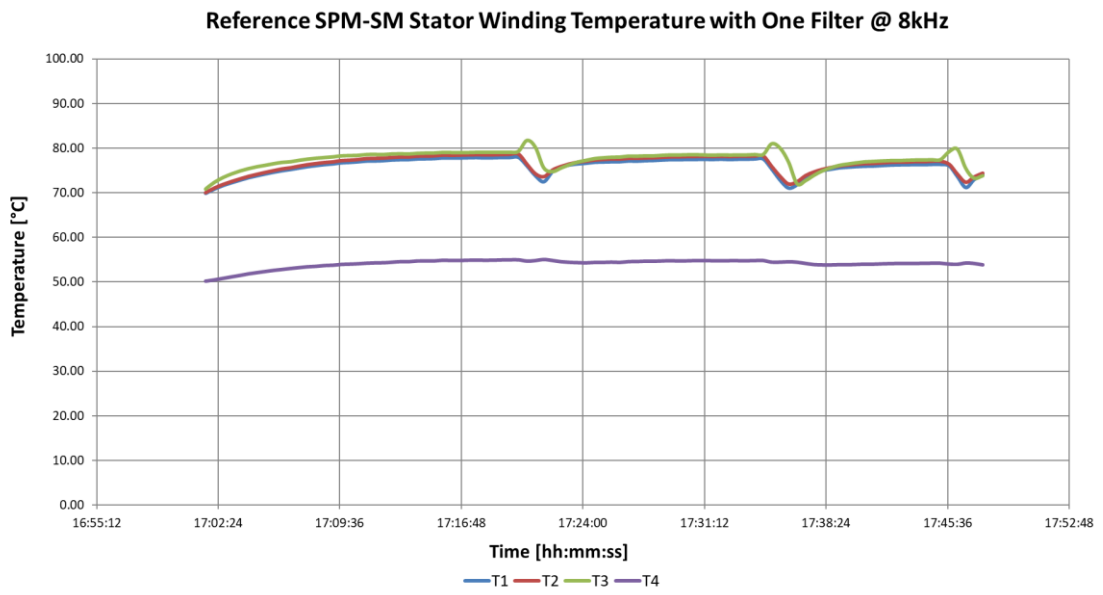


Figure 5-18: stator winding temperatures during thermal equilibrium with one inductive input filter @ 8 kHz.

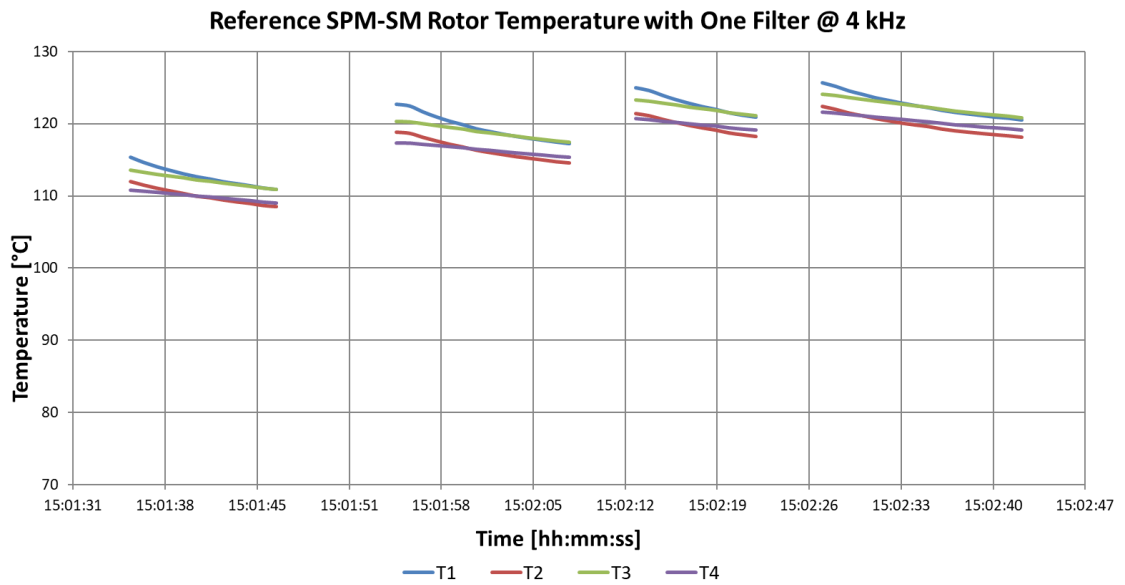


Figure 5-19: PMs temperatures during thermal equilibrium with one inductive input filter @ 4 kHz.

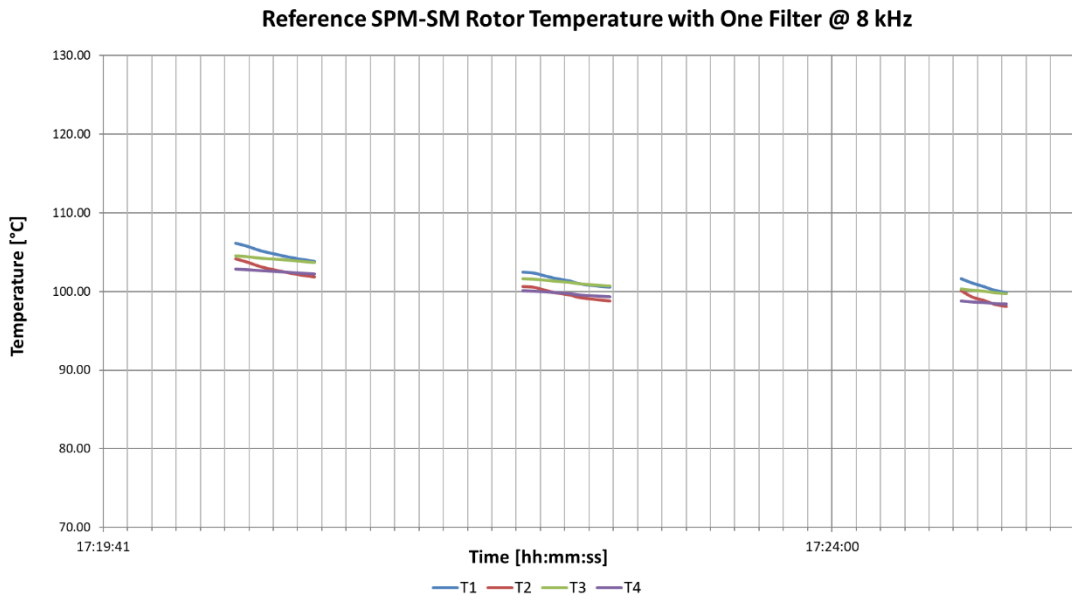


Figure 5-20: PMs temperatures during thermal equilibrium with one inductive input filter @ 8 kHz.



Figure 5-21: modified front motor flange.

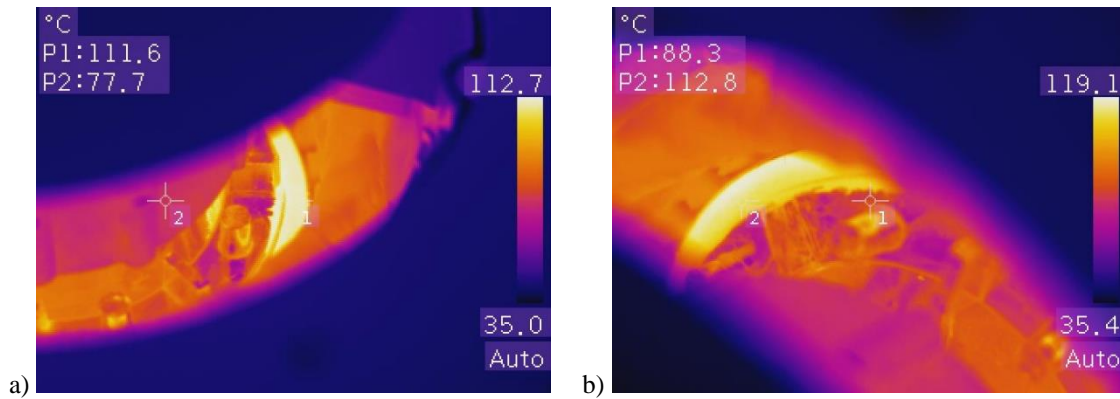


Figure 5-22: thermal picture of reference SPM machine during experimental tests taken through the modified motor flange.

The PM-SM with the proposed IPM rotor was manufactured and tested at different PWM switching frequencies. Figure 5-23 shows IPM rotor working temperature when the machine was fed by inverter at 4 kHz which corresponds to the worst condition from the demagnetization point of view. The thermal camera shows that PMs and rotor work between a save temperature range, thus PMs are preserved from demagnetization problems

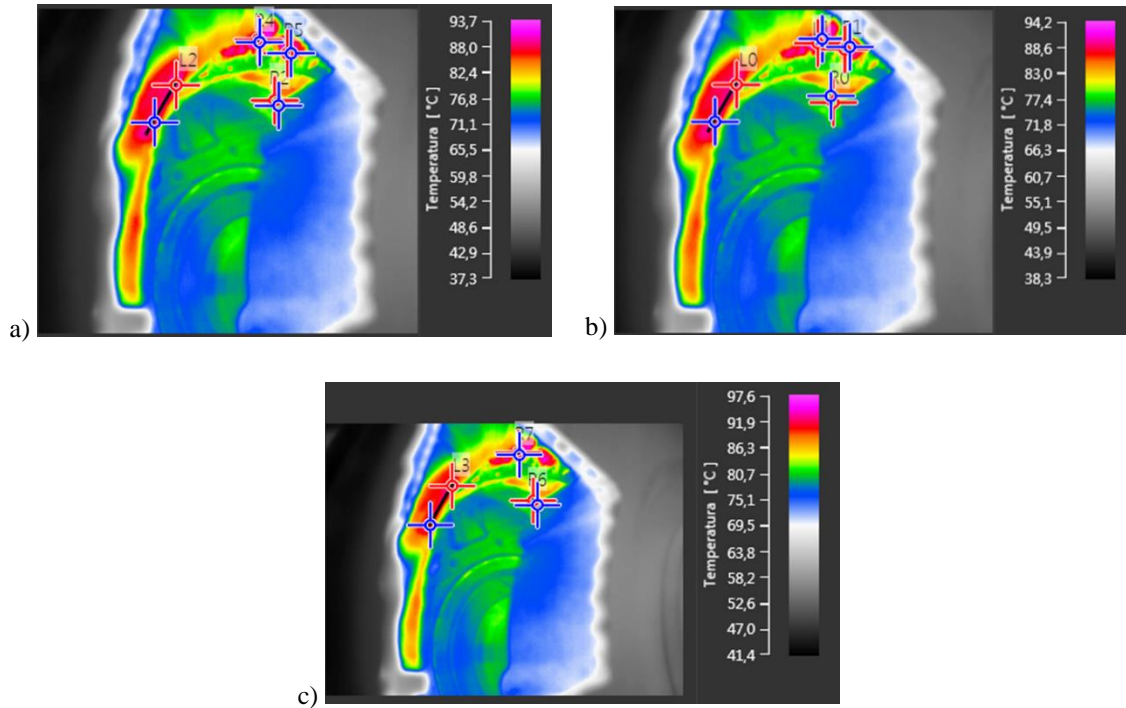


Figure 5-23: proposed IPM rotor working temperature at 4 kHz taken through the modified motor flange.

5.6. Activity Results on Permanent-Magnet Demagnetization Issues

The activity research aimed to improve the demagnetization fault-tolerant resistance of a low-cost PM-SM with distributed winding for industrial application.

The reference machine is a SPM-SM prone to PMs demagnetization because the PWM switching frequency of the inverter induces additional time harmonics inside stator currents that induces eddy currents in conductive rotor parts such as PMs. These eddy currents produce additional Joule losses which increases PMs working temperature and could drive PMs working point below the knee of demagnetization curve causing seriously demagnetization issue.

The rotor geometry of PM-SM was changed towards IPM topology in order to protect magnets against eddy currents and demagnetization. The design of the IPM took care as well as the reduction of leakage PMs magnetic flux and the improvement of mechanical resistance to centrifugal force stress.

The performance of the reference SPM motor and proposed IPM one was extensively analyzed and compared by means 2D-FEA and then by experimental tests. In fact, the proposed IPM rotor was manufactured after FEA validation in order to assess machine fault-resistance against demagnetization.

Both FEA and experimental results show that the proposed IPM rotor protects PMs against demagnetization, in particular when the motor is fed with the lowest PWM switching frequency of 4 kHz which corresponds to the most actual stressful operating condition for PMs of this application.

FEA results show an improvement of 40% of PMs losses, confirmed by experimental results which show an improvement around 40% too.

6. Ironless Dual-Rotor Surface Permanent-Magnet Machine for Flywheel Batteries

This research activity deals with a particular design of a SPM-SM for energy storage at household level. The design of this electrical machine has been carried out as part of European project IET Climate-KIC³ in the context of energy storage systems with the energy produced by means renewable sources.

The proposed electrical machine is part of a mechanical storage technology that is a flywheel battery of few kW for household application and coupled to a grid connected photovoltaic system on the roof (see Figure 6-1). The flywheel battery can accumulate and release energy by means an electrical machine which works as motor or as generator as function of the direction of the energy flow (motor: during energy accumulation; generator: during energy emission). Since the flywheel storage system is intended for household application its dimensions and self-discharge duration represent the most critical requirements [31]. The self-discharge duration corresponds to the time span when the system is disconnected from the grid, that is, the flywheel is neither accumulating nor releasing energy. The analyzed flywheel battery has to rotate at very high mechanical speed in order to store the required household energy capacity and to contain its dimension suitable for single house. The rated rotational speed is maintained during self-discharge periods.

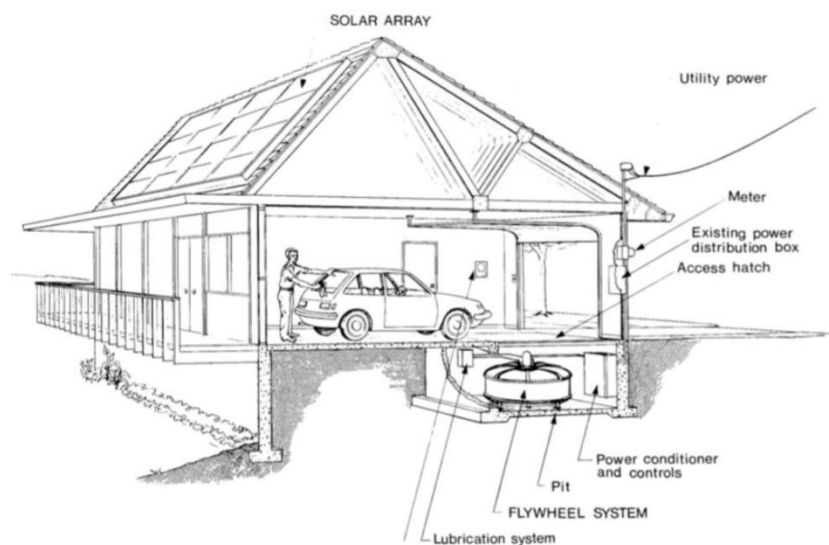


Figure 6-1: mechanical energy system in a domestic/residential scenario. The system breakdown is: flywheel battery, electrical machine, photovoltaic system for residential user connected to the grid [32].

Since the electrical machine is mechanically connected to the flywheel battery, it rotates at the same high mechanical rotational speed. The self-discharge duration could be deeply affected by mechanical losses, iron core losses and windage losses; according to this, the traditional iron core SPM-SM exhibits very high iron core losses due to PMs magnetic field which induces hysteresis and eddy current losses. This drawback could

³ <https://www.climate-kic.org/>

hardly reduce flywheel energy storage capacity during self-discharge period, reducing the economic advantage of the renewable energy time-shift, as it will be exposed in the following paragraphs.

With the aim to reduce the iron core losses during self-discharge duration, the ironless dual-rotor SPM-SM has been designed and optimized via FEA. The ironless solution allows eliminating iron losses, while the dual-rotor configuration allows increasing the magnetic paths magnetic permeance and increasing the air gap MMF to produce an electric-motive torque similar to that of iron core machine.

The performance of the proposed SPM-SM has been compared via FEA with that of an iron core SPM and of a pure SyncRel machine, since the latter topology is the most commonly used with flywheel battery application for peak shaving. Then the proposed machine has been prototyped and tested on test bench.

6.1. Distributed Energy Generation

The energy management has been becoming a key field both from economic and environmental point of views. In the last few years the production, distribution and the consume of energy became significant issues also because of greenhouse gas emissions issue, thus the push for a transition from fossil sources toward renewable energy sources (*decarbonization*) has been increased. Nevertheless, the transition from traditional fossil-energy-based centralized power systems to renewable-energy-based has been hampered by the cost of renewable energies and by the intrinsic intermittence and unpredictability of renewable energies, which reduces availability and causes grid instability.

Suitable energy storage, utilities and grid management policy can couple energy producers and consumers with urgent temporal behaviors, reducing electric power peaks and the need of additional power generation plants. Given the above, energy storage technology can enable the transition to renewable-energy-based distributed generation and reduce the time difference between energy production and use. A distributed energy storage system is the best suited to distributed energy sources for two reasons: it avoids the use of huge energy storage systems, since the storage size is a critical issue for any storage technology, and it prevents transmission and dispatching losses.

According to an economic point of view, an energy storage system reaches huge potential if its discharge duration is around few hours. Figure 6-2 ([33]) shows the most valued energy issues for different application categories; the energy storage systems and renewables are economically convenient when the renewable energy time-shift value proposition falls in the range of 2 to 5 five hours. In this case, the energy is charged with low-value electric energy generated using renewable energy, then it could be used or sold at a later time when is more valuable [33],[34].

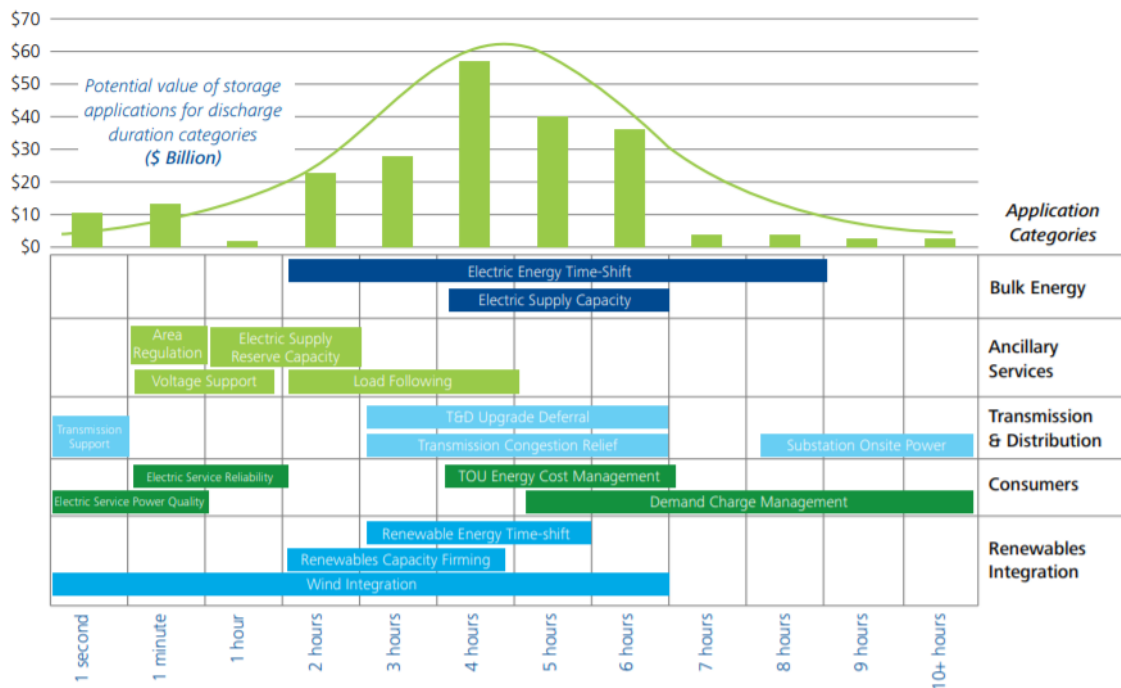


Figure 6-2: energy storage applications and corresponding values for various discharge durations (economics values are referred to USA ones for a life time of ten years) [33], [34].

The European Parliament Research Service showed that energy storage systems are one of the top ten technologies that would drastically change human begins lives in the next future [35]. The market offers several energy storage systems currently in active development that could be grouped into four categories: electrical, mechanical, thermal and chemical.

Chemical storage systems are wide spread and very effective for their high energy density and flexibility. However, from an environmental point of view their footprint is quite high, since they rely on precious and rare materials; moreover, they feature a pretty long charging time and a life time below ten years.

Mechanical storage systems feature a quite immediate charging time and are characterized by a smaller environmental footprint than chemical storage systems. Additional advantages of mechanical storage systems are: simpler production process, opportunity to re-use or recycle materials and a longer life time span. On the other hand, mechanical systems energy density is low, they feature important dimensions in order to store energy and the discharge duration is a critical issue.

Flywheel battery storage systems belong to mechanical storage category and they are mainly designed for peak shaving in energy distribution systems; commercial solutions are available and they can store up to hundreds kW for few seconds. The flywheel storage energy capacity depends on the moment of inertia (J) and the square of the mechanical rotational speed (ω), according to kinetic energy formula (see Eq. 6-1). Flywheel battery storage systems for household application feature high rotational speed, in order to contain flywheel inertia, and reach a high self-discharge duration.

The Table 6-1 compares the performance of the studied flywheel storage system for household application and a reference Li-Ion battery. Energy storage system specifications are tailored for a household system with grid connection and renewables.

Performance	Unit of Measurement	Proposed Flywheel Storage System	Equivalent Lithium-Ion Battery
Material	/	Steel	Li-Ion and Metals
Weight	[kg]	425	142.86
Electric Power	[W]	5	5
Energy Storage Capacity	[kWh]	3	3
Photovoltaic System	[kW]	3	3
Expected Life	[years]	30	10

Table 6-1: parameters comparison between MechSTOR flywheel storage system and benchmark lithium-ion battery available in the Ecoinvent library.

6.2. Electrical Machine Requirements

The electrical machine and its mechanical structures e.g. bearings, joint, vacuum system are key design devices in flywheel battery storage system. The electrical machine losses must be minimized in order to meet the self-discharge duration objective of few hours.

Traditional flywheel battery storage systems are designed for peak shaving in grid quality system; thus, they feature big dimensions and very low self-discharge duration (in the order of few seconds). These flywheel storage systems generally adopt a pure SyncRel machine in order to remove the self-braking phenomenon due PMs the electrical machine is disconnected. Other flywheel solutions mount an induction machine [36], [37].

The following flywheel battery storage system is for a distributed energy storage system of few kW at household level with a self-discharge duration of few hours in order to achieve the renewable energy time-shift specifications. The technical data of the proposed flywheel storage system have been reported in Table 6-1.

The structure of the flywheel battery is a steel cylinder and it is designed assuming a single household user connected to the grid by means of a photovoltaic system on the roof. The rated rotational speed of the flywheel and of the electrical machine, which is consequently related to the electric frequency, has been chosen by fulfilling typical floor area and volume of a household appliance and centrifugal stress constraints. By so doing, a rated rotational speed of 9000 r/min, corresponding to $\omega_m = 942 \frac{rad}{s}$, is necessary to meet an energy storage capacity of 3 kWh. This value has been computed according the theoretical kinetic relationship shown in Eq. 6-1.

$$U = \frac{1}{2} J \omega^2 \quad \text{Eq. 6-1}$$

Where J is the mass moment of inertia of a cylinder disc, ρ is material density, wheel radius R and height h .

$$J = \frac{\pi}{2} \rho R^4 h \quad \text{Eq. 6-2}$$

The Table 6-2 shows the geometrical parameters of the analyzed flywheel battery storage system.

Parameter	Value	Unit of Measurement
Steel Density	7850	[kg/m ³]
Radius	0.34	[m]
Height	0.15	[m]
Mass Moment of Inertia	24.72	[kg*m ²]
Rotational Speed	9000	[rad/s]

Table 6-2: mechanical parameters of household flywheel storage system.

The following research activity focused on the design of the electrical machine for this household flywheel battery system with the aim to minimized the total amount of machine losses.

As aforementioned written in previous chapters, SPM-SMs are appreciated for their high power density ratio, high power factors, high efficiency and reduced Joule losses, but for this high-speed application an iron core SPM-SM is not suitable due to high number of losses during self-discharge phase when the electrical machine is at no load condition. In fact, during self-discharge the PMs magnetic field induces hysteresis and eddy current losses inside iron core structure which at 9000 r/min could be particularly remarkable. Moreover, the PMs magnetic field links with stator winding inducing a variable current and thus an electro-motive force which acts like a brake when the grid is disconnected.

Given the above, this activity led to the design, optimization and test of a working prototype of an ironless dual-rotor SPM-SM called MechSTOR.

The design of the ironless dual-rotor SPM machine has been optimized via FEA in order to: get close to iron core SPM machines performance, to minimize electrical machine losses and to meet specification of Table 6-1. The dual-rotor configuration allows increasing the MMF provided by PMs and reduces the flux path reluctance providing a second yoke on the internal side of the machine [38]-[40].

The performance of the MechSTOR was compared via FEA with that of an iron core SPM-SM and pure SyncRel machine at 9000 r/min. The iron core machines were designed and optimized to meet the performance of the flywheel battery storage system.

6.3. Finite Element Analysis of Iron Core and Ironless Surface Permanent-Magnet Machines

The analyzed electrical machine has to fulfill two performance benchmarks in order to be efficient and, in particular, to achieve the required few hours of self-discharge duration of a flywheel battery system.

The first benchmark is the traditional energy efficiency η_1 given by the ratio of output power to input power; thus, it is the electro-mechanical conversion efficiency from the mechanical flywheel to the grid and vice versa.

The second benchmark is the self-discharge duration which depends on the retained energy when the grid is disconnected from the flywheel battery; this second benchmark will be denoted as η_2 in the following.

The two benchmarks are contradictory, since different design choices are needed to achieve them. The energy conversion efficiency η_1 would lead toward an electrical machine design which aims to maximize the power density in order to restrain electric load and magnetic load. High values of η_1 could be achieved by PMs and low reluctance magnetic circuits, but one of the main drawbacks for this application are iron core losses due to hysteresis and eddy currents which reduces self-discharge duration because of their self-braking effect when the grid is disconnected. The MechSTOR machine has been design considering as principal benchmark the self-discharge duration in order to meet the renewable energy time-shift proposition.

This paragraph shows the comparison in terms of FEA performance of the proposed ironless dual-rotor SPM-SM with two traditional iron core synchronous machines: a SPM-SM and a pure SyncRel machine.

The Figure 6-3 shows the three machine geometries and the winding arrangement of: iron core SPM-SM (denoted as SPM_{IC}), pure SyncRel machine (denoted as SyncRel) and MechSTOR.

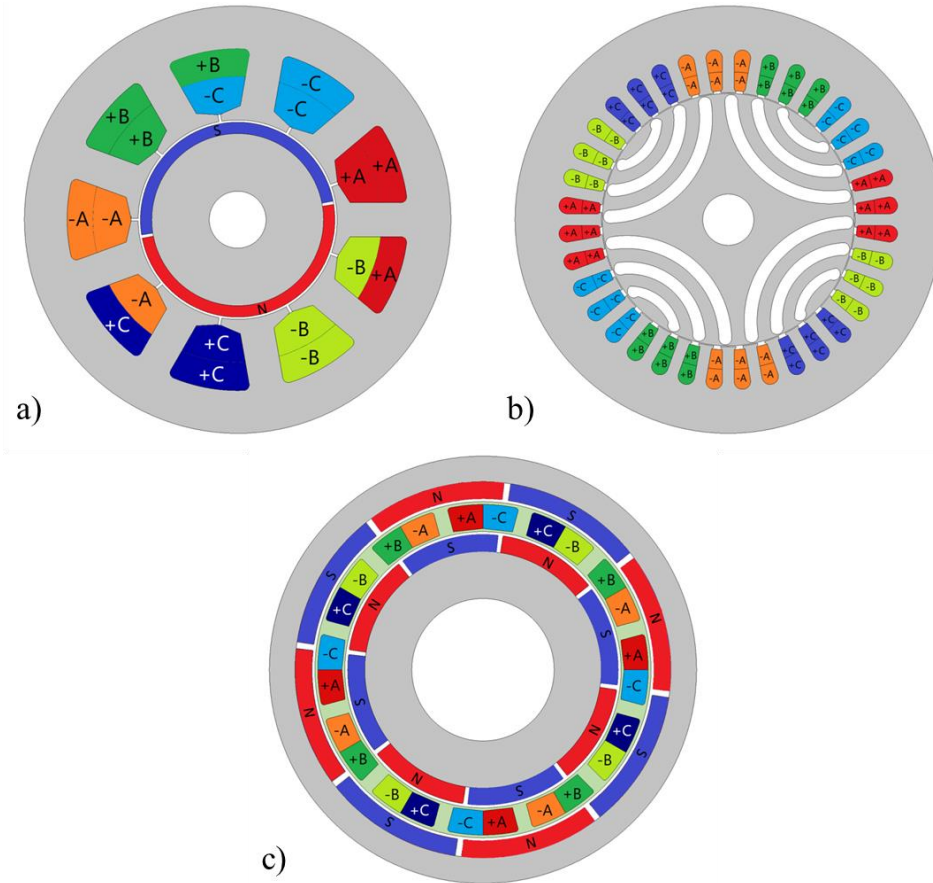


Figure 6-3: geometries and winding arrangements of: a) iron core surface permanent-magnet machine (SPM_{IC}), b) pure SyncRel machine (SyncRel) and c) iron less dual-rotor synchronous machine (MechSTOR).

The design choices of SPM_{IC} have been driven with the aim to reduce the iron core losses, thus improving its performance in terms of η_2 during self-discharge operation. According to this, special non-oriented lamination steel NO20 has been adopted because of its low core losses density; indeed, NOXX electric steels are suitable for electrical machines for high speed applications. Another design choice aimed to limit iron core losses has been the choice of the slot-pole combination, the SPM_{IC} has been designed assuming a 9-2 combination in order to minimize the electric frequency considering that is proportional to mechanical frequency by means the pole pairs number p (see Eq. 6-3).

$$f_e = p \cdot f_m \quad \text{Eq. 6-3}$$

This choice allows limiting iron core losses, since they are strictly related to electric frequency according to Steinmetz's equations, shown in Eq. 6-4.

$$\begin{aligned} P_{Fe_{hyst}} &= k_{hyst} \cdot f_e \cdot \hat{B}^k \\ P_{Fe_{ec}} &= k_{ed} \cdot f_e^2 \cdot \hat{B}^k \end{aligned} \quad \text{Eq. 6-4}$$

Where k_{hyst} and k_{ed} are constants depending on the material type, \hat{B} is peak value of the induced magnetic flux, k is called Steinmetz's coefficient and varies from 1.8 to 2.2 and P_{Fehyst} and P_{Feed} are specific iron losses per volume [W/m^3] or per mass [W/kg] due to hysteresis and eddy current.

The SyncRel machine has been designed with 36-4 slot-pole combination and stator and rotor laminations are made of silicon iron electric steel M330-35A.

The Figure 6-4 shows the flux density distribution of the SPM_{IC} and SyncRel at rated load where the same range of flux density distribution has been assumed in order to compare the two machines. The SPM_{IC} exhibits higher machine induction because of PMs.

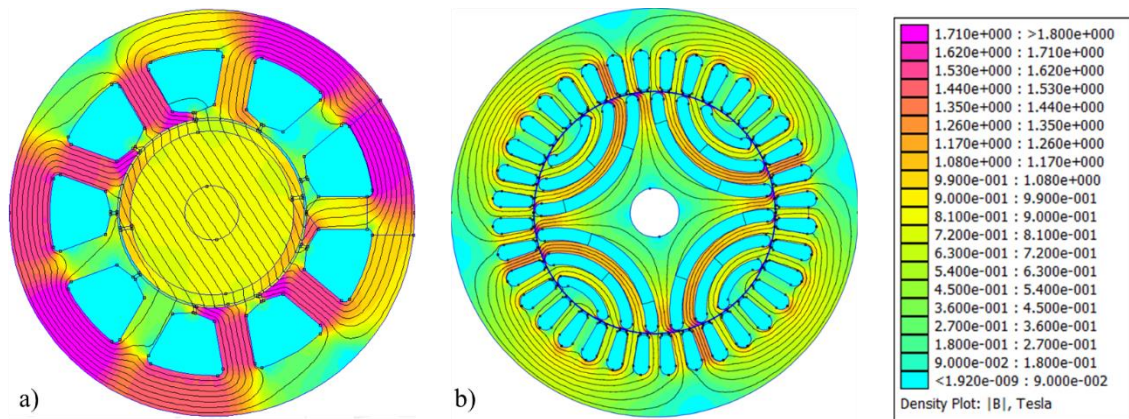


Figure 6-4: magnetic flux density distributions at rated load of a) SPM_{IC} and b) SyncRel.

Hence, the machine design aims to maximize electrical machine performance during self-discharge period, thus improving η_2 , the design of ironless dual-rotor SPM-SM has been studied and optimized via FEA in order to achieve machine performance close to an iron core machine, minimize total machine losses and meet specifications of Table 6-1.

The choice of the dual-rotor configuration reduces magnetic flux reluctance, that is, it allows minimizing the MMF drops along magnetic flux paths. Specifically, the dual-rotor is formed by two concentric SPM rotors among which is placed a stator coil, as shown in Figure 6-3c). Thanks to this design expedient, the external and internal rotor yokes form the external paths of the magnetic circuit, while the internal paths are PMs and stator coils. The 12-8 slot-pole combination has been chosen for the MechSTOR in order to achieve the right trade-off between EMF harmonic content, winding factor k_{fill} , and electric frequency in the operating range. The external rotor outer diameter has been fixed to 150 mm, then stator slots and magnet heights have been optimized in order to achieve the maximum torque for a given value of copper losses density (per unit of stack length) and to satisfy thermal constraints. Figure 6-5 shows the magnetic flux density distribution of MechSTOR at rated condition over the same range values of Figure 6-4

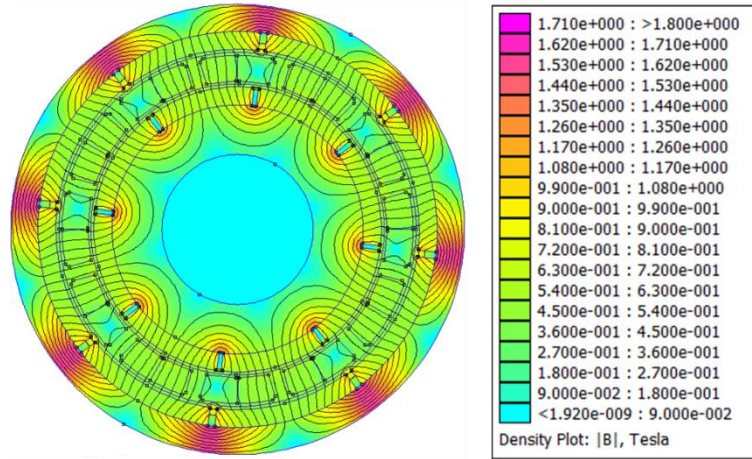


Figure 6-5: magnetic flux density distribution at rated condition of MechSTOR.

The Table 6-3 summarizes the geometrical parameters of the three analyzed machines: SPM_{IC} , SyncRel and MechSTOR. The SyncRel machine needs the longest lamination stack length, while SPM_{IC} the shortest one. Given the shortest lamination stack and the lower number of pole pairs, the SPM_{IC} has a lower PM volume than ironless dual-core SPM-SM.

The Figure 6-6 shows the mean torques of the three machines which has nearly the same value. The SyncRel machine exhibits the highest torque ripple than the two SPM machines, since an intrinsic drawback of this machine topology.

The Figure 6-7 compares power losses components as a function of mechanical speed of the three machines at load conditions. As expected, power losses increase as the mechanical frequency increases, and it is worth noticing how machine topology influences the distribution of power losses components among PMs, iron core and copper. The Figure 6-8 shows the iron core power losses distribution between stator and rotor cores of the three machines at load conditions; the iron core losses of SPM_{IC} are mainly inside the rotor core, while iron core losses are more equally distributed in the SyncRel machine.

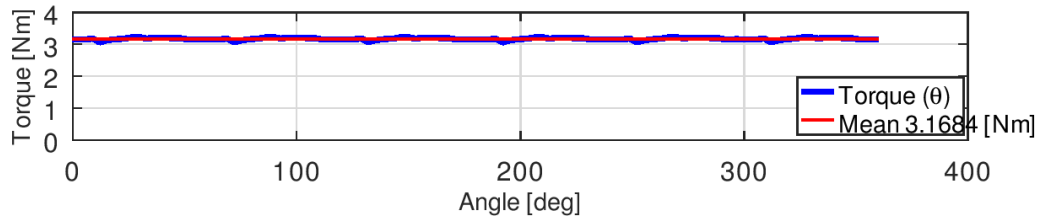
The Figure 6-9 compares the three machines performance in terms of conversion efficiency η_1 , the MechSTOR exhibits the highest conversion efficiency around 95.3% at 9000 r/min.

Related to the flywheel battery storage application, the benchmark η_2 has to be as low as possible in order to improve the self-discharge duration and meet the renewable energy time-shift economic proposition. The SyncRel machine does not exhibit core losses at no load, since none PM is present. On the other hand, SPM machines exhibit some power losses also at no load due to PMs which induce a variable magnetic flux with electrical machine rotation. The Figure 6-10 compares no load power losses of SPM_{IC} and MechSTOR: at 9000 r/min the iron core power losses are near 25 W and 1 W, respectively.

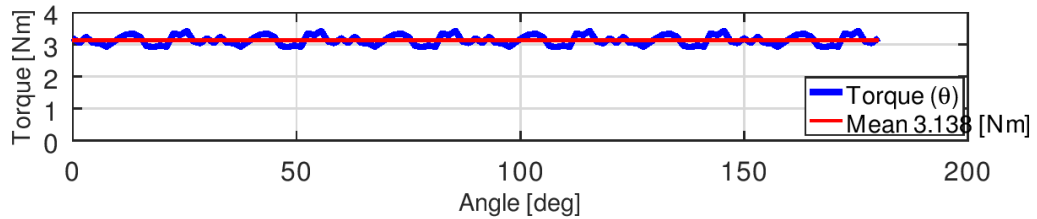
	SPM_{IC}	SyncRel		MechSTOR	Unit of Measurement
Stator Outer Diameter	150	150	External Rotor Outer Diameter	150	[mm]
			External Rotor Inner Diameter	132	
Stator Inner Diameter	90	104	Internal Rotor Outer Diameter	82	[mm]
			Internal Rotor Inner Diameter	50	
Lamination Stack Length	30	62	Lamination Stack Length	55	[mm]
Air Gap	0.8	0.3	External Air Gap	1	[mm]
			Internal Air Gap	1	
Stator Slots	9	36	Stator Slots	12	//
Pole Pairs	1	2	Pole Pairs	4	//
PM Total Volume	$2.31 \cdot 10^{-5}$	0	PM Total Volume	$2.13 \cdot 10^{-4}$	[m ³]

Table 6-3: geometrical parameters of SPM_{IC} , SyncRel and MechSTOR.

Surface Permanent-Magnet Machine



Pure Reluctance Machine



Mechstore

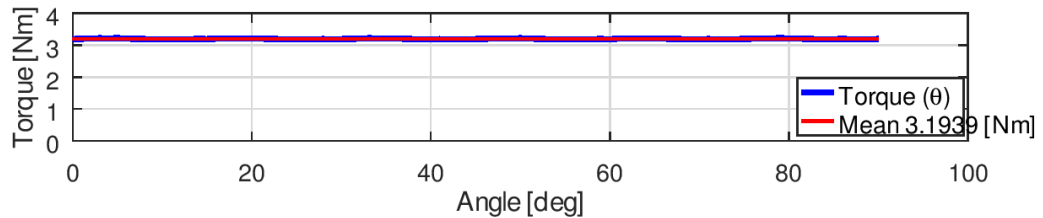


Figure 6-6: torque profiles of SPM_{IC} , SyncRel and MechSTOR.

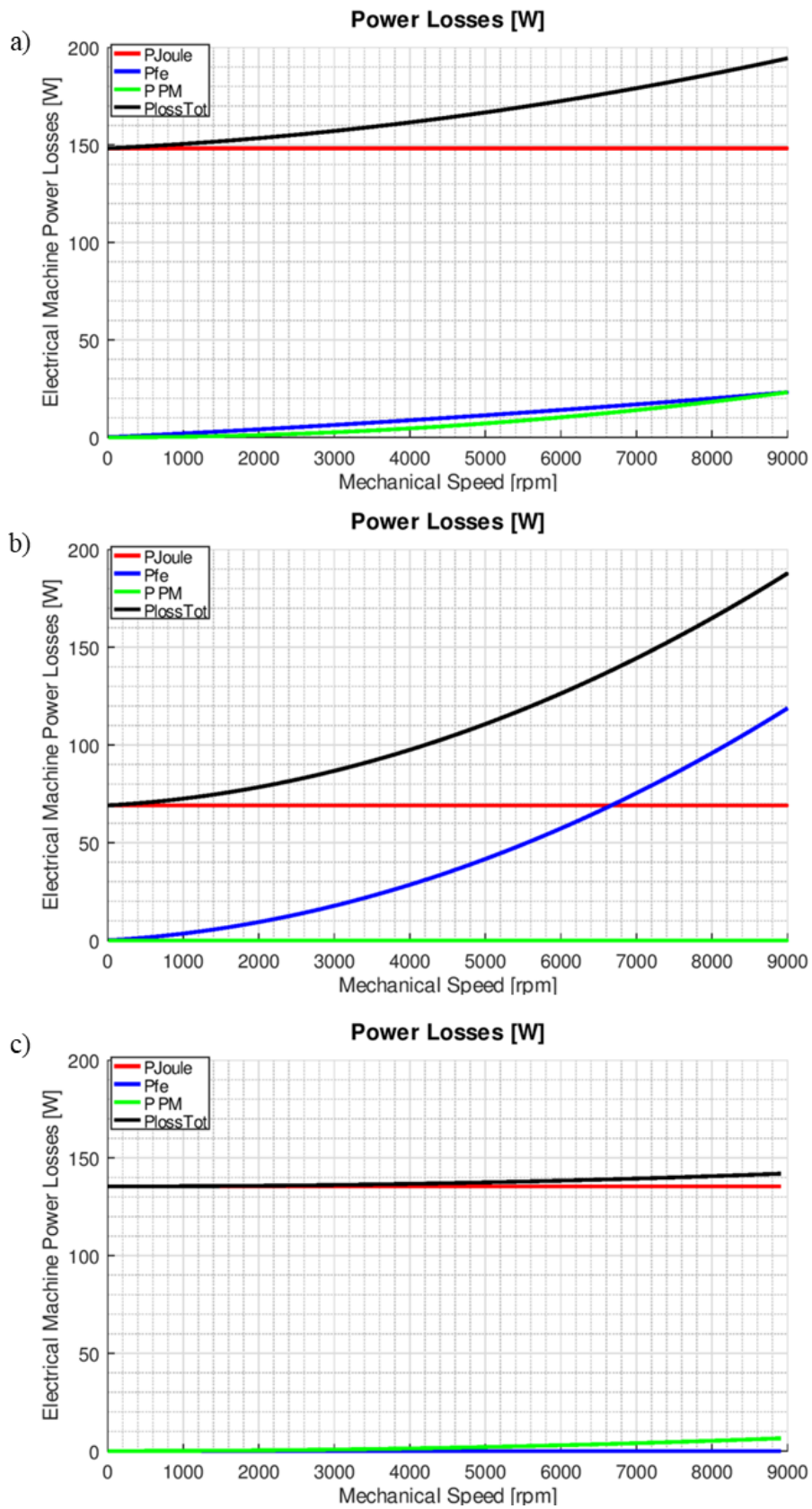


Figure 6-7: power losses as a function of mechanical speed at rated load of: a) SPM_{IC} , b) SyncRel and c) MechSTOR.

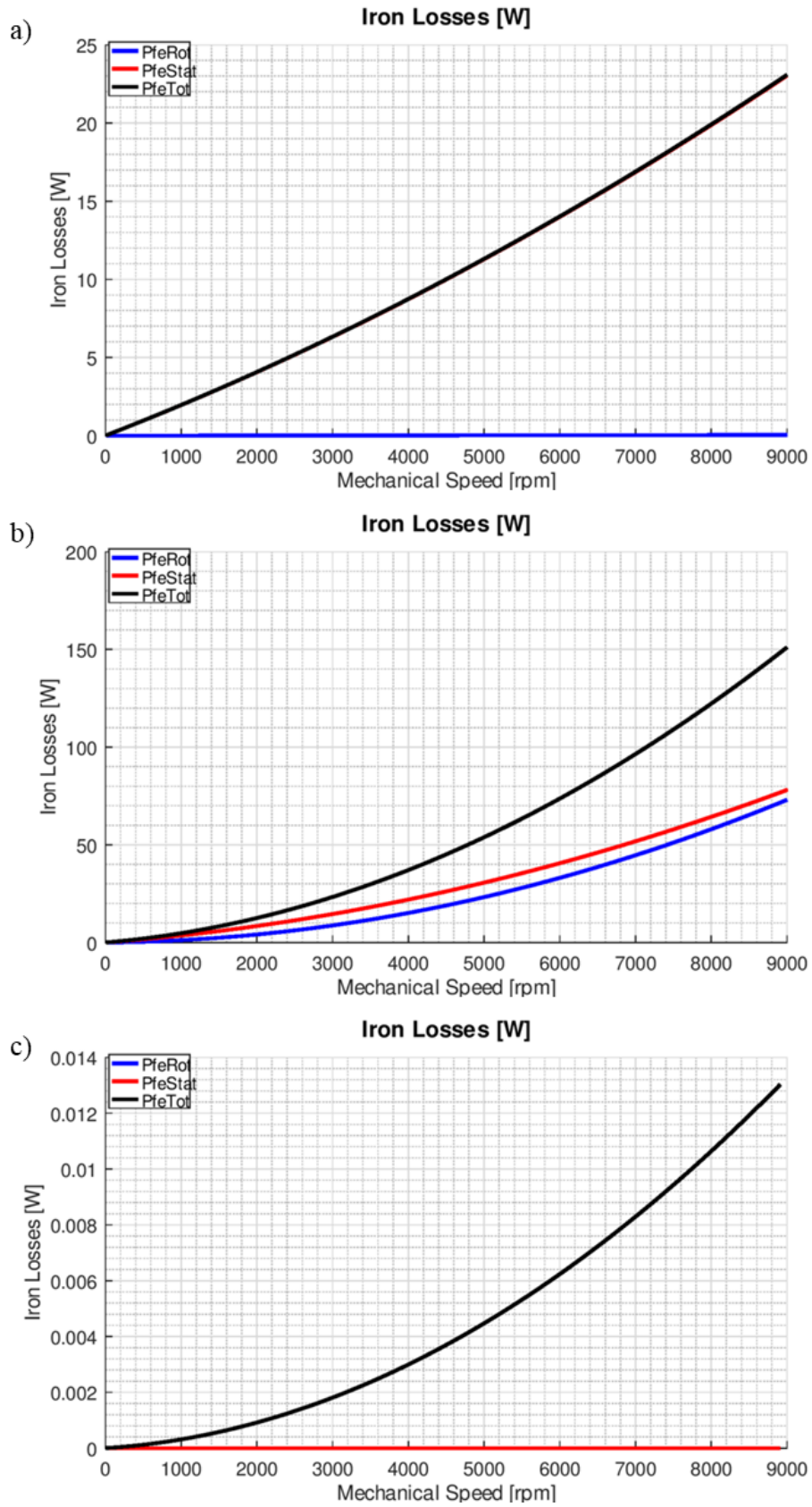


Figure 6-8: iron core losses decomposition as a function of mechanical speed of: a) SPM_{IC} , b) SyncRel and c) MechSTOR.

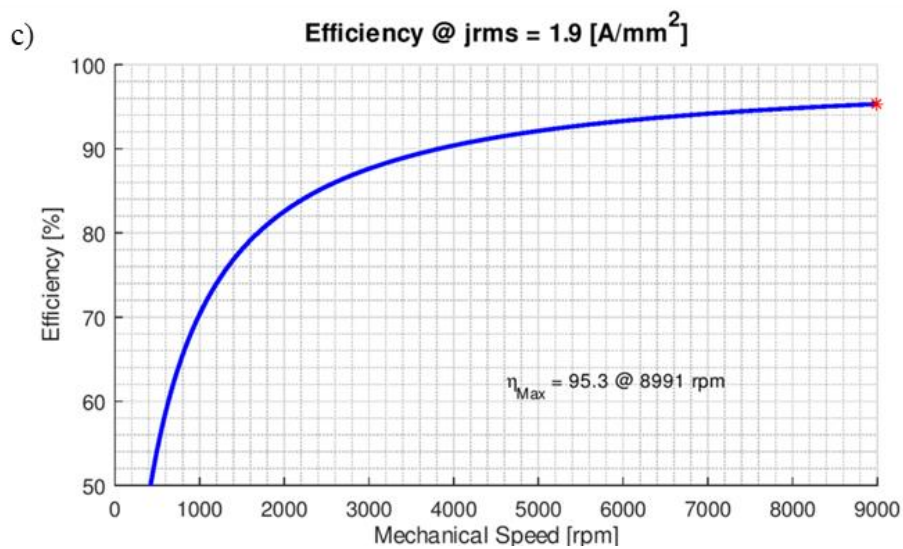
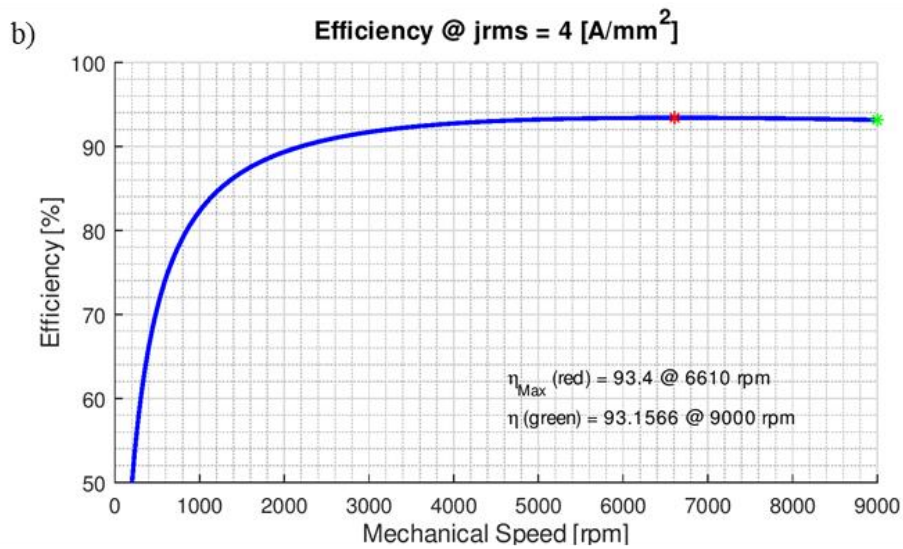
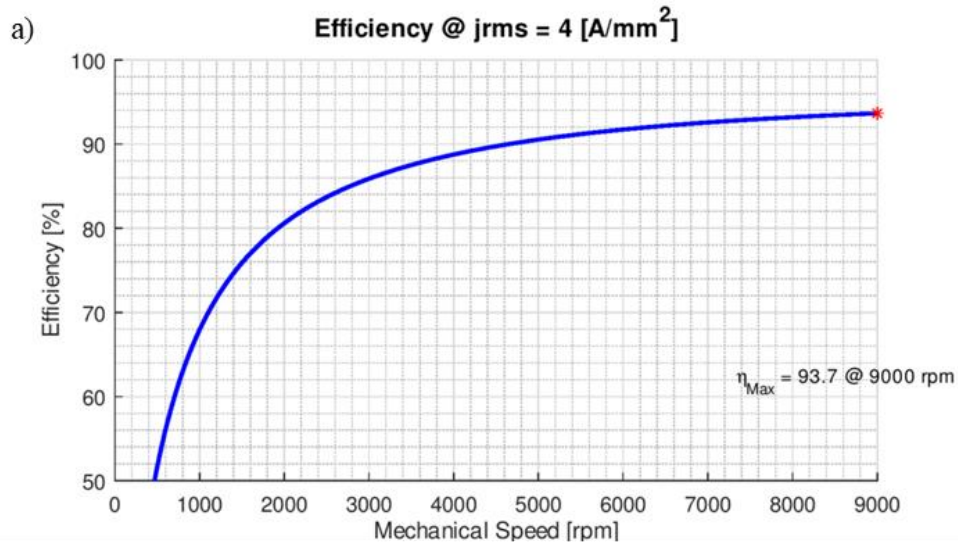


Figure 6-9: conversion efficiency as function of mechanical speed of: a) SPM_{IC} , b) SyncRel and c) MechSTOR.

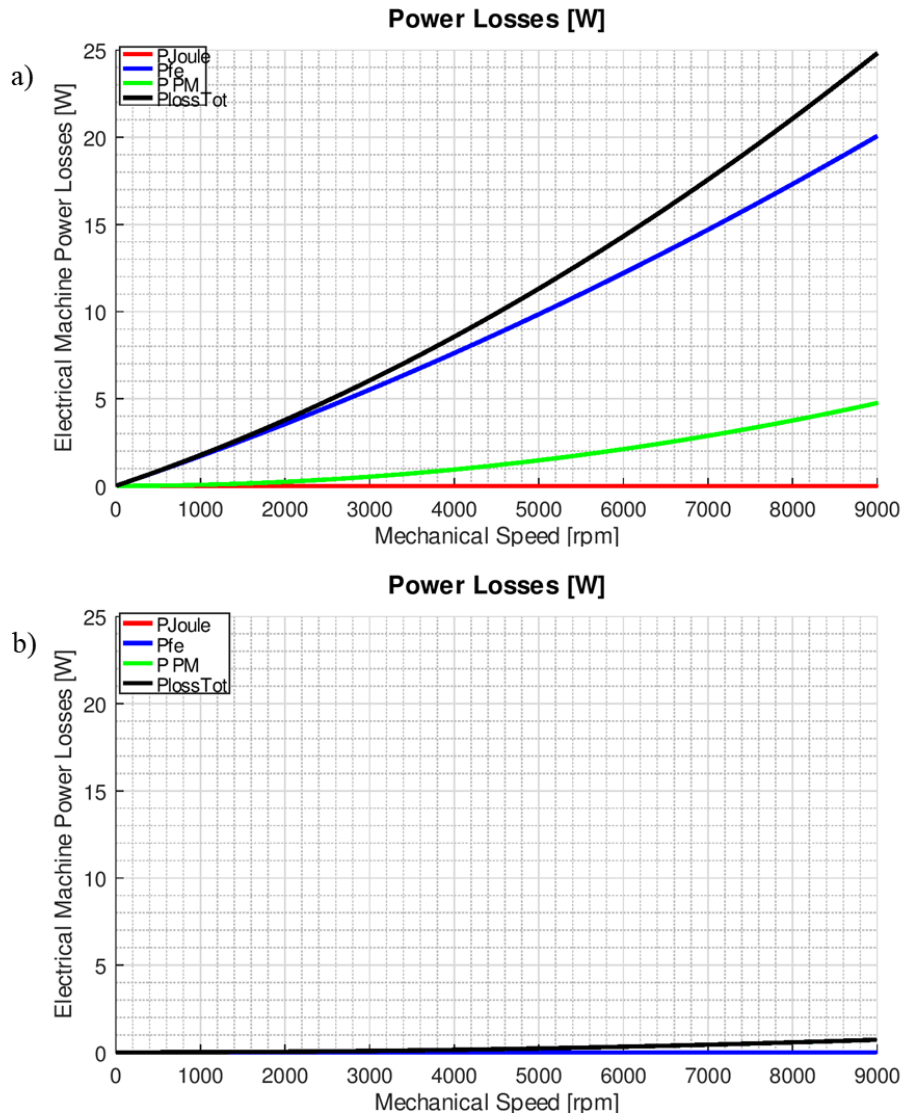


Figure 6-10: power losses as a function of mechanical speed at no load of: a) SPM_{IC} and c) MechSTOR.

According to FEA results, the proposed ironless dual-rotor SPM-SM (MechSTOR) has the best performance in terms of conversion efficiency η_1 and very low power losses during self-discharge condition. For these reasons MechSTOR represents a good electrical machine for household flywheel storage system. The SPM_{IC} has the highest power density, but due to its iron core structure has low performance in terms of η_1 and η_2 at rated condition. Finally, SyncRel machine is the most suitable machine for self-discharge condition, but has the lower conversion efficiency at rated mechanical speed.

6.4. MechSTOR Prototype

A prototype of MechSTOR has been realized in order to validate FEA simulation results. The manufactured prototype is shown in Figure 6-11.

Since MechSTOR is an ironless machine, windings conductors are not located inside stator iron core slots, thus a particular manufacturing process was needed to produce MechSTOR stator. The magnetic wires were rounded on a jig in order to achieve a desired winding configuration (see Figure 6-3c) and filling factor, then stator winding has been encapsulated with epoxy resin and reinforced with a special nylon fiber to achieve a higher structural strength and to handle the form variation during the cooling down process.

The end windings of each coil have been connected outside the rear flange, as shown Figure 6-12, in order to allow different options of connection from zero to four parallel connections. This connection solution would allow to test the machine performance also at low speeds only by changing the number of equivalent series turns without re-winding stator coils.

The PMs are made of NdFeB.

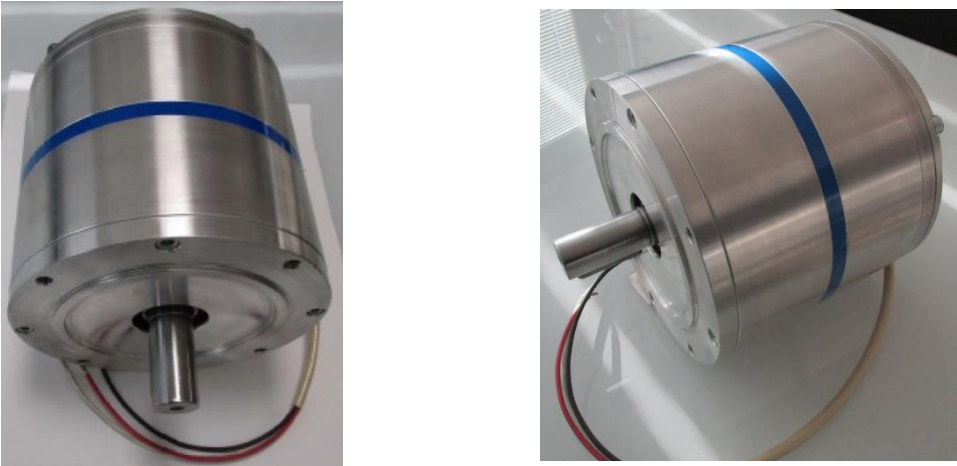


Figure 6-11: prototype of ironless dual-rotor SPM-SM (MechSTOR).

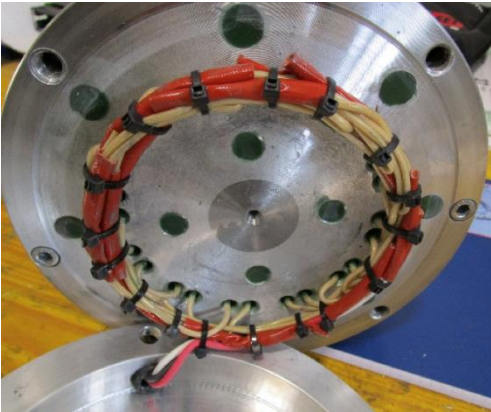


Figure 6-12: MechSTOR coil connection.

6.5. Experimental Tests of MechSTOR Prototype

The MechSTOR prototype was tested to validate the proposed electrical machine. Since neither the flywheel battery system nor the power electronics were available, it was not possible to test the electrical machine as a motor, therefore MechSTOR was tested only as a generator.

MechSTOR was mechanically connected to the shaft of a prime mover asynchronous motor, controlled by means a speed control loop. The role of the prime mover was to mimic the mechanical flywheel storage system providing the input mechanical power for the generator. The mechanical physical quantities were measured by means a high precision torque meter over torque range 0÷50 Nm.

The electric load consists of three different resistances which were connected to MechSTOR prototype: 26.5 Ω , 57 Ω and 73 Ω . The electric physical quantities were measured by means a high precision three-phase power analyzer. The Figure 6-13 shows the set up on the test bench.



Figure 6-13: test set up for MechSTOR prototype.

Tests were performed running the MechSTOR prototype over a speed range from 1000 r/min to 9000 r/min with a step of 1000 r/min between two adjacent points. The maximum speed was limited to 5000 r/min at the lowest resistive load of 26.5 Ω because of the higher currents.

The Figure 6-14 shows the conversion efficiencies η_1 performed by MechSTOR at the three different resistive loads. Experimental results show an almost constant profile of the conversion efficiency over a wide mechanical speed range. The conversion

efficiency at 9000 r/min is lower than the one estimated via FEA, in fact η_1 is 86.72 % at 57 Ω and 84.68 % at 73 Ω .

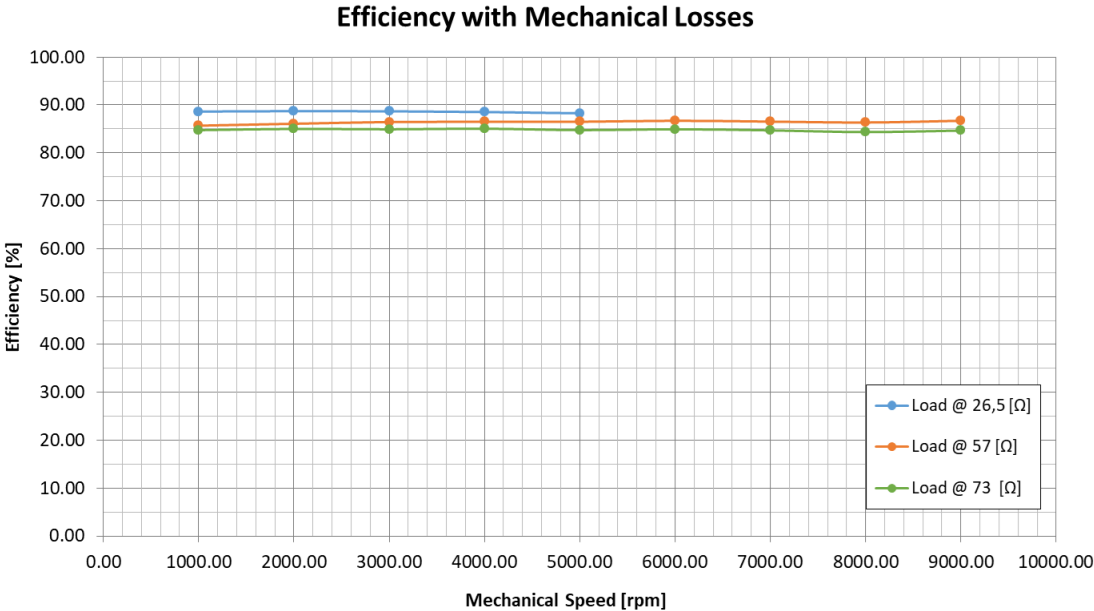


Figure 6-14: MechSTOR efficiency with mechanical losses as a function of mechanical speed at different electric loads.

In order to investigate the results deviation, a no-load test was performed running MechSTOR prototype from 1000 r/min to 9000 r/min and the mechanical quantities were measured and sampled by means the torque meter and the power analyzer. The Figure 6-15 shows the no-load test result which reveals the presence of a mechanical losses component having a quadratic relationship with the mechanical speed. The additional mechanical losses could be attributed to the low-quality bearings mounted on MechSTOR prototype.

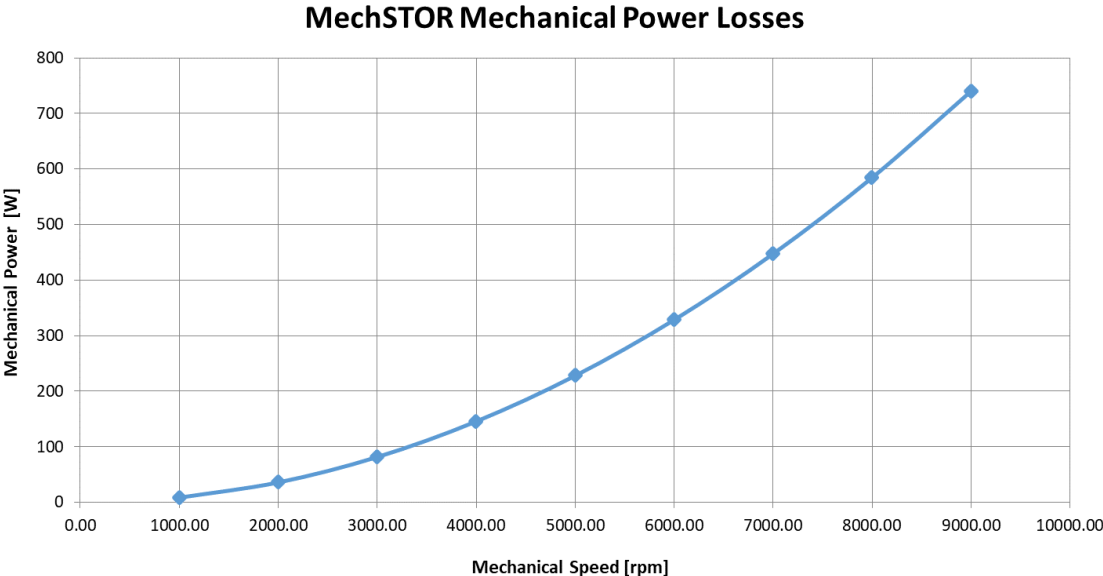


Figure 6-15: MechSTOR mechanical losses measured during no-load test.

Given the above, the mechanical losses at no-load have been subtracted to mechanical power measured during load tests in order to compare properly FEA and experimental results. The Figure 6-16 shows the MechSTOR corrected conversion efficiencies η_1 and as it can be seen conversion efficiency is higher than 90 % over the entire mechanical speed range. Considering the conversion efficiency at rated mechanical speed of 9000 rpm, η_1 is equal 97.63% at 57 Ω and 94.14 Ω at 73 Ω .

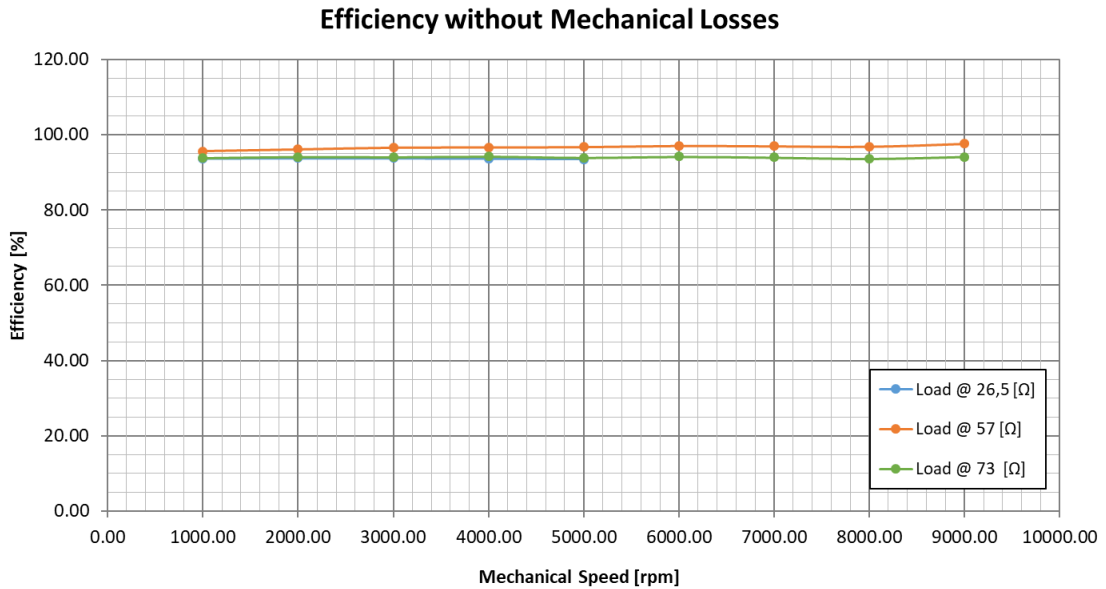


Figure 6-16: MechSTOR efficiency without mechanical losses as a function of mechanical speed at different electric loads.

6.6. Activity Results

This research activity aimed to design and optimize an electrical machine for household flywheel battery storage system of few kWh of storage capability. In fact, the flywheel storage system has to reach the objective of few hours of self-discharge duration to be economically attractive according to renewable energy time-shift proposition.

A particular SPM-SM has been designed, optimized and tested with a working prototype in order to satisfy the application requirements. The proposed SPM-SM is an ironless dual-rotor SPM-SM called MechSTOR.

The absence of the traditional iron core structure is one of the main features of this electrical machines and it allows removing iron core losses contribution. In fact, iron core losses could be very important for this specific flywheel storage application, since a mechanical rotational speed of 9000 r/min is necessary to store the required energy given the little flywheel dimensions.

The second peculiarity of MechSTOR is the dual-rotor configuration which allows reducing the reluctance of the magnetic circuit paths and thus increasing the magnetic load for the torque production.

An extensive FEA has been carried out on three topologies of electrical machine: traditional iron core SPM-SM and pure SyncRel machine and the proposed ironless dual-rotor SPM-SM. The performance at rated load and no-load conditions have been analyzed in order to compare machines performance in terms of conversion efficiency η_1 and in particular of self-discharge duration at no-load operation, denoted as η_2 . The self-discharge duration is the most important benchmark in order to guarantee the few hours of energy storage duration when the grid is disconnected. FEA results show that MechSTOR has the best performance in terms of conversion efficiency during motor/generator operation and very low power losses at no load operation.

The MechSTOR was prototyped and tested on a laboratory test bench as generator, since the set up for motor operation is more complicated and there were not the flywheel and inverter technology. The experimental results validate the performance of FEA analysis, but it was found out the importance of good-quality bearing in order to reduce mechanical losses components which could affect self-discharge duration.

7. Design Optimization Issues for Pure Synchronous Reluctance Machines

This chapter deals with design optimization of pure synchronous reluctance (SyncRel) machines. Nowadays, they represent an interesting alternative to IMs, PM-SMs and switched reluctance machines both in terms of machine performance and fault-tolerant capability.

SyncRel machines are appreciated for their torque density, high flux-weakening capability, high saliency ratio yielding them suitable for sensorless control applications [41] and the absence of rare-earth magnets [42]. On the other hand, SyncRel machines exhibit a high cogging torque and torque ripple due to the reduced air gap thickness g which causes a strong interaction between high harmonic orders of the stator and rotor MMFs.

The torque ripple is an unavoidable drawback, but the state-of-the-art has been proposed many studies on rotor design methods to reduce the impact of cogging torque and torque ripple of SyncRel machine [43]–[50]. In fact, a very careful rotor design allows limiting cogging torque and torque ripple while obtaining an adequate torque density.

The paragraph §7.1 recalls some design principal of SyncRel machine, particularly focused on the rotor, while for the stator design could be designed following the analytical method proposed in chapter §3.

Given the above with the aim to further reduce the pulsating torque of SyncRel machines, the paragraph §7.2 describes the contribution of this work in the rotor design of SyncRel machines and also of permanent-magnet assisted synchronous reluctance (PMSyncRel). The research activity proposes an analytical design method consisting of an asymmetrical layout of rotor flux-barriers. The flux-barriers shifting allows to set the undesired MMF harmonic orders in phase opposition and the result is the cancellation of the pulsating torque related to those harmonic components. The method effectiveness has been validated via FEA for different SyncRel and PMSyncRel slot-pole combinations.

The SyncRel design methods could also be used to improve the fault-tolerant capability of the machines [46], [51]. The absence of PMs entails an intrinsic fault-tolerant reliability because their presence could cause short-circuit currents and breaking torque that could arise in case of fault [52], [53]. Also switched reluctance machines have an intrinsic fault-tolerant reliability due to the low magnetic coupling of motor phases and the independence of their power converters phases [54][55], they have the high torque ripple and the nonlinear inductance profiles [56].

Since the literature has very few researches dealing with the fault-tolerant design and analysis of SyncRel machine, the paragraph §7.3 show the contribution of this work proposing a design and optimization method for pure SyncRel machines with a dual three-phase winding for fault-tolerant applications. Several design solutions, in terms of winding arrangements and machine geometry have been investigated in order to achieve a good reliability both in healthy and faulty operation conditions. The fault-tolerant

reliability is evaluated in terms of the following benchmarks: torque quality, unbalanced magnetic force and magnetic coupling between the two three-phase winding when one winding is healthy and the other in faulty condition.

7.1. Principles of Pure Reluctance Machines

The two-axis rotational reference of pure SyncRel machines has a different convention [42], [57]-[58], as mentioned in chapter §2. The axis convention is generally adopted for the design and the control of SyncRel machines and it corresponds to an axis rotation of 90° of the PM synchronous $d - q$ reference (see Figure 7-1). According to this, the role of the synchronous inductances $L_{sd} - L_{sq}$ is reversed; thus, the direct axis corresponds to the rotor magnetic path with the lowest reluctance per each pole as shown in Figure 7-2. Hereafter, the two-axis rotational frame of SyncRel machine will be denoting with capital letters $D - Q$ in order to distinguish it from that of PM-SM.

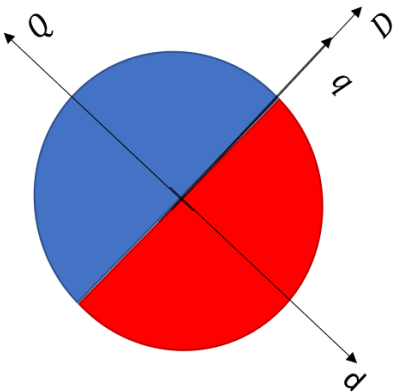


Figure 7-1: $D - Q$ two-axis rotational frame for SyncRel machine.

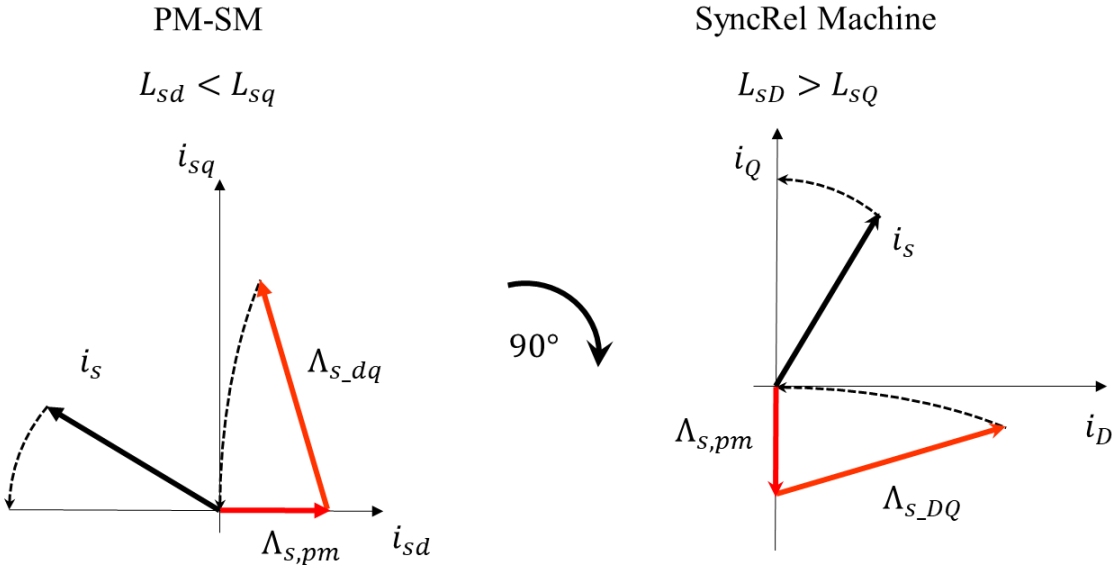


Figure 7-2: current and magnetic flux vectors convention on $d - q$ (left side) for PM-SMs and $D - Q$ current plane (right side) for SyncRel and PMSyncRel machines.

The 90° rotation modifies the expression of the saliency ratio ξ in Eq. 7-1 and of mechanical torque expression in Eq. 7-2.

$$\xi = \frac{L_{sD}}{L_{sQ}} \quad \text{Eq. 7-1}$$

$$T_{mec} = \frac{3}{2}p[\Lambda_{s,pm}i_{sD} + (L_{sD} - L_{sQ})i_{sD}i_{sQ}] \quad \text{Eq. 7-2}$$

The term of the output torque related to PM is not present in the pure SyncRel machine, while there is in PMSyncRel machines. According to this, the mechanical torque of pure SyncRel machines depends only on the reluctance term as in Eq. 7-3.

$$T_{mec} = \frac{3}{2}p[(L_{sD} - L_{sQ})i_{sD}i_{sQ}] \quad \text{Eq. 7-3}$$

7.1.1. Torque and Power Factor

Ideally the SyncRel machine should have an infinite D-axis permeance, while the Q-axis should have an infinite reluctance, as shown in Figure 7-3a). This condition would lead to a torque angle of 90° and a unitary power factor. Actually, SyncRel machine has non-zero magnetization current (i_{sD}) and a non-zero Q-axis magnetic flux (Λ_{sQ}) as shown in Figure 7-3b). The non-zero Q-axis flux would be compensated by the PM flux in PM-SM.

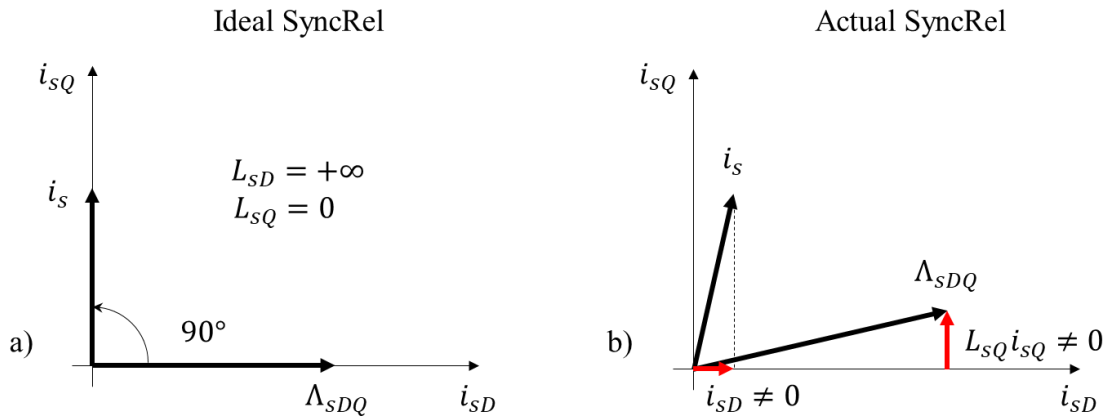


Figure 7-3: ideal and actual SyncRel machine.

The D- and Q-axis synchronous inductances can be split in two terms: the leakage term and magnetizing one as in Eq. 7-23.

$$\begin{cases} L_{sD} = L_{s\sigma} + L_{s,mD} \\ L_{sQ} = L_{s\sigma} + L_{s,mQ} \end{cases} \quad \text{Eq. 7-4}$$

The leakage terms are generally omitted in the mechanical torque equation, since leakage fluxes do not contribute to the torque production. According to this the Eq. 7-2 can be written in term of the magnetizing components.

$$T_{mec} = \frac{3}{2}p[(L_{s,mD} - L_{s,mQ})i_{sD}i_{sQ}] \quad \text{Eq. 7-5}$$

On the other hand, the leakage inductance terms affect the SyncRel power factor as it can be seen in Eq. 7-7 which expresses the power factor as a function of synchronous inductance.

$$\cos \varphi \leq \frac{L_{sD} - L_{sQ}}{L_{sD} + L_{sQ}} \quad \text{Eq. 7-6}$$

$$\cos \varphi \leq \frac{L_{s,mD} - L_{s,mQ}}{L_{s,mD} + L_{s,mQ} + 2L_{s\sigma}} \quad \text{Eq. 7-7}$$

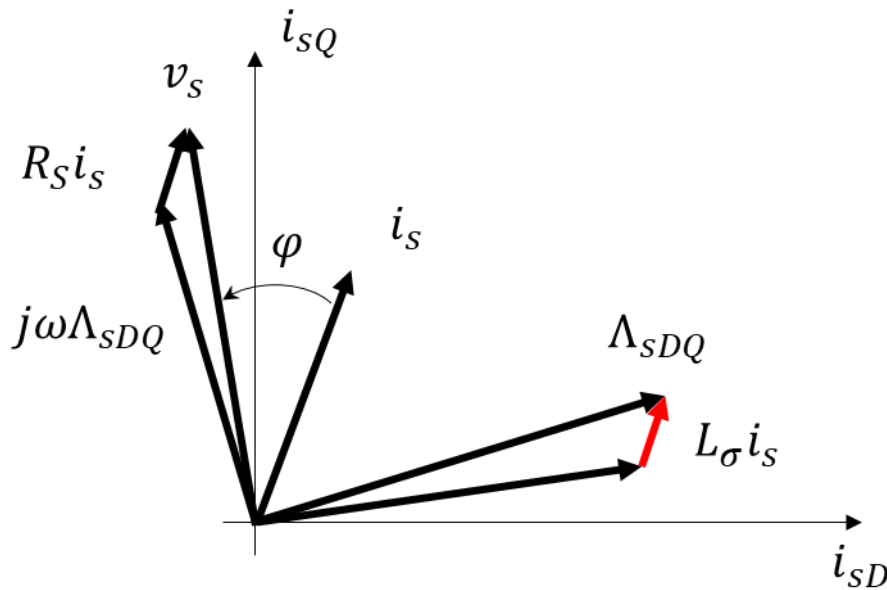


Figure 7-4: phasor diagram of pure SyncRel machine.

A useful parameter to study the design of pure SyncRel machine is the anisotropy factor k_{DQ} defined as follows:

$$k_{DQ} = 1 - \frac{L_{mQ}}{L_{mD}} \quad \text{Eq. 7-8}$$

The ideal SyncRel machine would have an anisotropy factor equal to one. A proper design of the SyncRel rotor could lead to the maximization of the anisotropy factor.

Another important factor to take into account during the design of a pure SyncRel machine is the magnetizing flux λ_{mD} which is expressed as follows:

$$\lambda_{s,mD} = L_{s,mD} i_{sD} \quad \text{Eq. 7-9}$$

The output torque can be expressed in terms of the anisotropy factor k_{DQ} and magnetizing flux $\lambda_{s,mD}$ as shown in Eq. 7-11.

$$T_{mec} = \frac{3}{2} p \left(1 - \frac{L_{s,mQ}}{L_{s,mD}}\right) L_{s,mD} i_{sD} i_{sQ} \quad \text{Eq. 7-10}$$

$$T_{mec} = \frac{3}{2} p k_{DQ} \lambda_{s,mD} i_{sQ} \quad \text{Eq. 7-11}$$

The output torque is maximized when both the anisotropy factor k_{DQ} and magnetizing flux are maximized $\lambda_{s,mD}$. On the other hand, the D-axis current i_{sD} is limited due to thermal constraint; therefore in order to increase the magnetizing flux $\lambda_{s,mD}$ is necessary to maximize the magnetizing D-axis inductance.

The pure SyncRel power factor is related to synchronous inductances and the current angle, respect with the D-current axis, by the Eq. 7-12.

$$\cos\varphi = \frac{\frac{L_{sD}}{L_{sQ}} - 1}{\sqrt{\left(\frac{L_{sD}}{L_{sQ}}\right)^2 \cdot (\sin\gamma)^{-2} + (\cos\gamma)^{-2}}} \quad \text{Eq. 7-12}$$

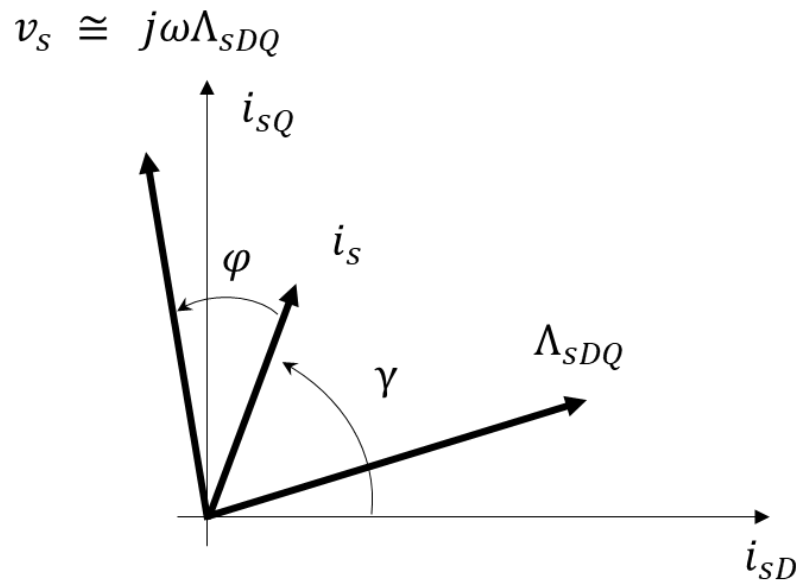


Figure 7-5: phasor representation of voltage, current and linkage flux on D-Q reference frame.

7.1.2. Rotor Basic Design

The Figure 7-6 shows the geometry of a single rotor pole; the main rotor geometry characteristics are the flux-barriers, the flux-guides and the rotor slots.

The rotor flux-barriers are the air cavities in the rotor that sometimes could be partially or totally filled with PMs materials such as ferrite or rare-earth. The number of flux-barriers per pole is represented with n_{lay} (i.e. number of layers) and they affect the Q-axis insulation. On the other hand, the flux guides are alternated to flux-barriers and affect the D-axis conduction.

The rotor slots are the flux-barriers ends and their angular positions along the rotor air are the key parameters to minimize the torque ripple and the additional core losses due to high order harmonics. Generally, rotor slots are denoted with the symbol N_r .

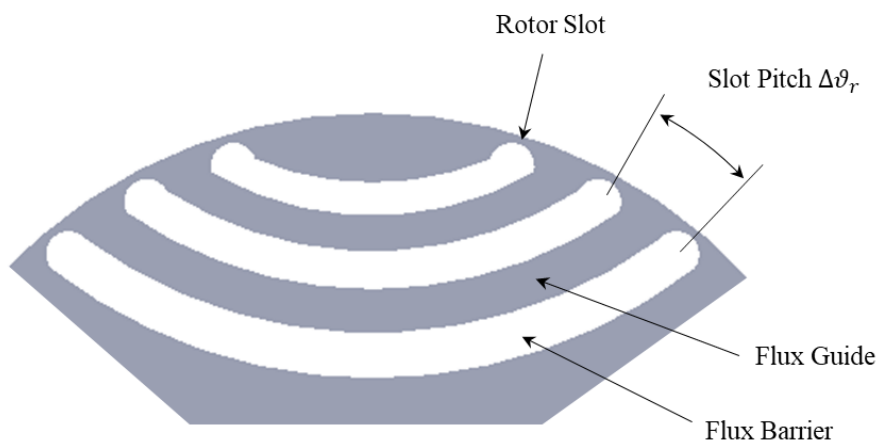


Figure 7-6: one rotor pole geometry.

The sum of the flux-barrier radial thickness is denoted as the total insulation l_a , while the sum of flux-guides radial thickness is denoted as total iron l_{Fe} (see Figure 7-7).

$$l_a = \sum_{k=1}^{n_{lay}} l_k \quad \text{Eq. 7-13}$$

$$l_{Fe} = R_g - l_a - R_{shaft} \quad \text{Eq. 7-14}$$

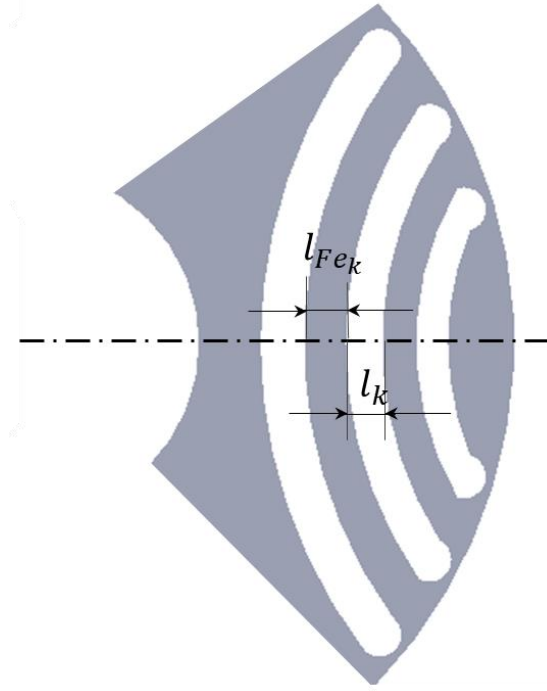


Figure 7-7: identification of flux-barrier and flux-guide thicknesses.

7.1.3. D-axis Magnetizing Inductance $L_{s,mD}$

The D-axis magnetizing inductance $L_{s,mD}$ can be expressed as follows:

$$L_{s,mD} = \frac{\pi}{2} \cdot \mu_0 \cdot \left(\frac{N_{ph}}{p} \right)^2 \cdot \frac{R_g \cdot L_{stk}}{k_C \cdot g} \quad \text{Eq. 7-15}$$

where k_C is the Carter's coefficient, N_{ph} is the number of turns in series per phase, p the pole pair number, R_g the rotor outer radius and L_{stk} the lamination stack length.

There are some basic design guidelines for the rotor design in order to avoid unwanted reductions of D-axis magnetizing inductance. Generally, the following design rules should be taken into account:

- The air gap should be smaller than $\frac{1}{100}$ of the pole pitch;
- The flux-guides should avoid a premature saturation. The rule-of-thumb is that the rotor flux-guides flux density peak value $\hat{B}_{flux-Fe}$ should be less than or equal to the stator yoke flux density peak value \hat{B}_y .

The Figure 7-8a) show an example of a good design of rotor flux-guides thickness (i.e. D-axis inductance), in fact the flux-guides magnetic flux density peak value is less or equal to the stator yoke magnetic flux density peak value. On the other hand, Figure 7-8b) shows a wrong design, since there is a premature saturation of flux-guides parts (the rotor iron is more loaded than stator iron yoke).

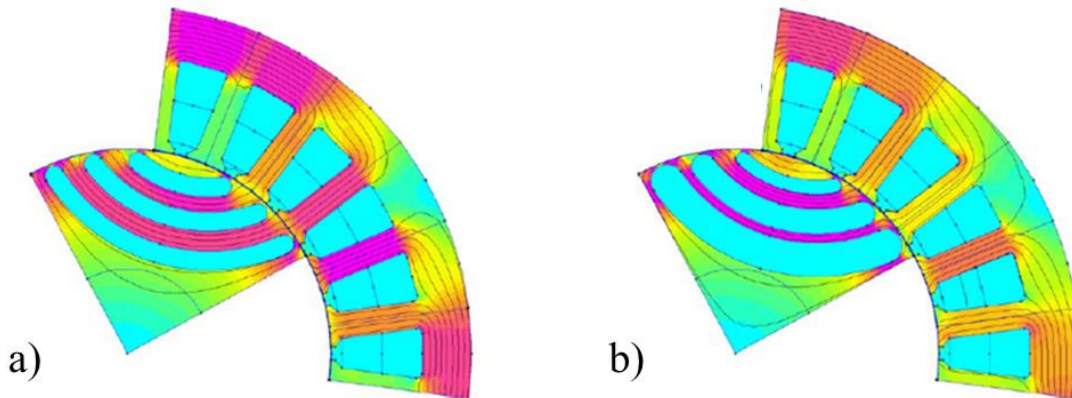


Figure 7-8: on the left-side a good design of flux-guides thickness (a), while on the right-side a wrong design of flux-guides thickness (b).

7.1.4. Q-axis Magnetizing Inductance $L_{s,mQ}$

The Q-axis magnetizing inductance can be split into two terms: the circulating term $L_{s,cQ}$ and the flow-through one $L_{s,fQ}$.

$$L_{s,mQ} = L_{s,cQ} + L_{s,fQ} \quad \text{Eq. 7-16}$$

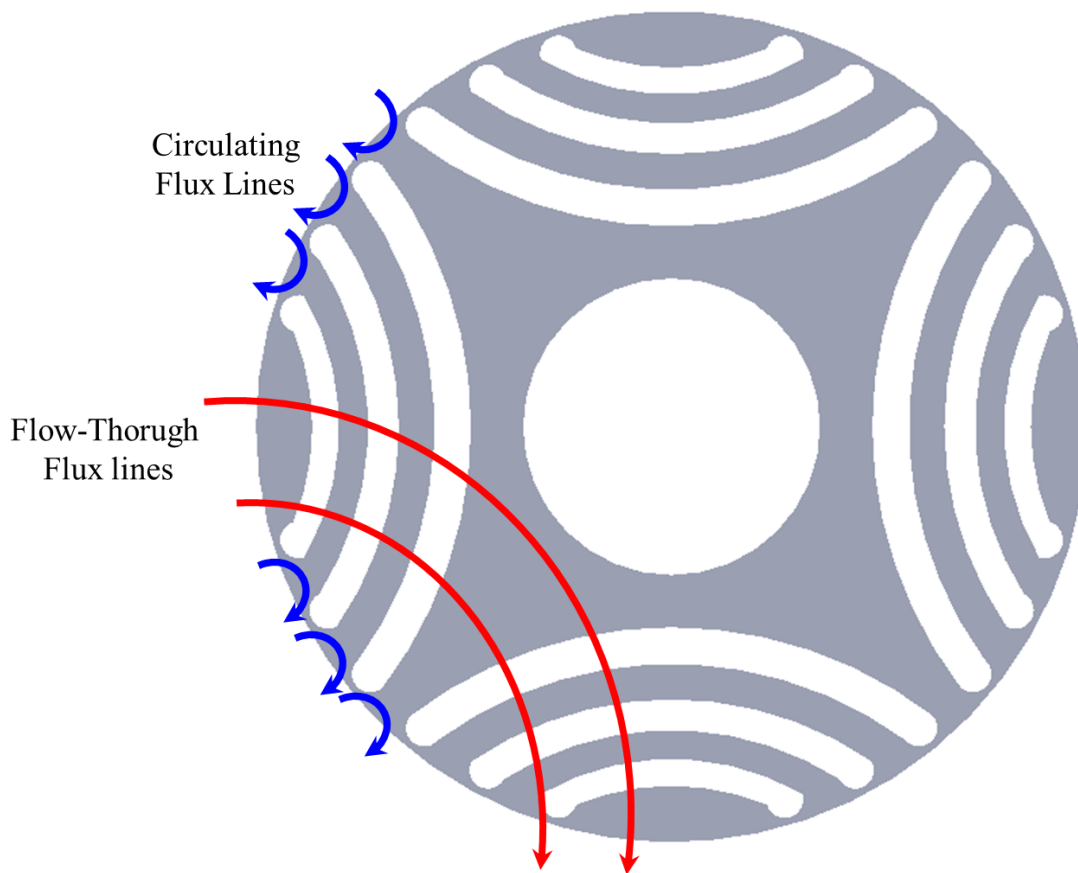


Figure 7-9: Q-axis inductance components: circulating term (blue arrows) and flow-through term (red arrows).

The Figure 7-10 shows a magnet circuit model of rotor Q-axis which is useful to study the Q-axis linkage flux $\Lambda_{s,mQ}$ and therefore the magnetizing Q-axis inductance $L_{s,mQ}$. The Q-axis magnetic circuit (see Figure 7-10) is formed by:

- MMF generators f_k which represents the Q-axis components of stator MMF;
- A net of permeances divided in flux-barriers p_b and air gap flux tubes p_g .

The electric steel is assumed as a magnetic short-circuit, thus there is not a drop of MMF, while all permeances components are assumed with the same value because of the regular rotor pitch.

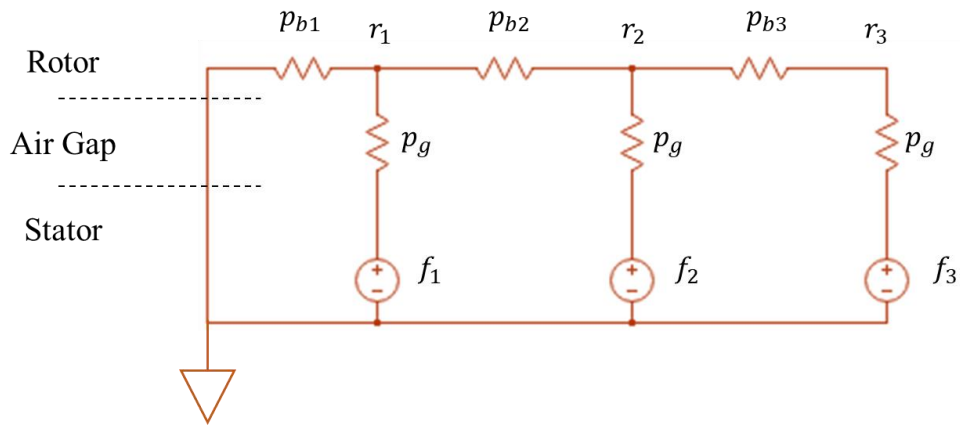


Figure 7-10: magnetic circuit model of a half magnetic pole on the Q-axis.

7.1.4.1. Q-axis MMF Staircase

Ideally, the Q-axis MMF is a sinusoidal wave with an amplitude equal to Eq. 7-17.

$$\frac{Ni_{sQ}}{\sqrt{3}p} [Am] \quad \text{Eq. 7-17}$$

The MMF generators of the magnetic circuit model in Figure 7-10 are the averages values of the sinusoidal wave over the angular span of each rotor flux-guide where θ_{r1} , θ_{r2} , etc. are the positions of the rotor slots. The more the layers, the more the steps of the staircase. The Figure 7-11 shows the staircase of an half pole of the rotor of Figure 7-9 correspondent to the magnetic circuit of Figure 7-10.

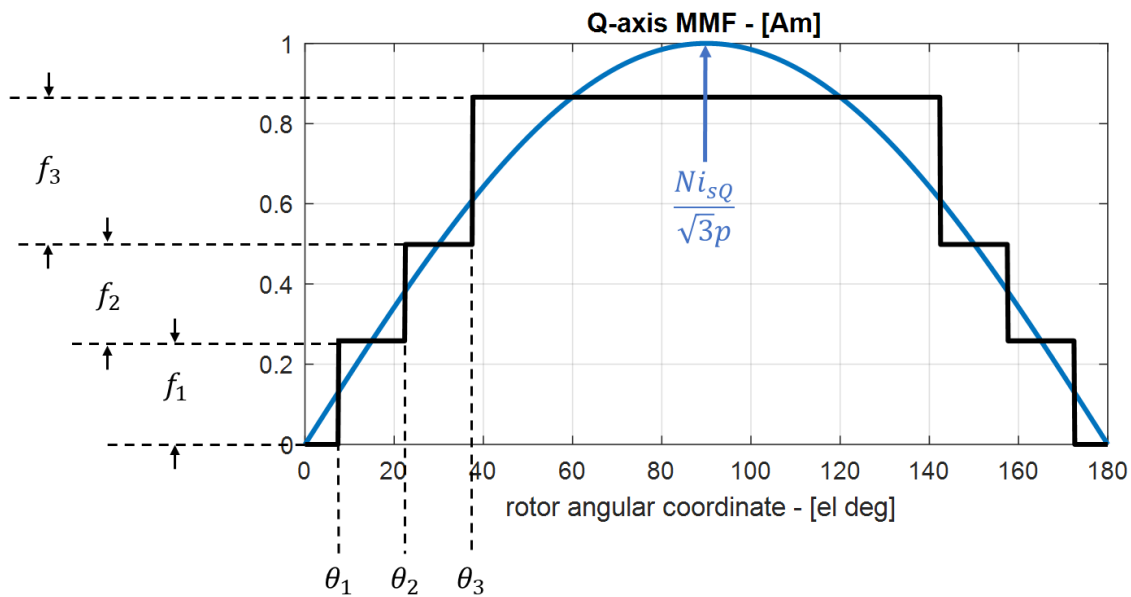


Figure 7-11: Q-axis MMF staircase of a rotor pole.

The sinusoidal Q-axis MMF can be split in the two components related to the two Q-axis inductance terms of Eq. 7-16. The two MMF component are:

- The staircase component that supplies the flow-through flux represented by the MMF generators of Figure 7-10;
- The residual MMF which is the difference between the sinusoidal waveform and the staircase. The residual MMF generates the circulating flux component.

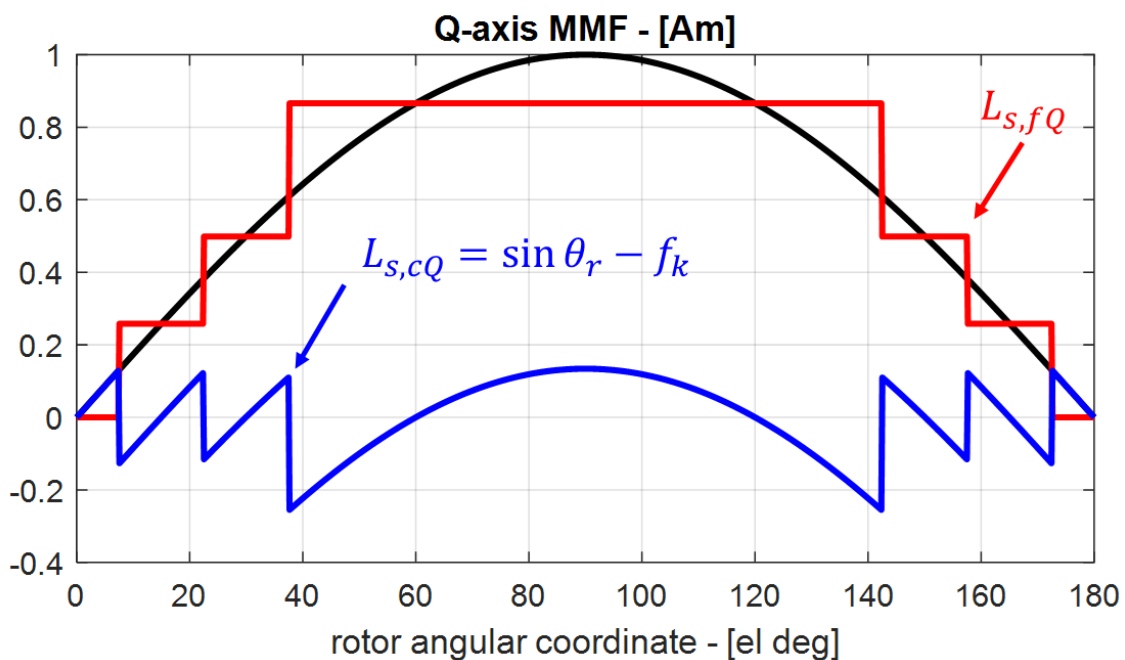


Figure 7-12: stator Q-axis MMF with flow-through component (red solid line) and circulating flux component (blue solid line).

7.1.4.2. Circulating Flux Component $L_{s,cQ}$

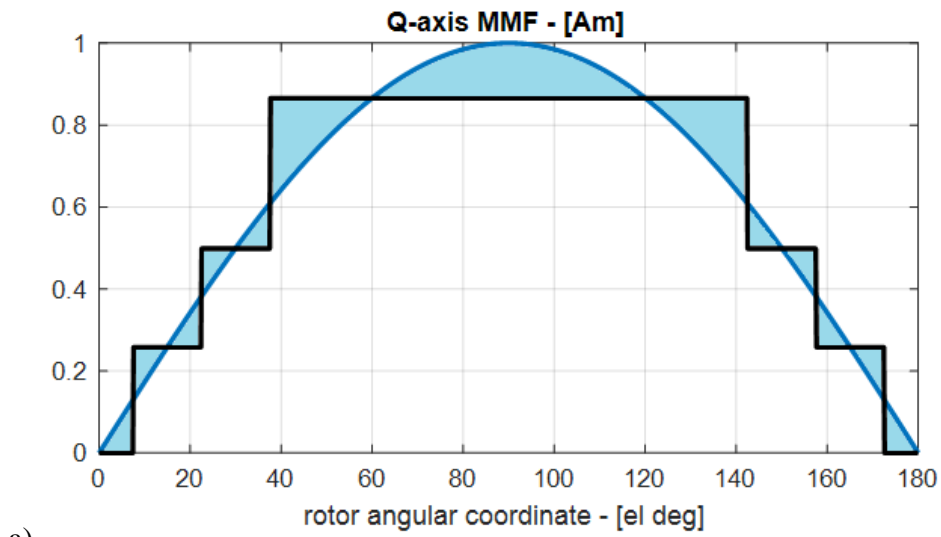
The circulating flux component is related to the circulating term $L_{s,cQ}$ of the Q-axis magnetizing inductance. Under the assumption of sinusoidal stator MMF the circulating term of Q-axis inductance can be evaluated as in Eq. 7-18 [51], [59], [60].

$$\frac{L_{s,cQ}}{L_{s,mD}} = 1 - \frac{4}{\pi} \cdot \sum_{k=1}^{n_{lay}} f_k^2 \cdot \Delta\theta_r \quad \text{Eq. 7-18}$$

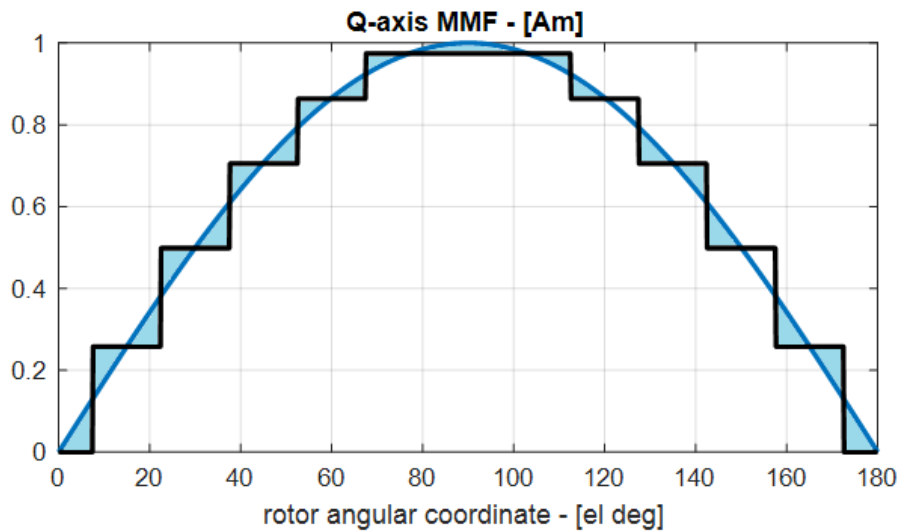
If the machine has a regular pitch, there is a simplified formulation of Eq. 7-18.

$$\frac{L_{s,cQ}}{L_{s,mD}} = \frac{\pi}{12} \cdot \frac{1}{N_r^2} \propto \frac{1}{n_{lay}^2} \quad \text{Eq. 7-19}$$

As it can be noticed by Eq. 7-19, the $L_{s,cQ}$ decreases quickly as the number of layers n_{lay} increases. On the other hand, a rotor with more layers produces a staircase that better mimic the ideal sinusoidal MMF waveform as shown in Figure 7-13. Therefore, a rotor with a higher number of layers has a reduced MMF harmonic content.



a)



b)

Figure 7-13: circulating-flux MMF component for different numbers of layers: a) 3 layers and b) 5 layers.

Authors of [51], [59], [60] demonstrate that a number of layers equal to three or higher allows to improve the MMF content as also shown in Eq. 7-14.

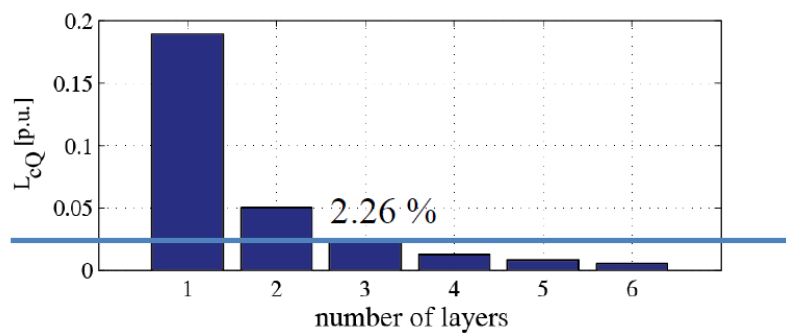


Figure 7-14: Q-axis circulating inductance component as a function of number of layers. [61]

7.1.4.3. Flow-Through Component $L_{s,fQ}$

The flow-through component of Q-axis inductance is computed by solving the magnetic circuit model of Figure 7-10 where the key parameters are the air gap thickness g and the rotor flux-barriers dimensions l_k and s_k identified in Figure 7-15a).

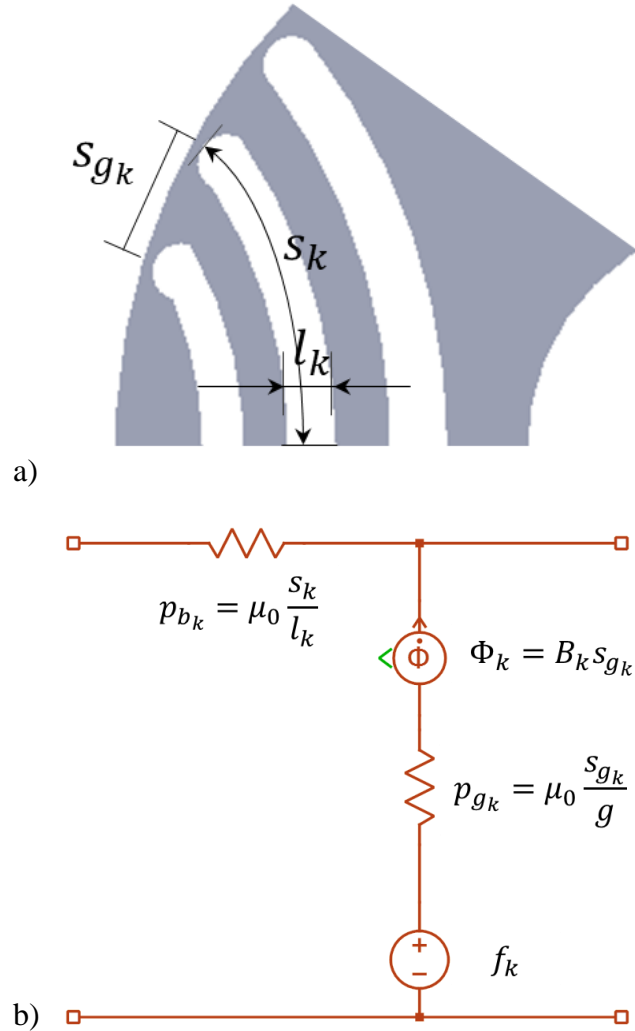


Figure 7-15: identification of main flux-barrier parameter on a half rotor pole and the equivalent magnetic model.

The solution of the magnetic model of Figure 7-15b) leads to the Eq. 7-20 [51], [59], [60].

$$\frac{L_{s,fQ}}{L_{s,mD}} = \frac{4}{\pi} \cdot \sum_{k=1}^{n_{lay}} p_{bk} \cdot (\Delta f_k)^2 \quad \text{Eq. 7-20}$$

where Δf is the width of k^{th} stair of the staircase MMF as shown in Figure 7-16.

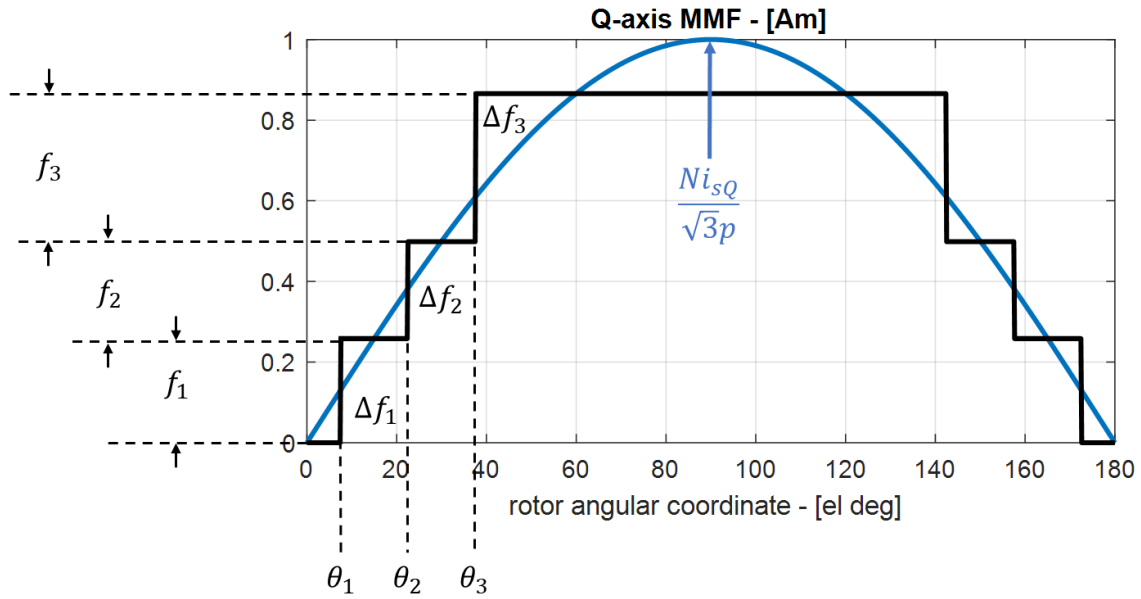


Figure 7-16: definition of Δf_k in the staircase Q-MMF.

The flow-through component is dominated by the total insulation l_a which is the sum of all layers thickness; it is worth noticing that the number of layers has nothing to do with the flow-through Q-inductance component.

$$\frac{L_{s,fQ}}{L_{s,mD}} \propto \frac{pg}{l_a} \quad \text{Eq. 7-21}$$

If the insulation is too higher, the $L_{s,fQ}$ decreases as well as the $L_{s,mD}$ due to a premature flux-guides saturation. As aforementioned said, the peak magnetic flux density of rotor flux-guides should be less than equal to the peak magnetic flux value of the stator yoke (Figure 7-8).

7.1.5. Harmonic Losses

Another stray effect of pure SyncRel machine is the harmonic losses due to stator and rotor slotting. Moreover, core harmonic losses are an addition speed dependent loss term that sums up with the fundamental core losses.

The stator and rotor slots combination that minimizes harmonic losses is the one that maximizes the torque ripple and is expressed by Eq. 7-22. This behavior is clearly shown in Figure 7-17.

$$N_s = N_r$$

Eq. 7-22

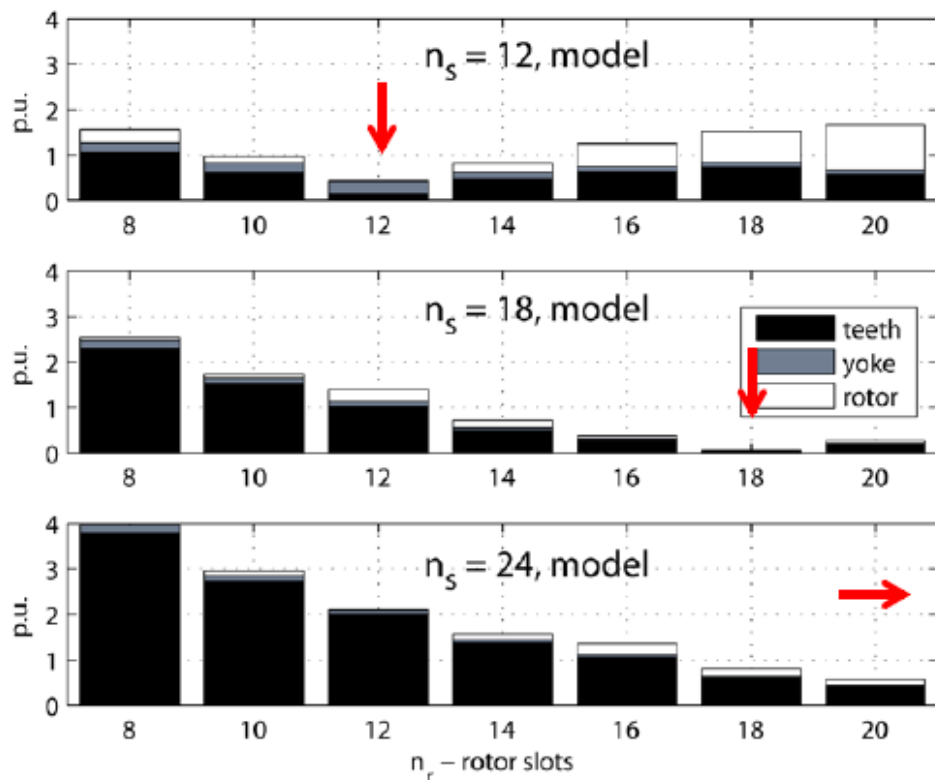


Figure 7-17: stator (black and grey areas) and rotor (white) harmonic core losses as a function of rotor slots N_r , for different stator slots $N_s = 12, 18$ and 24 . [69]

The total machine losses increase when the distance between N_s and N_r increases. In fact, a large difference between stator and rotor slots could lead to abnormal high-speed losses.

Given the above, in order to minimize the impact of harmonic losses the number of rotor and stator slots should be as close as possible. Another important consideration is that between stator and rotor slots, the part having the lower number of slots (i.e. larger pitch) is the one which suffers of more harmonic losses.

- If $N_s < N_r$ harmonic losses are concentrated on the stator;
- If $N_s > N_r$ harmonic losses are concentrated on the rotor.

7.2. Analytical Design Method for Reducing for Pulsating Torque in Pure and Assisted SyncRel Machines

As mentioned at the beginning of this chapter one of the main drawbacks of SyncRel machine is the high cogging torque and torque ripple. These unwanted phenomena could be mitigated by means a proper rotor design. According to this, the following paragraph shows the contribution of this research activity to further reduce pulsating torque of SyncRel machine proposing an analytical rotor design method with an asymmetrical layout of rotor flux-barriers.

The reference machines are three different slot-pole combinations: 36-4, 36-6 and 48-8 shown in Figure 7-18. Table 7-1 reports the main characteristics of the three reference machines and they have been studied both as pure SyncRel and PMSyncRel machines filling the rotor flux-barriers with ferrite PMs. The PMSyncRel machine will be also denoted as Flux Assisted Synchronous Reluctance (FASyR) in the following figures,

The rotor flux-barrier were initially designed following the analytical rules from [44], [62]-[64] and no iterative optimization or genetic algorithms were employed in order to prove the effectiveness of the proposed method. Then the design has been refined applying the proposed rotor flux-barriers shifting method both for SyncRel and PMSyncRel machines.

The rotor flux-barriers, hence PMs ferrite in PMSyncRel, are designed with constant thickness in order to avoid preferential paths for Q-axis flux and with rounded edges in order to minimize the mechanical stress concentration on the external ribs facing the air gap [65], [66].

The PM thicknesses are designed in order to place all magnets at the same working point [67], [68] and to reproduce the ideal air gap staircase of the flux density distribution [43].

Finally, the mean flux density along the iron flux-guides set approximately to the same value in the stator yoke for the reasons mentioned in the paragraph of design rules.

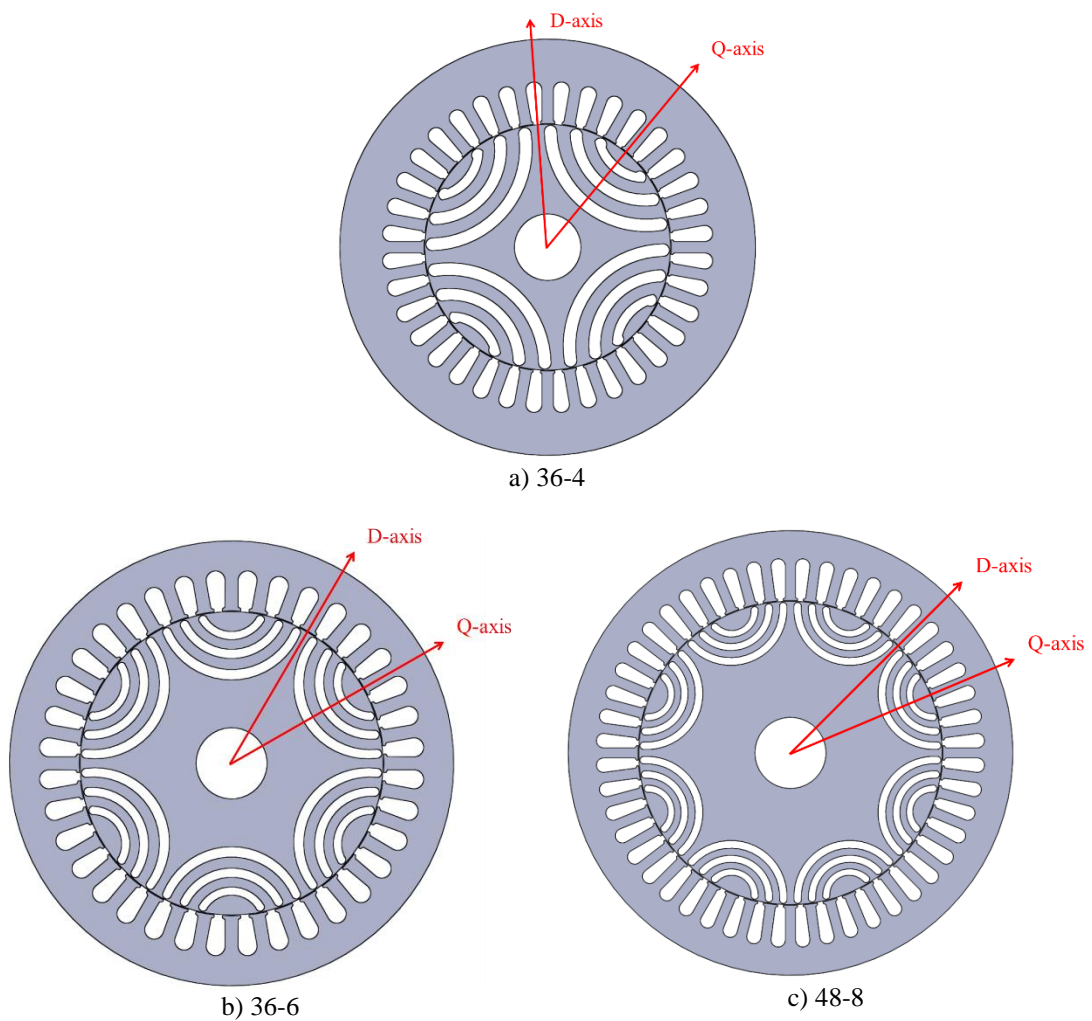


Figure 7-18: geometries of reference machines.

Slot-Pole Combination	36-4, 36-6 and 48-8	Unit of Measurement
Stator Outer Diameter	175	[mm]
Lamination Stack Length	110	[mm]
Slot Conductors	10	-
FEA Mechanical Speed	1000	[r/min]
Rated Current Density	4.5	[A_{RMS}/mm^2]
Overload Current Density	9.0	[A_{RMS}/mm^2]
Filling Factor	0.45	-

Table 7-1: reference machines main characteristics.

7.2.1. Torque Ripple Origin and Limitation Methods

The torque ripple of SyncRel and PMSyncRel machines has been studied by many authors [44], [45], [63], [69]. It is due to the interaction between high order harmonics of air gap MMF produced by the stator and high order harmonics of rotor MMF as shown in Figure 7-19.

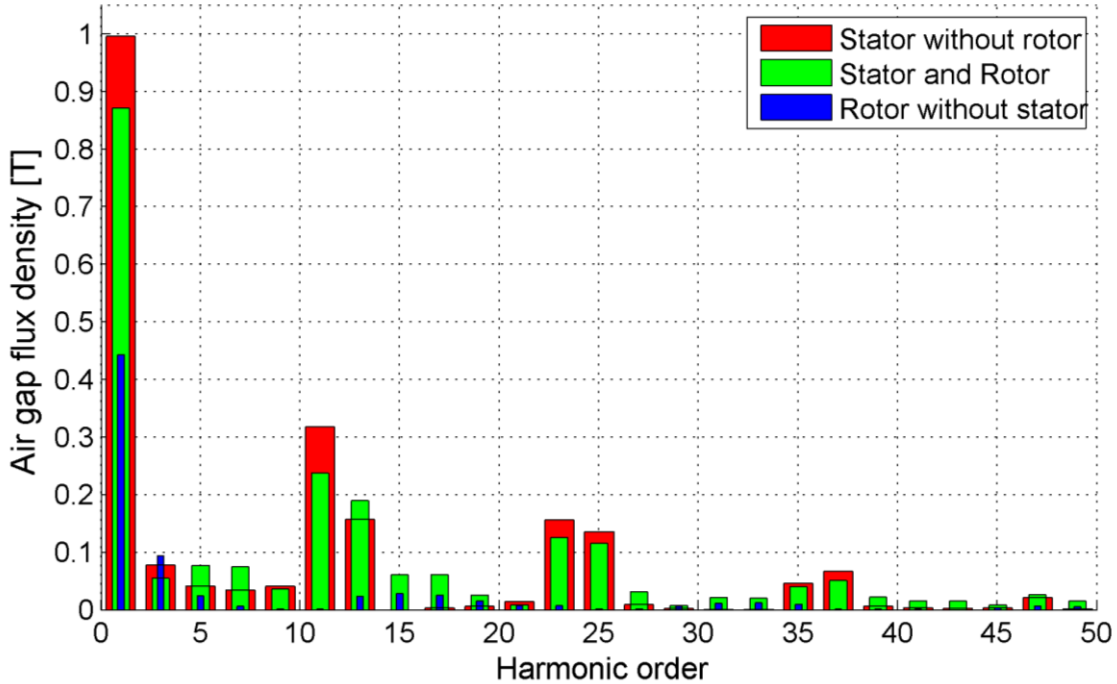


Figure 7-19: stator and rotor MMF harmonic spectra comparison of 36-6 reference machine.

Stator fundamental MMF harmonic moves at the synchronous speed, while the other stator MMF harmonics move with different speed depending on the i^{th} harmonic order. On the other hand, all rotor MMF harmonics move at the same synchronous speed, therefore only fundamental stator and rotor harmonics have the same phase angle and produce a constant output torque, whereas the other harmonics produce pulsating torque.

The three reference machines have been designed with an integer slot winding in order to get an integer SPP number and thus reduce the pulsating torque. In general, if the SPP is integer, the main source of high order harmonics can be attributed to slots harmonics.

Hereafter, are recalled two design expedients that can be applied to reduce stator and rotor harmonics interaction in order to limit torque ripple.

7.2.1.1. Number of Rotor Flux-Barriers

The appropriate number of stator slots and rotor flux-barriers is a key point to strongly reduce torque ripple, cogging torque and iron losses [44], [45], [63].

Given N_s and N_r the stator slots number and rotor slots per pole pair, the corresponding spatial harmonics are given by Eq. 7-23 and Eq. 7-24, respectively [62].

$$(hN_s \pm 1) \quad \text{Eq. 7-23}$$

$$(hN_r \pm 1) \quad \text{Eq. 7-24}$$

When Eq. 7-22 is true, there is a strong interaction between stator and rotor spatial harmonics, thus in order to avoid this condition the number of rotor slots N_r should be equal to $N_s \pm 4$, thus the number of rotor flux-barriers should be at least 2 because each flux-barrier has two rotor slots. In addition, it is preferable to have a rotor flux-barrier number at least equal to three in order to minimize ribs leakage flux and increase saliency ratio, hence the output torque. Table 7-7 shows the chosen stator and rotor slots and rotor flux-barriers number of the three reference machines.

Reference Machine	N_s	N_r	Flux-Barriers per Pole
36-4	18	14	3.5 = 3 flux-barriers + 1 virtual
36-6	12	16	4 = 3 flux-barriers + 1 virtual
48-8	12	16	4 = 3 flux-barriers + 1 virtual

Figure 7-20: stator and rotor slots and flux-barrier number of the reference machines.

7.2.1.2. Step-Skewing Technique

The step-skewing consists in the harmonic cancellation through an appropriate phase shifting of the given harmonic. Typically, electrical machines designers adopt stator or rotor skewing or step-skewing in order to reduce torque ripple, cogging torque or undesirable content [70].

Stator and rotor should be skewed by the angle θ_{skew} which corresponds to the period of the fundamental undesired harmonic and it allows achieving the maximum reduction of the undesired harmonics. On the other hand, skewing causes an unwanted reduction of the fundamental component of the main machine signals which are inversely proportional to skewing angle.

In case of step-skewing the angle between each step is expressed as follows:

$$\theta_{step_skewing} = \frac{\theta_{skew}}{N_{step}} \quad \text{Eq. 7-25}$$

where N_{step} is the number of steps that is the number of rotor lamination parts having a specific value of $\theta_{step_skewing}$.

Each step forces the undesired harmonic in phase opposition, thus for the superposition principle harmonic orders which are not multiples of the chosen steps are neglected.

It is worth noting that the sum of step-skewing angles $\theta_{step_skewing_i}$ is always lower than the skewing angle θ_{skew} and it is valid the following expression.

$$\lim_{N_{step} \rightarrow +\infty} \frac{\theta_{skew}}{N_{step}} = \theta_{skew} \quad \text{Eq. 7-26}$$

In general, the rotor skewing is not so common in IPM electrical machines, because assembly is more complicated.

7.2.2. Analytical Design Method with Flux-Barrier Shifting

The state-of-the-art offers some solutions adopting flux-barriers shifting; among them a remarkable one is reported in [71] and in [45], [72] which is the evolution on [71] named Machaon rotor. The authors propose a rotor solution consisting of two types of poles with different rotor flux-barriers pitches in the same rotor lamination in order to compensate the torque ripple. However, this effective method requires a high number of FEA simulations to find the right pair or machines which can work together to compensate each other the undesired harmonics. The authors of [73] and [74] tested other different types of asymmetric rotor flux-barriers.

The aim of this research activity is to provide a general design approach starting from consolidated design rules [44], [63], [69] and then introducing rotor flux-barriers shifting in the same rotor lamination like the concept presented in Machaon rotor. The main difference is that with the proposed method the shifting angles are analytically computed like for step-skewing method.

The rotor asymmetry is computed by ideally dividing the rotor lamination along its Q-axes and then shifting rotor flux-barriers belonging to these sectors by the computed shifting angle. The concept is visually shown in Figure 7-21 for the rotors of the three reference machines.

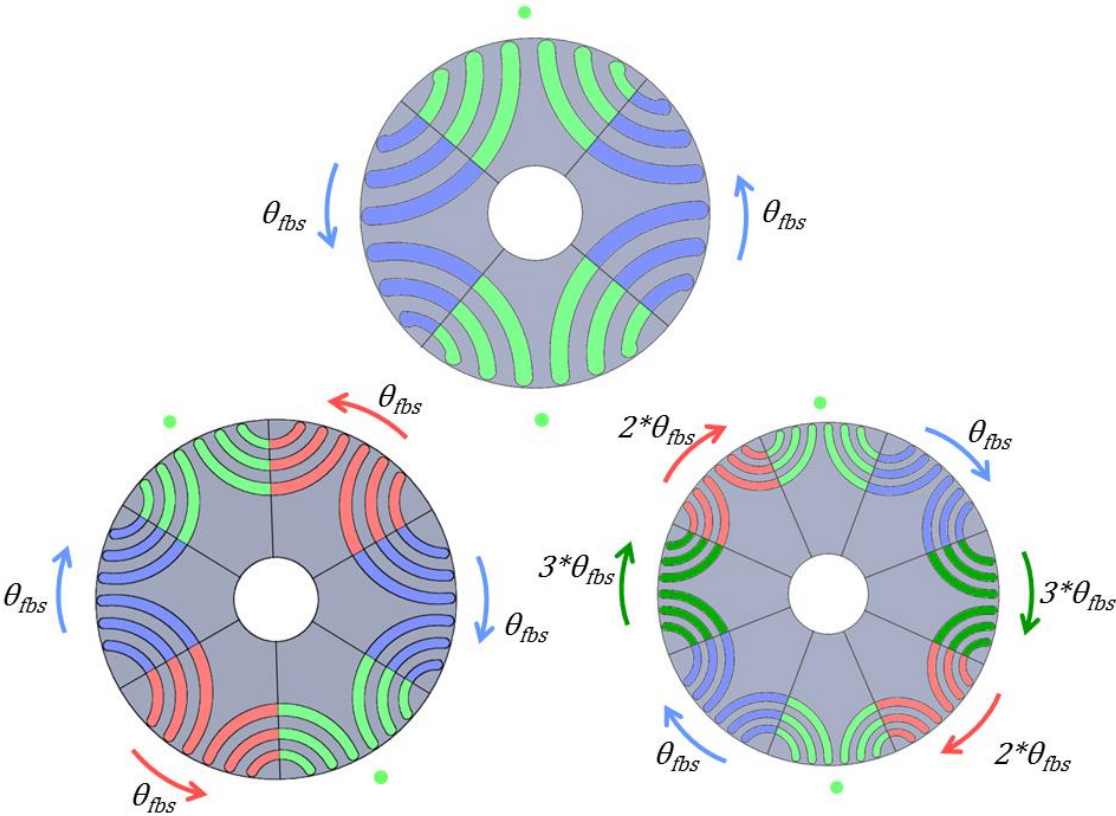


Figure 7-21: layout of shifted flux-barriers for the three reference machines. (The different colors highlight the different shifting sectors).

The air gap induction staircase remains approximately unchanged and no other unwanted harmonics are superimposed. If the proper shifting angle is found, the undesired harmonics are set in phase opposition, therefore they are deleted.

The computation of the shifting angle starts from the analysis of the FFT of the air gap MMF where the most unwanted harmonics are characterized with the corresponding wave length λ_{uh} . Since the undesired harmonics are generally the spatial ones induced by stator slots and rotor flux-barriers, the corresponding wave lengths, referred to the air gap pole pitch τ , can be expressed with Eq. 7-27 and Eq. 7-28, respectively for the rotor flux-barriers and stator slots harmonics.

$$\lambda_{fbsr} = \frac{2\tau}{N_r} \quad \text{Eq. 7-27}$$

$$\lambda_{fbss} = \frac{2\tau}{N_s} \quad \text{Eq. 7-28}$$

Given the wave length λ_{fbsi} , the flux-barrier shifting angle is expressed as follows:

$$\theta_{fbs} = \frac{\lambda_{fbsi}}{pR_g} \quad \text{Eq. 7-29}$$

where i subscript can be r or s depending on the main source of undesired harmonics between the rotor flux-barriers or stator slots.

This approach allows to analytically determining the shifting angle of rotor flux-barriers respect to their original position. It worth noting that different layouts are possible, but the rotor has to be symmetrical in order to avoid unwanted unbalance radial force. The layout adopted in Figure 7-21 is symmetrical according the shifting sequence of rotor shifting sectors and minimize the difference between the pole pitches. Table 7-2 summarizes the shifting angles of the analyzed reference machines.

Origin of the Undesired Harmonics	Shifting Angle	36-4	36-6	48-8	Unit of Measurement
Rotor Flux-Barriers	θ_{fbsr}	6.429	2.500	1.406	[deg]
Stator Slots	θ_{fbss}	5.000	3.333	1.875	[deg]

Table 7-2: flux-barriers shifting angles.

According to Table 7-2, the objective of harmonics cancellation can be obtained by applying the smallest shifting angle θ_{fbs} for each slot-pole combination.

The chance to analytically compute the position of each flux-barrier allows to greatly reducing the design time. Nevertheless, a subsequent design optimization of the shifted flux-barriers is possible with the aim to improve machines performance. The optimization process would be easier and faster, since the main objective was the torque ripple reduction.

7.2.3. Method Validation via Finite Element Analysis

The proposed method offers two possible flux-barriers shifting layouts to reduce torque ripple: the first using Eq. 7-27 and the second using Eq. 7-28. The two possible solutions are validated and compared via FEA for the three reference machines which have been simulated using the same current density and slot filling factor. The torque ripple was analyzed at rated current density of $4.5 A_{RMS}/mm^2$ and at overload current density of $9 A_{RMS}/mm^2$ in order to validate the robustness of the proposed method.

Since the cogging torque is equal to slot pitch for SyncRel machines with integer SPP [75], the proposed rotor flux-barrier shifting for stator slot harmonics elimination could be a valid solution to reduce cogging torque as shown in Figure 7-24 for the 48-8 reference machine. The cogging torques comparison of the no-shifted reference machine with the cogging torques of the two possible flux-barrier shifting are shown in Figure 7-22:Figure 7-24 for 36-4, 36-6 and 48-8 respectively.

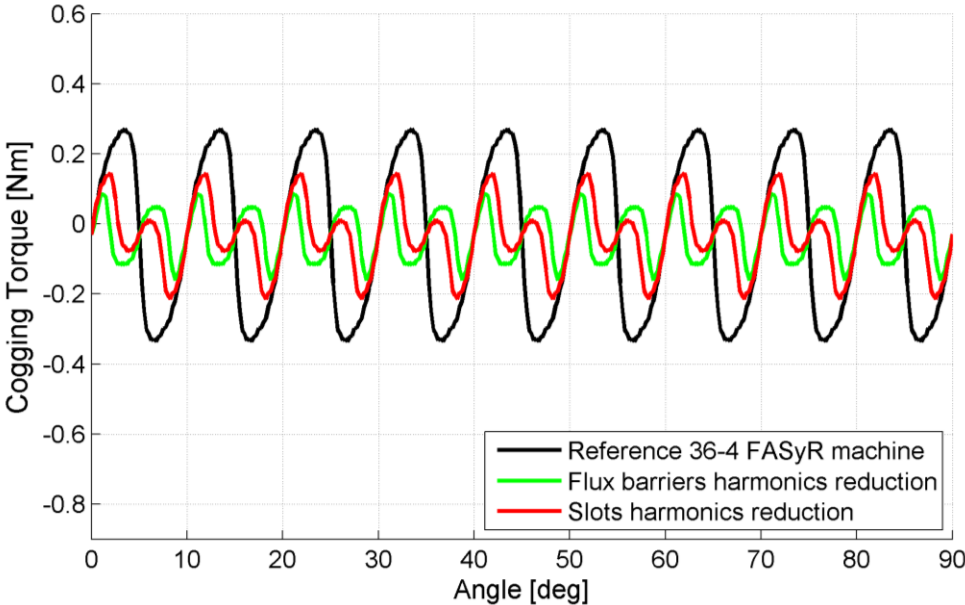


Figure 7-22: cogging torque comparison of 36-4 reference machine.

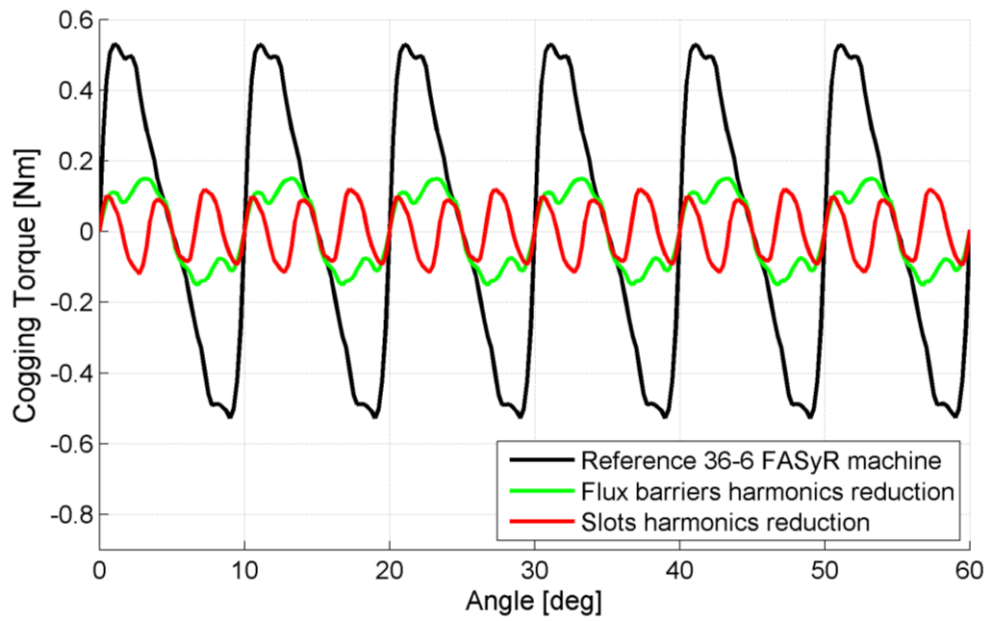


Figure 7-23: cogging torque comparison of 36-6 reference machine.

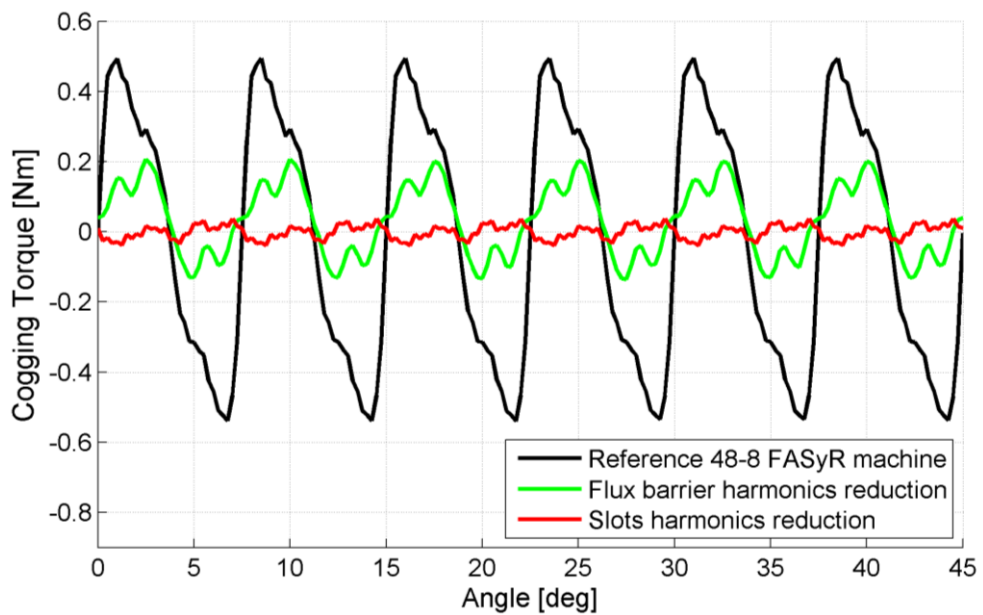


Figure 7-24: cogging torque comparison of 48-8 reference machine.

The rotor flux-barrier improves also the electromotive force waveforms, as shown in Figure 7-25÷Figure 7-27 representing the electromotive waveform of one phase at 1000 r/min of the three reference machines.

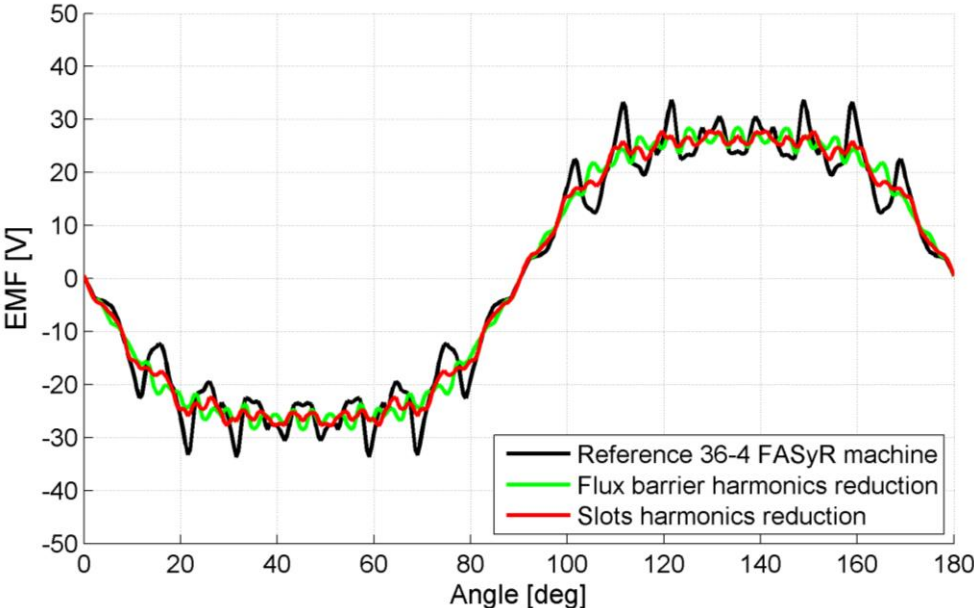


Figure 7-25: EMF comparison of 36-4 reference machine.

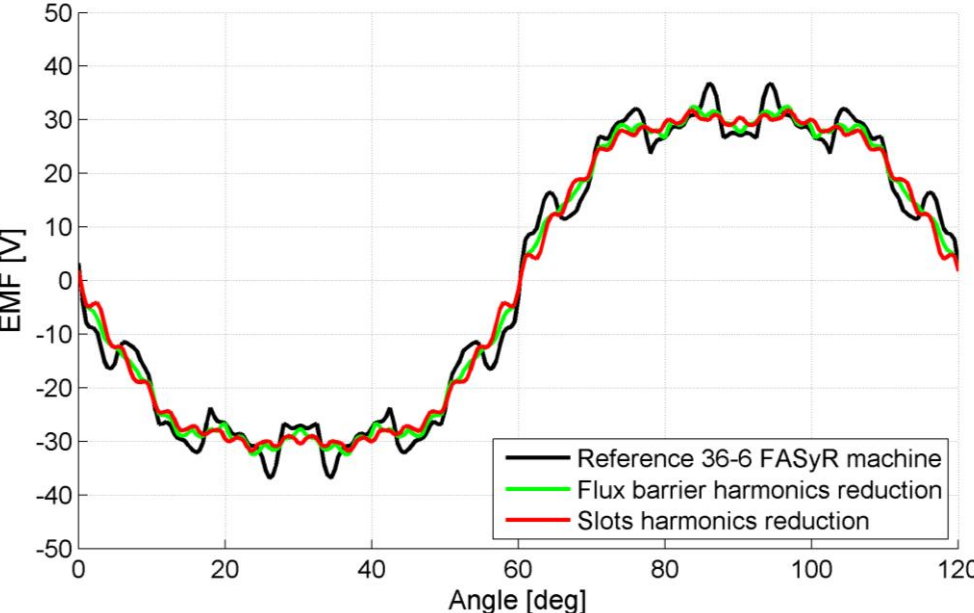


Figure 7-26: EMF comparison of 36-6 reference machine.

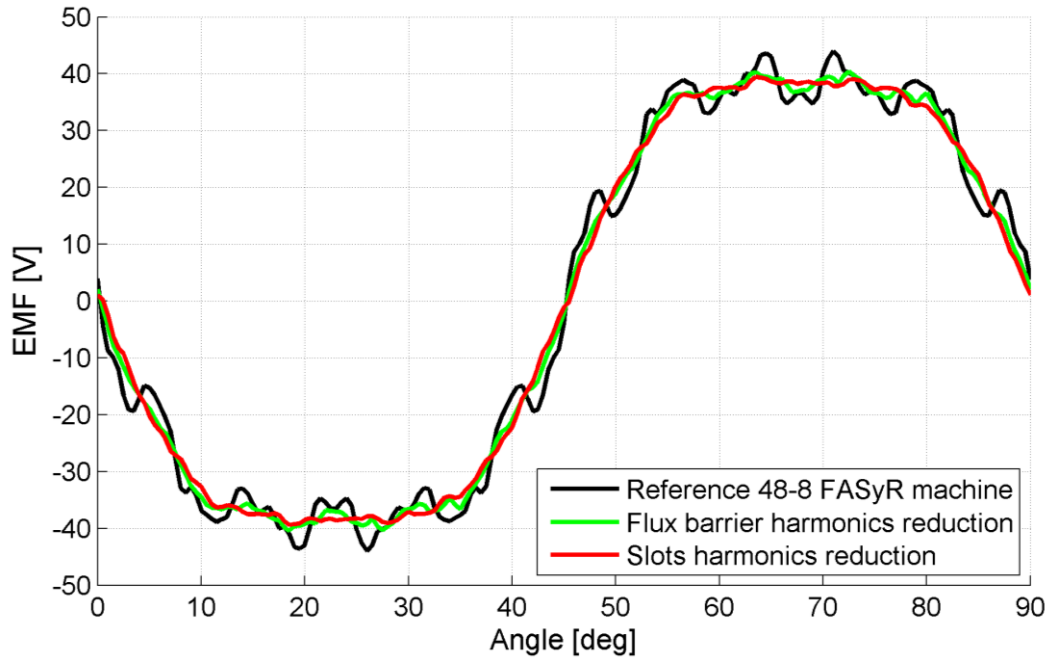


Figure 7-27: EMF comparison of 48-8 reference machine.

Finally, rated torque and torque ripple are shown in Figure 7-28÷Figure 7-30 at rated current density, while Figure 7-31÷Figure 7-36 show the corresponding FFT. The overload torque and torque ripple are shown in Figure 7-37÷Figure 7-39 at the corresponding overload current density. The figures show the results both for the SyncRel and PMSyncRel topologies.

Table 7-3÷Table 7-5 summarize FEA results of simulated reference machines where the pure SyncRel machine results are shown in round brackets.

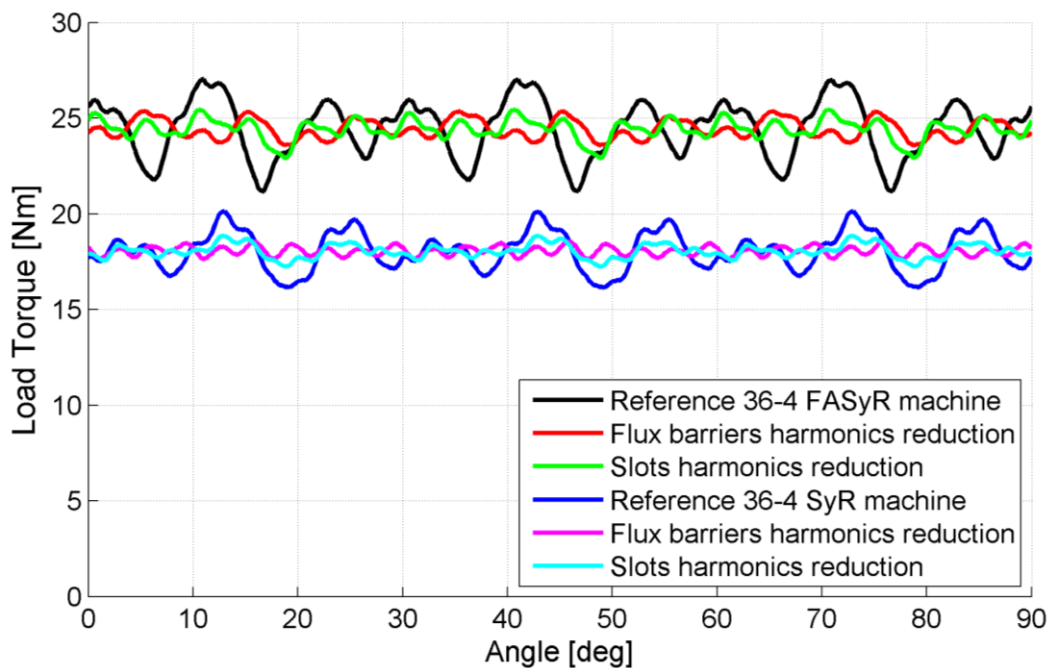


Figure 7-28: rated torque and torque ripple of PMSyncRel and SyncRel 36-4 reference machine.

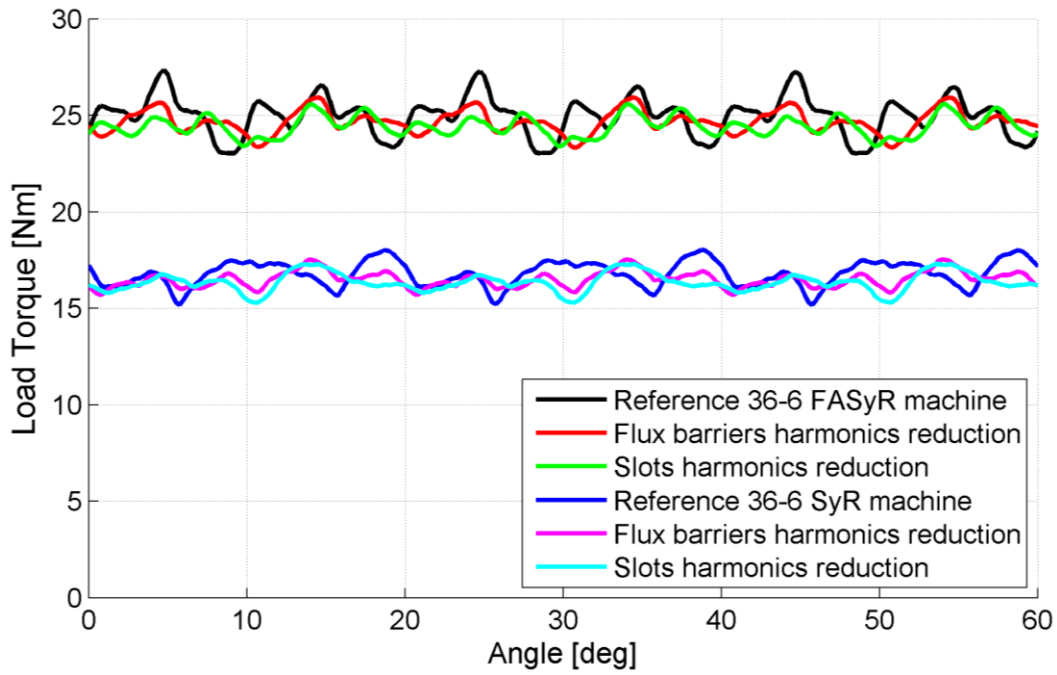


Figure 7-29: rated torque and torque ripple of PMSyncRel and SyncRel 36-6 machine.

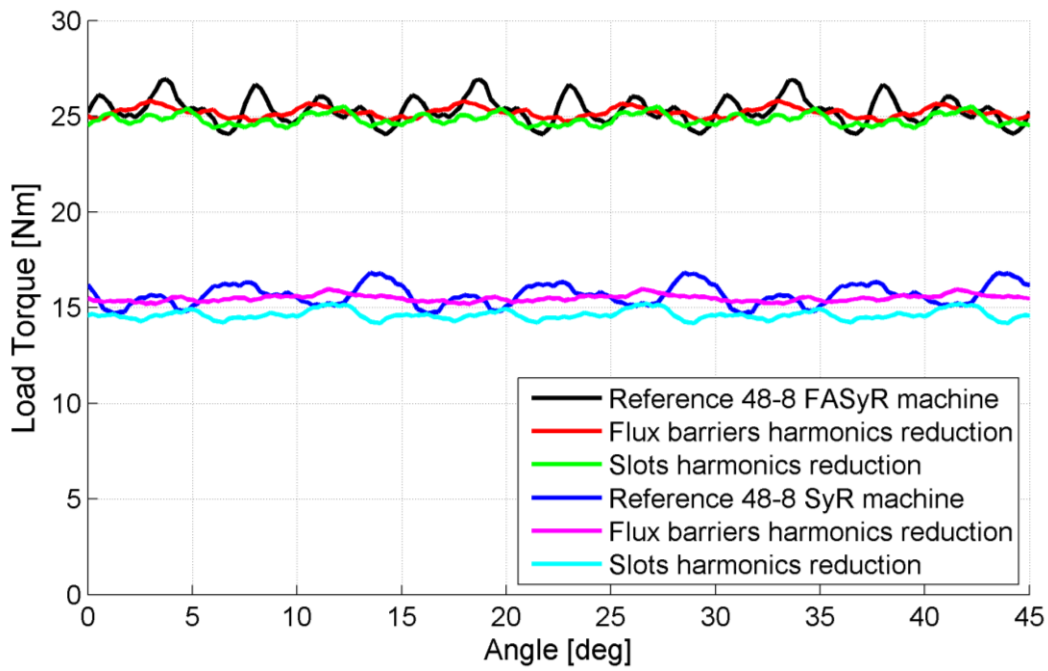


Figure 7-30: rated torque and torque ripple of PMSyncRel and SyncRel 48-8 machine.

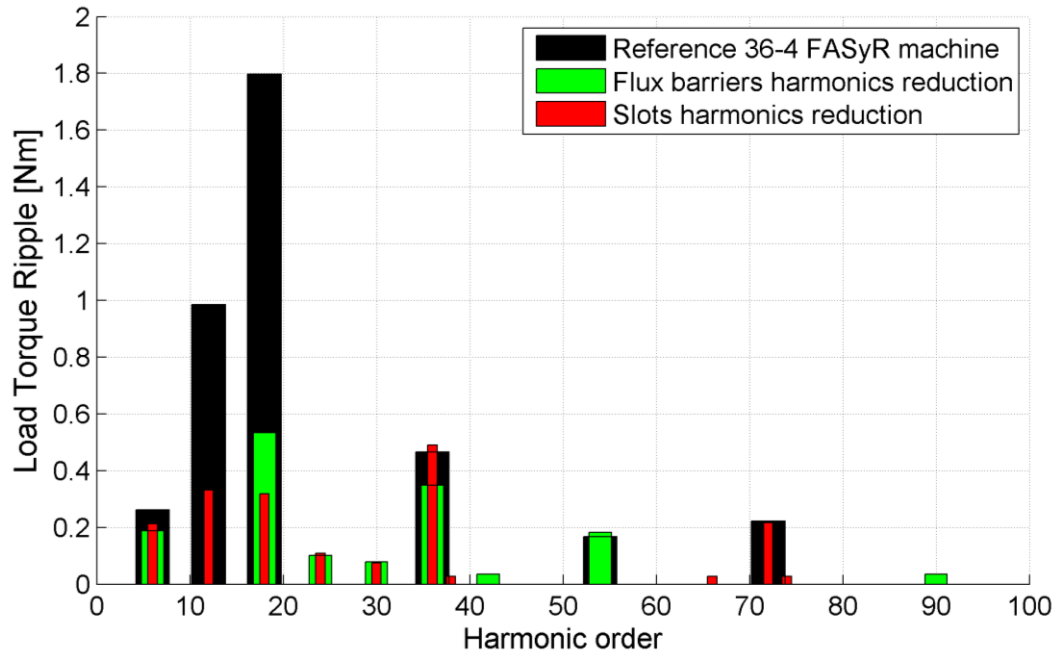


Figure 7-31: rated torque harmonic spectra of 36-4 PMSyncRel.

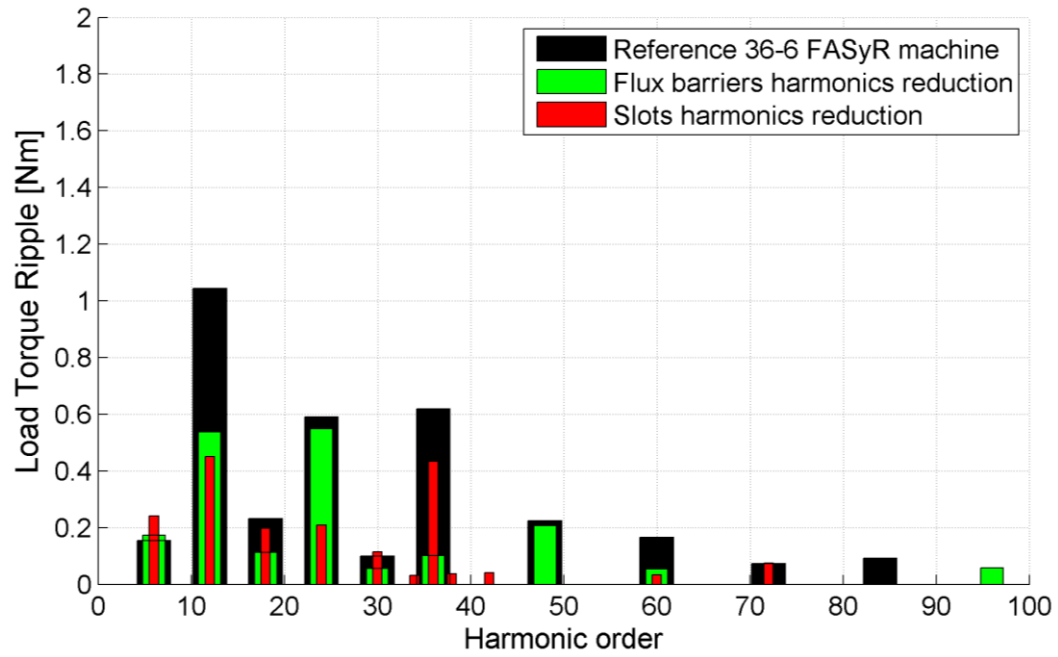


Figure 7-32: rated torque harmonic spectra of 36-6 PMSyncRel.

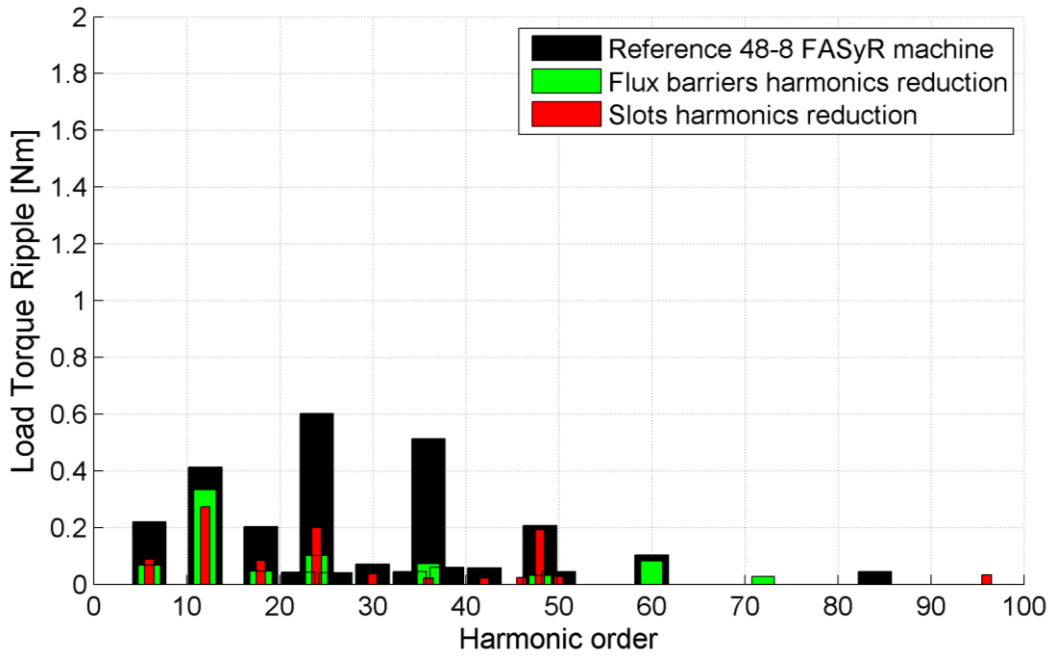


Figure 7-33: rated torque harmonic spectra of 48-8 PMSyncRel.

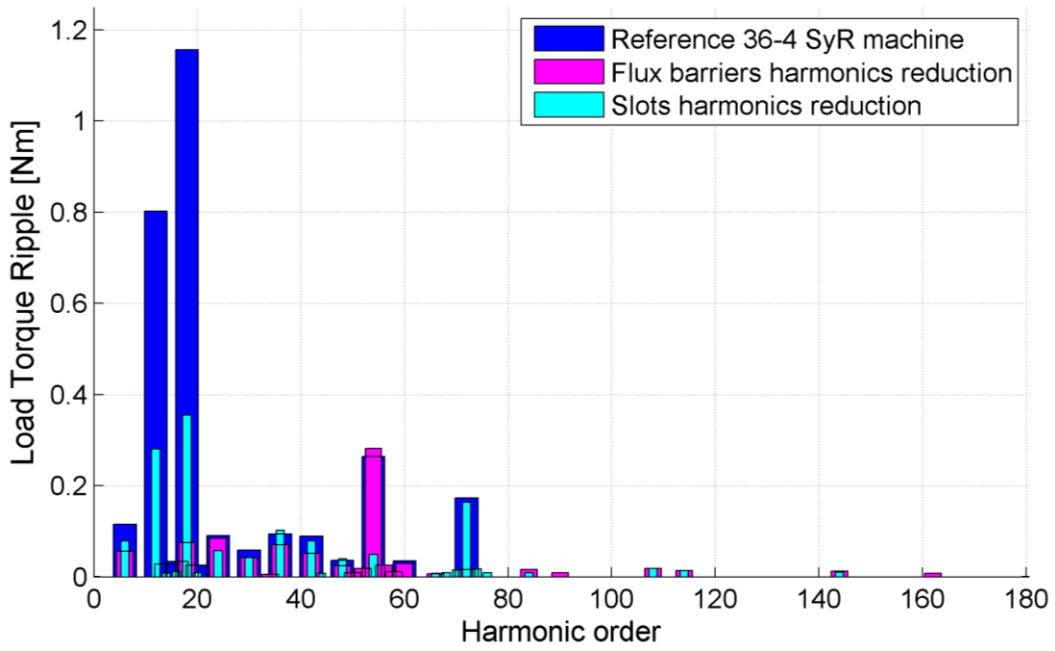


Figure 7-34: rated torque harmonic spectra of 36-4 SyncRel.

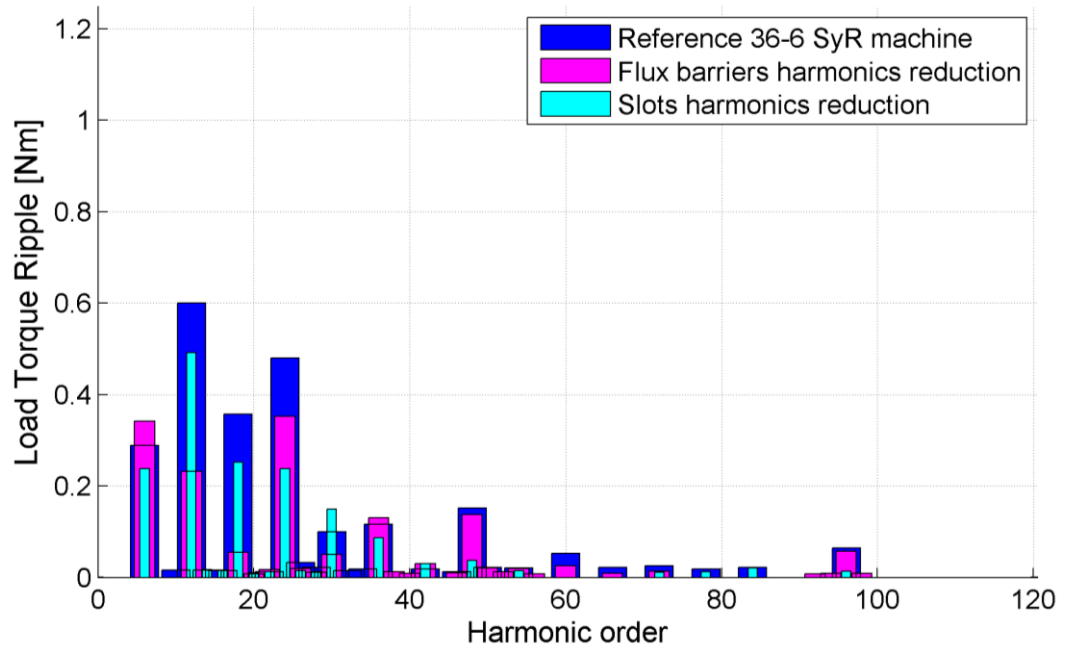


Figure 7-35: rated torque harmonic spectra of 36-6 SyncRel.

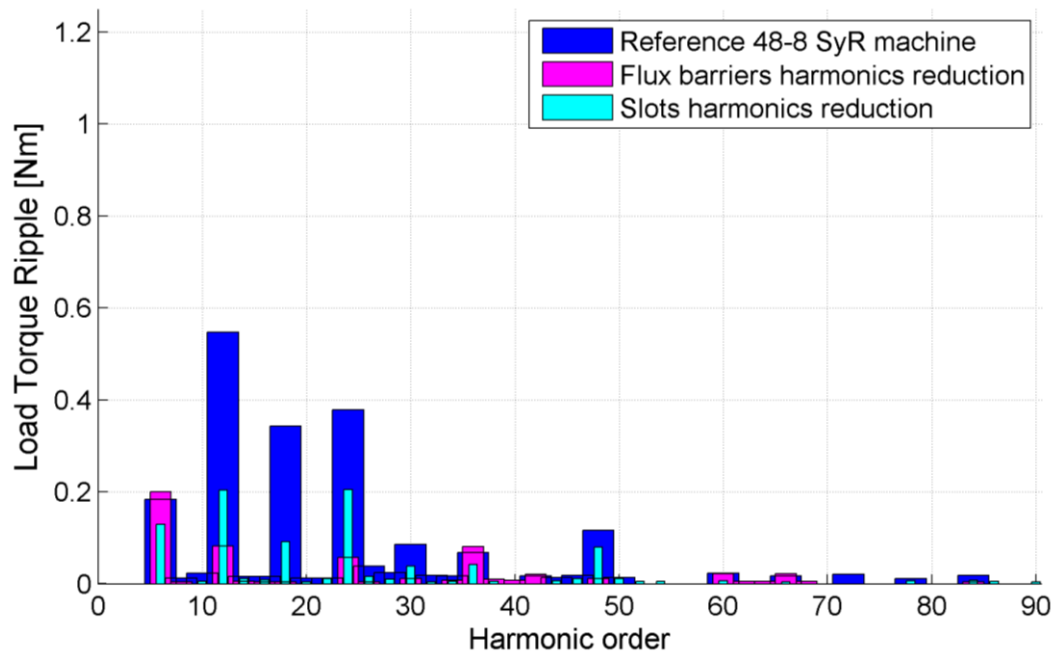


Figure 7-36: rated torque harmonic spectra of 48-8 SyncRel.

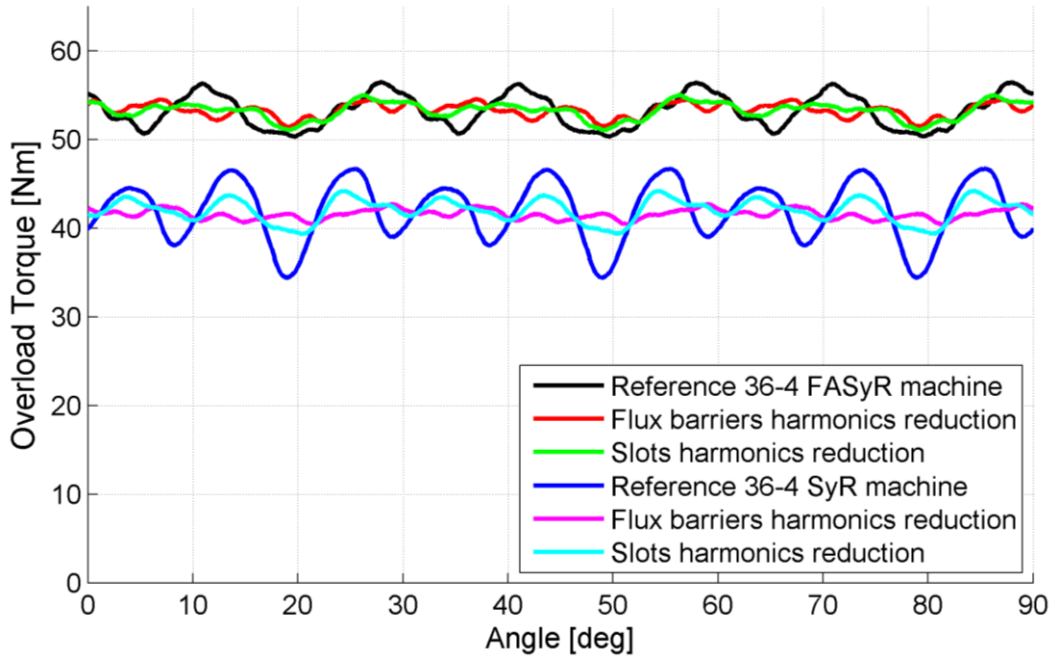


Figure 7-37: rated torque and torque ripple of PMSyncRel and SyncRel 36-4 machine.

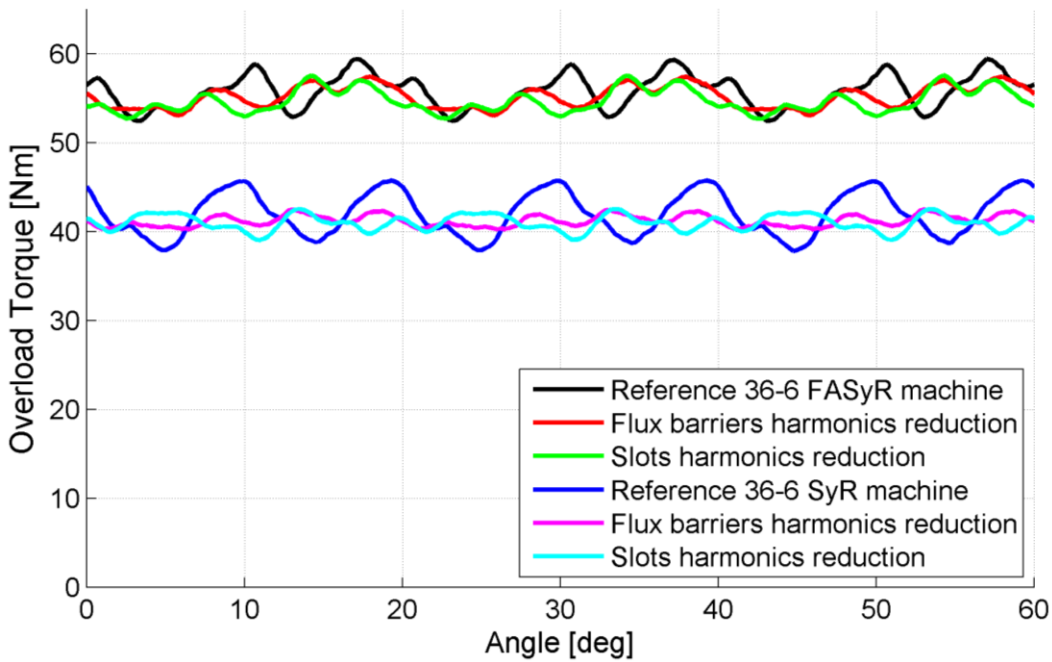


Figure 7-38: rated torque and torque ripple of PMSyncRel and SyncRel 36-6 machine.

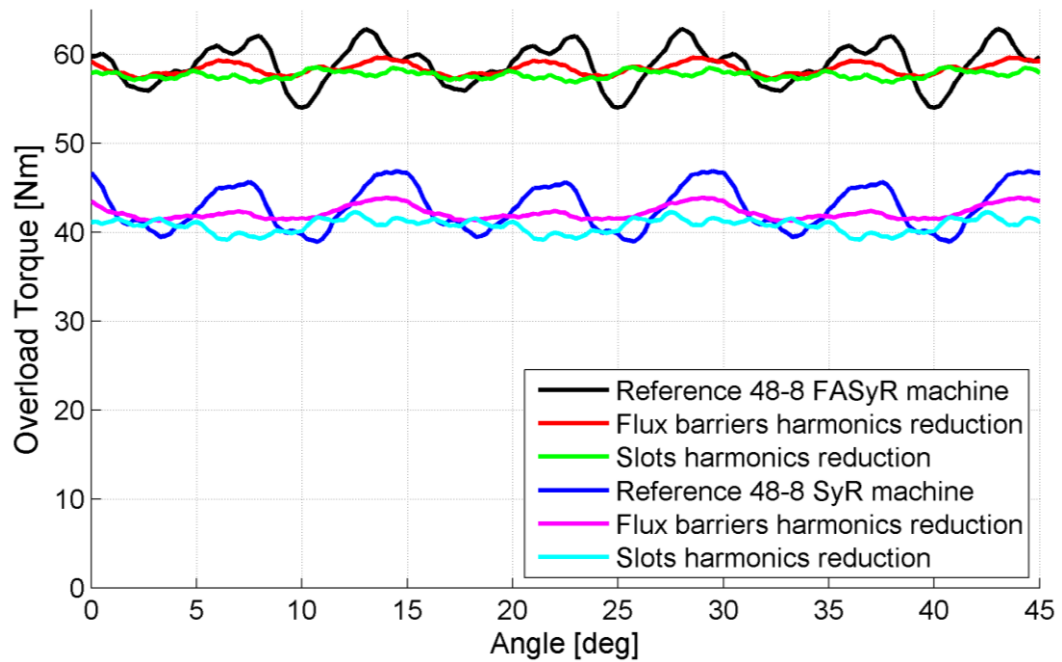


Figure 7-39: rated torque and torque ripple of PMSyncRel and SyncRel 48-8 machine.

36-4 PMSyncRel and (SyncRel)				
Parameter	Unit of Measurement	Reference Machine	Flux-Barrier Har. Reduction	Stator Slots Har. Reduction
EMF _u @ 1000 r/min	[V _{RMS}]	21.7	21.5	21.5
Cogging Torque	[Nm]	0.61	0.25	0.36
Cogging Torque in p.u.	[%]	2.50	1.02	1.48
Power Factor	-	0.936 (0.749)	0.936 (0.749)	0.936 (0.749)
Rated Torque	[Nm]	24.4 (18.0)	24.4 (18.1)	24.4 (18.1)
Torque Ripple	[Nm]	5.9 (4.0)	1.8 (0.9)	2.6 (1.6)
Torque Ripple in p.u.	[%]	24.0 (22.1)	7.4 (5.2)	10.6 (9.1)
Overload Torque	[Nm]	53.2 (42.0)	53.3 (41.6)	53.3 (42.0)
Overload Torque Ripple	[Nm]	6.2 (12.3)	3.1 (2.3)	4.0 (4.8)
Overload Torque Ripple in p.u.	[%]	11.6 (29.4)	5.8 (5.5)	7.5 (0.12)

Table 7-3: performance comparison of reference 36-4 machine without flux-barrier shifting and with the two possible shifting alternatives.

36-6 PMSyncRel and (SyncRel)				
Parameter	Unit of Measurement	Reference Machine	Flux-Barrier Har. Reduction	Stator Slots Har. Reduction
EMF _u @ 1000 r/min	[V _{RMS}]	25.1	24.7	24.6
Cogging Torque	[Nm]	1.10	0.30	0.25
Cogging Torque in p.u.	[%]	4.40	1.22	1.03
Power Factor	-	0.921 (0.667)	0.921 (0.662)	0.921 (0.659)
Rated Torque	[Nm]	25.0 (16.8)	24.7 (16.5)	24.4 (16.3)
Torque Ripple	[Nm]	4.3 (2.9)	2.6 (1.9)	2.2 (1.6.3)
Torque Ripple in p.u.	[%]	17.4 (17.0)	10.6 (11.2)	9.2 (12.3)
Overload Torque	[Nm]	55.7 (42.0)	55.2 (41.2)	54.7 (41.0)
Overload Torque Ripple	[Nm]	7.0 (7.9)	4.4 (2.3)	5.0 (3.5)
Overload Torque Ripple in p.u.	[%]	12.5 (18.8)	7.9 (5.5)	9.1 (8.5)

Table 7-4: performance comparison of reference 36-6 machine without flux-barrier shifting and with the two possible shifting alternatives.

48-8 PMSyncRel and (SyncRel)				
Parameter	Unit of Measurement	Reference Machine	Flux-Barrier Har. Reduction	Stator Slots Har. Reduction
EMF _u @ 1000 r/min	[V _{RMS}]	31.9	31.5	31.3
Cogging Torque	[Nm]	1.04	0.34	0.08
Cogging Torque in p.u.	[%]	4.11	1.35	0.32
Power Factor	-	0.892 (0.599)	0.891 (0.592)	0.890 (0.522)
Rated Torque	[Nm]	25.3 (15.7)	25.2 (15.5)	24.8 (14.6)
Torque Ripple	[Nm]	2.9 (2.2)	1.1 (0.8)	1.2 (1.0)
Torque Ripple in p.u.	[%]	11.4 (13.8)	4.3 (5.1)	4.7 (6.9)
Overload Torque	[Nm]	58.8 (42.8)	58.4 (42.2)	57.7 (40.8)
Overload Torque Ripple	[Nm]	8.9 (8.0)	2.4 (2.6)	1.8 (3.2)
Overload Torque Ripple in p.u.	[%]	15.1 (18.6)	4.1 (6.2)	3.0 (7.7)

Table 7-5: performance comparison of reference 48-8 machine without flux-barrier shifting and with the two possible shifting alternatives.

7.3. Design Optimization for Fault-Tolerant Applications

The machine design and optimization are important instruments to limit pulsating torque of SyncRel machine, but they can also be used to improve the fault-tolerant machine capability. Nowadays, a fault-tolerant oriented design is assuming more and more attention also from the literature community due to spread of electrical machines many industries where safety is one of the key requirements.

The pure SyncRel machine is a valid machine topology for fault-tolerant application, thanks to its intrinsic reliability since PMs are absent. Unfortunately, the state-of-the-art presents few research activities deal with the fault-tolerant design and analysis.

In order to fill this gap this research activity shows the design of pure SyncRel machine with dual three-phase windings focusing on its fault-tolerant capability evaluated in terms of mean torque reduction, torque ripple, unbalanced magnetic radial force and magnetic coupling between healthy and faulty conditions.

The dual three-phase drive system increases the fault reliability, while containing the total cost of the motor drive [76], [77]. In fact, the proposed solution requires standard three-phase components and a single motor, unlike fully redundant systems composed by two inverters and two motors or multi-phase machines that requires dedicated power converters and switches [78]÷[80].

The machine characteristics are summarized in Table 7-6 where the stator is a standard lamination and the Figure 7-40 shows a slice of the rotor geometry with three flux-barriers per pole.

Parameter	Value	Unit of Measurement
Stator Outer Diameter	170	[mm]
Stator Inner Diameter	115	[mm]
Stator Slots	36	-
Pole Pairs	4	--
Slot Height	17.5	[mm]
Tooth Width	5.3	[mm]
Lamination Stack Length	85	[mm]
Winding Layers	2	-
Current Density	6	$\left[\frac{A_{RMS}}{mm^2}\right]$
Rated Current	8	[A]
DC BUS Voltage	350	[V _{DC}]

Table 7-6: dual three-phase characteristics.

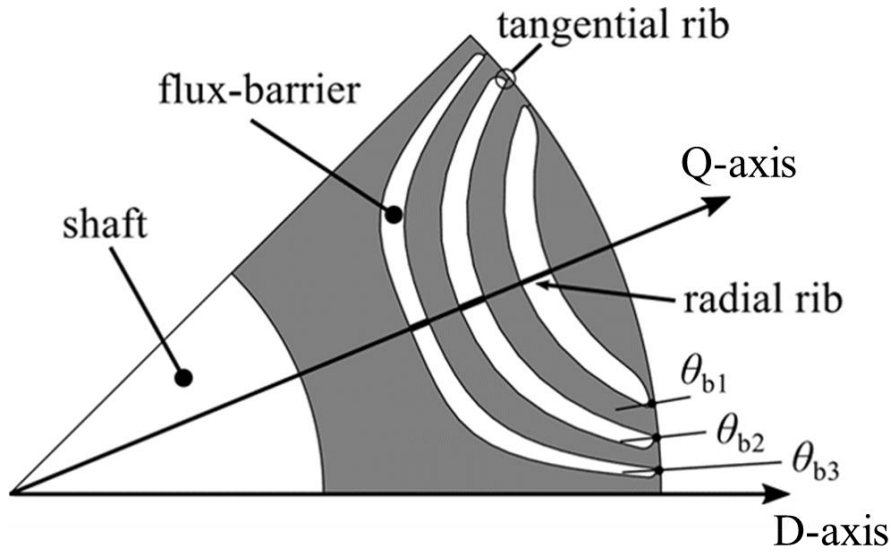


Figure 7-40: one rotor pole geometry of the analyzed dual three-phase SyncRel motor.

7.3.1. Dual Three-Phase Winding Arrangement

The motor winding consists of two identical and electrically independent three-phase windings, each supplied by a standard three-phase inverter (see Figure 7-41). If the fault of one winding occurs, only the healthy one continues to operate, while the faulty winding is disconnected. The phases of the three-phase windings are labeled as A_1, B_1, C_1 and A_2, B_2, C_2 ; winding 1 is always assumed as the healthy one, while the other could be normally fed, disconnected or short-circuited in case of: healthy, Open Circuit Fault (OCF) (Figure 7-42) or Short-Circuit Fault (SCF) (Figure 7-43) conditions.

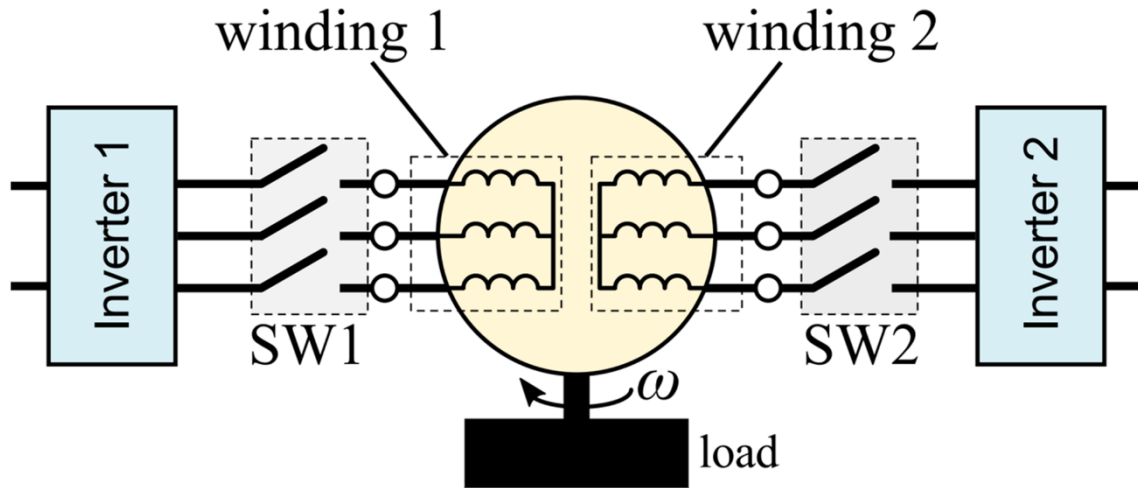


Figure 7-41: dual three-phase drive system.

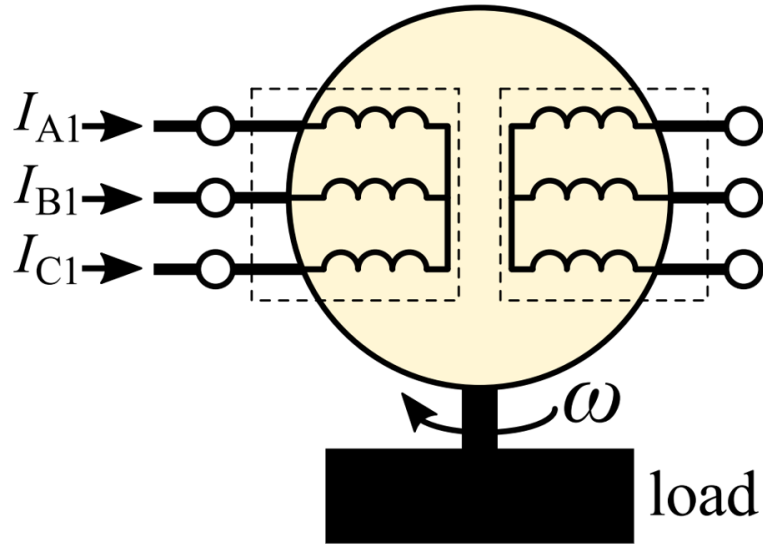


Figure 7-42: winding 2 in three-phase open-circuit fault (OCF) condition.

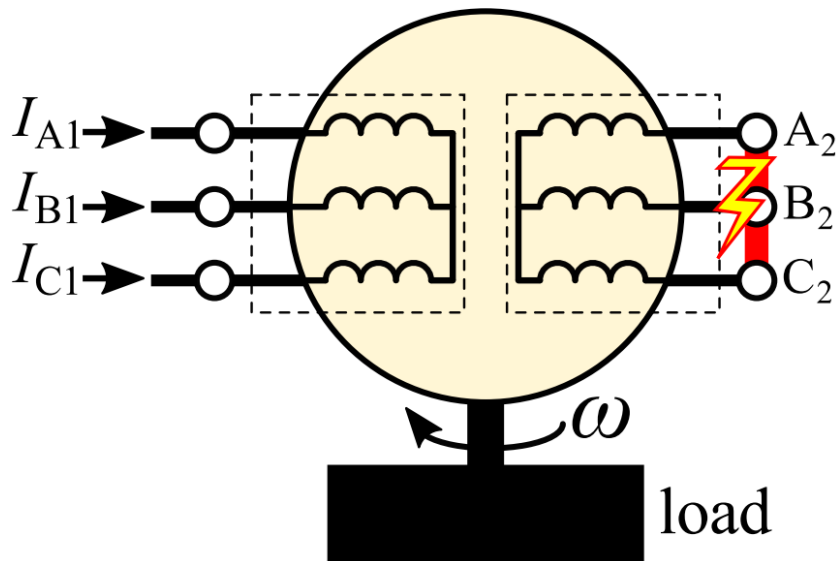


Figure 7-43: winding 2 in three-phase short-circuit fault (SCF) condition.

The two three-phase windings have distributed double-layer (DL) configuration and they could be arranged, as shown Figure 7-44, only with the give slot-pole combination of Table 7-6 [76], [81]. The first configuration W-11-12 is not feasible because of the very unbalanced radial force that arises in faulty condition due to high winding distribution asymmetry along stator periphery [81]. Only W-12-12 is feasible and it can be arranged in two different coils distribution: *aligned* and *shifted*, as shown in Figure 7-44b) and Figure 7-44c). The two arrangements differ in the position of winding 1 magnetic axis A_1 with respect to the boundary of winding regions. In the W-12-12 *aligned*, the angular position of A_1 -axis is 35° , while in W-12-12 *shifted* the axis is rotated in clockwise direction of 10° equivalent to one slot pitch angle.

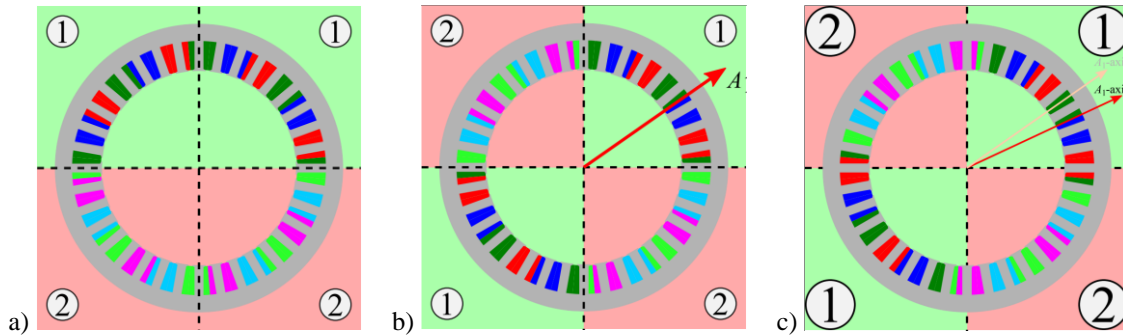


Figure 7-44: Dual three-phase winding arrangements: a) W-11-12, b) W-12-12 *aligned* and c) W-12-12 *shifted*. The areas of the same color are occupied by the same winding and the arrow A shows the position of the magnetic axis of winding 1.

The aim of this research activity is to improve the fault-tolerant reliability of SyncRel machine focusing on rotor geometry design. A multi-objective differential evolution (MODE) algorithm has been used for optimization via FEA, then the fault effect of one of three-phase have been investigated.

7.3.2. Machine FEA Optimization

The electrical machine has been fed with a rated RMS current density of $6 A_{RMS}/mm^2$ both in health on OCF faulty condition for the performance evaluation. The optimization process has been carried out adopting two different optimization strategies:

- Healthy Optimization (H-OPT) which objectives are maximize the mean torque and minimize the torque ripple only at healthy conditions;
- Healthy-Faulty Optimization (HF-OPT) which objectives are maximize the mean torque and minimize the torque ripple both at healthy and OCF conditions.

The computation of each rotor flux-barrier and iron channel thickness have been carried out as a function of the magnetic insulation ratio k_{air} .

$$k_{air} = 2 \frac{\sum_i l_i}{D_g - D_{sh}} \quad \text{Eq. 7-30}$$

where l_i is the thickness of the i^{th} flux-barrier near the Q-axis, D_g and D_{sh} are rotor outer and shaft diameters.

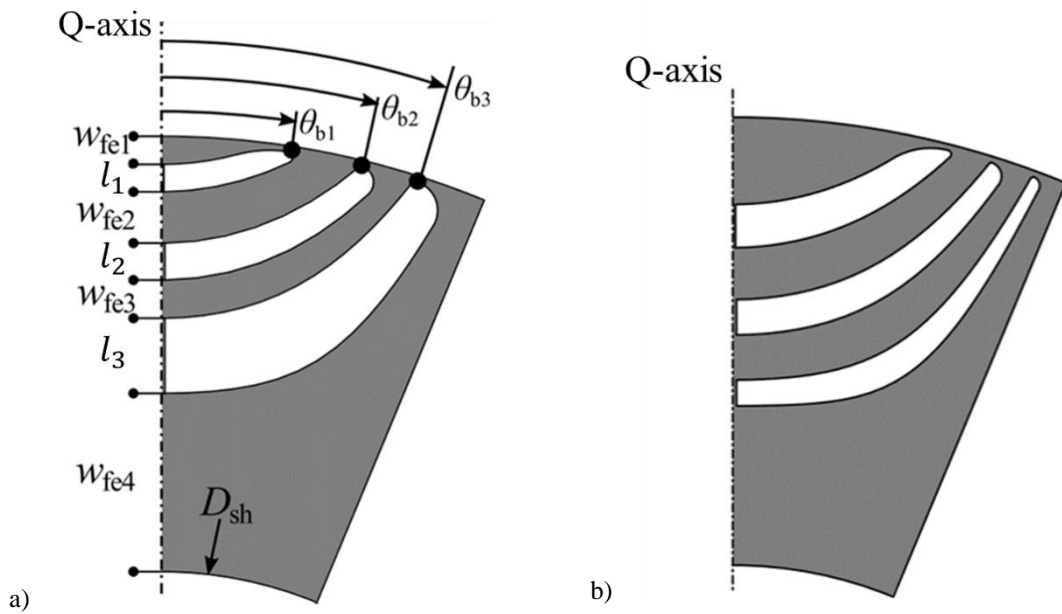


Figure 7-45: rotor geometries of the selected individuals with a) H-OPT strategy and b) HF-OPT strategy.

7.3.2.1. Optimization According to H-OPT Strategy

The Figure 7-46 shows the optimization plane according to H-OPT strategy. The horizontal axis reports the mean torque and the vertical axis the percentage torque ripple, while the red circle markers indicate the Pareto front individuals. According to H-OPT, the mean torque of Pareto front ranges from 13.4 Nm to 13.7 Nm, while the torque ripple has a high variation.

The shape of rotor flux-barrier close to the air gap becomes sharper as the torque ripple decreases because the flux-barrier shape hardly affects the magnetic flux distribution within tangential iron ribs.

The geometry of the selected Pareto individual is shown in Figure 7-45a), it has the lowest torque ripple, nearly 1%, with a mean torque of 13.5 Nm. The rotor flux-barrier angles respect to Q-axis are $\theta_{b1} = 34.8^\circ$, $\theta_{b2} = 55.1^\circ$ and $\theta_{b3} = 71^\circ$, while the insulation ratio is 0.44.

Simulating the selecting individual in OCF condition entails a mean torque reduction around the 50% and an increase of the torque ripple of 11 times than the one at healthy condition.

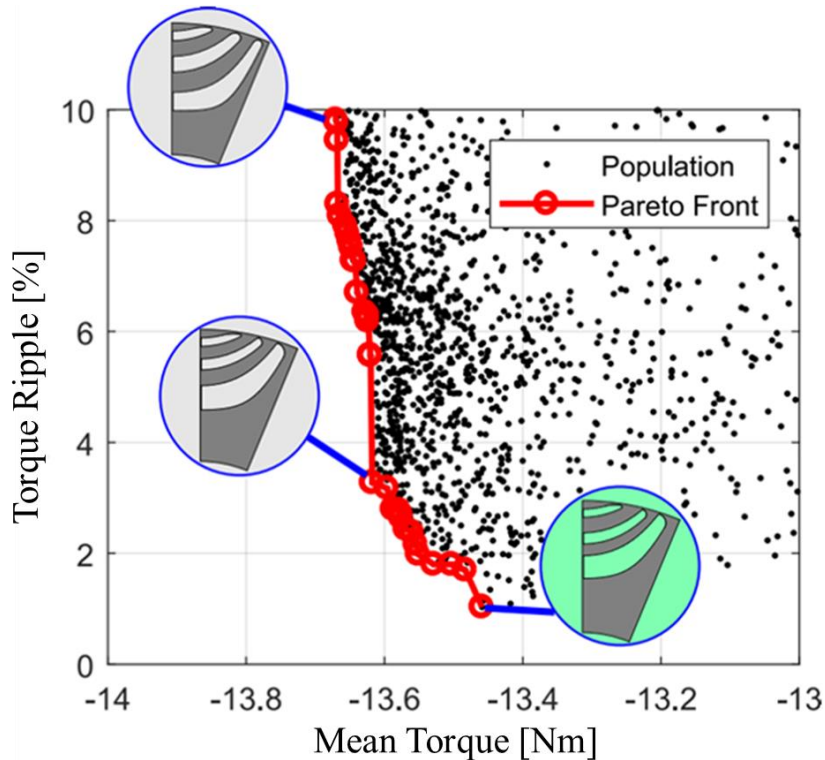


Figure 7-46: objective plane of H-OPT strategy.

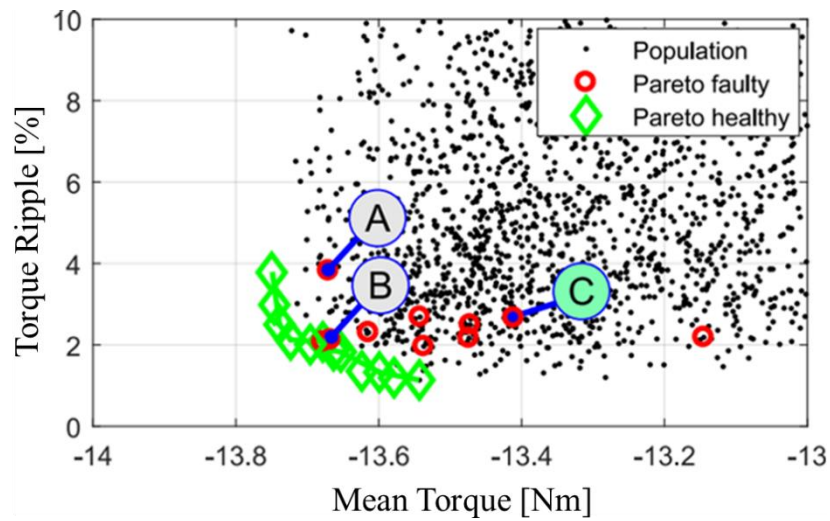
7.3.2.2. Optimization According to HF-OPT

The objective planes according to HF-OPT strategy are shown in Figure 7-47. The green diamond markers are the non-dominated individuals in the healthy objective plane i.e. healthy Pareto front, while the red circle markers are the non-dominant individuals in the faulty objective plane, i.e. faulty Pareto front.

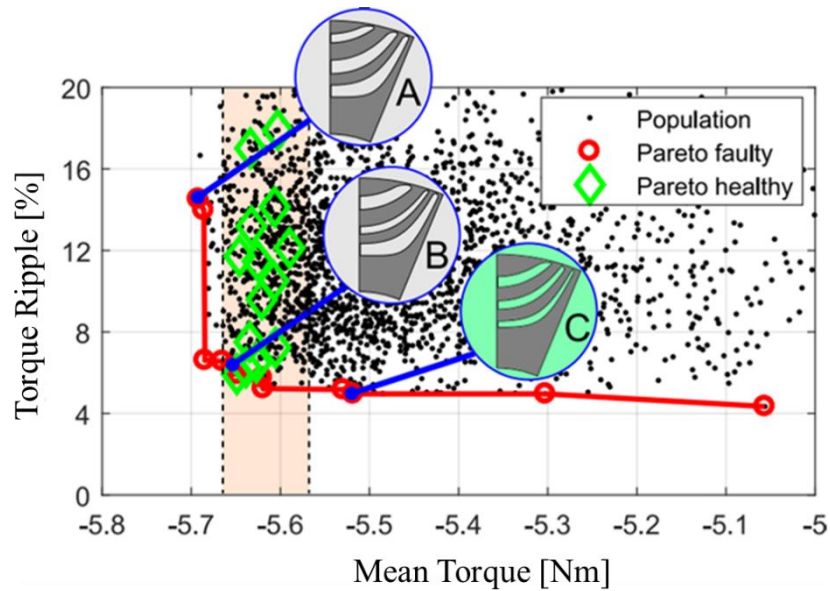
According to the objective plane of Figure 7-47a), the mean torque of healthy Pareto front ranges from 13.5 Nm to 13.8 Nm with a torque ripple lower than 4%. Faulty Pareto front has a mean torque between 13 Nm and 13.7 Nm with a limited torque ripple variation between 2% and 4%.

The faulty individuals present the same behavior in the faulty objective plane: they are distributed over wide mean torque between 5 Nm and 5.7 Nm with limited torque ripple variation between 4.3% and 6.6%. On the other hand, healthy Pareto individuals are characterized by a high torque ripple variation with a limited mean torque variation in the highlighted area of Figure 7-47b). The rotor geometry variation is shown in Figure 7-47b) and it can be noticed that the angle of flux-barrier close to the air gap tends to increase as the torque ripple decreases and the inner flux-barrier tends to move away from the D-axis.

The selected individual has been chosen with the aim to minimize the faulty torque ripple objective; thus, individual C of Figure 7-47b) is the selected one.



a)



b)

Figure 7-47: objective planes of HF-OPT strategies a) healthy conditions and b) faulty conditions.

7.3.3. Dual Three-Phase Windings Magnetic Mutual Coupling

The SyncRel motor performs the same mean torque and torque ripple with both the two feasible winding arrangements i.e. *W-12-12 aligned* and *W-12-12 shifted*. However, in case of fault the *shifted* arrangement exhibits a lower magnetic mutual coupling between the two three-phase windings, thus it should be preferred in order to limit the amplitude of the induced voltages and currents.

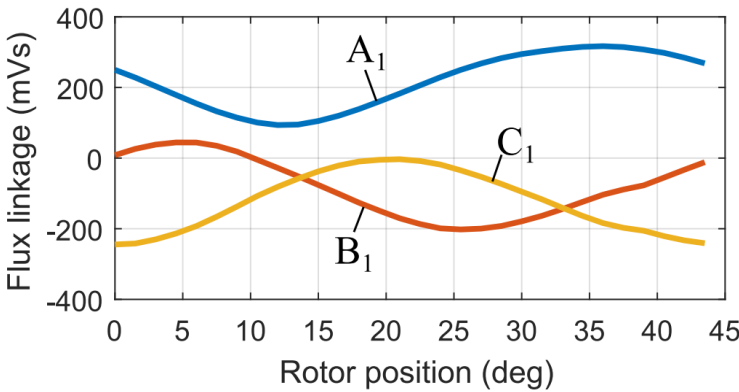
The mutual coupling measurement is carried out via FEA imposing a constant current amplitude, as $I_{A_1} = 8 A$ and $I_{B_1} = I_{C_1} = -4 A$, in the healthy winding and assuming the other one as disconnected (OCF).

According to SyncRel $D - Q$ axes reference, the Figure 7-48a) shows the flux linkage of the healthy phase (winding 1) and the flux assumes its maximum, or minimum, value when the rotor D-axis, or Q-axis, is aligned with the magnetic phase axis. The Figure

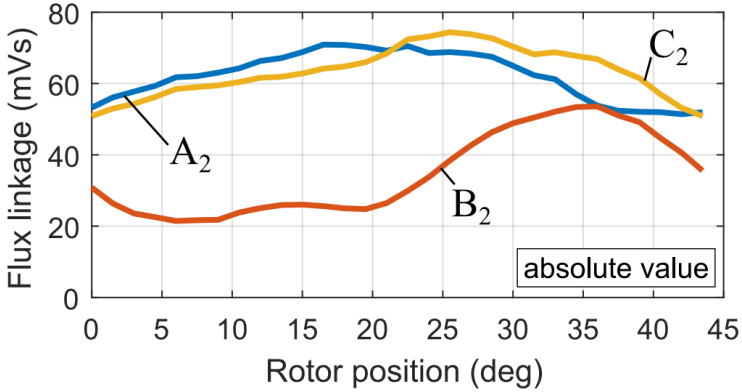
7-48b) and Figure 7-48c) show the flux linkage of the faulty winding (winding 2) assuming respectively W-12-12 *aligned* and *shifted*.

As anticipated the W-12-12 *shifted* arrangement shows a lower induced magnetic coupling, since the maximum induced magnetic flux is 40% less than the one with the *aligned* arrangement. This phenomenon is also confirmed by the magnetic flux density distribution shown in Figure 7-49 for the *aligned* and *shifted* arrangements. The Figure 7-49b) clearly shows that the magnetic coupling with the faulty winding is lower than the equivalent one on the *aligned* arrangement.

FEA results shows that W-12-12 *shifted* arrangement is the preferred solution from the magnetic coupling reduction point of view.



a)



b)

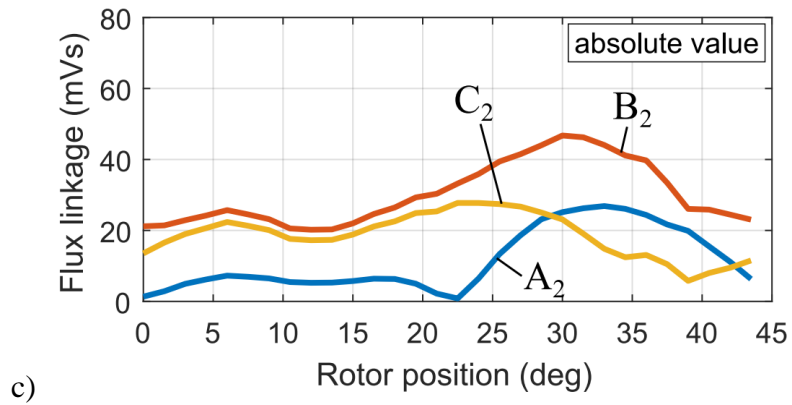


Figure 7-48: flux linkage as a function of rotor mechanical angle. Only the winding 1 is fed: a) healthy winding, b) faulty winding of W-12-12 *aligned* and c) faulty winding of W-12-12 *shifted*.

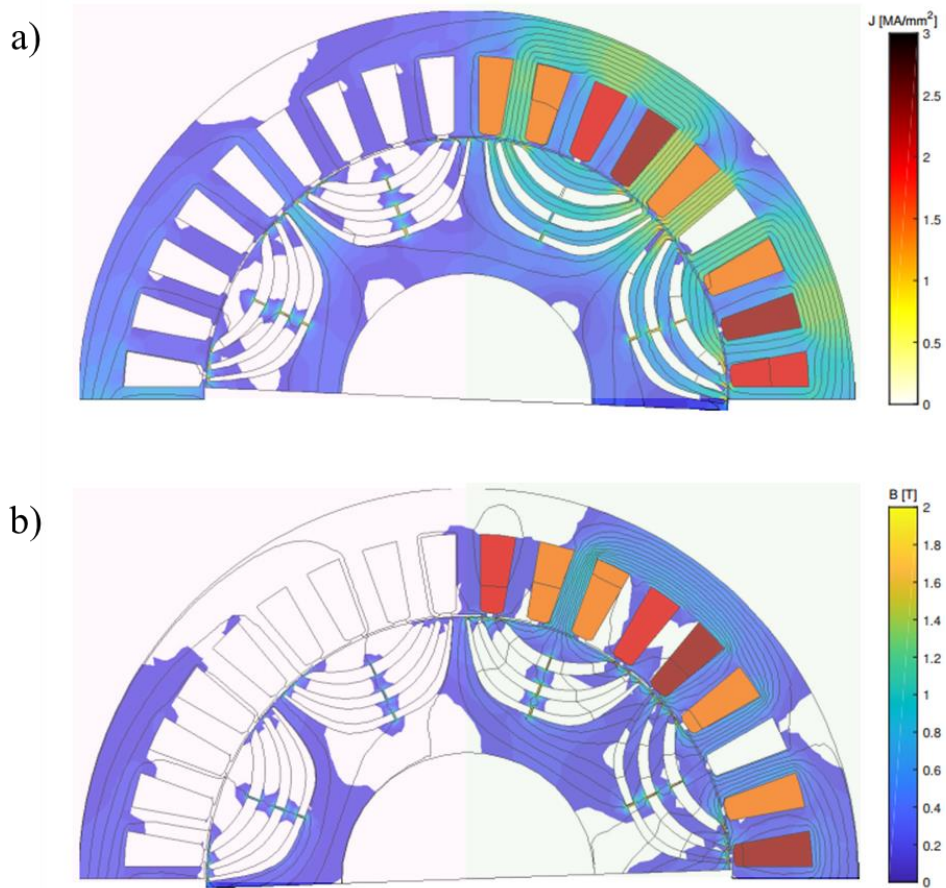


Figure 7-49: magnetic flux density distribution of a) W-12-12 *aligned* and b) W-12-12 *shifted*.

7.3.4. Magnetic Model Variations

According to the control point of view, it is important to assess the variation of the machine magnetic model between the healthy and faulty conditions. This is particularly important in case of sensorless control.

The Figure 7-50 compares the constant torque loci of the machine in healthy and OCF operating conditions; the current circle limit, MTPA and MTPV curves are also represented. It could be noticed that the two control strategies are valid both for the healthy and faulty conditions. The working points A, B and C represent the base speed and two flux-weakening point and they have been used to analyze machine performance in terms of torque.

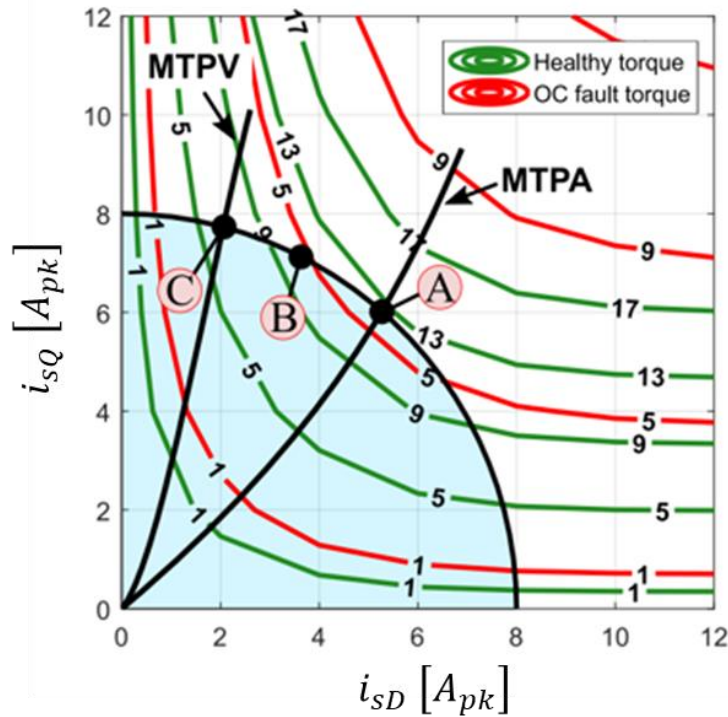


Figure 7-50: constant torque loci on i_{sD} - i_{sQ} plane and control strategies.

The Figure 7-51 shows the magnetizing curves along D- and Q-axis described as Eq. 7-31. The black solid lines are the magnetizing curves without cross-saturation phenomenon corresponding to Eq. 7-32.

$$\begin{cases} \Lambda_{sD} = \Lambda_{sD}(I_{sD}, I_{sQ}) \\ \Lambda_{sQ} = \Lambda_{sQ}(I_{sD}, I_{sQ}) \end{cases} \quad \text{Eq. 7-31}$$

$$\begin{cases} \Lambda_{sD} = \Lambda_{sD}(I_{sD}, 0) \\ \Lambda_{sQ} = \Lambda_{sQ}(0, I_{sQ}) \end{cases} \quad \text{Eq. 7-32}$$

In faulty OCF operating condition, the D-axis linkage flux Λ_{SD} of point $D_F(I_{SD} = 8A; I_{SQ} = 0)$ is 5.3% higher than the equivalent point in healthy operating condition D_H because of the lower saturation of iron paths due to the absence of cross-coupling. As I_{SQ} increases, the magnetic linkage flux reduction in faulty OCF condition is higher than the one in healthy condition, 21% and 11% respectively.

The flux-linkage variation along the Q-axis is similar to that of D-axis, but amplified. In particular, the mutual coupling causes a flux reduction around 27.3% at healthy operating condition (point Q'_H) and of 39% at faulty OCF operating condition (point Q'_F).

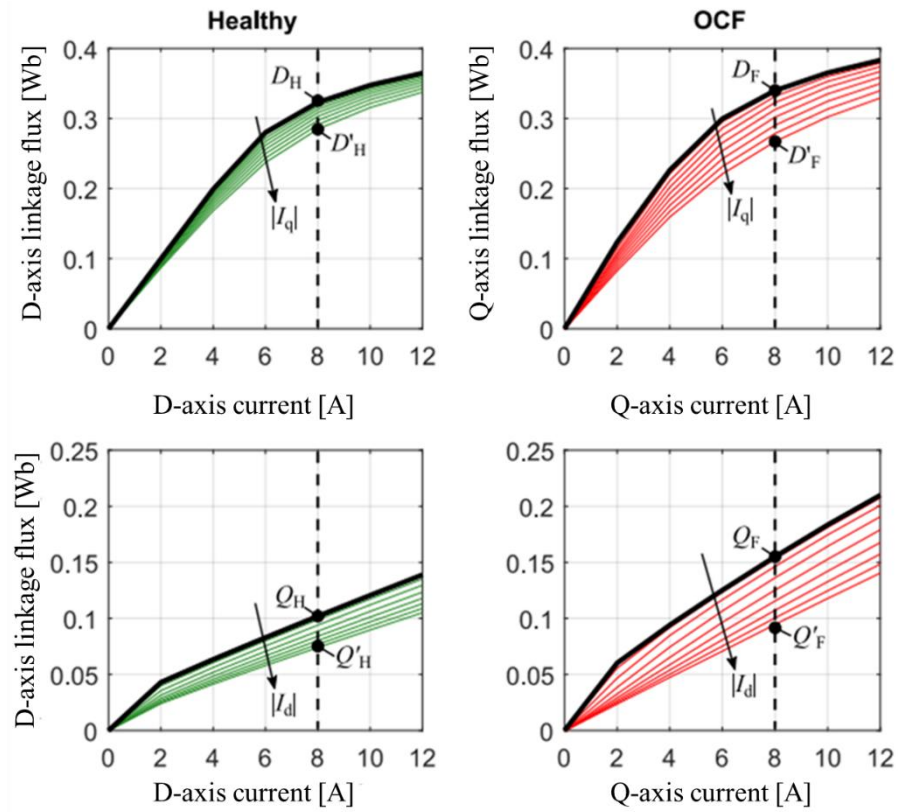


Figure 7-51: magnetizing characteristic curves along D- and Q- axis at healthy (left side) and faulty OCF (right side) operating conditions.

7.3.5. Torque Behavior Variations

The torque behavior at healthy, OCF and SCF operating condition is analyzed and compared for operating working points A, B, C of Figure 7-50.

The Figure 7-52 shows and compares the torque profiles corresponding to point A at the base speed. Figure 7-52a) represents the torque profile at healthy operating conditions where it is recognizable the slot harmonic ripple superimposed with the 3rd order harmonic due fractional slot winding⁴.

The Figure 7-52c) shows the torque profile at SCF faulty operating conditions which presents a higher oscillation than the torque profile at OCF faulty condition shown in Figure 7-52b). This phenomenon could be explained analyzing the magnetic flux density distribution respectively at OCF and SCF operating condition in Figure 7-53. According Figure 7-53a) at OCF operating condition, the magnetic load is higher than the one of Figure 7-53b) as well as the number of magnetic flux flowing in the faulty region (pink shaded area). In case of SCF faulty operating condition, the short-circuit currents affect the magnetic flux density distribution by limiting the leakage flux of the healthy winding and reducing the magnetic load. The higher torque oscillation is ascribable to the short-circuit currents amplitude that are function of the rotor position and speed. As a confirmation of this, the Figure 7-54 compares the torque profile at SCF operating condition with the short-circuit currents of the faulty winding and it can be seen that the maximum torque variations occurs to the rotor position where the short-circuit currents amplitude is maximum.

Table 7-7 summarizes the mean torque and torque ripple values at different operating condition and W-12-12 winding arrangement for three different working points. The mean torque at SCF operating condition is the same for the two W-12-12 winding arrangements, while the *aligned* one presents a lower torque ripple than the *shifted* one. On the other side the W-12-12 *shifted* presents a lower short-circuit current amplitude than the *aligned* arrangement.

⁴ $SPP = \frac{Q}{m \cdot 2 \cdot p} = \frac{36}{6 \cdot 2 \cdot 4} = 0.75$

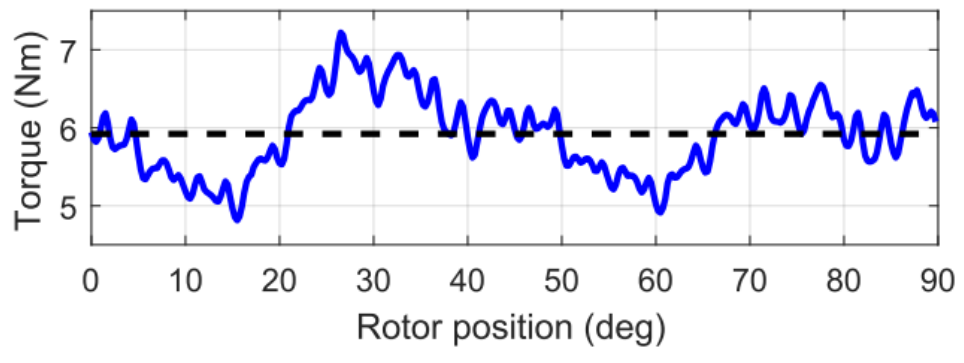
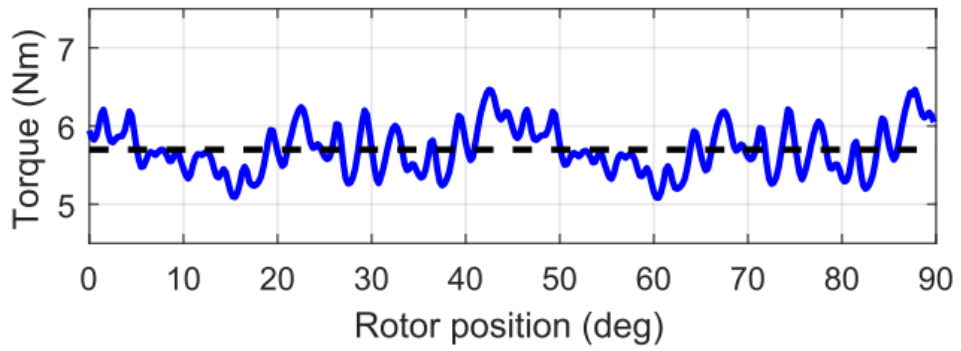
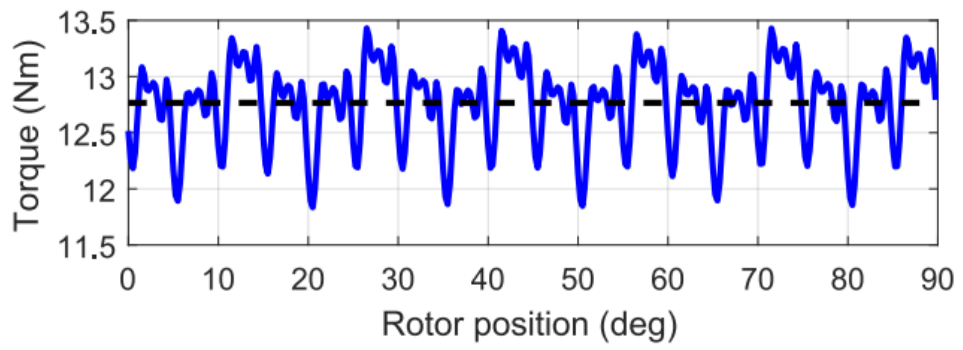


Figure 7-52: torque profiles as a function rotor position in the base speed at a) healthy, b) OCF and c) SCF working conditions.

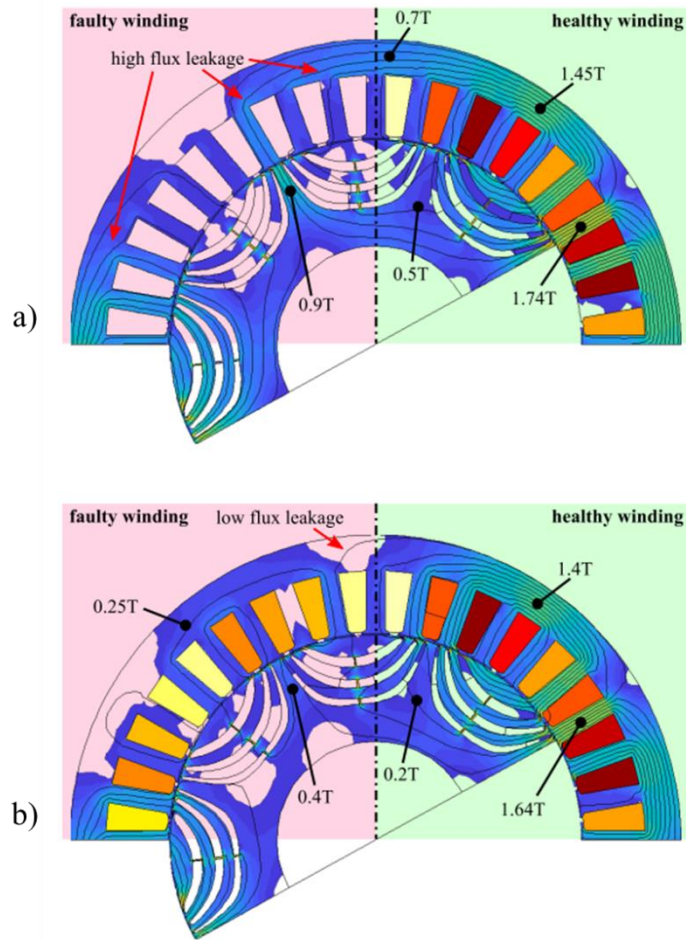


Figure 7-53: magnetic flux density distribution at a) OCF and b) SCF faulty operating conditions with the same rotor position.

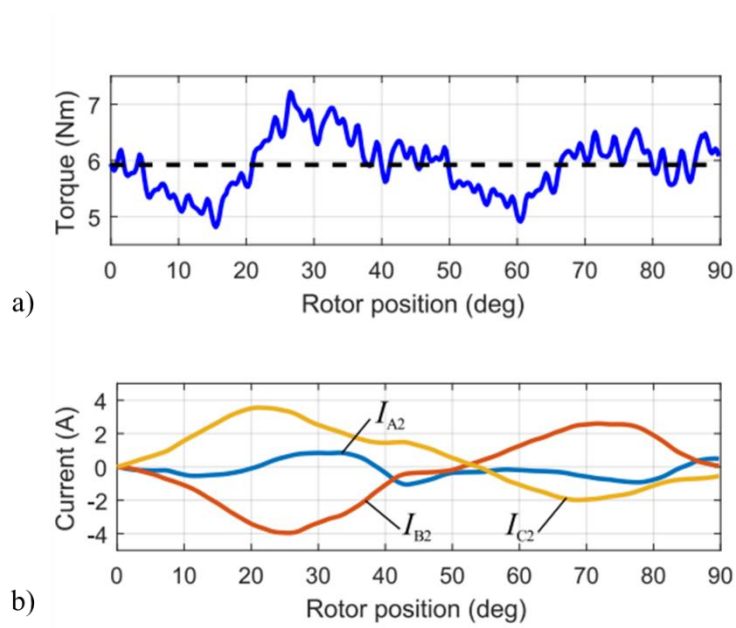


Figure 7-54: a) torque profile and b) short-circuit currents as a function of rotor position at SCF faulty operating condition.

Working Point	Current [A]	Phasor Current Angle [deg]	Mechanical Speed [r/min]	Healthy		OCF		SCF Aligned			SCF Shifted		
				Mean Torque [Nm]	Torque Ripple [%]	Mean Torque [Nm]	Torque Ripple [%]	Mean Torque [Nm]	Torque Ripple [%]	Isc [A]	Mean Torque [Nm]	Torque Ripple [%]	Isc [A]
A	8	138	800	12.7	2.8	5.7	5.5	5.9	7.5	4.0	5.9	8.4	3.5
B	8	148	900	11.9	3.2	5.3	7.4	5.5	9.5	4.7	5.5	9.7	3.5
C	8	158	1000	9.3	4.0	1.2	9.6	4.3	12.8	5.2	4.4	12	3.3

Table 7-7: simulated working points in several healthy and faulty operating conditions.

7.4. Research Activities Results

This chapter shows two different research activities related to the design of pure SyncRel machines aimed to address two different design issues typical of SyncRel machines.

Paragraph §7.2 proposes an analytical design method to limit the pulsating torque phenomenon of SyncRel machines and PMSyncRel. The method is based on undesired harmonics cancellation by means a geometrical shift of rotor flux-barriers. The flux-barrier shifting angles are computed using the wavelength of the undesired high harmonics of the air gap MMF which could arise from rotor flux-barriers Eq. 7-27 and stator slots Eq. 7-28.

The proposed method was validated via FEA on three different slot-pole combinations and the results demonstrate the effectiveness of the proposed method. The torque ripple reductions are: around the 62% of 48-8 machine at rated current density, around the 48.8% of 36-6 machine and around the 69.5% for the 36-4 machine. It is worth noticing that the choice of the most suitable shifting angle depends on the specific machine geometry and design. From a manufacturing costs point of view, the proposed method can be implemented without any additional costs with respect to traditional SyncRel and PMSyncRel machines.

The second research activity deals with the proper rotor design and stator winding arrangement of a dual three-phase pure SyncRel machine to improve machine fault-tolerant capability.

The design optimization has been carried out according to two different optimization strategies. The first one adopts healthy mean torque and torque ripple as cost functions, while the second one considers also faulty mean torque and torque ripple. Optimization results show a better effectiveness of the second approach, denoted as HF-OPT, since it yields to good mean torque and torque ripple results both at healthy and faulty operating conditions. Then, the motor geometry which exhibited the most acceptable compromise in terms of healthy and faulty performance was chosen and further analyzed by means of FEA. In addition, two different winding arrangements were analyzed: W-12-12 *aligned* and *shifted*. The two winding arrangements yield to similar performance in terms of mean torque and torque ripple at healthy and faulty conditions, but the *shifted* one has a lower magnetic mutual coupling when one three-phase winding is not working.

The analysis of machine magnetic model shows a high magnetic sensitivity to the operating conditions and to the cross-saturation phenomenon, which should be taken into account in case of sensorless control strategies.

Finally, the performance comparison between open circuit (OCF) and short-circuit faults (SCF) shows a higher mean torque and torque ripple of SCF than OCF. This result is due to the short-circuit currents flowing inside the faulty phases. In addition, the lower mutual magnetic coupling of W-12-12 *shifted* has an advantageous effect on the short-circuit currents which has a lower amplitude, thus lower Joule losses in faulty operating condition.

8. Conclusions

The present work shows an extensive research activity on the design of synchronous electrical machines. This machine typology is now one of the most adopted in different industries; in particular the permanent-magnet topology is appreciated for its high torque density, high power factor and high efficiency. Beside the permanent-magnet also the reluctance synchronous machine is gaining more and more interest thanks to its high torque density, extended flux-weakening capability and a lower manufacturing cost due to the absence of permanent-magnets.

The state-of-the-art offers many studies on the design of synchronous electrical machines such as design methods to reduce torque ripple and cogging torque. Nevertheless, many design issues are still open and the spread of electrical machines opened new scenarios from the design point of view. In fact, reliability and fault-tolerant capability are some of most important features required to machine designer in order to guarantee adequate machine performance over a long service lifetime and to safeguard human beings safety and health.

The research activities carried out during this PhD course aimed to address a part of the still open design issue in order to improve the knowledge related to the design of electrical machines. The main issues addressed in this thesis have been oriented to the improvement electrical machine performance with a particular focus on the machine reliability and fault-tolerant capability. The main contributions presented in this thesis are listed in the following:

- The chapter §3 proposes a simple analytical design method for surface permanent-magnet synchronous machines aiming to study the most suitable machine geometry to meet the performance requirements. The single design variable of the proposed method is the stator bore diameter, while the other parameters are fixed by the designer. In order to compare different slot-pole combinations the performance is referred to the stator diameters ratio. The machine performance has been compared assuming two different assumptions: the first assumes constant current density, while the second assumes constant Joule losses. The first approach could be considered as a design oriented to the maximum performance, while the second approach takes into account the thermal constraint due to Joule losses.

The results of the analytical method have been validated via FEA and they show a pretty good agreement between analytical and FEA results if the analytical method includes also the leakage air gap magnetic flux component. If the leakage magnetic flux is neglected the analytical model overestimates machine performance.

A geometry feasibility index has been defined by dividing the analytical results to FEA ones. This index could be an instrument for the machine designer to understand which stator bore diameters are the ones that allow to obtain good machine performance.

The two design approaches show that the maximum machine torque is obtained at two different stator bore diameters. A design oriented to maximize machine performance show a higher stators diameter ratio (i.e. a shorter stator bore diameter) than a design oriented to limit the thermal stress. This fact leads also to a lower

power factor due to the increasing of the winding inductance because of the greater slot area .

- Chapter §4 present a design method oriented to machine robustness with respect to typical manufacturing imperfections related to rotor mechanical defect or permanent-magnet defects intrinsically introduced by the manufacturing process. The main contribution of this research activity is the analysis of the influence of slot-pole combination on the machine robustness. In fact, the results on different slot-pole combinations of fractional-slot surface permanent-magnet machine with a double-layer arrangement show that some combinations are more sensitive to manufacturing imperfections than other ones. For instance, 12-10 and 12-14 combinations have good robustness to imperfections since their performance index at defective condition have a very little variation with respect to those at healthy conditions. On the other hand, 9-8 and 9-10 are the slot-pole combinations exhibiting a high sensitivity to manufacturing defects.

The proposed design method could be used to choose the most suitable slot-pole combination when the machines sensitivity is one of the most important requirements in the machine design;

- In Chapter §5 the fault-tolerant capability of low-cost surface permanent-magnet machine prone to permanent-magnet demagnetization has been increased by means a new rotor design. Low-cost machines have been gained more and more interest among electrical machine manufacturer because allow to moving from the traditional induction motor to the more efficient permanent-magnet synchronous machine while containing the manufacturing cost.

Unfortunately, permanent-magnets are prone to demagnetization because of the low PWM switching frequency to limit switching losses and low winding inductance due to machine size. These conditions increase phase current ripple which induces additional eddy currents inside permanent-magnets and increase permanent-magnet working temperature.

In order to overcome this drawback, the contribution of this research activity has been the design of a inner permanent-magnet rotor in order to protect them from current ripple and thus reducing their working temperature. The improvement of the proposed rotor has been validated both via finite element analysis and experimental tests.

- The contribution of chapter §6 is the design of an ironless dual-rotor surface permanent-magnet synchronous machine for a mechanical renewable energy storage system for household application. The proposed ironless solution eliminates iron core losses during the self-braking duration in order to meet the time-shift proposition of renewable energy storage systems. In addition, the dual-rotor configuration allows increasing the magnetic permeance of the magnetic paths obtaining the similar in terms of torque density of the iron core machines.

The proposed ironless dual-rotor solution has been compared with iron core surface permanent-magnet magnet and pure synchronous reluctance machines by means an extensive FEA simulation activity.

The ironless dual-rotor machine has been prototyped and tested. The experimental results show the good performance in terms of conversion efficiency, but pointed

out the importance of a good mechanical bearing system in order to limit mechanical losses during self-discharge duration.

- The paragraph §7.1 shows an analytical design method to reduce the pulsating torque of synchronous reluctance motor by means rotor flux-barriers shifting angle. Three different slot-pole combinations of pure and permanent-magnet assisted reluctance machines have been designed according to the analytical design rules without employing iterative optimization or genetic algorithms. Then the flux-barrier shifting angle has been computed as a function of the wavelength of the undesired high harmonics.

The proposed method has been validated via FEA for the three reference machines and the simulation results confirm the effectiveness in pulsating torque reduction both at rated and overload current densities. It worth noting that two shifting angles could be used as a function of the main source of high order harmonics between stator slots and rotor flux-barriers.

- The contribution of the research activity presented at paragraph §7.2 is a design method for dual three-phase pure reluctance machine for fault tolerance applications. The proposed rotor geometry is the one which allows to minimize the torque ripple at faulty condition and it has been chosen among different machine geometries optimized according to two different optimization strategies.

The chosen individual has been analyzed both at healthy and faulty conditions with two different winding arrangement denoted as aligned and shifted. FEA results show that the two winding arrangement have the same performance in terms of mean torque and torque ripple, but the shifted arrangement has a lower mutual magnetic coupling at faulty condition. The lower magnetic coupling allows also to mitigating the amplitude of the short-circuit current and thus of the correlated Joule losses.

From a machine control point of view, the magnetic model of the dual three-phase machine has a strong variation from healthy conditions due cross-saturation. This phenomenon is particularly pronounced for the Q-axis inductance. Thus, the variation of the magnetic model has to be taken into account in case of sensorless control strategy.

References

- [1] IEC TS NP 60034-31: 2018, Rotating Electrical Machines – Part 31: Selection of energy-efficient motors including variable speed applications – Application guide;
- [2] R.P. Feynman, R. B. Leighton, M. Sands, “La Fisica di Feynman”, Zanichelli Editore, ISBN-10 8808221075, ISBN-13 978-8808221070, 2017
- [3] David Meeker, “Finite Element Method Magnetic”, User’s Manual, January 30, 2018. [Online] Available: <http://www.femm.info/wiki/Documentation/>;
- [4] Nicola Bianchi, “Calcolo delle Macchine Elettriche col Metodo degli Elementi Finiti”, 2001, CLEUP Scarl editore, ISBN 88 7178 528 2, ISBN 978 88 7178 528 8
- [5] “Speed’s Electric Machines, An Outline of some theory in the SPEED software for electric machine design”, lecture notes of TJE Miller of University of Glasgow 2002-2009;
- [6] I. Boldea, S. A. Nasar, “The induction machine handbook”, CRC Press, ISBN 0-8493-0004-5, 2002.
- [7] G.J.Retter, “Matrix and Space-Phasor Theory of Electrical Machines”, Akadémiai Kiadó, Budapest 1987, ISBN 963 05 4232 3;
- [8] Ronghai Qu and T. A. Lipo, "Analysis and modeling of air-gap and zigzag leakage fluxes in a surface-mounted permanent-magnet Machine," in IEEE Transactions on Industry Applications, vol. 40, no. 1, pp. 121-127, Jan.-Feb. 2004. doi: 10.1109/TIA.2003.821790;
- [9] L. Gasparin, A. Cernigoj, S. Markic and R. Fiser, "Additional Cogging Torque Components in Permanent-Magnet Motors Due to Manufacturing Imperfections," in IEEE Transactions on Magnetics, vol. 45, no. 3, pp. 1210-1213, March 2009. doi: 10.1109/TMAG.2009.2012561;
- [10] L. Wu et al., "Analysis of cogging torque in surface permanent magnet machine with manufacturing tolerances," IECON 2015 - 41st Annual Conference of the IEEE Industrial Electronics Society, Yokohama, 2015, pp. 004732-004737. doi: 10.1109/IECON.2015.7392839;
- [11] S. Jia, R. Qu, J. Li, Z. Fu, H. Chen and L. Wu, "Analysis of FSCW SPM servo motor with static, dynamic and mixed eccentricity in aspects of radial force and vibration," 2014 IEEE Energy Conversion Congress and Exposition (ECCE), Pittsburgh, PA, 2014, pp. 1745-1753. doi: 10.1109/ECCE.2014.6953629;
- [12] D. G. Dorrell, M. Hsieh and Y. Guo, "Unbalanced Magnet Pull in Large Brushless Rare-Earth Permanent Magnet Motors with Rotor Eccentricity," in IEEE Transactions on Magnetics, vol. 45, no. 10, pp. 4586-4589, Oct. 2009. doi: 10.1109/TMAG.2009.2022338;
- [13] R. Ginzarly, G. Hoblos, N. Moubayed, “Electromagnetic and vibration finite element model for early fault detection in permanent magnet machine”, IFAC-PapersOnLine, Volume 51, Issue 24, 2018, Pages 902-907, ISSN 2405-8963, <https://doi.org/10.1016/j.ifacol.2018.09.682>;
- [14] A. M. EL-Refaie and T. M. Jahns, "Optimal flux weakening in surface PM machines using fractional-slot concentrated windings," in IEEE Transactions on Industry Applications, vol. 41, no. 3, pp. 790-800, May-June 2005. doi: 10.1109/TIA.2005.847312;

- [15] A. M. El-refaie and T. M. Jahns, "Impact of Winding Layer Number and Magnet Type on Synchronous Surface PM Machines Designed for Wide Constant-Power Speed Range Operation," Conference Record of the 2006 IEEE Industry Applications Conference Forty-First IAS Annual Meeting, Tampa, FL, 2006, pp. 1486-1493. doi: 10.1109/IAS.2006.256726;
- [16] E. Fornasiero, L. Alberti, N. Bianchi and S. Bolognani, "Considerations on Selecting Fractional-Slot Nonoverlapped Coil Windings," in IEEE Transactions on Industry Applications, vol. 49, no. 3, pp. 1316-1324, May-June 2013. doi: 10.1109/TIA.2013.2251853;
- [17] N. Bianchi and S. Bolognani, "Design techniques for reducing the cogging torque in surface-mounted PM motors," in IEEE Transactions on Industry Applications, vol. 38, no. 5, pp. 1259-1265, Sept.-Oct. 2002. doi: 10.1109/TIA.2002.802989;
- [18] B. Boazzo, G. Pellegrino and A. Vagati, "Multipolar SPM Machines for Direct-Drive Application: A General Design Approach," in IEEE Transactions on Industry Applications, vol. 50, no. 1, pp. 327-337, Jan.-Feb. 2014. doi: 10.1109/TIA.2013.2271291;
- [19] J. Cros and P. Viarouge, "Synthesis of high performance PM motors with concentrated windings," in IEEE Transactions on Energy Conversion, vol. 17, no. 2, pp. 248-253, June 2002. doi: 10.1109/TEC.2002.1009476;
- [20] Bianchi, N.; Dai Prè, M.; Alberti, L.; Fornasiero, E. "Theory and Design of Fractional-Slot PM Machines", 1st ed.; CLEUP sc; Coop. Libreria Editrice Università di Padova: Padova, Italy, 2007; ISBN 978-88-6129-5;
- [21] IEC 60034-30-1: 2014, Rotating Electrical Machines – Part 30-1: Efficiency Classes of Line Operated AC Motors (Code IE);
- [22] C. Bianchini, M. Davoli, G. Pellegrino, F. Immovilli and E. Lorenzani, "Low cost PM synchronous servo-applications employing asynchronous-motor frame," 2015 IEEE Energy Conversion Congress and Exposition (ECCE), Montreal, QC, 2015, pp. 6090-6095. doi: 10.1109/ECCE.2015.7310513;
- [23] K. Yamazaki, M. Shina, Y. Kanou, M. Miwa and J. Hagiwara, "Effect of Eddy Current Loss Reduction by Segmentation of Magnets in Synchronous Motors: Difference Between Interior and Surface Types," in IEEE Transactions on Magnetics, vol. 45, no. 10, pp. 4756-4759, Oct. 2009. doi: 10.1109/TMAG.2009.2024159;
- [24] K. Yamazaki et al., "Reduction of magnet eddy current loss in interior permanent magnet motors with concentrated windings," 2009 IEEE Energy Conversion Congress and Exposition, San Jose, CA, 2009, pp. 3963-3969. doi: 10.1109/ECCE.2009.5316114;
- [25] A. Tessarolo, "A survey of state-of-the-art methods to compute rotor eddy-current losses in synchronous permanent magnet machines," 2017 IEEE Workshop on Electrical Machines Design, Control and Diagnosis (WEMDCD), Nottingham, 2017, pp. 12-19. doi: 10.1109/WEMDCD.2017.7947717;
- [26] K. Yamazaki and Y. Fukushima, "Effect of eddy-current loss reduction by magnet segmentation in synchronous motors with concentrated windings," 2009

- International Conference on Electrical Machines and Systems, Tokyo, 2009, pp. 1-6. doi: 10.1109/ICEMS.2009.5382795;
- [27] K. Yamazaki and A. Abe, "Loss Investigation of Interior Permanent-Magnet Motors Considering Carrier Harmonics and Magnet Eddy Currents," in *IEEE Transactions on Industry Applications*, vol. 45, no. 2, pp. 659-665, March-april 2009. doi: 10.1109/TIA.2009.2013550;
- [28] W. Huang, A. Bettayeb, R. Kaczmarek and J. Vannier, "Optimization of Magnet Segmentation for Reduction of Eddy-Current Losses in Permanent Magnet Synchronous Machine," in *IEEE Transactions on Energy Conversion*, vol. 25, no. 2, pp. 381-387, June 2010. doi: 10.1109/TEC.2009.2036250;
- [29] J. Li, Y. Xu, J. Zou, Q. Wang and W. Liang, "Analysis and Reduction of Magnet Loss by Deepening Magnets in Interior Permanent-Magnet Machines With a Pole/Slot Ratio of 2/3," in *IEEE Transactions on Magnetics*, vol. 51, no. 11, pp. 1-4, Nov. 2015, Art no. 8112004. doi: 10.1109/TMAG.2015.2445787;
- [30] N. Boubaker, D. Matt, P. Enrici, F. Nierlich, G. Durand, F. Orlandini, X. Longère, J.S. Aïgba, Study of eddy-current loss in the sleeves and Sm–Co magnets of a high-performance SMPM synchronous machine (10kRPM, 60kW), *Electric Power Systems Research*, Volume 142, 2017, Pages 20-28, ISSN 0378-7796, <https://doi.org/10.1016/j.epsr.2016.08.045>;
- [31] R. Hebner, J. Beno and A. Walls, "Flywheel batteries come around again," in *IEEE Spectrum*, vol. 39, no. 4, pp. 46-51, April 2002. doi: 10.1109/6.993788;
- [32] Sandia, "Conceptual design of a flywheel energy storage system," Sandia Laboratories, no. 4, 1979;
- [33] Deloitte, "Energy storage: Tracking the technologies that will transform the power sector," 2015. [Online] Available: <https://www2.deloitte.com/content/dam/Deloitte/no/Documents/energy-resources/energy-storage-tracking-technologies-transform-power-sector.pdf>;
- [34] J. Eyer; G. Corey, "Energy storage for electricity grid: Benefits and market potential assessment guide. A case study for the doe energy storage system program," Sandia Report, 2010. [Online]. Available: <https://www.sandia.gov/ess-ssl/publications/SAND2010-0815.pdf>;
- [35] L. V. Woensel, G. Archer, "Ten Technologies which could change our liver. Potential impacts and policy implications", EPRS – European Parliamentary Research Service. Scientific Foresight (STOA) Unit. 2015. [Online] Available: http://www.europarl.europa.eu/EPRS/EPRS_IDAN_527417_ten_trends_to_change_your_life.pdf;
- [36] H. Akagi and H. Sato, "Control and performance of a doubly-fed induction machine intended for a flywheel energy storage system," in *IEEE Transactions on Power Electronics*, vol. 17, no. 1, pp. 109-116, Jan. 2002. doi: 10.1109/63.988676;
- [37] G. Cimuca, S. Breban, M. M. Radulescu, C. Saudemont and B. Robyns, "Design and Control Strategies of an Induction-Machine-Based Flywheel Energy Storage System Associated to a Variable-Speed Wind Generator," in *IEEE Transactions on Energy Conversion*, vol. 25, no. 2, pp. 526-534, June 2010. doi: 10.1109/TEC.2010.2045925;

- [38] K. Liu, X. Fu, M. Lin and L. Tai, "AC Copper Losses Analysis of the Ironless Brushless DC Motor used in a Flywheel Energy Storage System," in *IEEE Transactions on Applied Superconductivity*, vol. 26, no. 7, pp. 1-5, Oct. 2016, Art no. 0611105. doi: 10.1109/TASC.2016.2602500;
- [39] I. M. Higginson, H. Hess and J. D. Law, "Ironless permanent magnet synchronous machine stiffness calculations for flywheel energy storage systems," 2011 IEEE International Electric Machines & Drives Conference (IEMDC), Niagara Falls, ON, 2011, pp. 1357-1362. doi: 10.1109/IEMDC.2011.5994803;
- [40] S. Jang, D. You, K. Ko and S. Choi, "Design and Experimental Evaluation of Synchronous Machine Without Iron Loss Using Double-Sided Halbach Magnetized PM Rotor in High Power FESS," in *IEEE Transactions on Magnetics*, vol. 44, no. 11, pp. 4337-4340, Nov. 2008. doi: 10.1109/TMAG.2008.2001499;
- [41] N. Bianchi, E. Fornasiero and S. Bolognani, "Effect of Stator and Rotor Saturation on Sensorless Rotor Position Detection," in *IEEE Transactions on Industry Applications*, vol. 49, no. 3, pp. 1333-1342, May-June 2013. doi: 10.1109/TIA.2013.2253437;
- [42] A. Vagati, "The synchronous reluctance solution: a new alternative in AC drives," *Proceedings of IECON'94 - 20th Annual Conference of IEEE Industrial Electronics*, Bologna, Italy, 1994, pp. 1-13 vol.1. doi: 10.1109/IECON.1994.397741;
- [43] A. Vagati, B. Boazzo, P. Guglielmi and G. Pellegrino, "Design of Ferrite-Assisted Synchronous Reluctance Machines Robust Toward Demagnetization," in *IEEE Transactions on Industry Applications*, vol. 50, no. 3, pp. 1768-1779, May-June 2014. doi: 10.1109/TIA.2013.2284302;
- [44] A. Vagati, M. Pastorelli, G. Franceschini and C. Petrace, "Design of low-torque-ripple synchronous reluctance motors," *IAS '97. Conference Record of the 1997 IEEE Industry Applications Conference Thirty-Second IAS Annual Meeting*, New Orleans, LA, USA, 1997, pp. 286-293 vol.1. doi: 10.1109/IAS.1997.643040;
- [45] N. Bianchi, S. Bolognani, D. Bon and M. D. Pre, "Rotor flux-barrier design for torque ripple reduction in synchronous reluctance motors," *Conference Record of the 2006 IEEE Industry Applications Conference Forty-First IAS Annual Meeting*, Tampa, FL, 2006, pp. 1193-1200. doi: 10.1109/IAS.2006.256683;
- [46] R. Moghaddam and F. Gyllensten, "Novel High-Performance SynRM Design Method: An Easy Approach for A Complicated Rotor Topology," in *IEEE Transactions on Industrial Electronics*, vol. 61, no. 9, pp. 5058-5065, Sept. 2014. doi: 10.1109/TIE.2013.2271601;
- [47] R. R. Moghaddam, F. Magnussen and C. Sadarangani, "Novel rotor design optimization of synchronous reluctance machine for high torque density," *6th IET International Conference on Power Electronics, Machines and Drives (PEMD 2012)*, Bristol, 2012, pp. 1-4. doi: 10.1049/cp.2012.0256;
- [48] G. Pellegrino, F. Cupertino and C. Gerada, "Automatic Design of Synchronous Reluctance Motors Focusing on Barrier Shape Optimization," in *IEEE Transactions on Industry Applications*, vol. 51, no. 2, pp. 1465-1474, March-April 2015. doi: 10.1109/TIA.2014.2345953;

- [49] F. Cupertino, G. Pellegrino and C. Gerada, "Design of Synchronous Reluctance Motors With Multiobjective Optimization Algorithms," in *IEEE Transactions on Industry Applications*, vol. 50, no. 6, pp. 3617-3627, Nov.-Dec. 2014. doi: 10.1109/TIA.2014.2312540;
- [50] A. Vagati, A. Canova, M. Chiampi, M. Pastorelli and M. Repetto, "Design refinement of synchronous reluctance motors through finite-element analysis," in *IEEE Transactions on Industry Applications*, vol. 36, no. 4, pp. 1094-1102, July-Aug. 2000. doi: 10.1109/28.855965;
- [51] T. A. Lipo, A. Vagati, T. Miller, L. Malesani, I. Boldea, and T. Fukao, "Synchronous Reluctance Motors and Drives – A Novel Alternative.", Denver: IEEE Industry Applications Society, 1994;
- [52] N. Bianchi, M. D. Pre and S. Bolognani, "Design of a fault-tolerant IPM motor for electric power steering," in *IEEE Transactions on Vehicular Technology*, vol. 55, no. 4, pp. 1102-1111, July 2006. doi: 10.1109/TVT.2006.877716;
- [53] B. A. Welchko, T. M. Jahns, W. L. Soong and J. M. Nagashima, "IPM synchronous machine drive response to symmetrical and asymmetrical short circuit faults," in *IEEE Transactions on Energy Conversion*, vol. 18, no. 2, pp. 291-298, June 2003. doi: 10.1109/TEC.2003.811746;
- [54] A. G. Jack, B. C. Mecrow and J. A. Haylock, "A comparative study of permanent magnet and switched reluctance motors for high-performance fault-tolerant applications," in *IEEE Transactions on Industry Applications*, vol. 32, no. 4, pp. 889-895, July-Aug. 1996. doi: 10.1109/28.511646;
- [55] P. Azer, J. Ye and A. Emadi, "Advanced Fault-Tolerant Control Strategy for Switched Reluctance Motor Drives," 2018 IEEE Transportation Electrification Conference and Expo (ITEC), Long Beach, CA, 2018, pp. 20-25. doi: 10.1109/ITEC.2018.8450151;
- [56] T. J. Miller, "Switched reluctance motors and their control," ser Monographs in electrical and electronic engineering. Magna Physics, 1993. [Online] Available: https://books.google.it/books/about/Switched_Reluctance_Motors_and_Their_Con.html?id=DtpiQgAACAAJ&redir_esc=y;
- [57] A. Vagati, M. Pastorelli and G. Franceschini, "High-performance control of synchronous reluctance motors," in *IEEE Transactions on Industry Applications*, vol. 33, no. 4, pp. 983-991, July-Aug. 1997. doi: 10.1109/28.605740;
- [58] A. Vagati, A. Canova, M. Chiampi, M. Pastorelli and M. Repetto, "Design refinement of synchronous reluctance motors through finite-element analysis," in *IEEE Transactions on Industry Applications*, vol. 36, no. 4, pp. 1094-1102, July-Aug. 2000. doi: 10.1109/28.855965
- [59] N. Bianchi and T.M. Jahns, et al, Tutorials on "Design, Analysis and Control of Interior PM Synchronous Machines", IEEE IAS Annual Meeting, Seattle, Oct. 12, 2004 (Chapter 6);
- [60] Vagati, A.; Fratta, A.; Franceschini, G.; Rosso, P., "AC motors for high-performance drives: a design-based comparison," *Industry Applications, IEEE Transactions on*, vol.32, no.5, pp.1211,1219, Sep/Oct 1996;
- [61] G. Pellegrino, "PM-Assistend Synchronous Reluctance Machines", Politecnico of Torino and University of Wisconsin, Madison [Lecture Notes]

- [62] N. Bianchi, "Synchronous reluctance and interior permanent magnet motors," 2013 IEEE Workshop on Electrical Machines Design, Control and Diagnosis (WEMDCD), Paris, 2013, pp. 75-84. doi: 10.1109/WEMDCD.2013.6525167;
- [63] S. Han, T. M. Jahns and W. L. Soong, "Torque Ripple Reduction in Interior Permanent Magnet Synchronous Machines Using the Principle of Mutual Harmonics Exclusion," 2007 IEEE Industry Applications Annual Meeting, New Orleans, LA, 2007, pp. 558-565. doi: 10.1109/07IAS.2007.90;
- [64] N. Bianchi and T. Jahns, "Analytical of ipm motor- part i. analytical approach in design, analysis, and control of interior pm synchronous machines", *Conf. Rec. IEEE IAS Tutorial Course Notes, Seattle*, pp. 3.1-3.3, Oct 2005;
- [65] M. Barcaro, G. Meneghetti and N. Bianchi, "Structural Analysis of the Interior PM Rotor Considering Both Static and Fatigue Loading," in *IEEE Transactions on Industry Applications*, vol. 50, no. 1, pp. 253-260, Jan.-Feb. 2014. doi: 10.1109/TIA.2013.2268048;
- [66] E. C. Lovelace, T. M. Jahns, T. A. Keim and J. H. Lang, "Mechanical design considerations for conventionally-laminated, high-speed, interior PM synchronous machine rotors," IEMDC 2001. IEEE International Electric Machines and Drives Conference (Cat. No.01EX485), Cambridge, MA, USA, 2001, pp. 163-169. doi: 10.1109/IEMDC.2001.939292;
- [67] N. Bianchi, E. Fornasiero and W. Soong, "Optimal selection of PM flux linkage in a PM assisted synchronous reluctance machine," 2014 International Conference on Electrical Machines (ICEM), Berlin, 2014, pp. 1341-1347. doi: 10.1109/ICELMACH.2014.6960356;
- [68] P. Guglielmi, B. Boazzo, E. Armando, G. Pellegrino and A. Vagati, "Magnet minimization in IPM-PMASR motor design for wide speed range application," 2011 IEEE Energy Conversion Congress and Exposition, Phoenix, AZ, 2011, pp. 4201-4207. doi: 10.1109/ECCE.2011.6064342;
- [69] G. Pellegrino, P. Guglielmi, A. Vagati and F. Villata, "Core Losses and Torque Ripple in IPM Machines: Dedicated Modeling and Design Tradeoff," in *IEEE Transactions on Industry Applications*, vol. 46, no. 6, pp. 2381-2391, Nov.-Dec. 2010. doi: 10.1109/TIA.2010.2072971;
- [70] N. Bianchi and S. Bolognani, "Design techniques for reducing the cogging torque in surface-mounted PM motors," in *IEEE Transactions on Industry Applications*, vol. 38, no. 5, pp. 1259-1265, Sept.-Oct. 2002. doi: 10.1109/TIA.2002.802989;
- [71] N. Bianchi, S. Bolognani, D. Bon and M. Dai Pr e, "Torque Harmonic Compensation in a Synchronous Reluctance Motor," in *IEEE Transactions on Energy Conversion*, vol. 23, no. 2, pp. 466-473, June 2008. doi: 10.1109/TEC.2007.914357;
- [72] N. Bianchi, M. Degano and E. Fornasiero, "Sensitivity Analysis of Torque Ripple Reduction of Synchronous Reluctance and Interior PM Motors," in *IEEE Transactions on Industry Applications*, vol. 51, no. 1, pp. 187-195, Jan.-Feb. 2015. doi: 10.1109/TIA.2014.2327143;

- [73] M. Nashiki, A. Satake, Y. Kawai, T. Yokochi and S. Okuma, "A new flux-barrier-type reluctance motor with a slit rotor," in *IEEE Transactions on Industrial Electronics*, vol. 46, no. 6, pp. 1199-1206, Dec. 1999. doi: 10.1109/41.808010;
- [74] M. Sanada, K. Hiramoto, S. Morimoto and Y. Takeda, "Torque ripple improvement for synchronous reluctance motor using an asymmetric flux barrier arrangement," in *IEEE Transactions on Industry Applications*, vol. 40, no. 4, pp. 1076-1082, July-Aug. 2004. doi: 10.1109/TIA.2004.830745;
- [75] C. Bianchini, F. Immovilli, E. Lorenzani, A. Bellini and M. Davoli, "Review of Design Solutions for Internal Permanent-Magnet Machines Cogging Torque Reduction," in *IEEE Transactions on Magnetics*, vol. 48, no. 10, pp. 2685-2693, Oct. 2012. doi: 10.1109/TMAG.2012.2199509;
- [76] L. Alberti and N. Bianchi, "Impact of winding arrangement in dual 3-phase induction motor for fault tolerant applications," *The XIX International Conference on Electrical Machines - ICEM 2010*, Rome, 2010, pp. 1-6. doi: 10.1109/ICELMACH.2010.5607941;
- [77] L. Alberti and N. Bianchi, "Experimental Tests of Dual Three-Phase Induction Motor Under Faulty Operating Condition," in *IEEE Transactions on Industrial Electronics*, vol. 59, no. 5, pp. 2041-2048, May 2012. doi: 10.1109/TIE.2011.2171175;
- [78] Zhong Peng, Z. Zheng, Y. Li and Z. Liu, "Fault-tolerant control of multiphase induction machine drives based on virtual winding method," *2017 IEEE Transportation Electrification Conference and Expo (ITEC)*, Chicago, IL, 2017, pp. 252-256. doi: 10.1109/ITEC.2017.7993280;
- [79] Q. Chen, G. Liu, W. Gong and W. Zhao, "A New Fault-Tolerant Permanent-Magnet Machine for Electric Vehicle Applications," in *IEEE Transactions on Magnetics*, vol. 47, no. 10, pp. 4183-4186, Oct. 2011. doi: 10.1109/TMAG.2011.2146238;
- [80] L. Parsa and H. A. Toliyat, "Fault-tolerant five-phase permanent magnet motor drives," *Conference Record of the 2004 IEEE Industry Applications Conference, 2004. 39th IAS Annual Meeting.*, Seattle, WA, USA, 2004, pp. 1048-1054 vol.2. doi: 10.1109/IAS.2004.1348542;
- [81] C. Babetto and N. Bianchi, "Synchronous Reluctance Motor with Dual Three-Phase Winding for Fault-Tolerant Applications," *2018 XIII International Conference on Electrical Machines (ICEM)*, Alexandroupoli, 2018, pp. 2297-2303. doi: 10.1109/ICELMACH.2018.8506771;

Acknowledgments

I would like to thank Raw Power Srl at first, because it decided to invest on my capabilities, giving me chance to undertake the PhD course.

The PhD allows me to improve my knowledge on electrical machines and static energy conversion. In addition, thank to my research activity results, I had the opportunity to travel and visit new places around the world. These experiences have been deeply elevated my person, since I met and knew new realities and people involved in the same research field.

My heartfelt thanks go to Prof. Claudio Bianchini who followed me along my growth and training path, from the end of the Master Degree to the present day. He always believed in my capabilities, thus who am I and what I know is also the result of his support.

Thanks go to Prof. Emilio Lorenzani as my PhD tutor.

Sincere thank goes to my family which has always supported my choices.

Finally, my most devoted and sincere thank goes to Doctor Francesco Merli and the staff of the hematology unit of Arcispedale Santa Maria Nuova of Reggio Emilia (Italy). In fact, thanks to their therapies and resolution, I had the chance to seize every opportunity that the life gave to me.

Ringraziamenti

In primo luogo, i miei ringraziamenti sono indirizzati a Raw Power Srl che tre anni fa ha deciso di investire nelle mie capacità, offrendomi la possibilità di intraprendere il percorso del dottorato di ricerca.

Il dottorato mi ha permesso di ampliare le mie conoscenze sulle macchine elettriche e sulla conversione statica dell'energia. Inoltre, grazie ai risultati dall'attività di ricerca, ho avuto l'opportunità di viaggiare e visitare nuovi luoghi attorno al mondo. Queste esperienze hanno notevolmente arricchito la mia persona, poiché ho potuto incontrare e conoscere nuove realtà e persone coinvolte negli stessi ambiti di ricerca.

Sentiti ringraziamenti, sono indirizzati al Prof. Claudio Bianchini che mi ha accompagnato nel mio percorso di crescita e formazione, dalla fine della laurea magistrale ad oggi. Ha sempre creduto nella mia persona e quello che sono e so oggi è anche grazie al suo sostegno.

Ringraziamenti vanno al Prof. Emilio Lorenzani che mi seguito con l'incarico di tutor nel corso di dottorato.

Ringraziamenti vanno anche alla mia famiglia che come sempre ha sostenuto le mie scelte.

Infine, il ringraziamento più affettuoso e sincero è rivolto al Dott. Francesco Merli e allo staff del reparto di Ematologia dell'Arcispedale Santa Maria Nuova di Reggio Emilia perché è grazie alle loro cure e alla loro determinazione, se ho potuto cogliere tutte le opportunità che la vita mi ha offerto.

Appendix

A. Brief Review of Vectors

Many physical quantities can be expressed with vectors where a vector is an element of a vector space. According to the specific vector space, a vector can be identified by its vector space identity e.g. if a vector belongs to a Euclidean space, it is called Euclidean vector. Each vector is defined by:

- A magnitude which is the length of the segment;
- A direction.

Generally, if a physical quantity is vector, it is written by a letter with above arrow i.e. \vec{A} . Graphically, vectors are represented with arrows as shown in Figure 0-1.

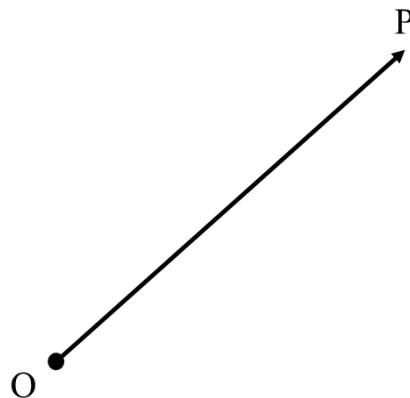


Figure 0-1: graphic representation of a vector.

The point O is denoted as point of application, while point P is the free end. If the coordinates of the point O are given the vector is denoted as a *bound vector*, otherwise is denoted as *free vector*.

Given a Cartesian coordinate system for a three-dimensional space, a free vector can be represented with three numbers e.g. its amplitude and two direction cosines, or the three vector projections along the three axes, also called Cartesian components. Considering the bound vector \vec{A} in the three-dimensional space, it can be identified by six numbers: the three Cartesian components (A_x, A_y, A_z) and its direction cosines $(\cos \alpha, \cos \beta, \cos \gamma)$. Between the Cartesian components and direction cosines subsist the following expressions:

$$\begin{cases} \vec{A}_x = |\vec{A}| \cos \alpha \\ \vec{A}_y = |\vec{A}| \cos \beta \\ \vec{A}_z = |\vec{A}| \cos \gamma \end{cases} \quad \text{Eq. 0-1}$$

The Figure 0-2 shows the vector \vec{A} on two-dimensional Cartesian plane, thus the z-axis component is equal to zero.

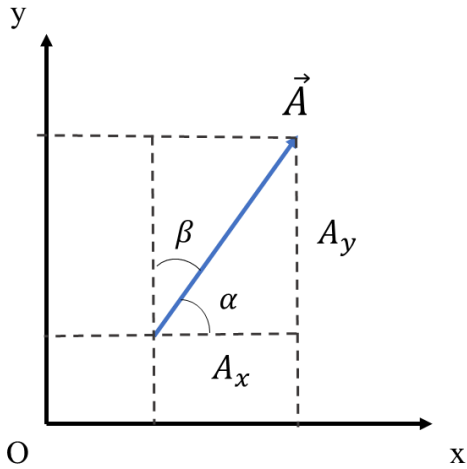


Figure 0-2: representation of vector components and direction cosines on the Cartesian plane.

A particular vector is the unity vector which has the magnitude equal to one and it is represented as \hat{A} . The Cartesian components of the unity vector coincide with its direction cosines. Considering a three-dimensional space, the Cartesian components of the unity vector in Eq. 0-2 represent a Cartesian coordinate system basis.

$$\hat{i} = (1,0,0); \hat{j} = (0,1,0); \hat{k} = (0,0,1) \tag{Eq. 0-2}$$

In a three-dimensional space, a vector \vec{A} can be expressed as the linear combination of the Cartesian coordinate system basis and vector Cartesian components (A_x, A_y, A_z) .

$$\vec{A} = A_x\hat{i} + A_y\hat{j} + A_z\hat{k} = \vec{A}_x + \vec{A}_y + \vec{A}_z \tag{Eq. 0-3}$$

According to this, the unity vector of the Cartesian coordinate system is used to characterize vector \vec{A} on the three-dimensional space because it is used to identify its direction in the space.

Recall of Products with Vectors

Given the vector \vec{A} , there are three different products that can be applied:

- Scalar multiplication;
- Dot product or scalar product;
- Cross product.

Scalar Multiplication

The scalar multiplication is the product between a vector \vec{A} and a scalar value or a real number $\varphi = \varphi(x, y, z, t)$.

$$\varphi\vec{A} = (\varphi\vec{A}_x, \varphi\vec{A}_y, \varphi\vec{A}_z) = \varphi\vec{A}_x + \varphi\vec{A}_y + \varphi\vec{A}_z \quad \text{Eq. 0-4}$$

The factor is a vector with the same direction and point of application of vector \vec{A} , but with multiplied amplitude. The properties of the scalar multiplication are:

- Additivity in the scalar: $(c + d)\vec{A} = c\vec{A} + d\vec{A}$;
- Additivity in the vector: $c(\vec{A} + \vec{B}) = c\vec{A} + c\vec{B}$;
- Compatibility of product of scalar with scalar multiplication: $c(d\vec{A}) = (cd)\vec{A}$;
- Multiplying by 1 does not change a vector: $1\vec{A} = \vec{A}$;
- Multiplying by 0 gives the zero vector: $0\vec{A} = \vec{0}$;
- Multiplying by -1 gives the additive inverse: $(-1)\vec{A} = -\vec{A}$.

Dot or Scalar Product

Given two vectors $\vec{A} = \vec{A}(x, y, z)$ and $\vec{B} = \vec{B}(x, y, z)$, the dot product or scalar vector is expressed with the formula:

$$\vec{A} \cdot \vec{B} = |\vec{A}| \cdot |\vec{B}| \cos \theta = A_x B_x + A_y B_y + A_z B_z \quad \text{Eq. 0-5}$$

The factor is a scalar and it could be seen as the product of \vec{A} amplitude and it can be seen as the scalar projection of vector \vec{B} in the direction of vector \vec{A} , or vice versa (see Figure 0-3).

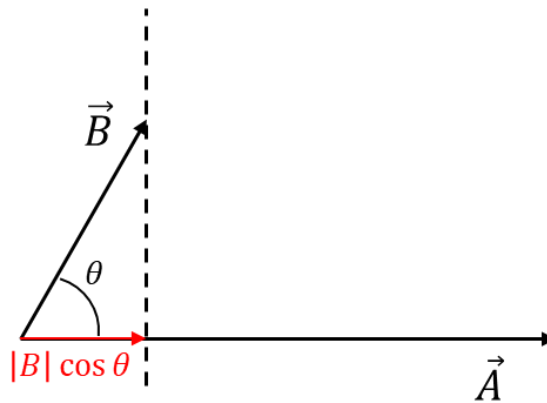


Figure 0-3: scalar projection of vector \vec{B} in the direction of vector \vec{A} .

The properties of the dot product are:

- Commutative: $\vec{A} \cdot \vec{B} = \vec{B} \cdot \vec{A}$;
- Distributive over vector addition: $\vec{C} \cdot (\vec{A} + \vec{B}) = \vec{C} \cdot \vec{A} + \vec{C} \cdot \vec{B}$;
- Not associative;
- $\vec{A} \cdot \vec{A} = A^2$;

- The factor is zero if:
 - $\vec{A} = 0$;
 - $\vec{B} = 0$;
 - $\theta = 90^\circ$ or 270° .

Cross or Vector Product

Given two vectors $\vec{A} = A(x, y, z)$ e $\vec{B} = B(x, y, z)$, the cross product is expressed with the formula:

$$\vec{C} = \vec{A} \times \vec{B} = |\vec{A}| \cdot |\vec{B}| \sin \theta \quad \text{Eq. 0-6}$$

The factor is a vector which is orthogonal to the plane containing vectors \vec{A} and \vec{B} as shown in Figure 0-4.

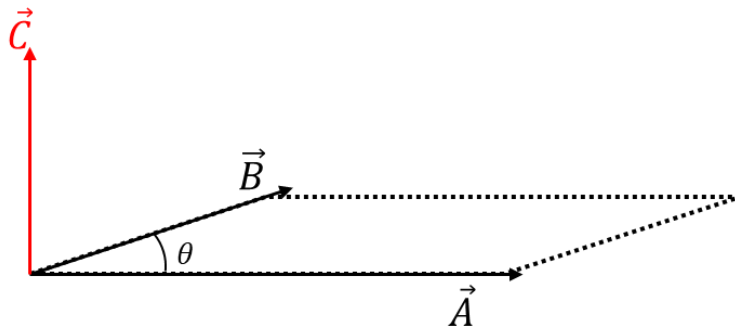


Figure 0-4: representation of the vector product.

The vector product can also be expressed with the matrix notation as the formal determinant.

$$\vec{C} = \vec{A} \times \vec{B} = \det \begin{pmatrix} \vec{i} & \vec{j} & \vec{k} \\ A_x & A_y & A_z \\ B_x & B_y & B_z \end{pmatrix} \quad \text{Eq. 0-7}$$

$$\vec{i}A_yB_z + \vec{j}A_zB_x + \vec{k}A_xB_y - \vec{i}A_zB_y - \vec{j}A_xB_z - \vec{k}A_yB_x \quad \text{Eq. 0-8}$$

$$\vec{C} = \vec{A} \times \vec{B} = (A_yB_z - A_zB_y)\vec{i} + (A_zB_x - A_xB_z)\vec{j} + (A_xB_y - A_yB_x)\vec{k} \quad \text{Eq. 0-9}$$

The properties of the vector product are:

- Distributive: $\vec{C} \times (\vec{A} + \vec{B}) = \vec{C} \times \vec{A} + \vec{C} \times \vec{B}$;
- Not associative;
- Not commutative;
- The factor is null if:
 - $\vec{A} = 0$;

- $\vec{B} = 0$;
- $\theta = 0^\circ$ or 180°
- The factor is maximum if $\vec{A} \perp \vec{B}$;
- The factor is minimum if $\vec{A} \parallel \vec{B}$.

B. Scalar and Vectors Fields

This chapter is a short review of the concepts of scalar and vector fields, these concepts underpin Maxwell's equations.

Scalar Field

The scalar field is a function which links a scalar value to every point of a space.

$$F: \mathbb{R}^n \rightarrow \mathbb{R} \quad \text{Eq. 0-10}$$

The scalar quantity is described by a real number \mathbb{R} called scalar and a unit of measure is often linked to the scalar. Thus, the scalar field φ is a space region where every point has linked a scalar quantity:

$$\varphi = \varphi(x, y, z, t) \quad \text{Eq. 0-11}$$

Physically, the scalar quantity is independent on the space dimension and the coordinate system. Furthermore, in physics, scalar fields often describe a potential energy associated to a force as it will be shown later. The force is a vector field and it can be defined as the gradient of the potential energy scalar field.

Vector Field

The vector field assigns a vector to every point of a subset of space. For instance, a vector field in a plane could be visualized as a collection of arrows with a given magnitude and direction, each attached to a point in the plane.

Vector fields could be used to model speed and direction of a moving flow throughout a space, this physical meaning leads to the notions of divergence and curl used to completely describe the behavior the vector field flow throughout a space. The physical meanings of the divergence and curl are going to be described in the following.

A vector field on a domain in n-dimension Euclidean space can be represented as a vector-values function associating a n-tuple of real numbers to each point of the domain. The vector representation depends on the coordinate system and the transformation law in passing from one coordinate system to the other is well-defined.

Given a subset X in \mathbb{R}^n , a vector field is represented by a vector-valued function:

$$F: X \rightarrow \mathbb{R}^n \quad \text{Eq. 0-12}$$

where F should be continuous and k -times continuously differentiable. Given a plane the corresponding function that associates a vector to each point of the plane is expressed as:

$$\vec{A} = \vec{A}(x, y, t) \tag{Eq. 0-13}$$

The field vector in the space is expressed as:

$$\vec{A} = \vec{A}(x, y, z, t) \tag{Eq. 0-14}$$

Flow of a Vector Field

The flow of the vector field $\vec{A} = \vec{A}(x, y, z, t)$ through the open surface Σ (see Figure 0-5) is expressed as the surface integral of Σ of the dot product of the vector field \vec{A} and the outward-pointing normal \vec{n} of the infinitesimal part of surface Σ .

$$Flow = \int_{\Sigma} \vec{A} \cdot \vec{n} d\Sigma \tag{Eq. 0-15}$$

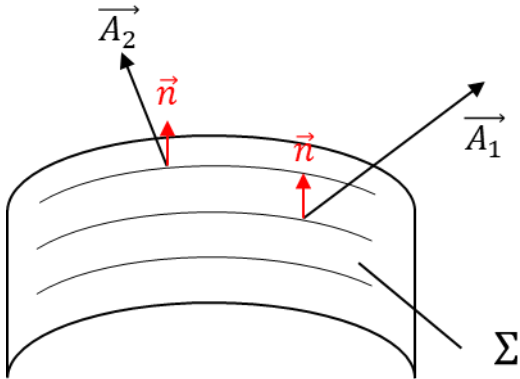


Figure 0-5: representation of the flow of a vector field \vec{A} .

The Eq. 0-15 can be seen as the sum of the infinitesimal flows through each infinitesimal surface as expressed with the formula:

$$dFlow = \vec{B} \cdot \vec{n} d\Sigma \tag{Eq. 0-16}$$

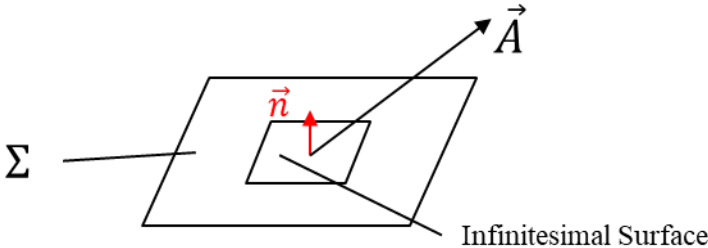


Figure 0-6: infinitesimal flow of vector \vec{A} .

Circulation of a Vector Field

Given a vector field $\vec{A} = \vec{A}(x, y, z, t)$ and a closed boundary Γ , the circulation of the vector field \vec{A} is the line integral around the boundary Γ of the dot product of vector field \vec{A} and the unit vector \vec{dl} along the border Γ .

$$\text{Circulation} = \oint_{\Gamma} \vec{A} \cdot \vec{dl} \quad \text{Eq. 0-17}$$

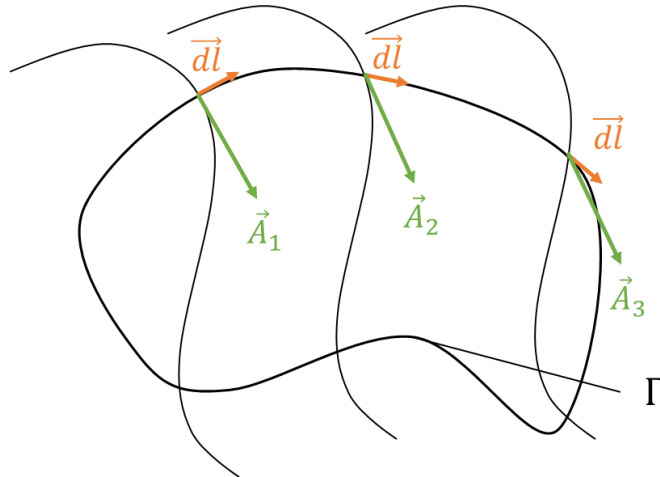


Figure 0-7: representation of the circulation of a vector field \vec{A} .

Nabla Operator

Given three-dimensional Euclidian space \mathbb{R}^3 elicited by a Cartesian coordinate system $\{x, y, z\}$ which unit vectors are $\hat{i}, \hat{j}, \hat{k}$, Nabla (symbol ∇) is expressed as:

$$\nabla \triangleq \frac{\partial}{\partial x} \hat{i} + \frac{\partial}{\partial y} \hat{j} + \frac{\partial}{\partial z} \hat{k} \quad \text{Eq. 0-18}$$

Thus, Nabla is a vector differential operator used in vector calculus. According to the three types of vector product, three distinct differential operators are expressed with Nabla:

- Gradient (∇);
- Divergence ($\nabla \cdot$);
- Curl ($\nabla \times$).

Thus, Nabla could be considered a fictitious vector that could be used to study the vectors fields by the application of differential operations.

Gradient

The gradient is the scalar multiplication between Nabla and a scalar field φ . Given a three-dimensional scalar field:

$$\varphi = \varphi(x, y, z, t) \quad \text{Eq. 0-19}$$

The gradient operator on the scalar field φ constructs out a vector field expressed with the following formula:

$$\nabla\varphi = \left(\frac{\partial\varphi}{\partial x}; \frac{\partial\varphi}{\partial y}; \frac{\partial\varphi}{\partial z}\right) = \frac{\partial\varphi}{\partial x}\vec{i} + \frac{\partial\varphi}{\partial y}\vec{j} + \frac{\partial\varphi}{\partial z}\vec{k} \quad \text{Eq. 0-20}$$

According to physics, the gradient points out the maximum variation of the scalar field φ .

Divergence

Given a three-dimensional vector field:

$$\vec{A} = \vec{A}(x, y, z, t) \quad \text{Eq. 0-21}$$

The dot or scalar product between Nabla and the vector field gives a scalar field. This differential operation is called divergence of the vector field \vec{A} and is expressed with the formula:

$$\nabla \cdot \vec{A} = \left(\frac{dA_x}{dx} + \frac{dA_y}{dy} + \frac{dA_z}{dz}\right) \quad \text{Eq. 0-22}$$

This differential operation is applied on each point of the space belonging to the vector field.

In physical terms, the divergence of a vector field is the extent to which the vector field behaves like a source at a given point, thus the divergence shows sources or sinks of the vector field \vec{A} .

A vector field is called solenoidal if it has zero divergence everywhere.

Divergence Theorem or Gauss' Theorem

The divergence theorem relates the flow of vector field to the behavior of the tensor field inside the surface.

Given the vector field \vec{A} and the volume τ contained by the closed surface Σ , the divergence theorem states that the volume integral over τ of the divergence of \vec{A} is equal to the flow of the vector field \vec{A} through the closed boundary Σ .

$$\oint_{\tau} \nabla \cdot \vec{A} d\tau = \int_{\Sigma} \vec{A} \cdot \vec{n} d\Sigma \quad \text{Eq. 0-23}$$

If volume integral of the divergence of is zero, also the flow of the vector field through closed boundary is zero. This means that the incoming flow is equal to outgoing flow, thus there aren't any source of sinks of the vector field \vec{A} .

$$\oint_{\tau} \nabla \cdot \vec{A} d\tau = 0 \quad \text{Eq. 0-24}$$

$$\int_{\Sigma} \vec{A} \cdot \vec{n} d\Sigma = 0 \quad \text{Eq. 0-25}$$

Curl

Given a three-dimensional vector field:

$$\vec{A} = \vec{A}(x, y, z, t) \quad \text{Eq. 0-26}$$

The cross product between Nabla and the vector field gives a vector field. This differential operation is called curl of the vector field \vec{A} and is expressed with the formula:

$$\nabla \times \vec{A} = \hat{i} \left(\frac{\partial A_z}{\partial y} - \frac{\partial A_y}{\partial z} \right) + \hat{j} \left(\frac{\partial A_x}{\partial z} - \frac{\partial A_z}{\partial x} \right) + \hat{k} \left(\frac{\partial A_y}{\partial x} - \frac{\partial A_x}{\partial y} \right) \quad \text{Eq. 0-27}$$

This formula derives from the matrix notation of cross product of Nabla and \vec{A} :

$$\nabla \times \vec{A} = \det \begin{pmatrix} \hat{i} & \hat{j} & \hat{k} \\ \frac{\partial}{\partial x} & \frac{\partial}{\partial y} & \frac{\partial}{\partial z} \\ A_x & A_y & A_z \end{pmatrix} \quad \text{Eq. 0-28}$$

It is important to stress that the curl operator uses the cross product and thus it makes sense only in a three-dimensional system. The curl is applied on each point of the space belonging to the vector field.

From a physical point of view the curl describes the rotation trend of the vector field in a three-dimensional space.

A vector field with zero curl everywhere is called conservative field and does not present a rotation trend.

Stokes' Theorem

Given a vector field \vec{A} , an open surface Σ and its boundary Γ , the flow of cross product of field vector \vec{A} through the surface Σ is equal to the circulation of the vector field \vec{A} along the boundary Γ .

$$\int_{\Sigma} (\nabla \times \vec{A}) \cdot \vec{n} d\Sigma = \oint_{\Gamma} \vec{A} \cdot d\vec{l} \quad \text{Eq. 0-29}$$

If the first term of Eq. 0-29 is zero, the vector field \vec{A} hasn't the trend to rotate on itself.

Laplace Operator or Laplacian

The Laplace operator or Laplacian is a differential operator given by the cross product of Nabla by itself as expressed with the formula:

$$\nabla \cdot \nabla = \nabla^2 = \frac{\partial^2}{\partial x^2} + \frac{\partial^2}{\partial y^2} + \frac{\partial^2}{\partial z^2} \quad \text{Eq. 0-30}$$

The Laplace operator can be applied to both a scalar field or a vector field; in latter case the Laplace operator is applied to each component of the vector field.

C. Charge Conservation Law

The charge conservation law expresses the invariance of charge inside a volume τ closed by the boundary surface Σ as shown in Figure 0-8.

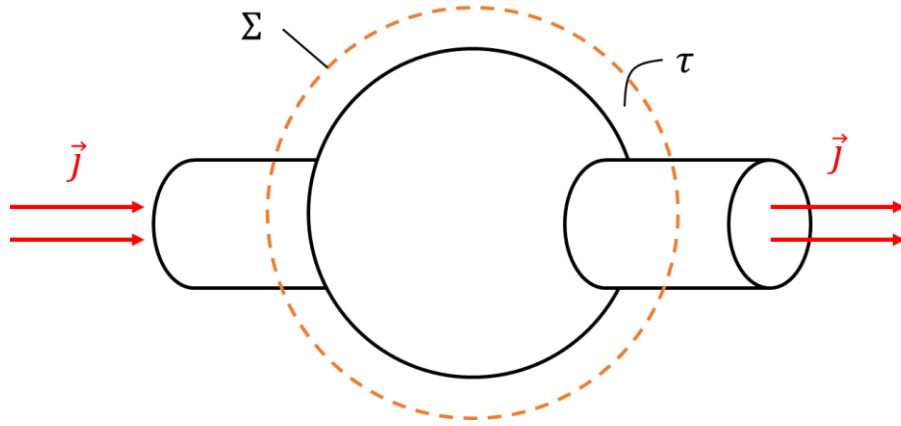


Figure 0-8: representation of charge conservation law.

The differential form of the charge conservation law is expressed as:

$$\nabla \cdot \vec{j} = -\frac{\partial \rho}{\partial t} \quad \text{Eq. 0-31}$$

The law conservation can be expressed also with integral formulation by applying the volume integral on the both equation members.

$$\int_{\tau} \nabla \cdot \vec{j} d\tau = \int_{\tau} -\frac{\partial \rho}{\partial t} d\tau \quad \text{Eq. 0-32}$$

$$\int_{\tau} \nabla \cdot \vec{j} d\tau = -\frac{\partial}{\partial t} \int_{\tau} \rho d\tau \quad \text{Eq. 0-33}$$

Applying the divergence theorem on the first member of Eq. 0-33 as follows:

$$\oint_{\Sigma} \vec{j} \cdot \vec{n} d\Sigma = -\frac{\partial}{\partial t} \int_{\tau} \rho d\tau \quad \text{Eq. 0-34}$$

The first member is the flow of current density through the boundary surface Σ that corresponds to the electric current i , while the second member is the volume integral on τ of the charge density per unit volume that correspond of total charge Q contents in volume τ . Thus, Eq. 0-34 becomes:

$$i = -\frac{\partial Q}{\partial t} \quad \text{Eq. 0-35}$$

D. Clarke's and Park's Transformations

This chapter recalls the well-known transformation matrixes used in the field vector control to transform a three-phase system in to a two-phase system synchronous with the rotor rotational speed.

Clarke's Transformation: from a three-phase system to a two-axis stationary frame

The Clarke's Transformation is a mathematical transformation to simplify the analysis of three-phase systems. The three-phase winding is transformed in a two-axis system in the stationary frame composed by $\alpha - \beta$ windings perpendicular to each other.

The complete form of Clarke's transformation matrix could be at constant amplitude (see Eq. 0-36) or at constant power (see Eq. 0-37). The result of Clarke's transformation is a two-axis stationary system where α and β are the perpendicular component, while o is homopolar component.

$$\begin{bmatrix} \alpha \\ \beta \\ o \end{bmatrix} = \frac{2}{3} \cdot \begin{bmatrix} 1 & -\frac{1}{2} & -\frac{1}{2} \\ 0 & \frac{\sqrt{3}}{2} & -\frac{\sqrt{3}}{2} \\ \frac{1}{2} & \frac{1}{2} & \frac{1}{2} \end{bmatrix} \cdot \begin{bmatrix} u \\ v \\ w \end{bmatrix} \quad \text{Eq. 0-36}$$

$$\begin{bmatrix} \alpha \\ \beta \\ o \end{bmatrix} = \sqrt{\frac{2}{3}} \cdot \begin{bmatrix} 1 & -\frac{1}{2} & -\frac{1}{2} \\ 0 & \frac{\sqrt{3}}{2} & -\frac{\sqrt{3}}{2} \\ \frac{1}{\sqrt{2}} & \frac{1}{\sqrt{2}} & \frac{1}{\sqrt{2}} \end{bmatrix} \cdot \begin{bmatrix} u \\ v \\ w \end{bmatrix} \quad \text{Eq. 0-37}$$

In general, the homopolar component is the linear combination of phases u, v, w equal to each other. In addition, since the three-phase system is assumed to be symmetric (the three voltages are out-of-sync of 120° among them and have the same amplitude) and currents are balanced, the homopolar component o is equal to zero.

The following equation is guaranteed by the wye-connection of the three-phase system.

$$u + v + w = 0 \quad \text{Eq. 0-38}$$

Thus, according to the first Kirchhoff's Principle (KCL), expressed as Eq. 0-39, the three current are linearly dependent and the system can be completely described by two currents. Given the above, a three-phase system could be symmetric, but unbalance and a homopolar component could arise.

$$i_{su} + i_{sv} + i_{sw} = 0 \quad \text{Eq. 0-39}$$

The vectoral sum of the three stator currents i_{su} , i_{sv} , i_{sw} produces the rotating current phasor \vec{i}_s . In the two-axis stationary frame the current phasor can be broken up in two components: $i_{s\alpha} - i_{s\beta}$ as shown in Figure 0-9.

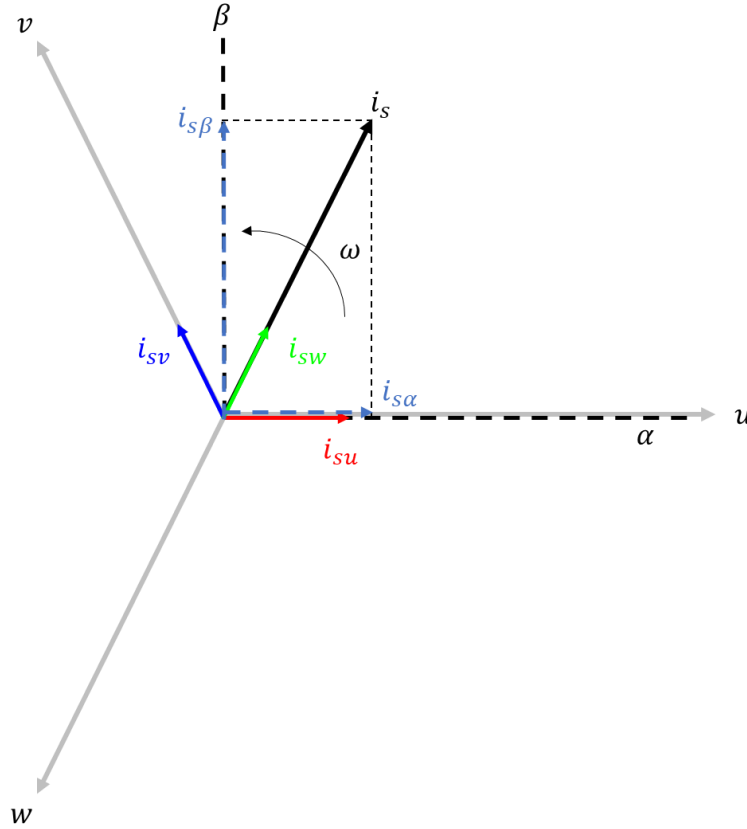


Figure 0-9: current phasor i_s representation on three-phase system and on two-axis stationary frame.

The currents $i_{s\alpha}$ and $i_{s\beta}$ flow through two imaginary coils whose axes lay respectively on α -axis and β -axis.

$$\begin{cases} i_{s\alpha} = i_{su} \cos 0 - i_{sv} \cos \frac{3\pi}{2} - i_{sw} \cos \frac{4\pi}{3} \\ i_{s\beta} = i_{su} \sin 0 + i_{sv} \sin \frac{3\pi}{2} - i_{sw} \sin \frac{4\pi}{3} \end{cases} \quad \text{Eq. 0-40}$$

$$\begin{cases} i_{s\alpha} = i_{su} - \frac{i_{sv}}{2} - \frac{i_{sw}}{2} \\ i_{s\beta} = \frac{\sqrt{3}i_{sv}}{2} - \frac{\sqrt{3}i_{sw}}{2} \end{cases} \quad \text{Eq. 0-41}$$

If current phasor \vec{i}_s lays on α -axis, the current components of vectors i_{sb} and i_{sc} along the β -axis should cancel with each other. This condition can be expressed as:

$$\begin{cases} i_{s\alpha} = i_s \\ i_{s\beta} = 0 \end{cases} \quad \text{Eq. 0-42}$$

In addition, considering the equation Eq. 0-39, the current component of phase u can be expressed as:

$$i_{su} = -(i_{sv} + i_{sw}) \quad \text{Eq. 0-43}$$

Considering Eq. 0-43 and the first equation of the system in Eq. 0-41, the $i_{s\alpha}$ current component becomes as:

$$i_{s\alpha} = i_{su} - \frac{-(i_{sv} + i_{sw})}{2} \quad \text{Eq. 0-44}$$

$$i_{s\alpha} = i_{su} + \frac{i_{su}}{2} \quad \text{Eq. 0-45}$$

$$i_{s\alpha} = \frac{3i_{su}}{2} \quad \text{Eq. 0-46}$$

The current component $i_{s\alpha}$ is $\frac{3}{2}$ higher than i_{su} , thus in order to apply the correct constant amplitude transformation, the multiplication factor $\frac{2}{3}$ must be used.

The system of equations in Eq. 0-41 is valid also for voltage components on α -axis and β -axis.

$$\begin{cases} v_{s\alpha} = v_{su} - \frac{v_{sv}}{2} - \frac{v_{sw}}{2} \\ v_{s\beta} = \frac{\sqrt{3}v_{sv}}{2} - \frac{\sqrt{3}v_{sw}}{2} \end{cases} \quad \text{Eq. 0-47}$$

The matrix form of current and voltage components are expressed on α -axis and β -axis by means of Clarke's transformation as follows:

$$\begin{bmatrix} i_{sa} \\ i_{s\beta} \end{bmatrix} = K \begin{bmatrix} 1 & -\frac{1}{2} & -\frac{1}{2} \\ 0 & \frac{\sqrt{3}}{2} & -\frac{\sqrt{3}}{2} \end{bmatrix} \cdot \begin{bmatrix} i_{su} \\ i_{sv} \\ i_{sw} \end{bmatrix} \quad \text{Eq. 0-48}$$

$$\begin{bmatrix} v_{sa} \\ v_{s\beta} \end{bmatrix} = K \begin{bmatrix} 1 & -\frac{1}{2} & -\frac{1}{2} \\ 0 & \frac{\sqrt{3}}{2} & -\frac{\sqrt{3}}{2} \end{bmatrix} \cdot \begin{bmatrix} v_{su} \\ v_{sv} \\ v_{sw} \end{bmatrix} \quad \text{Eq. 0-49}$$

where K is the coefficient which defines a constant amplitude or a constant power transformation. In order to simplify the matrix form of Eq. 0-48 and Eq. 0-49, the compact forms are introduced:

$$[i_s]_{\alpha\beta} = T_{uvw}^{\alpha\beta} [i_s]_{uvw} \quad \text{Eq. 0-50}$$

$$[v_s]_{\alpha\beta} = T_{uvw}^{\alpha\beta} [v_s]_{uvw} \quad \text{Eq. 0-51}$$

where $T_{uvw}^{\alpha\beta}$ is the Clarke's transformation from a three-phase system to a two-axis stationary frame system.

The Clarke's transformation can be applied also maintaining constant the power, in this case the coefficient K value is computed so that the $T_{uvw}^{\alpha\beta}$ matrix is an orthogonal matrix. By so doing the product of $T_{uvw}^{\alpha\beta}$ and its transpose matrix $T_{uvw}^{\alpha\beta t}$ is equal to the identity matrix I .

$$K \begin{bmatrix} 1 & -\frac{1}{2} & -\frac{1}{2} \\ 0 & \frac{\sqrt{3}}{2} & -\frac{\sqrt{3}}{2} \end{bmatrix} \cdot K \begin{bmatrix} 1 & 0 \\ -\frac{1}{2} & \frac{\sqrt{3}}{2} \\ -\frac{1}{2} & -\frac{\sqrt{3}}{2} \end{bmatrix} = I \quad \text{Eq. 0-52}$$

$$K^2 \begin{bmatrix} \frac{3}{2} & 0 \\ 0 & \frac{3}{2} \end{bmatrix} = I \quad \text{Eq. 0-53}$$

$$\frac{3K^2}{2} \begin{bmatrix} 1 & 0 \\ 0 & 1 \end{bmatrix} = \begin{bmatrix} 1 & 0 \\ 0 & 1 \end{bmatrix} \quad \text{Eq. 0-54}$$

$$\frac{3K^2}{2} = 1 \quad \text{Eq. 0-55}$$

$$K^2 = \frac{2}{3} \quad \text{Eq. 0-56}$$

$$K = \sqrt{\frac{2}{3}} \quad \text{Eq. 0-57}$$

Thus, the Clarke's matrix transformation $T_{uvw}^{\alpha\beta}$ for constant power is expressed as:

$$T_{uvw}^{\alpha\beta} = \sqrt{\frac{2}{3}} \cdot \begin{bmatrix} 1 & -\frac{1}{2} & -\frac{1}{2} \\ 0 & \frac{\sqrt{3}}{2} & -\frac{\sqrt{3}}{2} \end{bmatrix} \quad \text{Eq. 0-58}$$

The transpose Clarke's matrix transformation is used to pass from the two-axis stationary frame to the three-phase system.

$$T_{uvw}^{\alpha\beta -1} = K \cdot \begin{bmatrix} 1 & 0 \\ -\frac{1}{2} & \frac{\sqrt{3}}{2} \\ -\frac{1}{2} & -\frac{\sqrt{3}}{2} \end{bmatrix} \quad \text{Eq. 0-59}$$

$$\begin{bmatrix} i_{su} \\ i_{sv} \\ i_{sw} \end{bmatrix} = K \cdot \begin{bmatrix} 1 & 0 \\ -\frac{1}{2} & \frac{\sqrt{3}}{2} \\ -\frac{1}{2} & -\frac{\sqrt{3}}{2} \end{bmatrix} \cdot \begin{bmatrix} i_{s\alpha} \\ i_{s\beta} \end{bmatrix} \quad \text{Eq. 0-60}$$

$$\begin{bmatrix} v_{su} \\ v_{sv} \\ v_{sw} \end{bmatrix} = K \cdot \begin{bmatrix} 1 & 0 \\ -\frac{1}{2} & \frac{\sqrt{3}}{2} \\ -\frac{1}{2} & -\frac{\sqrt{3}}{2} \end{bmatrix} \cdot \begin{bmatrix} v_{s\alpha} \\ v_{s\beta} \end{bmatrix} \quad \text{Eq. 0-61}$$

Park's Transformation: from two-axis stationary frame to two-axis rotational frame

The Park's transformation is used to pass from the two-axis stationary frame $\alpha - \beta$ to the two-axis rotational frame $d - q$ which rotates synchronously with the rotor angular speed ω . The current phasor i_s has constant amplitude and angular speed $\omega = \frac{d\theta}{dt}$ and it is out-of-phase of a generic angle γ respect d-axis as shown in Figure 0-10.

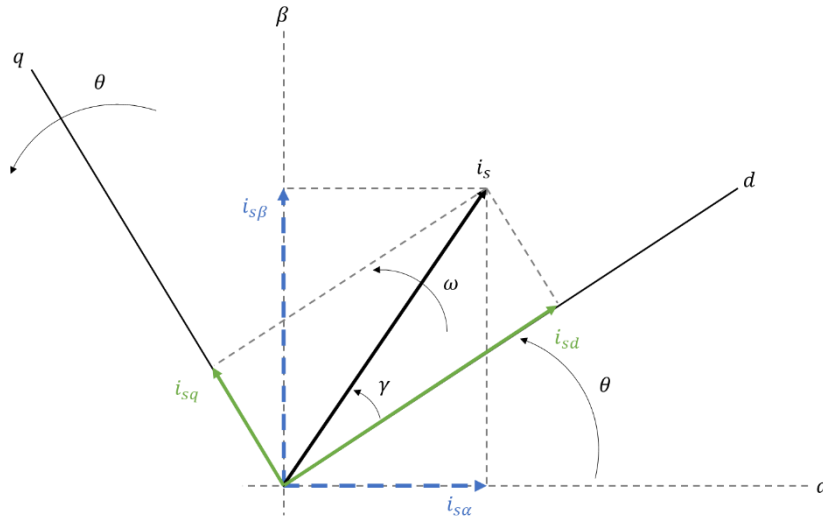


Figure 0-10: current phasor i_s representation on stationary two-axis frame and rotational two-axis frame.

The Eq. 0-62 shows the Park's transformation which corresponds to the rotation matrix.

$$\begin{bmatrix} d \\ q \end{bmatrix} = \begin{bmatrix} \cos \theta & \sin \theta \\ -\sin \theta & \cos \theta \end{bmatrix} \cdot \begin{bmatrix} \alpha \\ \beta \end{bmatrix} \quad \text{Eq. 0-62}$$

According to Eq. 0-62, current phasor i_s can be broken up in two components i_{sd} and i_{sq} as a function of the stationary components $i_{s\alpha}$ and $i_{s\beta}$.

$$\begin{cases} i_{sd} = i_{s\alpha} \cos \theta + i_{s\beta} \sin \theta \\ i_{sq} = -i_{s\alpha} \sin \theta + i_{s\beta} \cos \theta \end{cases} \quad \text{Eq. 0-63}$$

As for the stationary frame, the two current components flow through two imaginary coils which axes lay respectively on d -axis and q -axis and rotates with constant angular speed ω .

The main advantage of the $d - q$ rotating frame is that electrical quantities have constant amplitude and rotate with angular speed ω , so they are time invariant.

The matrix forms of current and voltage components on the $d - q$ frame are expressed by Eq. 0-64 and Eq. 0-65, while show the compact form.

$$\begin{bmatrix} i_{sd} \\ i_{sq} \end{bmatrix} = \begin{bmatrix} \cos \theta & \sin \theta \\ -\sin \theta & \cos \theta \end{bmatrix} \cdot \begin{bmatrix} i_{s\alpha} \\ i_{s\beta} \end{bmatrix} \quad \text{Eq. 0-64}$$

$$\begin{bmatrix} v_{sd} \\ v_{sq} \end{bmatrix} = \begin{bmatrix} \cos \theta & \sin \theta \\ -\sin \theta & \cos \theta \end{bmatrix} \cdot \begin{bmatrix} v_{s\alpha} \\ v_{s\beta} \end{bmatrix} \quad \text{Eq. 0-65}$$

$$[i_s]_{dq} = T_{\alpha\beta}^{dq} [i_s]_{\alpha\beta} \quad \text{Eq. 0-66}$$

$$[v]_{dq} = T_{\alpha\beta}^{dq} [v_s]_{\alpha\beta} \quad \text{Eq. 0-67}$$

The transpose matrix of Park's transformation is used to pass from the rotational two-axis frame $d - q$ to the static two-axis frame $\alpha - \beta$.

$$T_{\alpha\beta}^{dq^t} = \begin{bmatrix} \cos \theta & -\sin \theta \\ \sin \theta & \cos \theta \end{bmatrix} \quad \text{Eq. 0-68}$$